Novel Particle Sizing Techniques

By Rui Chen, MEng.

Thesis submitted to the University of Nottingham for the degree of Doctor of Philosophy

June 2013

Abstract

Two novel approaches to particle size measurement are investigated; these are designated as Particle Movement Displacement Distribution (PMDD) method and Separated Multiple Image Technique (SMIT). An advantage of these methods compared with the established particle sizing methods of Static Light Scattering (SLS) and Dynamic Light Scattering (DLS) is that PMDD and SMIT do not suffer from the intensity weighting problem that affects SLS and DLS.

The performance of the PMDD method is examined through computer simulations and through analysis of pre-existing experimental data. The SMIT method is investigated through computer simulations and through the construction and use of an optical system.

The ability of both methods was measured through the assessment of an 'area error' measure which gives an estimate of the accuracy of a recovered particle size distribution. This area error measure varies between 0 and 2; with 0 corresponding to a perfectly recovered distribution. Typically a good inversion of DLS data can achieve an area-error value of 0.32 to 0.34 and this figure (along with the recovered mean particle size and standard deviation of the distribution) was used to judge quantitatively the success of the methods.

The PMDD method measures the centre of individual particles in each image. A vector histogram is formed based on the connection between the centres in the first image and the centres in the next image. This vector histogram contains information

about the particle size distribution. A maximum likelihood data inversion procedure is used to yield a particle size distribution from this data.

The SMIT method is similar to the Static Light Scattering (SLS) method, but it combines angular dependent intensity method and individual visualisation method together to recover individual particle sizes without an intensity weighting. A multi-aperture mask and wedge prisms are utilised in this method to capture particle images formed from light scattered into a number of selected directions. A look-up table is then used to recover the individual particle sizes, which are then formed into a histogram.

For the PMDD method, computer simulation results established the optimum values for parameters such as the time interval between frames, the exposure time and the particle concentration and also investigated the effects of different noise sources. For mono-modal size distributions, the PMDD method was shown through computer simulation to be capable of recovering a particle size distribution with an area error of around 0.27 which compares well with the typical DLS result. PMDD results were also recovered from mono-modal experimental data with mean particle sizes close to the manufacturers quoted particle mean size. However, recovery of bi-modal distributions was found to be not so successful; for bi-modal distributions, the recovered distributions generally had only a single peak, which, of course gives a very poor area-error figure. This result compares poorly with the particle tracking method 'Nano Particle Tracking Analysis' which is able to recover bi-modal distributions. For this reason further research was concentrated on an image intensity method (SMIT).

For the SMIT method, computer simulation results established the optimum values for parameters such as the particle concentration and also investigated the effects of different noise sources and of aberrations in the optical system. The SMIT method was shown through computer simulation to be capable of recovering particle size distributions for both mono-modal and bi-modal distributions. The area error values obtained were in the range 0.24 to 0.45, and most of the results are good compared to the DLS value.

The major problem with the SMIT method was found to be the presence of a small number of recovered particle radii much larger (or smaller) than the true sizes. These errors were attributed to ambiguities in the look-up table system used to convert the relative intensity data values into particle sizes. Two potential methods to reduce the influence of these ambiguities were investigated. These were, firstly by combining Brownian motion movement data from tracking individual particles over a few frames of data, and secondly by combining an estimate of the total scattered intensity from a particle with the normal SMIT data to constrain the look-up procedure.

In computer simulations both approaches gave some improvement but the use of the total scattered intensity method gave the better results. In a computer simulation this method managed to improve the area-error from 0.37 for SMIT alone to 0.25 for SMIT combined with this extra information.

Based on the success of these computer simulation results, an experimental SMIT system was constructed and tested. It was found necessary to first calibrate the optical system, to account for the different optical transmission coefficients of the different

prisms/optical paths. But using a particle sample with particles of known size to calibrate; other particle sizes were successfully recovered from the experimental data using the original SMIT data processing. A majority of the recovered particle radius were close to the manufacturers quoted particle mean radius.

Attempts to implement the total intensity approach to enhance the SMIT were found not be successful due to the difficulty in measuring the small displacements in particle positions required with sufficient accuracy. A possible alternative design to overcome this problem is suggested in the future work section 7.2.

Acknowledgements

It is a pleasure to thank all of those who made this thesis possible. First of all, I would like to thank my supervisor Dr John Walker for his enthusiastic guidance and patient support and encouragement throughout the time of this project. I have been greatly inspired by his insightful knowledge and expertise. I am also deeply indebted to Dr. Nam Trung Huynh for his assistance and useful discussions. It has been a great pleasure working with the people in Applied Optics Group. This thesis would not have been possible without the input from all of them.

The moral support from my family and friends has motivated me and I would like to show my gratitude to my whole family for their wonderful love and support. I sincerely thank my parents and my husband, who have always been there for me. I hope I have made them proud. Many thanks must go to my dear friends who have made my life rather interesting throughout this period.

Finally, I would like to thank the school of Electrical and Electronic Engineering – the University of Nottingham (Tower Innovation Scholarship) who provided this research funding.

Contents

1 Introduction and Background Information

This chapter describes the importance of particle sizing in a number of application areas. It then reviews both non-optical and optical techniques and summarises the motivation and aims of the work in this thesis. It concludes with an outline of the thesis chapters.

1.1 Particles; their Application and Characterization

One definition of the word, particle is an extremely tiny portion of matter, such as an atom or electron in physics (1). However, the particles of concern in this thesis are nanoparticles, globules, proteins, colloids and larger specks of matter, up into the hundreds of microns. They exist in different forms; such as bubbles or droplets suspended in liquid, air or solid forms. Many particles exist around our daily life. Particle characterization is an attempt to describe a particle. Usually, it does not refer to the particles' chemical makeup but to their sizes and shapes. There are many fields that rely heavily on particle technologies (4, 15, 18).

- Food and drinks
- Biotechnology
- Chemical and cosmetics
- Pharmaceutical: drug products
- Environmental science
- Metal, mining and minerals
- Materials industry

The size of fine particles affects material properties in many different ways. For example, the sizes of particles affect the taste and feel of peanut butter and chocolate; sugar refining (15), and the dissolution rates of milk and coffee (2, 4). For some chemical products (liquids, suspensions, or emulsions), particle size impacts on the fluid flow, heat and mass, and the settling rates of larger particles also depends on their size and density. Therefore, particle size is a key indicator to improve the performance of chemical products. Samples are easily found in plenty of cosmetic products, including lipsticks, mascara, moisturisers, eye shadows, toothpastes etc. The skin should rapidly absorb moisturisers, and therefore the particle size should generally be less than 200nm. Particles are commonly used in the pharmaceutical area. Particle size is important for dissolution. Because small particles dissolve more quickly than larger ones, it determines drugs behaviour (3). Similarly, the specification of soil and sediments in the environmental industry also relies on particle characterization. Particle size determines the strength and stability of soil and properties related to transport and retention of water, heat and nutrients. In addition, particle characterization is crucial in the materials industry, which has an extremely diverse range of products. These include adhesive, ceramic material, building construction materials, polymers, plastic, rubber, paper, surface coasting, in automotive, aerospace etc (5). Titanium dioxide used in papers defines the brightness of the finished product. The size distribution of particles determines the clarity of print (for toners) or surface finish, such as flat and gloss. In aircraft studies, the droplet size in a fuel spray defines the speed and efficiency of combustion, which directly influences engine performance (4). The extremely broad applications of particle characterization have led to particle analysis technique developing rapidly over the past few decades.

There are a number of parameters to characterise particles, such as size, shape, volume, density, refractive index and etc. The most common and important properties are size and shape. In industrial and commercial products, particles cover a range from a few nanometres to a few millimetres. However, this thesis focuses on the submicron range.

Particles can be any shape, including spherical or irregular shape. If a particle is a sphere, it is easy to study. However, if it is irregular in shape, its characterisation is more complex. Normally, radius or diameter is used to describe spherical particles. For non-spherical particles, equivalent sphere approximations (equivalent diameter or equivalent radius) are employed to define the particles. There are lots of ways to define equivalent diameter. Table **1.1** illustrates some different ways to calculate equivalent diameters.

Table 1.1: Some Equivalent Diameters

Symbol	Name	Definition
$\mathbf{d_v}$	Volume diameter	Diameter of a sphere with the same volume as the particle.
$\mathbf{d_s}$	Surface diameter	Diameter of a sphere with the same surface area as the particle.
$\mathbf{d_d}$	Drag diameter	Diameter of a sphere with the same viscous drag as a particle in a fluid at the same velocity.
$\mathbf{d_{sk}}$	Stokes' diameter	Diameter of a sphere of similar density having the same limiting velocity when falling under gravity in a viscous medium.
$\mathbf{d_p}$	Projected area	Diameter of a circle having the same area as the projection of the particle.

Table 1.1: Some equivalent diameters (3).

Due to the different definitions and different methods, the equivalent sphere approximations may be different. How to choose a suitable equivalent diameter depends on different demands. If you wish to study the pigment covering power of a material, it is better to select projected area diameter as the equivalent diameter (3).

1.1 Non-optical Particle Sizing Techniques

There are a large number of particle analysis techniques, especially particle sizing techniques. Based on different techniques and theories, different instruments are designed to address specific problems and satisfy specific demand. From hundreds of microns to a few nanometres, particles cover quite a large range. The properties of different sizes of particles change a lot. Therefore, finding one instrument or technique to suit every particle sizing need and solve all the particular problems, is impossible in practice. Some common particle sizing techniques have their own specifications and working ranges in order to suit particular demands and tasks (3, 4, 6, 72). The most common non-optical particle sizing techniques used to date are: sieving, sedimentation, electrical zone sensing, and acoustic analysis. With the rapid development of lasers, electronics, optics and computing techniques, optical particle sizing techniques now play a crucial role in particle sizing analysis due to their high accuracy, rapid measurement time and ease of control. In this section, the traditional non-optical particle sizing techniques will be presented, whilst the optical particle sizing techniques are discussed in the following section.

1.1.1 Sieving

Sieving is probably the oldest and simplest technique used for particle separation since Egyptian times. Since the 16th century, sieving has been in common use. It is used to classify powders into different size ranges. In the mid-19th century, attributed to the high precision sieves made, sieving techniques became popular to size particles. In 1867, Von Rittinger (3, 6) introduced a system of using a series of sieves, starting with 75μm and increasing in aperture by steps of $\sqrt{2}$, known as $\sqrt{2}$ progression. There are lots of standards in different countries, but the international standard is based on $\sqrt{2}$ progression. Although sieving is an old and traditional particle sizing method, it is still an essential tool for particle sizing nowadays (3, 6).

Different sizes of sieve are utilised to classify samples into two parts: the samples retained on the screens and the samples passed through them. In practice, according to sample sizes and their size distribution, five or six sieves are employed to sort particles. From top to bottom, the sizes of sieves are decreasing. Consequently, the samples can pass through them in sequence and be classified into different size ranges (4).

Sieving is a relatively straightforward method with simple principles and equipment and it is low cost. The sieving technique is suitable for the following conditions (3):

- The sample is fairly coarse, normally above 100 μm. The holes can not be extremely small to classify very small particles.
- The samples should be separated particles and can easily flow.

- The samples contain different densities (difficult for sedimentation), different refractive indices (difficult for light scattering) or are water-soluble or conductive (difficult for a Coulter counter).

However, when particles are under the following conditions, it is better not to use the sieving method (3).

- The samples are under 100μm.
- The particles are fragile.
- High precision of particle sizing is needed.
- The powder easily acquires an electrostatic charge.
- The particles are in the form of needles. When a particle passes through the sieve, it needs two dimensions of the particle smaller than the holes. However, if the third dimension is too long, according to weight and gravity theory, the particle will lie in the stable position. Thus, it is hard to pass through the holes and may cause an ambiguous result.

1.1.2 Sedimentation

A number of instruments have been devised for sedimentation. They generally depend on two conditions: a gravitational field (called gravitational sedimentation) or a centrifugal field (centrifugal sedimentation). According to their terminal velocity in the fluid, particle sizes can be deduced (3, 4).

The relationship between settling velocity and particle size is described by Stokes law:

$$v = \frac{g(\rho_s - \rho_l)d_{sk}^2}{18\eta} \tag{1.1}$$

$\boldsymbol{d_{sk}}$ is the Stokes' diameter discussed in Table **1.1**. The parameters $\boldsymbol{\eta}$, $\boldsymbol{v}$, $\boldsymbol{\rho_s}$, $\boldsymbol{\rho_l}$ and $\boldsymbol{g}$ represent the viscosity of suspension liquid, particle terminal velocity, particle density, liquid density and gravitational acceleration, respectively (3).

There are two types of analysis methods for sedimentation: incremental and cumulative. The incremental method finds the size distribution by measuring the concentration of particles at a particular depth as a function of time, whereas the latter one finds the total amount of material, which has settled out as a function of time. According to the initial state of the samples, they can also be classified as line start or homogeneous methods. At the beginning, a line-start method prepares all samples on the top of sedimentation fluid, whereas a homogeneous method assumes that the samples are uniformly distributed in the fluid. Therefore, based on different combinations of force field, different measurement location in the fluid and different particle initial state, sedimentation instruments have different arrangements (3, 4, 7).

Although it is one of the earliest and simplest techniques for particle sizing, it is widely used in some industrial areas such as paint pigment and drinks. Unfortunately, there are some limitations associated with sedimentation. All samples must have a low concentration and be within a certain size range in order to avoid interactions between particles and interference from other forces or motions. Basically, the solid concentration should not exceed 1-2% in most experiments. Because very small particles move more quickly under Brownian motion; this will bring in a large disturbance (9). In addition, low concentration can also reduce wall effects. Normally, particles from 0.5 to 100 μm are suitable in a gravitational sedimentation experiment,

whereas particles can be smaller from 0.05 to 5 μm under the centrifugal sedimentation method (3, 4). In practice, if some of the particles are non-spherical, the measured size distribution will be biased toward larger particles and broader than the real distribution. This is also a weakness of sedimentation.

1.1.3 Electrical Zone Sensing

The electrical zone sensing method, which is also called "Coulter Counter" was first used for particle sizing in the 1950's by W. H. Coulter (3, 4). It is used widely in some pharmaceutical areas. Its working principle, which is very simple, is illustrated in Figure **1.1**.

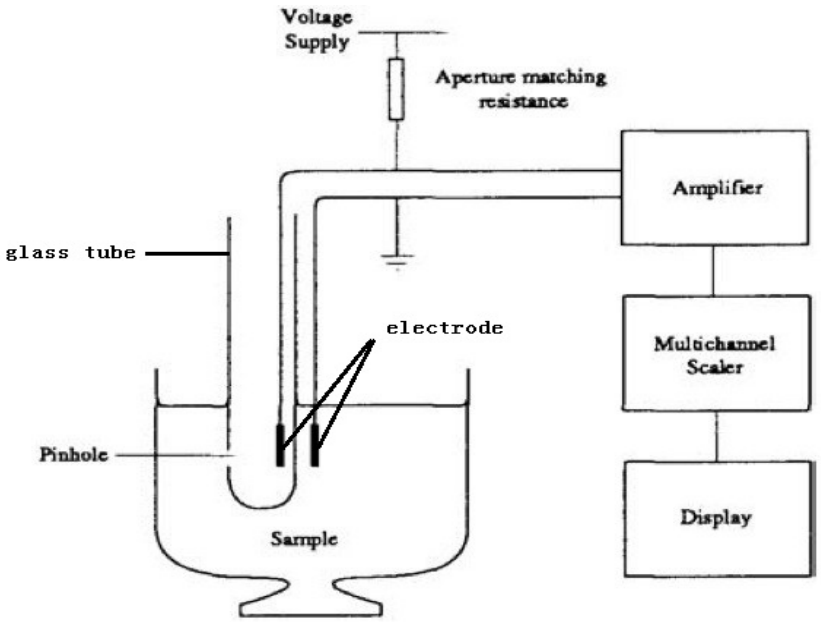

Figure 1.1: The principle of the Coulter Counter (**3**).

The glass tube is immersed in the suspension, which normally is a 0.9% sodium chloride (NaCl) solution. Two electrodes are placed inside and outside the pinhole to form a small current between them. When particles pass through the pinhole, the resistance of the orifice varies slightly. Obviously, smaller particles produce smaller resistance changes; larger particles lead to greater resistance changes. Consequently, particle sizes can be determined by measuring the changes of resistance. A Coulter Counter measures the amplitude of the voltage pulse to measure resistance and hence deduce particle sizes (3, 4, 8, 15, 18).

Electrical zone sensing is suitable for particle sizes between micrometre and millimetre; small particles are significantly influenced by background noise in suspension. In addition, sedimentation of large particles in the electrolyte should be avoided.

In practice, the impulse signal is very weak when a particle passes through the pinhole. Any interference or vibration can cause small signals between the electrodes and bring in errors to the real results. This is a serious problem of electrical zone sensing. Also, if a sample has a broad size range, large particles easily block the pinhole. Sometimes, if two particles pass through the pinhole together, the size measured is larger than the real one (3).

1.1.4 Acoustic Spectroscopy

Acoustic spectroscopy or acoustic attenuation spectroscopy is another technique to size particles. The basic principle of acoustic spectroscopy is that: ultrasonic transducers are used to transmit and measure the attenuation of sound waves as a

function of frequency (normally from 1 to 150MHz), and then from the attenuation spectrum, particle size distribution and concentration information can be deduced (4, 20).

The main advantage of this technique compared with others is that it can examine particles in a wide concentration range (typically 0.5% -50% in volume). It is suited for the analysis of suspensions of solid particles and emulsions of liquid droplets (12). It is normally used in cosmetic and pharmaceutical industries or for ceramic products. Because the emulsions are complex, any dilution process may destroy the structure characteristics or reduce the stability of cosmetics or drugs.

It also works in a wide size range, from 0.01 to 1000μm (4, 11). However, the disadvantage is also obvious. This method is sensitive to parameter changes, including density, the sound attenuation, heat capacity, liquid viscosity and the particle shear rigidity. Even one of these parameters may alter the results, sometimes significantly.

In contrast to the acoustic method, electroacoustic spectroscopy is more complex. It measures the interaction of electric and acoustic fields. Sound waves are generated by a high frequency electric field across a concentrated suspension. In practice, however, there are several limitations to the use of electroacoustic spectroscopy. For instance, since this technique is based on electric field, the particles should be charged. Also, the particle density should be different from the liquid (4, 11). According to Andrei S. Dukhin (11, 13, 14) and Philip J Goetz (13, 14), acoustic is much more powerful than electroacoustic for particle size characterization, whereas electroacoustic is better to measure zeta potential than acoustic.

1.1.5 Other Non-Optical Particle Sizing Methods

In this chapter, four different non-optical particle sizing techniques have been discussed. Besides these, there are some other techniques to size particles, such as the Chromatographic method (4, 74, 75), gas sorption (4, 76) etc. Gas sorption is suitable to examine the surface areas of particles. Each method has its own attractions, and it is formulated for some particular application. Xu. R (4) discussed some non-familiar methods, but they are useful in some specific fields. Mercury Porosimetry and Capillary Flow Porometry deal with pore size determination; Streaming Potential Measurement is suitable for zeta potential determination; Pulsed Field Gradient Nuclear Magnetic Resonance determines diffusion coefficient and Dielectric Spectroscopy can measure surface characterizations of liquid-borne colloids.

1.2 Optical Particle Sizing Techniques

1.2.1 Light Scattering Phenomenon

When a light beam passes through a perfectly homogeneous medium (with constant refractive index), it progresses in a straight line. If a light beam illuminates a piece of matter in some inhomogeneous medium, light can be absorbed or scattered, or both, depending on the wavelength of the light and the optical properties of the material. The total attenuation of incident light energy, which is described as extinction can be divided into two parts: absorption and scattering.

$$\text{Extinction} = \text{Absorption} + \text{Scattering}$$

Absorption occurs when the energy of incident light is converted into a different type by particles, such as heat. A leaf appears green; this can be explained as its surface absorbs the red component of light.

Light scattering can be explained by electromagnetic theory (4, 25, 29, 30, 73). Under most conditions, light performs like an oscillating electromagnetic wave. According to Maxwell's equations, light is composed of oscillating electric and magnetic fields, and particles are composed of discrete electric charges. Light can excite the charges in the particles to oscillate, and then the oscillating charges radiate secondary electromagnetic waves. These second electromagnetic waves are scattered waves. Theoretically, the scattered light observed from one particle is the superposition of incident wave from the initial source and the secondary waves from the scatterers.

Depending on whether the frequency of the scattered light is the same as that of the original incident light, these waves can be classified into (4):

i) Elastic (also known as Quasi-Elastic) scattering in which the frequency of detected light is different from the incident light typically by a few to a few hundred Hz (the frequency of visible light is of the order of 10^{14}Hz). The frequency differences come from the translational and rotational motions of the scattering particles. Frequency changes due to translational motions of the particles are known as Doppler shifts. Rayleigh scattering (from molecules and particles much smaller than the wavelength of the light) and Mie scattering (from molecules and particles of the same order of size as the wavelength of the light) are examples of Elastic (or Quasi-Elastic) scattering.

ii) Inelastic scattering in which the frequency changes are much larger than a few hundred Hz. The frequency differences come from the involvement of other forms of energy, such as the resonant vibrational and rotational energy states of the scatterers in Raman scattering.

All the particle analysis techniques described in this thesis are dominated by elastic (or quasi-elastic) scattering.

Most particle analysis techniques assume that the detected light has been scattered only once i.e. incident light from the source is scattered by each particle and this scattered light is detected. This is described as single scattering. However, in practice, some multiple scattering will occur in which particles are excited by the incident light and the light scattered from other particles (15). In order to ensure that single scattering is dominant, it is important to keep the sample dilute. There will always be some small fraction of multiple-scattered light but most of the available instruments ensure that single scattering is dominant by limiting the sample concentration so that the total light scattered by the sample is less than about 0.1 of the incident light (3, 88, 89).

Another important assumption, made in a number of light-scattering particles analysis techniques, is that particles scatter independently. In order to ensure independent scattering, the typical mutual distances need to be greater than 20 times the radii of the particles (25). Consequently, lower sample concentration is necessary to minimise multiple scattering and ensure independent scattering.

Some fundamentals and supporting background knowledge about light scattering are provided here, and some further details and information have been talked about in many optics books already (3, 4, 25, 26, 29).

The research of the nature of light dates back to the 17th century. Snell's law, Newton's rings, Huygens' Principle and Fermat's Principle are some of the fundamental theories of light. Thanks to these great scientists, they made huge contributions for later studies. Later, at the beginning of 1800s, Young and Fresnel studied diffraction phenomena. At the same time, Young also explained light polarisation phenomena.

Later in the 19th century, Maxwell's equations became the basis of theoretical and computational methods describing light scattering. Many authors, including Rayleigh, Mie, Fraunhofer, Gans and Debye, made outstanding achievements. The first systematic study of light scattering took place by John Tyndall in 1869. He pointed out light scattering from aerosols and large particles in suspensions. In 1871, based on Tyndall's theory, Rayleigh pointed out that: the scattering intensity is proportional to the intensity of incident light and the square of the volume or sixth power of the diameter of the particle, and inversely proportional to the fourth power of wavelength of light (4, 25). Due to different wavelength portions of the sunlight scattered by particles in the atmosphere such as droplets, dust or vapour, it explained why the sky is blue in the midday and orange or red at sunrise and sunset. Rayleigh scattering is applied for particle dimension much smaller than the wavelength of light. In 1908, Gustav Mie formulated a complete mathematical-physical theory of the scattering of electromagnetic radiation by all size of isotropic spherical particles in any medium (3, 4). Mie theory predicts the characteristic variations in angles versus scattering

intensity by the interaction with a spherical particle. Meanwhile, in 1910, Albert Einstein researched on fluctuation theory of light scattering (3, 50) and established the Stokes-Einstein equation, which is extremely useful for Dynamic light scattering. Later, Rayleigh-Gans-Debye scattering was proposed, which was an extension of the Rayleigh scattering.

In the 1960s, light scattering technique became popular and was broadly used instead of other particle sizing methods due to the use of lasers as the light sources and the application of powerful microcomputers for mathematically complex calculation. Nowadays, light scattering theory is still used in many industries. There are many manufacturers producing particle-characterisation machines, such as Malvern UK, Beckman Coulter, and Brookhaven Instruments. These products are utilised in different areas: some of them are used to detect particle sizes; some of them are capable to examine particle shapes, whereas some of them measure zeta-potential or refractive indices of samples.

The following sections will describe four kinds of particle sizing methods, which are based on optical microscopy and image analysis, static light scattering, dynamic light scattering and Nano-particle tracking analysis.

1.2.2 Microscopy and Image Analysis

One of the simplest particle sizing methods is to take an image or images of a sample of particles and then to analyse the individual particle images. The major advantage of microscopy and image analysis over most other methods of size analysis is that the particle profile itself is measured, rather than some property which is dependent on particle size. It examines individual particles, and therefore the nature of the particles including shape and size can be observed.

However, due to the nature of individual evaluation, it is time-consuming. Modern automatic image analysis enables rapid analysis for particles but usually many images must be captured.

Typically a frame might contain of the order of 200 particle images. The statistical error in counting N particles into a particle-size histogram channel (or bin) is simply the square root of N. Consequently the precision increases in proportion to the square root of the number of particles analysed. For example, if a count that was a factor of ten more accurate was needed, the number of particles (and correspondingly the counting time) would have to be increased by a factor of one hundred (3). Considering a simple example for the case of an approximately uniform particle size distribution between certain limits, for a particle size histogram with 15 channels and a requirement of, say, 5% accuracy on each channel then a total of $15 * (100/5)^2 =$ 6,000 separate particles would need to be imaged and analysed. Hence for 200 particles per frame this would amount to 30 frames of independent sets of particles.

In early image analysis using optical microscopy, the resolution obtainable (~0.4 μm) limited its minimum particle size to around one micrometre. Sheppard and Shotton

(70) enhanced the traditional optical microscopy technique by using confocal laser scanning microscopy to provide a lower size limit, and a resolution of 0.2 μm is attainable. Near-field scanning optical microscopy (71), in which a very small light source very close to the sample is scanned, can achieve a resolution of 20nm but the imaging technique is very slow compared to conventional wide-field optical microscopy. Modern Scanning or Transmission Electron microscopy (SEM/TEM) provides a significantly higher resolution and can image smaller particles. The details of this technique can be found in the books by Renliang Xu (4) and Terrence Allen (6). Modern transmission electron microscopy (TEM) has a size range of 1nm to 5μm.

In spite of its impressive resolution the EM method requires a well-trained analyst as well as expensive equipment. Complex sample preparation is another significant problem for microscopy and image analysis. Normally, the particle information is obtained from two dimensions of particles and as mentioned in the sieving method section above, particles often lie in a stable state, and therefore if particles are non-spherical or even with needle shape, it may lead to significant errors in a particle size distribution. A further problem with the technique is the difficulty in measuring particles that overlap or are obscured by other particles; this problem is clearly illustrated in **Figure 1.2** which shows a TEM picture of magnetite nanoparticles with diameter of 10-30nm (102).

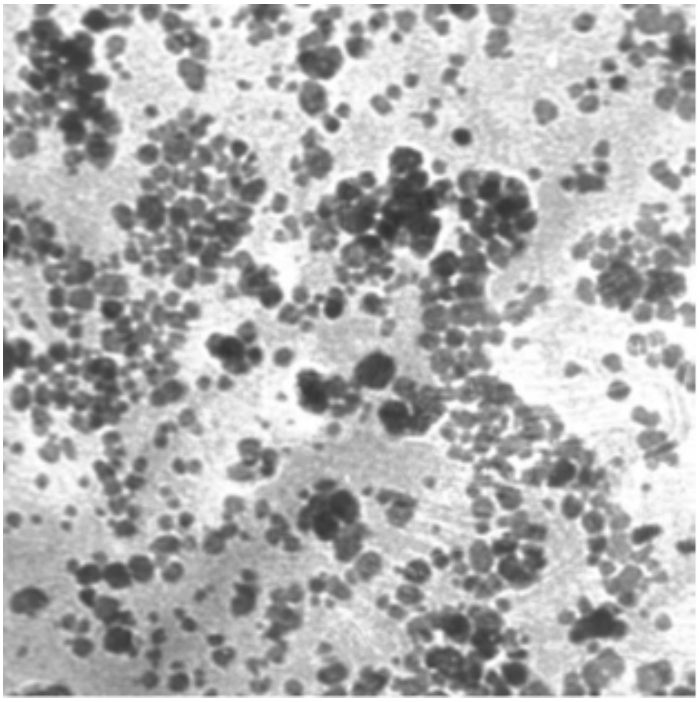

Figure 1.2: Typical TEM picture obtained from the magnetite nanoparticles (102).

The EM technique only operates on dry samples. A serious risk is that sometimes, dried particles have different sizes, shapes or even masses compared with those in suspension. Alexander (10) pointed out that shrinking of the particles during drying seems to be the most serious risk in the microscopy and image analysis technique.

1.2.3 Static Light Scattering

Static light scattering is another common particle sizing technique in many industry fields over the last thirty years, which is also known as laser diffraction.

This technique is based on the relationship between the scattered intensity at an angle and their sizes (33, 34). The basic setup of the static light scattering measurement is shown in Figure **1.3**.

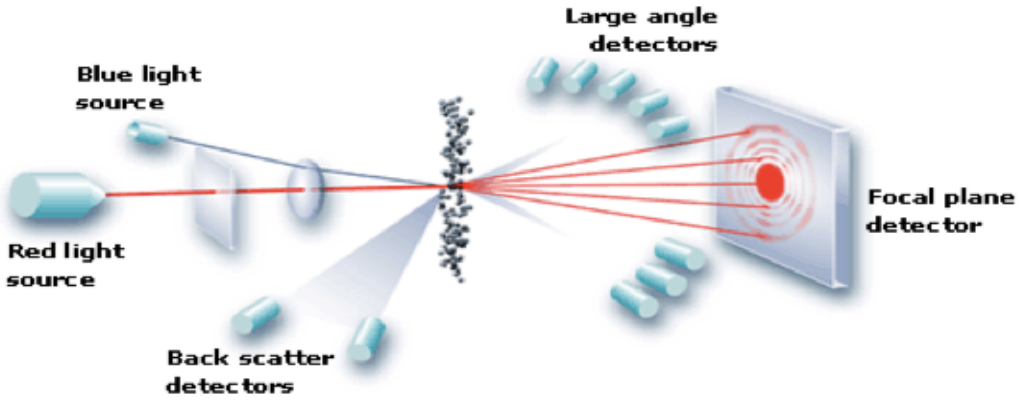

Figure 1.3: The basic principles and setup of static light scattering, also known as laser diffraction measurement (34).

A basic setup is composed of laser light source, samples, a series of detectors, and computers. A laser source generates a coherent light with fixed wavelength. A He-Ne gas laser is commonly used as a light source. A series of detectors are provided to measure the light pattern over a wide range of angles. The scattering intensity from every circular aperture in front of the detector contains the information of particle sizes. Computer is utilised to analyse and recover particles size.

Some old existing instruments are based on Fraunhofer approximation, which is suitable for particles larger than the wavelength of light. However, if the particle size is close to the light wavelength, the scattering becomes complex. Later, laser diffraction technique is no longer restricted to Fraunhofer theory. Instead, Rayleigh and Mie introduced the theory that predicted how scattering intensity depended on particle sizes. Theoretically, the scattering intensity is a function of wavelength of light, scattering angle, particle sizes, and refractive indices of particles and the medium. The latest instruments rely on full Mie Theory, such as Mastersizer 2000 from Malvern UK (35), claiming to detect particles over a larger range from 0.02 to 2000 μm.

Static light scattering has a number of advantages. It is easy to use and fast to operate, typically less than one minute. In addition, samples can be dry powder, liquid suspensions or emulsions. Thus, it has replaced some traditional techniques, such as sieving and sedimentation for particles smaller than a few millimetres, and taken the place of the optical and electron microscopy for particles larger than some tens of nanometres. One difficulty with static light scattering is the complexity of the calculation (which are often approximate or use iterative methods). The use of different algorithms by different manufacturers leads to differences in the results from different instruments using the same sample. It is medium cost, and it needs high standard of equipment maintenance.

Under Mie theory, particles should be isotropic spherical particles. In practice, however, the particles are generally non-spherical but randomly oriented. In the late 20^{th} century, Mishchenko improved the T-matrix method which is initially developed by Waterman (41).

The T-matrix method extends the capability of Mie theory to calculate light scattering by non-spherical particles with various shapes and sizes. It is based on numerically solving Maxwell's equations (31, 36-38).

The T-matrix code has been found to be able to produce very accurate results (five or more exact decimal places) suitable for use as benchmarks (87, 98, 99). The obvious disadvantage of T-matrix code is that it only optimised for axially symmetric particles without sharp corners or edges, such as spherical particles, spheroids, finite circular cylinders and Chebyshev particles (36).

For a small particle whose diameter is much smaller than light wavelength, the angular intensity distribution not only depends on the size, shape, orientation and refractive index of the particle, but also depends on the polarisation of the light illuminating the particle (39).

The Stokes parameters are used to demonstrate the state of the polarisation of light. The definition of Stokes parameters are as follows:

$$\begin{aligned} I &= I_0 + I_{90} \\ Q &= I_0 - I_{90} \\ U &= I_{45} - I_{135} \\ V &= I_R - I_L \end{aligned} \tag{1.2}$$

I describes the total intensity of the optical beam; ***Q*** describes the preponderance of linear horizontal polarized light over vertical polarized light; ***U*** represents the preponderance of horizontal+45^o light over horizontal-45^o polarized light and ***V*** is the preponderance of right circularly polarized light over left circular polarized light (40).

It is convenient to arrange the Stokes parameters as a Stokes vector with (4 x 1) column, and it is rewritten as:

$$S = \begin{bmatrix} I \\ Q \\ U \\ V \end{bmatrix} \tag{1.3}$$

In order to represent the output beam after polarisation, a scattering matrix known as Mueller Matrix is used to manipulate Stokes vectors. The input beam is characterised

by $\boldsymbol{S_i}$; the output beam is represented by $\boldsymbol{S_s}$; the polarisation components are characterised by a (4 x 4) Mueller matrix (52).

$$\begin{bmatrix} I_S \\ Q_S \\ U_S \\ V_S \end{bmatrix} = \begin{bmatrix} m_{11} & m_{12} & m_{13} & m_{14} \\ m_{21} & m_{22} & m_{23} & m_{24} \\ m_{31} & m_{32} & m_{33} & m_{34} \\ m_{41} & m_{42} & m_{43} & m_{44} \end{bmatrix} \begin{bmatrix} I_i \\ Q_i \\ U_i \\ V_i \end{bmatrix} \tag{1.4}$$

This matrix equation can be replaced by the simple equation.

$$S_s = M \times S_i \tag{1.5}$$

The T-matrix or Transition Matrix method was initially described by Waterman (41) to solve Maxwell's equations for electromagnetic radiation scattered by single homogeneous non-spherical particle in a given direction based on Huygens' Principle. Later, based on the general concept from Waterman, Mishchenko et al (31, 36-38, 41) utilised the T-matrix method for arbitrary non-spherical particles and then the T-matrix approach became a powerful and widely used tool for non-spherical particles (85-87). For isolated spherical particles, the T-matrix method is equivalent to Mie Theory.

Based on Mishchenko's theory (31, 36-38, 41), an array of $\boldsymbol{I_S(\theta, r)}$ for a range of particles with radii $\boldsymbol{r}$ can be calculated. Assuming the particle sizes follow a discrete distribution $\boldsymbol{f(r_n)}$ and the intensity of light scattering by the particle with radius $\boldsymbol{r_n}$ at angle $\boldsymbol{\theta_m}$ is $\boldsymbol{I_S(\theta_m, r_n)}$, therefore, the intensity of the light scattered in all directions can be indicated as follows:

$$\begin{bmatrix} [I_S(\theta_1)] \\ [I_S(\theta_2)] \\ . \\ . \\ [I_S(\theta_M)] \end{bmatrix} = \begin{bmatrix} I_S(\theta_1,r_1) & I_S(\theta_1,r_2) & ... & I_S(\theta_1,r_N) \\ I_S(\theta_2,r_1) & I_S(\theta_2,r_2) & ... & I_S(\theta_2,r_N) \\ . & . & . & . \\ . & . & . & . \\ I_S(\theta_M,r_1) & I_S(\theta_M,r_2) & ... & I_S(\theta_M,r_N) \end{bmatrix} \begin{bmatrix} f(r_1) \\ f(r_2) \\ . \\ . \\ f(r_N) \end{bmatrix} \quad (1.6)$$

where $f(r_n)$ represents the particle size distribution, N and M represents the number of particle sizes and the number of scattering angles respectively.

The transformation matrix can be rewritten in a convenient way, defined as:

$$H_{MN} = I_S(\theta_M, r_N) \quad (1.7)$$

where H_{MN} is the component of matrix H.

The Fortran code for generating the scattering matrix can be obtained from (101), and thus a scattered light intensity $I_S(\theta, r)$ at angle θ from a particle size of r can be calculated.

As an example, for particles with the radius of 200nm, the normalised scattering intensities from 0^o to 180^o are shown in Figure **1.4**.

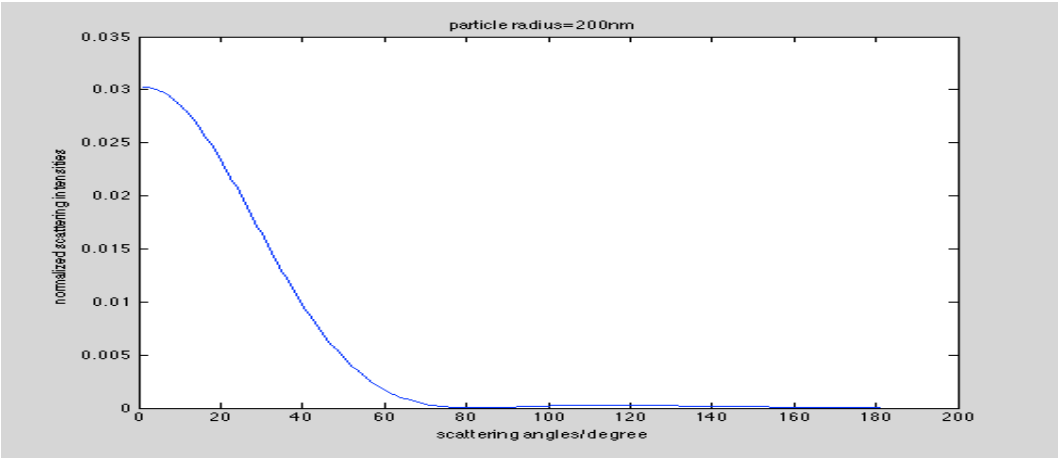

Figure 1.4: Normalised scattering intensities for a 200nm radius particle over 180 degree scattering angles. The refractive index of the medium is 1.33 and the refractive index of particles is 1.50.

As mentioned above, static light scattering is easy to use and fast to operate, typically less than one minute. In addition, samples can be dry powder, liquid suspensions or emulsions.

However it does have some drawbacks. Firstly, a particle size distribution is not directly measured. The measurement is the angular variation in scattered intensity $I_S(\theta_m)$, i.e. the right hand side of equation (1.6). To obtain the particle size distribution $f(r_n)$, it is necessary to invert equation (1.6). This inversion can be difficult to achieve with high accuracy. This inversion is particularly difficult when a sample contains a wide distribution as the contribution to the data set $I_S(\theta_m)$ from the larger particles is very much larger than the contribution from the smaller particles. This domination of the data (sometimes referred to as 'Intensity weighting') means that the size distribution for smaller particles is often recovered with very poor accuracy.

1.2.4 Dynamic Light Scattering

Dynamic Light Scattering (DLS), which is also known as Photon Correlation Spectroscopy (PCS) (sometimes called quasi-elastic light scattering) (3, 54) is one of the most useful particle-sizing techniques over the last few decades to analyse particles within sub-micrometre range, from a few nanometres to a few microns. A basic Dynamic light scatting setup measurement is displayed in Figure **1.5**.

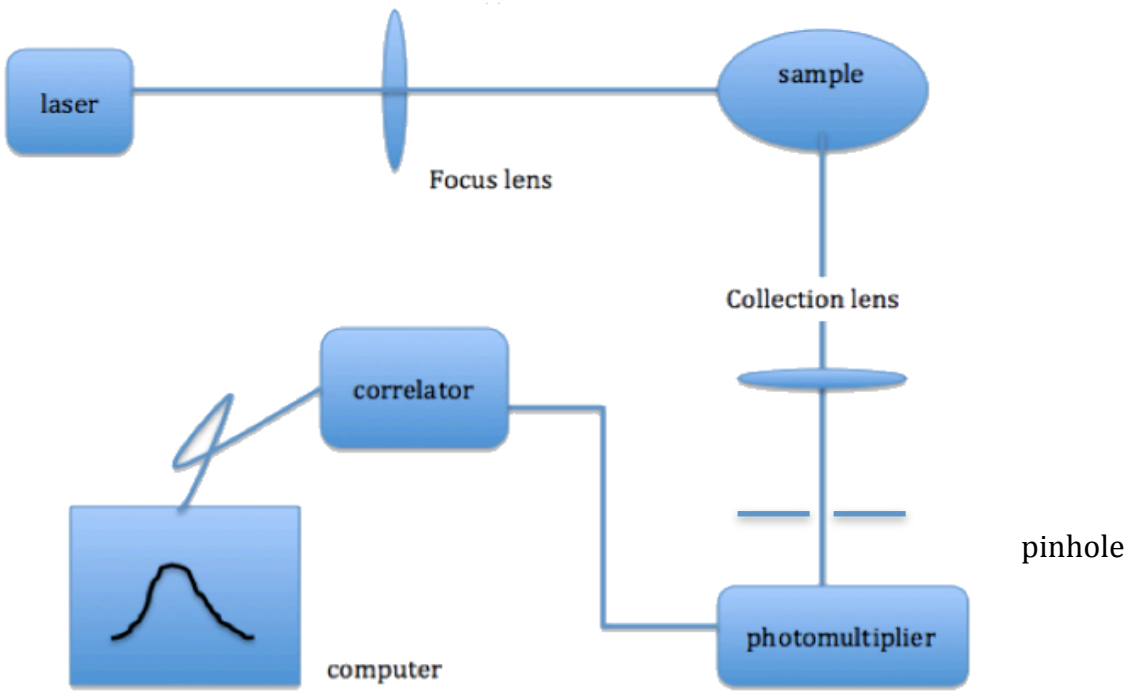

Figure 1.5: A typical Dynamic Light Scattering or PCS instrument (**3**, **4**).

A typical PCS instrument consists of these components: a laser light source, a sample module, a focus lens and a collection lens, a pinhole, photomultiplier (or another photon counter), a correlator and a computer. A linearly polarised laser is utilised to generate coherent light. The light source is focused to a small point by the focus lens and the collection lens collects the light scattered by the particles.

In **Figure 1.5** light scattered at 90 degree is collected, in principle there is no restriction on which scattering angle to use, however 90 degree is a popular choice as it enables the use of square sample cuvettes with the light entering and leaving the cuvette walls at right angles.

The light from the beam focus is selected using a pinhole, and transmitted to a photomultiplier, which provides a single electrical pulse for each photon detected. This signal passes to the correlator, which calculate the autocorrelation function of the

input string of photomultiplier pulses. Based on the autocorrelation function, a computer performs the appropriate data analysis to display a particle size distribution.

In dynamic light scattering, particle size information is extracted from fluctuations in scattered light intensity at a fixed angle. This fluctuation arises from the random movement of the particles in the scattering volume by Brownian motion. The smaller the particles are, the faster the Brownian motion will be. Therefore, the fluctuations in the light intensity caused by small particles are more rapid than for the larger ones. This means that the temporal autocorrelation of the intensity fluctuations from the smaller particles decays faster than the autocorrelation arising from the larger particles.

The diffusion coefficient is relevant to the temporal intensity fluctuations. If the diffusion coefficient can be obtained, the equivalent spherical diameters of the particles can be deduced from the Stokes-Einstein relation (3, 4, 42, 43). The diffusion coefficient is given by the following formula:

$$D = \frac{K_B T}{3\pi\eta d} \tag{1.8}$$

where $\boldsymbol{K_B}$ is the Boltzmann constant, $\boldsymbol{T}$ is temperature in Kelvin degrees, η is the dynamic viscosity of the solvent and $\boldsymbol{d}$ is the equivalent spherical diameter of the particle.

To analyse particle sizes by PCS, light intensity and autocorrelation function must first be considered (92).

In a real experiment system, the autocorrelation function of the detected photons is measured but this is equal to the autocorrelation of the intensity, which is usually

expressed as $g^{(2)}(\tau)$, this, in turn, is related to the amplitude autocorrelation function $g^{(1)}(\tau)$, by the relation,

$$g^{(2)}(\tau) = 1 + \left| g^{(1)} \right|^2 \tag{1.9}$$

For a ploy-disperse sample, $g^{(1)}(\tau)$ can be represented as a sum or an integral over a distribution of intensity weighted particle size f(R) by

$$g^{(1)}(\tau) = \int_0^\infty f(R) \exp(-\Gamma\tau) dR \tag{1.10}$$

Further details about the autocorrelation function can be found in appendix I.

The autocorrelation has an exponential form whose characteristic time is related to the particle size distribution. However a weakness of the method can be is illustrated in **Figure 1.6** which shows two simulated DLS autocorrelation data, $g^{(2)}(\tau)$, for 200nm particles (solid line) and a mixture of 100nm and 300nm particles (dashed line). The fact that the data for these two very different particle size distributions is so similar illustrates that seeking a solution that is consistent with noisy correlation data is an ill-posed inverse problem. For an ill-posed problem, the solution is not unique and may not be the one that provides the best fit to the data.

There are many ways to analyse the autocorrelation function of scattered light, such as the CONTIN method by Provencher (47), the singular value decomposition method (48) and the method of cumulants (49).

Recently, a Maximum Likelihood method was developed by Yunfei Sun (21, 22). This is another novel method for data inversion to recover particle size distributions,

which will be discussed in Chapter 2 and will be used to recover particle size distributions in this thesis

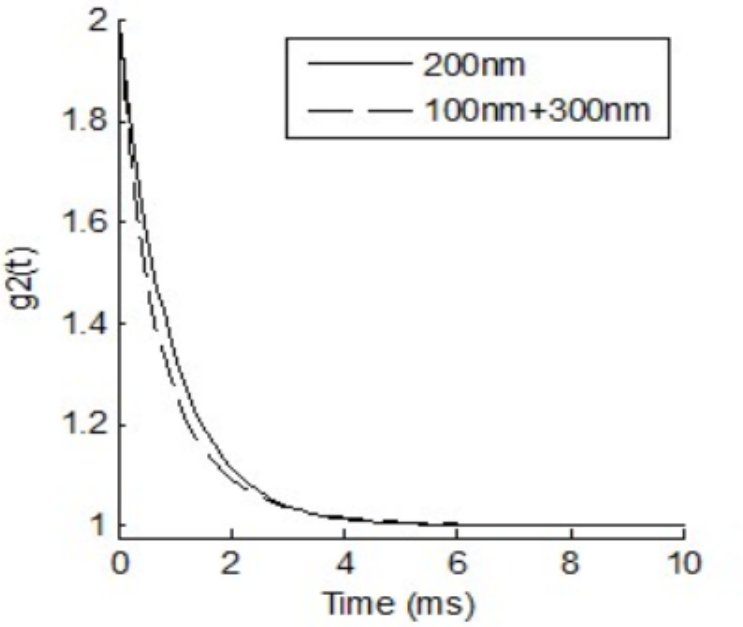

Figure 1.6: Simulated DLS data for 200nm particles (solid line) and mixture of 100nm and 300nm particles (dashed line).

This technique is not time-consuming. It succeeds in being able to provide an estimate of average size of particles within a few minutes. In addition, the equipment required is not very complex or expensive.

However, it suffers from similar difficulties to SLS, in that the extraction of size distributions from the data is problematic. As mentioned above the particle size distribution must be obtained by inversion of equations (1.9 and 1.10). This inversion is not straightforward, a number of inversion algorithms (listed above) have been proposed, which will all yield different results. Therefore there is no single 'correct' solution for any given set of data. Recovered distributions for complex, polydisperse sample types (eg. many biological sample types) are usually poorer than for more monodisperse samples.

In addition, as stated above, the particle size distribution f(R) is intensity weighted i.e. it represents the product of the number distribution and the scattering intensity for that particle radius. This means that if there is a wide distribution of particle sizes in a sample, the autocorrelation data is dominated by contributions from the larger particles. So, as for Static Light Scattering, the recovery of the distribution of the smaller particles is often very poor.

1.2.5 Nano-Particle Tracking Analysis

Nano-Particle tracking analysis (NTA) is a novel particle sizing method developed recently by Nanosight (97). The most recently developed system (95) was assessed in-depth due to its ability to see and size particles individually on a particle-by-particle basis (DLS being an ensemble technique where the measurement of an ensemble of particles is used to calculate a particle size distribution). This novel method is based on the Brownian motion theory and the Stokes-Einstein relation. It tracks different particles simultaneously and analyses the trajectories of Brownian motion from individual particles in the liquid (68). A large number of images are recorded with a certain time interval between the frames. In practice, a CCD camera, operating at 30 frames per second, is used to capture a video field of view approximately 100μm x 80 μm. Typically, it tracks particles over 900 frames or 30 seconds. The data processing consists in determining the movement of the individual particles through the video sequence through use of specific selection criteria, and then the mean squared displacement is determined for each particle track. The trajectories should be sufficiently long to ensure statistically accurate results, ignoring those which are so short (eg. below 5 or 10 frames) that the estimation of diffusion coefficient is

statistically inaccurate. The averaged distance each particle moved in two dimensions (**x** and **y**) in the image is automatically calculated. From this value, the particle diffusion coefficient **D**, can be obtained and, knowing the sample temperature **T**, solvent viscosity $\boldsymbol{\eta}$, and the time interval **t**, the particle hydrodynamic diameter **d** is identified according to the Stokes-Einstein equation (eq (1.14)) (68, 97):

$$\frac{\overline{(x,y)}^2}{4} = Dt = \frac{TK_B}{3\pi\eta d}t \qquad (1.11)$$

where $\boldsymbol{K_B}$ is Boltzmann's constant.

The schematic of the NTA apparatus set-up is shown in **Figure 1.7**. Finely focussed, 635nm (approximately 40mW) laser light is used as the light source to pass through a prism-edged optical flat. The NTA technique requires a small ($250\mu L$) sample of liquid containing particles at a concentration in the range of 10^7-10^9/mL, and the number of particles on the screen is approximately about 20-60 in the ideal concentration to analyse a sample.

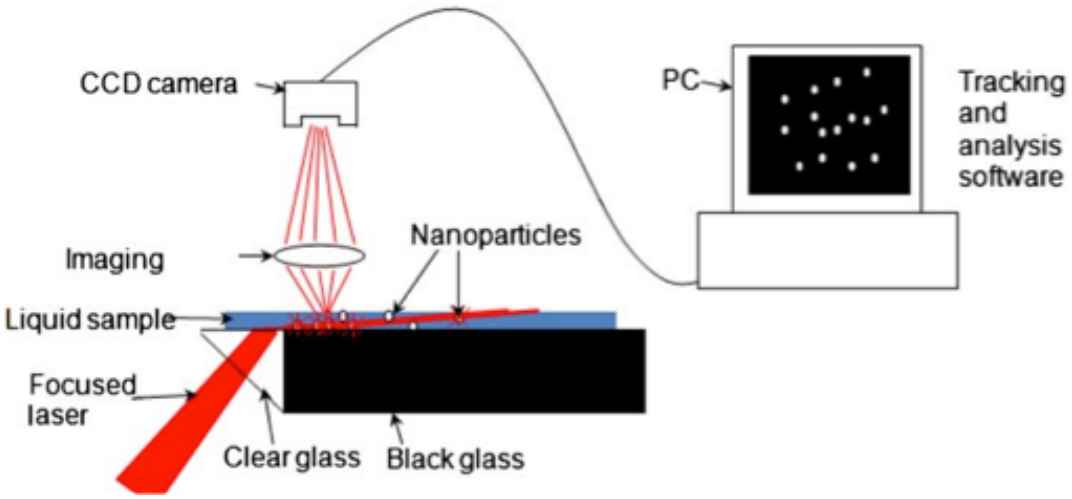

Figure 1.7: Schematic of NTA apparatus (Nanosight LM10 and LM20) (95).

Compared with DLS, NTA is a new method so users do not have much experience of using it. NTA can be time-consuming (5min-1hour per measurement) and requires some operational skills for the adjustment of software settings, but NTA enables the visualisation of the sample, and obtains size information based on the Brownian motion of individual particles. NTA is appropriate for sizing single and bi-modal samples (69).

The accuracy of the technique is limited by a number of factors.

Firstly, the particle positions need to be determined accurately; the image moment method is usually used and the accuracies possible are discussed in detail in the next chapter.

Secondly, because the particles also move in the non-measured z direction as well as in the x-y plane, particles can move out of the illuminated region after a limited number of positions have been recorded. This limits the length of the tracks and hence limits the statistical accuracy with which the average squared displacement (and hence the particle diameter) can be measured.

Thirdly, to track individual particles, some method to associate intensity peaks in one frame with the corresponding peaks in the next frame must be employed. The usual method is to assume that if a peak in a second frame is within some set distance of a peak in the first frame, and then it is assumed to arise from the same particle. However it is possible for this approach to fail, for example, if a particle leaves the illuminated region but another particle enters the region at a similar x, y position. If this occurs, a false track containing steps from two particles could be measured and lead to errors in the particle size distribution formed.

1.3 Motivation for the Work and Criteria for Assessment of the Results

1.3.1 Motivation and Aims of the Work

The previous section (1.2) has outlined four optical techniques to measure particle size distributions. Each of the methods has its strengths but also its weaknesses as listed in **Table 1.2**.

Techniques	Strengths	Weaknesses
Transmission Electron Microscopy	• Visualisation	• High cost • Complex sample preparation
Static Light Scattering	• Approved, reliable method • Minimum sample preparation necessary • Analysis of low concentration samples	• Medium cost, high standard of equipment maintenance • Intensity weighted method • Complexity of the data inversion (which are often approximate or use iterative methods
Dynamic Light Scattering	• Fast results • Well-established method	• Complex data inversion • Intensity weighted method • Poor for complex particle distributions (such as bi-modal)
Nanoparticle Tracking Analysis	• Ease to use • Sample visualisation • Good for both monodisperse and polydisperse samples	• Sample dilute necessary • New method-not much experience • Not always possible to obtain long tracks

Table 1.2: Comparisons of different techniques.

The motivation of the work in this thesis is to develop novel methods that attempt to retain the strengths of some of the techniques but to reduce the weaknesses.

The aim of the work is not to address a particular particle sizing application, but to investigate, develop and implement methods that have the potential to measure particle size distributions for particles in the sub-micron range, which can

(i) deliver size distributions with good accuracy (see discussion below),

(ii) deliver size distributions that are not intensity weighted, and,

(iii) operate successfully on a variety of size distribution forms i.e. can recover both mono-modal and bi-modal distributions.

Low cost and ease of operation and maintenance are other important criteria for the methods.

1.3.2 Assessment of Accuracy in Measuring Size Distributions

A difficult issue in particle sizing techniques is to specify the accuracy of the particle size distributions obtained so as to be able to compare the output of one technique with another. Most papers describing new techniques or revising data processing methods (4, 68), simply present example size distributions without any quantitative assessment of the accuracy of the output.

In experimental work, an assessment is particularly difficult as there is no 'gold standard' technique that can be used for comparison purposes and it is usually difficult to state with certainty the size distribution of a given sample (even if it contains particles manufactured to have a specified size) due to possible contamination and possible aggregation of particles.

Computer simulation gives a better opportunity to quantify the output of a technique (although, of course, the application of the results is only valid if the simulation closely matches a real experiment). Even when using computer simulations to assess methods (69, 97), most authors do not specify a quantitative accuracy figure.

A paper that does specify a quantitative measure is one comparing a number of data processing methods for dynamic light scattering (DLS) data (22). DLS is a long established technique that exploits the Brownian motion of particles. The methods investigated in chapters 2 to 4 of this thesis are also based on exploiting the Brownian motion of particles; so comparing their performance to the established DLS method is appropriate.

The paper (22) proposed an 'area error' measure to assess the accuracy of a number of different data inversion methods for DLS data; the mathematical form of this measure is defined in eq. (2.24). It was shown that for data simulated for a typical DLS experiment, the various techniques tested gave 'area error' values in the range of 0.6 (CONTIN) to 0.32 (ML) (a small value represents a better result).

Hence in this thesis the success of the techniques will be judged as performing well if they can achieve a lower 'area error' value than 0.32.

1.4 Thesis Outline

This chapter describes the importance of particle sizing in a number of application areas. It then reviews both non-optical and optical techniques and summarises the motivation and aims of the work in this thesis.

Inspired by the NTA technique, Chapter 2 describes an alternative technique that exploits Brownian motion to measure the size distribution of particles, called Particle Movement Displacement Distribution (PMDD). This method is proposed to overcome the limitation of being an intensity-weighted distribution, eg. DLS, and also to remove the necessity to track particles which can be problematic in the NTA method.

This method was first introduced in the thesis of Dr. Nam Trung Huynh and a joint paper describing this approach has been published in 2012 (57). Novel work on this technique is presented in Chapter 3 where extensive computer simulations were used to determine the optimal or acceptable experimental parameters including time interval, exposure time, photon and camera noises and sample concentration as well as the effect of aberrations in the optical arrangement effects.

Chapter 4 presents some comparisons of the results of the PMDD method with an implementation of a tracking method (based on the NTA approach) using both simulation results and the experimental data. It also presents some bi-modal simulation results of the PMDD method.

Chapter 5 presents another novel technique to size particles. It is an angular dependent intensity technique for particle sizing, which is called Separated Multiple Image Technique (SMIT). This method works on the same basic principle as static

light scattering but it is based on the angular dependent intensity and individual visualisation together. This provides potential to overcome the intensity weighting effect and removes the need for a data inversion algorithm. Thus, in principle it should be able to distinguish bi-modal particle size distributions.

Chapter 6 describes the implementation of a real experiment for SMIT. A four-aperture mask is used to form images and prisms are used to tilt light to certain particular angles. Experimental results are displayed with relevant analysis.

Finally, Chapter 7 makes a conclusion based on all the work carried out in the previous chapters. It also presents some suggestions for further work.

2 Particle Movement Displacement Distribution (PMDD)

2.1 Introduction

Chapter 2 will describe a novel approach to measure the size distribution of particles in the submicron range. Particles walk randomly and continuously, but this random Brownian movement contains information about particle size. This novel technique has some similarities to the NTA method described in Chapter 1. It is also based on the Brownian movements of particles and employs a similar illumination and imaging optical setup, but it does not need to track individual particles over many frames. It measures the centre of individual particles in each image. A vector histogram is formed based on the connection between the centres in the first image and the centres in the next image. In section 2.2, some basic knowledge about Brownian motion will be described. Section 2.3 introduces an image moment method, which is a method to determine the centres of particles. The chapter then continues by explaining the data processing of the Particle Movement Displacement Distribution (PMDD) method in Section 2.4. Section 2.5 presents a maximum likelihood inversion method developed by Y. Sun (21, 22) to recover a particle size distribution. Finally, Section 2.6 summarises the work that is presented in this chapter.

2.1 Brownian Motion

2.1.1 Brownian Motion Theory

A particle suspended in a fluid seems to do a random walk, which is described as Brownian motion in honour of botanist Robert Brown (23). Robert Brown (1773-1858), observed that small particles suspended in water are in random motion, and the random movement is extremely erratic motion, apparently without end. After Brown's observation, many scientists were interested in this phenomenon. In 1877, Desaulx (24) made the first good explanation of Brownian motion: Brownian motion is a phenomenon, which is caused by the thermal molecular motion in the fluid environment of the particles. Molecules from all sides hit a particle suspended in the liquid constantly and randomly. If the hit from one side is stronger than any other side, the particle will jump. This completely irregular jump in all directions is regarded as Brownian motion. Each single particle moves independently of the other particles. In 1905, Einstein determined a theoretical model of Brownian motion. The Stokes-Einstein relation determines the relationship between diffusion coefficient and particle size, which has been discussed in chapter 1.

In addition, according to Einstein's theory (55), the standard deviation of the random displacements of a particle in one direction in time $\boldsymbol{\Delta T}$ is given by formula (2.1):

$$\delta_n = \sqrt{2D\Delta T} \tag{2.1}$$

where, $\boldsymbol{D}$ is the diffusion coefficient, defined in equation (1.8)

As stated above the motion of a particle arises from the interaction with very many water molecules, therefore, the central limit theorem tells us that the distribution of

the movements will have a Gaussian form, hence a Brownian particle at the original point (***x, y, z***), after ***ΔT*** interval time, the next positions are:

$$\begin{aligned} x_{n+1} &= x_n + random \times \delta_n \\ y_{n+1} &= y_n + random \times \delta_n \\ z_{n+1} &= z_n + random \times \delta_n \end{aligned} \tag{2.2}$$

where x_n, y_n and z_n are the particle positions at time nΔt; x_{n+1}, y_{n+1} and z_{n+1} are the particle positions at time $(n+1)\Delta t$. where "***random***" is a Gaussian variable with zero mean and unity variance (55).

2.1.2 Brownian Motion Modelling

The PMDD method is effectively based on two assumptions. The first assumption is that the particles are in Brownian motion. Secondly, it is assumed that the particles should be spheres or have equivalent spherical diameters.

The Brownian movements of two particles in three dimensions are displayed in **Figure 2.1**. The diameters of both of the particles are 200nm. **Figure 2.1** simulates random movements of the two particles for ten times. The time interval is one second. The red star represents the starting point and the black square is the ending point. It is clear to see every displacement is not exactly the same due to the extremely erratic movement, but the erratic movement follows the rules in equation **(2.2)**.

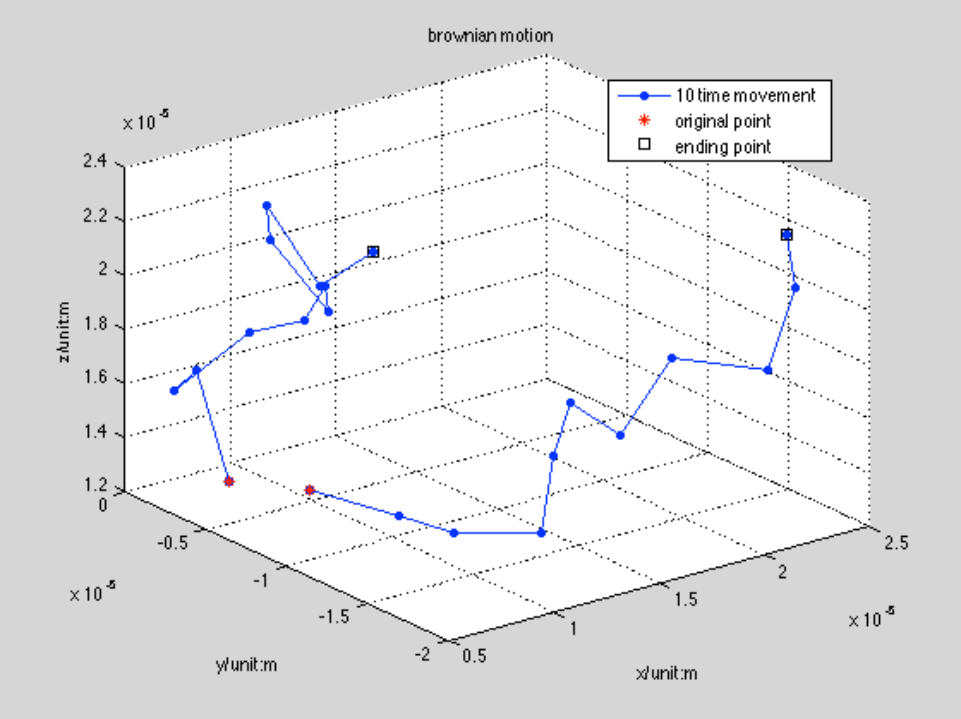

Figure 2.1: Two particles with radius equal to 100nm. The red stars and black squares represent the original positions and final positions of the two particles respectively. The blue line represents 10 time random walks in 10 seconds when the time interval is one second. The temperature is 20 degrees centigrade and the assumed viscosity of the water is 10^{-3} Pa.s.

2.2 Image Moment Method

The basic idea of the PMDD method is to analyse the connection between the particle centres in the first image and the centres in the next image. Therefore, finding accurate particle centres is necessary, and it is a prerequisite of obtaining an accurate particle movement displacement distribution.

Particles in the image always appear to be some blurred spots. The blurred spots may show a distribution of intensities which follow a mathematical function known as a point spread function (PSF). In a perfect system, the PSF is the Airy irradiance

distribution function centred on the Gaussian image point (56). In a real optical system, however, because of diffraction, optics aberration, out of focus effects and photon and detector noise, the distribution of measured intensities is not exactly an Airy irradiance distribution. It usually covers an area of several pixels on the image plane and generally, it will not be a circularly symmetric distribution. Therefore, it is necessary to determine the real particle position or the equivalent point of the object in the image, which is very important during analysis. Sometimes, the maximum intensity pixel or the centre of area is chosen to be the real position or the equivalent point. However, it does not give a precise measure because the intensity spreads across not only one pixel and the distribution is usually not symmetrical. It is therefore preferable to determine the centre of mass or centroid (58).

For a single particle, the distribution of the intensities usually covers an area of several pixels. Because the image moment method averages the intensity information over a number of pixels, the resulting centroid position may be determined to sub-pixel accuracy. If there is a set of values around some particular value, it may be useful to characterise the set in relation to its moments, which are the sums of integer powers of the values (58). The moments depend on the intensity of the object. There are some features about the moment method. It can be used regardless of location in the image and the size of the object.

If the intensity of an object in an image is defined by the function ***B(x, y),*** for digital images, the $(K + L)^{th}$ order of the moments is defined as:

$$B_{KL} = \sum_{x}\sum_{y} x^{K} y^{L} B(x, y) \tag{2.3}$$

In the two dimensional case, the centre of mass is given by (B_{10}, B_{01}):

$$B_{10} = \sum\sum xB(x,y) / B_{00}$$
$$B_{01} = \sum\sum yB(x,y) / B_{00} \qquad (2.4)$$

where $\boldsymbol{B_{00}}$ is the total intensity of the object.

In order to show the accuracy of the image moment method, **Figure 2.2** compares the original particle centres at random positions with the particle centres measured by the image moment method; the parameters used to produce these images are listed in **Table 2.1** below.

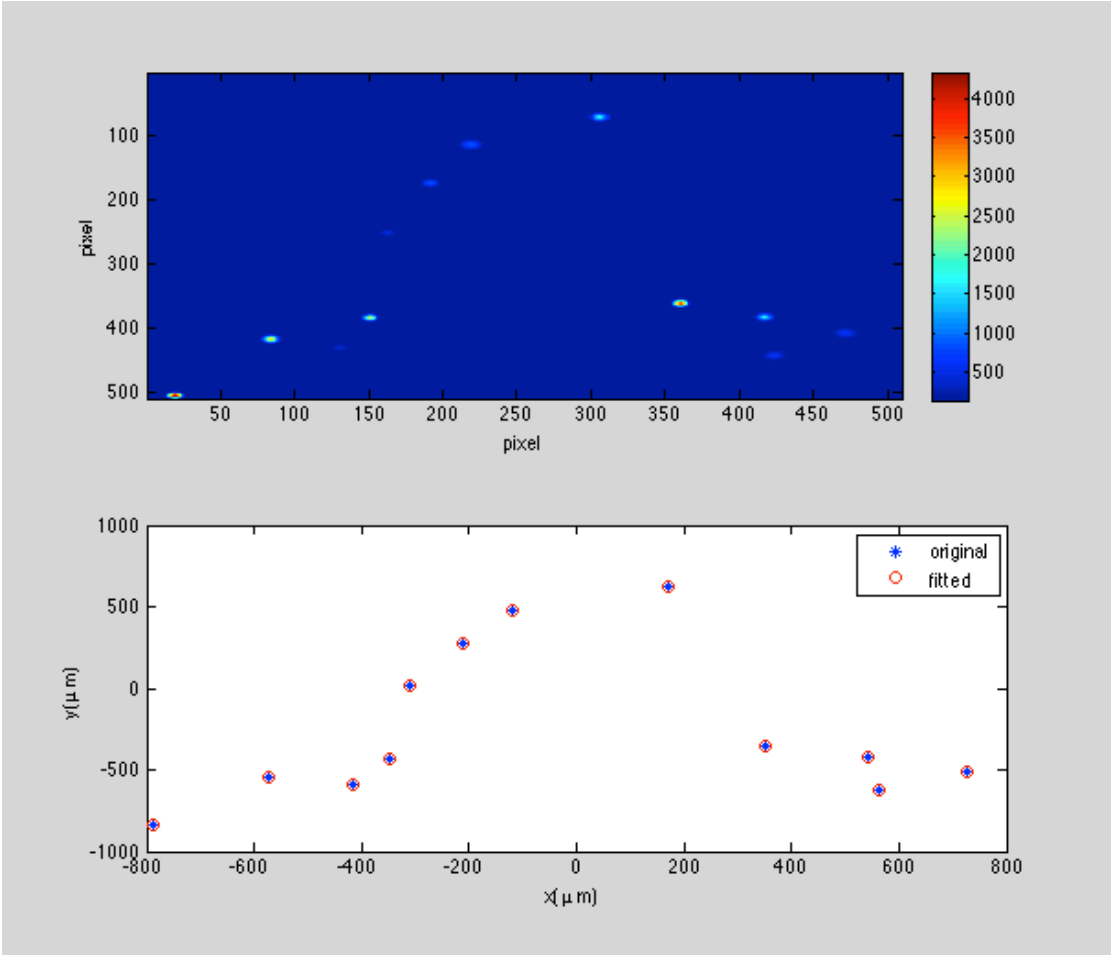

Figure 2.2: Particle centres found by the image moment method. Blue stars are the original particle positions, while red circles record the positions found by the image moment method.

Table 2.1 lists some parameters used to check the accuracy of the image moment method.

Particle radius	100nm
Pixel size	6.25 microns
Point spread function radius	35---45 microns
Number of photons	10^5---10^6

Table 2.1: Particle radius and pixel size.

The blue stars represent the original particle positions, whereas the red circles represent the fitted particle centres by the image moment method. Visually, the fitted particle centres are nearly the same as the real particle centres. Results from simulating around 11,000 different particles are presented in **Figure 2.3**. **Figure 2.3(a)** records the distribution of the particle centre errors in each dimension, x and y respectively, and **Figure 2.3(b)** records the distribution of the modulus value $\sqrt{\Delta x^2 + \Delta y^2}$ of the particle centre errors. In **Figure 2.3(b)**, 47% of the fitted particle centres have an error of less than 0.05 pixels, and 94% particle centres have an error of less than 0.1 pixels.

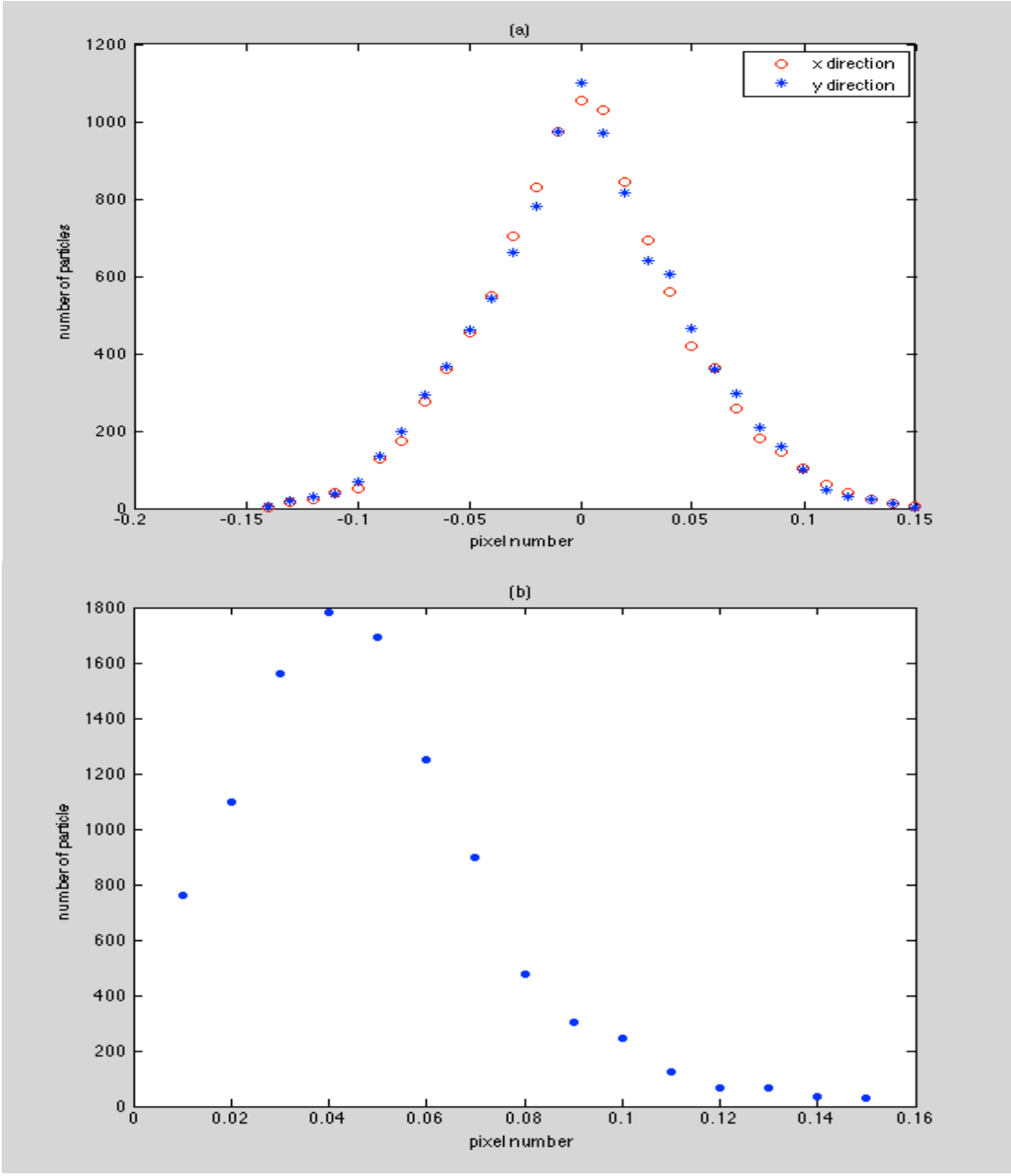

Figure 2.3: (a) The distribution of the particle centre errors obtained by the image moment method in each dimension. (b) The distribution of the modulus of the particle centre errors obtained by the image moment method.

The analysis and results above indicate that it is possible to obtain particle centres accurately by the image moment method. This result is in agreement with other existing literature (58, 77, 78). In particular in (78), the simulated process of digitizing was performed for the following pixel sizes 2.8, 6.8, 7.5, 9, 12.5, 17, 23, and 27 μm, and target sizes of 100 μm and 200 μm (diameter of circle) were used. For these conditions, it was found that the accuracy of the simple moment centroiding algorithm was between 0.05 to 0.1 pixels; which is in good agreement with the results shown in **Figure 2.3** above.

In the PMDD optics arrangement used for the experimental results, the actual (camera) pixels are 6.7 microns across, but the magnification of the sample cell to the camera was 6.6 therefore the effective pixel size is around 1 micron. This suggests that the particle displacements are measured to an accuracy of 0.1 microns or better. The typical width of the main peak in a particle movement distribution (see **Figure 2.6**) is around 4 microns. The effect of errors in the displacements will be to widen this peak by an amount less than the uncertainty in the particle displacements. Hence, as this is typically about forty times smaller than the width of the distribution, the effect of using the image moment method will be almost negligible.

2.3 Data Processing of Particle Movement Displacement Distribution Method

The Particle movement displacement distribution (PMDD) method is a novel technique that exploits Brownian motion. In this respect it is similar to DLS.

However, PMDD measures the random movement of individual particles rather than the averaged result of the random movement of a large number of particles, which is measured in DLS.

Fundamentally, a CCD camera obtains multiple frames of particles suspended in a liquid. Each image records the different particles' positions. The basic idea of the PMDD method is: from each image, the centres of particles are measured. A vector histogram is formed based on the connection between the centres in the first image and the centres in the next image.

A flow chart in **Figure 2.4** illustrates the process of PMDD method.

Figure 2.4 (a) records a series of frames with certain time interval between the frames and some of the particles come in or out of the field of view. The data processing consists in determining the displacement between an arbitrary particle centre in one frame and an arbitrary particle centre chosen from the subsequent image. The red dots are the particle centres in the previous image, whereas the black dots are the particle centres in the subsequent image in **Figure 2.4 (b).** The black lines represent the displacements between any two arbitrary particle centres.

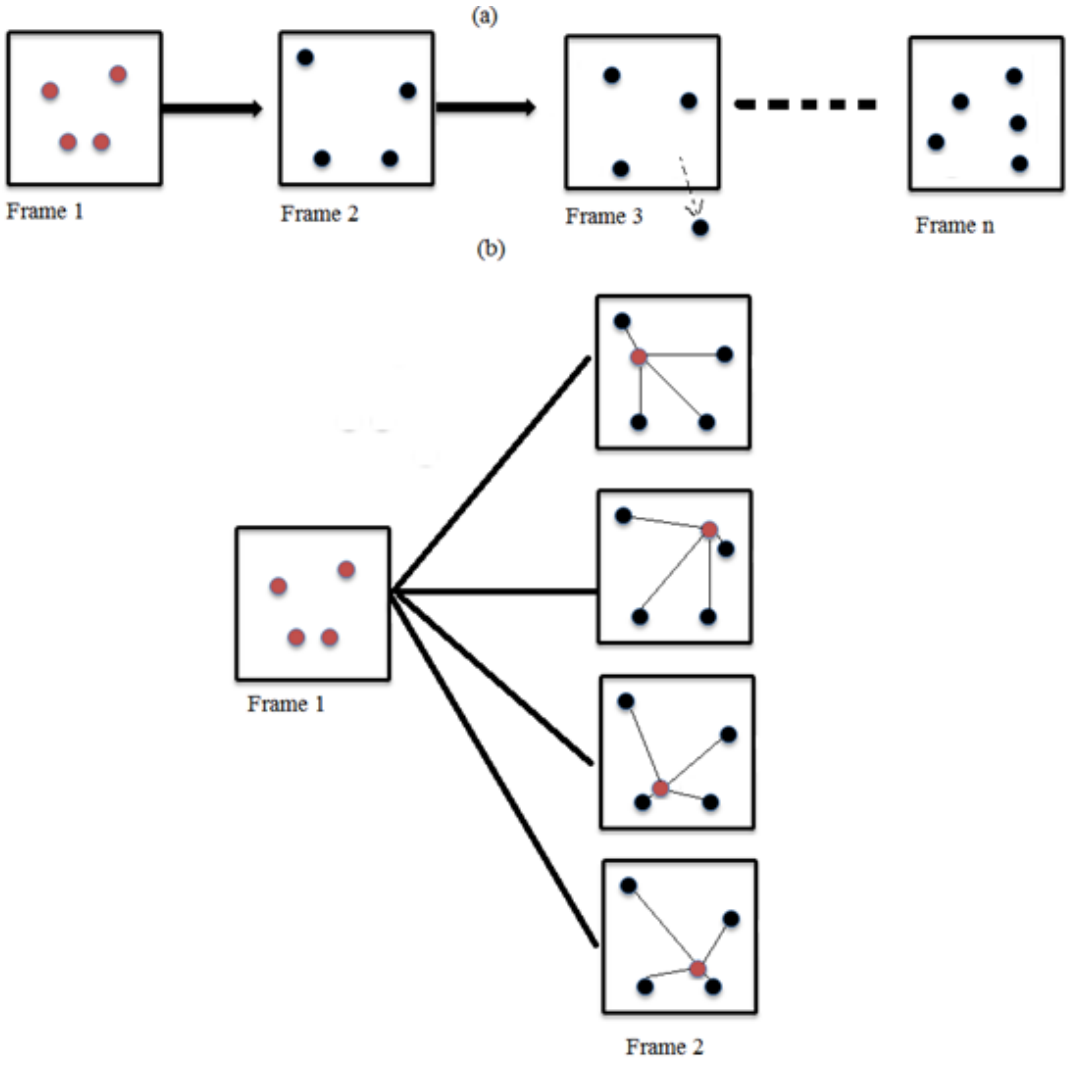

Figure 2.4: Flow chart of PMDD method. Figure 2.4 (a) records a number of images with a certain time interval between the frames; Figure 2.4 (b) measures the displacements between the particle centres in the previous frame and the particles centres in the next frame.

Figure 2.5 (1a) shows an example of an experimental frame of data obtained from a sample containing particles with a nominal radius of 200 nm. Particle centres in the first frame are marked as "o" in **Figure 2.5 (1b)**, whereas the "*" represents particle centres in the next frame with a one-second interval time.

Due to the Brownian movement of the particles, it is seen that most of the particle centres in the first frame have a next-frame centre in close proximity, and it may be

seen that some of the particle centres do not have a corresponding proximate centre in the previous or subsequent image. The missing particle centres can be explained by the particles moving in or out of the field of view or the illuminated region.

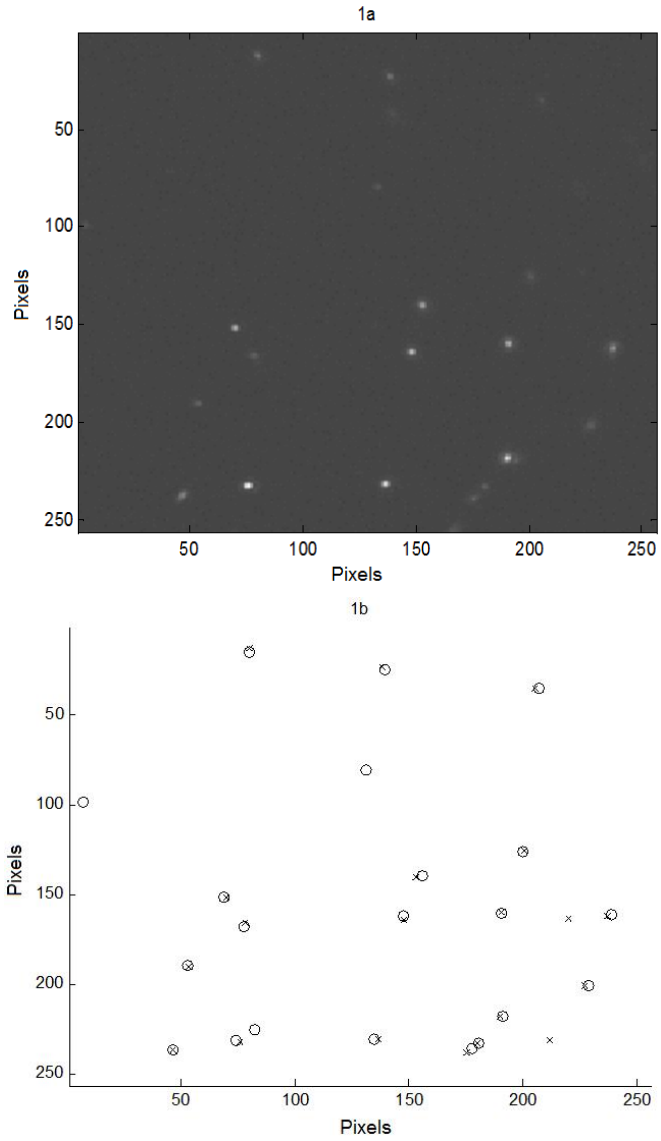

Figure 2.5: (1a) An image of 200nm radius polystyrene particles in a 10mm x10mm glass cell illuminated with a thin sheet of light (~20µm x 500µm) from a solid state laser ($\lambda = 532\text{nm.}$) focussed into the sample using a 50mm cylindrical lens and imaged with a 0.4 NA long working microscope objective. (1b) The circles are the peak centres derived from the image of Fig (1a). The crosses are the centres of the peaks from the next frame of data recorded one second later than the first frame, each frames of data was recorded with an exposure time of 25 milliseconds and digitised into 8 bits.

The general idea of PMDD method is based on the relationship between an arbitrary particle centre in the first frame and an arbitrary particle centre in the consecutive frame. Two particles centres (pairing) can either arise from the same particle (class ***I***) or arise from the different particles (class ***II***). The data processing is to calculate the displacement of each pairing. A histogram is formed from the displacements of class ***I*** and class ***II*** pairings. Comparing with the large displacement from two different particles, a smaller displacement is calculated from a class ***I*** pairing due to the Brownian movement of the particle. The procedure is then repeated from frames two and three, three and four, or any other two consecutive frames until to the last two frames. Finally, the distribution of the displacements is formed over the complete set of frames. Assuming there are ***n1*** particles in an arbitrary frame and there are ***n2*** particles in the subsequent frame, then there are ***n1*n2*** pairings with all the particles in the previous and subsequent frames. Some of the pairings arise from the same particle, class ***I***, and the remainder are classified as class ***II*** pairings arising from the different particles. Of course, there are maximum ***n1*** or ***n2*** (depending on the minimum of ***n1*** and ***n2***) class ***I*** pairings contributing to the histogram. It is a minority distribution comparing to the majority distribution from the unrelated particles in class ***II***. However, obviously, class ***I*** contains the important information about the particle size distribution. Because the displacement from any class ***II*** pairing arises from two unrelated particles. The distribution of the majority displacements from class ***II*** may extend over a wide range but does not contribute to the particle size information.

Figure 2.6 displays an example of a particle movement displacement distribution obtained from a computer-simulated experiment for particles with a true distribution with a lognormal form, a mean radius of 100 nm and a standard deviation of 20nm.

The normalised distribution is summed over 300 consecutive frames, the time interval is 1s, exposure time is 0.05 and no photon or detector noise was included.

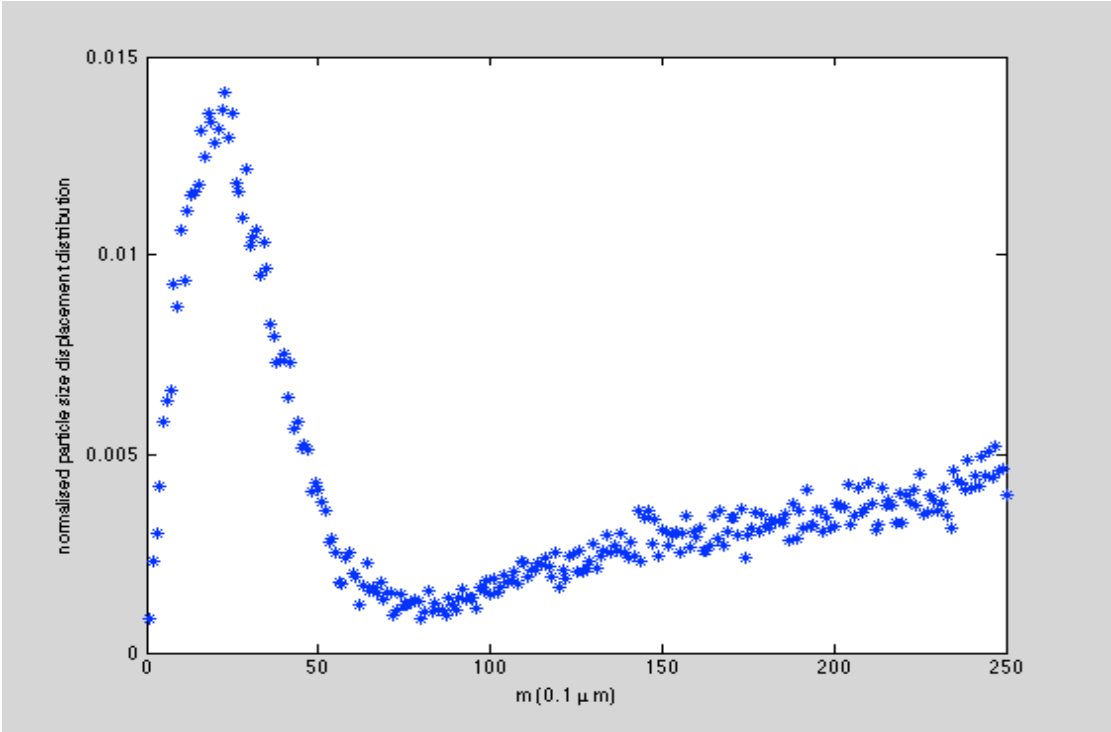

Figure 2.6: An example of a normalised particle movement displacement distribution. The x axis is m, which is defined in equation (2.6). The Blue stars represent the distribution obtained from a simulated experiment; the distribution has been normalised to make the sum of data values multiplied by the histogram bin width (up to the 500^{th} value) equal to unity.

The blue star in **Figure 2.6** is a histogram of the different displacements between any arbitrary particle centre in an image and any arbitrary particle centre in the next image. The reason this distribution has this form i.e. a broad peak sitting on top of a linear ramp is explained next (see paragraph after equation (2.12)).

Due to the random Brownian motion of the particles, the two-dimensional displacement distribution from class ***I*** pairs have a two-dimensional Gaussian shape with a standard deviation $\delta = \sqrt{2D\Delta T}$ (equation **(2.1)**). Most of these displacements

are concentrated within around 5 microns. The displacements between the different particles (class ***II***) distribute over a wider region compared with the displacements from class ***I***, and form a uniform two-dimensional distribution.

Although the particles actually move in three dimensions, the camera can only capture a two-dimensional image. Considering a particle at the original position (**0, 0**), because the particle undergoes Brownian movement, according to the theory of diffusion, the next position of this particle at a certain time interval follows a Gaussian distribution:

$$P(x,y)=\frac{1}{2\pi\delta^2}\exp\left(-\frac{x^2+y^2}{2\delta^2}\right) \tag{2.5}$$

where $\boldsymbol{\delta}$ is defined in equation **(2.1).**

Defining, $m=\sqrt{x^2+y^2}$, it can be explained that it is a circle whose centre is the origin of ***XOY*** coordinate with radius ***m***, and then the possible displacement (2.5) can be represented by a change of variables as a function of ***m***:

$$p(m)=\frac{2\pi m}{2\pi\delta^2}\exp\left(-\frac{m^2}{2\delta^2}\right)=\frac{m}{\delta^2}\exp\left(-\frac{m^2}{2\delta^2}\right) \tag{2.6}$$

For a number of particles with the distribution of ***f(R)***, the expected particle displacements from class ***I*** can be expressed with a form of:

$$p_I(m)=\int f(R)\frac{m}{\delta^2}\exp(-\frac{m^2}{2\delta^2})dR \tag{2.7}$$

The displacements from different particles in class ***II*** follow a two-dimensional uniform distribution because the different particles' positions in a sample are randomly distributed. Thus, the probability of a particle at position ***(x, y)*** on the ***XOY*** plane is expected to be a constant ***k'***.

$$p_{II}(x,y) = k' \tag{2.8}$$

where, the constant ***k'*** depends on the density of particles in the images. Then, by another change of variables, the probability of the random displacements from different particles can be expressed as:

$$p_{II}(m) = m.2\pi k' = mk \tag{2.9}$$

Finally, combining $p_I(m)$ and $p_{II}(m)$, the complete distribution g_m can be written as in equation **(2.10)**. The first term represents the real particles displacements in class ***I***, whereas the second term is the random movement displacements from the different particles in class ***II***.

$$g_m = p_I(m) + p_{II}(m) \tag{2.10}$$

It can be rewritten as:

$$g_m = \sum_n H_{m,n} f_n + km = Hf + km \tag{2.11}$$

where ***k*** is a constant; ***f*** is the particle size distribution; ***m*** is the movement of particles in formula **(2.6)**; $H_{m.n}$ is a transfer matrix.

$$H_{m,n} = \frac{m}{\delta_n^2} e^{-\frac{m^2}{\delta_n^2}} \tag{2.12}$$

Where $\boldsymbol{\delta_n}$ is movement which is defined in equation **(2.1)**.

Equation **(**2.10**)** and **(**2.11**)** explain Figure **2.5** mathematically. The broad peak arises from the first term on the right hand side of equation (2.10) and contains information about the particle size distribution; the linear ramp arises from the second term on the right hand side of equation (2.10) and contains information about the density of particles in the images; a higher density of particles leads to a steeper ramp.

Equations (2.10-2.12), indicate that Particle Movement Displacement Distribution (PMDD) data contains particle size information, especially in the first term from **class *I*** pairings. Hence, using a suitable inversion method, a particle size distribution can, in principle, be reconstructed. The inversion method will be discussed in the following section 2.4.

2.4 PMDD Data Inversion Algorithm

As outlined in the previous section the result of processing the particle positions in all the images recorded is a particle movement displacement distribution, such as **Figure 2.6**. In order to recover a particle size distribution, this data must be inverted, i.e. we wish to invert equation (2.11) to find a solution for f_n, the particle size distribution, from the data values g_m , the particle movement displacement distribution.

This is a similar problem to the inversion of DLS data. There are a number of data inversion methods that may be employed, including the CONTIN method by Provencher (47), the singular value decomposition method (48), the method of cumulants (49) and a recently developed Maximum Likelihood method (21, 22).

According to her work, the strengths of the ML method rely on its ability of taking into account the nature of the noise in the data. Furthermore, it does not assume any a-priori information about the particle size distribution. The performance of this algorithm has been tested through simulations and experiments for different particle distributions for DLS data with a number of noise levels. The retrieved average particle size error is usually within 10% of the original value. It has also been compared with the other inversion methods, and it has been demonstrated that the ML method provides better results in terms of fitting to the data and more accurate estimation of the size distribution than the alternative methods listed above. Further details about this method are discussed in (21, 22). In view of the demonstrated success of the ML algorithm in inverting DLS data and the similarity of the inversion required for PMDD data, it was decided to make use of this algorithm for the PMDD method to reconstruct particle size distributions.

2.4.1 Maximum Likelihood Data Inversion Algorithm for PMDD

The data distribution from PMDD is given by formula **(2.11)**. The component $(Hf + km)$ is the noise free distribution. The difference between $\boldsymbol{g_m}$ in formula **(2.10)** and the real distribution is the noise term. As the data are corrupted with Poisson noise, if we put $\lambda_m = \left(Hf^{(0)} + km \right)_m$, the probability of obtaining a data value of $\boldsymbol{g_m}$ is given by (51):

$$p_g\left(g_m\right) = e^{-\lambda_m} \frac{\left(\lambda_m\right)^{g_m}}{\left(g_m\right)!} \tag{2.13}$$

It is reasonable to assume that the component $\boldsymbol{g_m}$ of the image is the distribution of independent Poisson random variables with expectation values $\lambda_m = (Hf^{(0)} + km)_m$ (51). The corresponding probability of obtaining the complete set of data value $\boldsymbol{g_m}$ is given by:

$$\mathrm{p}\left(g:k,f\right)=\prod\nolimits_m\left(\frac{e^{-(km+Hf)_m}(km+Hf)_m^{g_m}}{g_m!}\right) \tag{2.14}$$

This probability must be non-negative. Consequently, in order to simplify the equations, the formula **(2.14)** can be expressed as the logarithmic likelihood function:

$$l\left(g:k,f\right)=\sum_m\left(g_m\ln(km+Hf)_m-(km+Hf)-\ln(g_m!)\right) \tag{2.15}$$

In equation **(2.15)**, there are two unknown parameters; the particle size distribution $\boldsymbol{f}$ and the linear gradient of particles random movements $\boldsymbol{k}$ in class ***II***. A Maximum Likelihood data procedure is applied to yield the best-fitted particle size distribution $\boldsymbol{f}$ and the gradient $\boldsymbol{k}$ at the same time.

Case 1: the particle size distribution $\boldsymbol{f}$.

The differentiation of $l\left(f\right)$ with respect to f_m is:

$$\frac{\partial l(f(g:k,f))}{\partial f_n}=\sum_m\frac{\partial}{\partial f_n}\left\{\left(g_m\ln(km+Hf)_m-(km+Hf)-\ln(g_m!)\right)\right\} \tag{2.16}$$

Performing the differentiation, the equation can be simplified as:

$$\frac{\partial l\left(g:k,f\right)}{\partial f}=\sum_m\left\{-H_{mn}+g_m\frac{H_{mn}}{Hf+km}\right\} \tag{2.17}$$

To find the maxima of $l(f((g:k,f))$, let the equation **(2.17)** equals to zero, and then

$$\sum_m H_{mn} = \sum_m g_m \frac{H_{mn}}{Hf + km} \tag{2.18}$$

In order to find the suitable ***f***, the equation **(2.18)** yields to:

$$f \cdot \sum_m H_{mn} = f \cdot \sum_m g_m \frac{H_{mn}}{Hf + km} \tag{2.19}$$

Finally, an iterative algorithm of the particle size distribution is formed as follows:

$$f^{(p+1)} = \frac{f^{(p)} \times \sum_m H_{mn} \left\{ \frac{g_m}{Hf^{(n)} + km} \right\}}{\sum_m H_{mn}} \tag{2.20}$$

where $\boldsymbol{H_{mn}}$ is explained in eq. (2.12).

Case 2: the linear gradient of particles random movements ***k*** in class ***II***.

The differentiation of $l(f((g:k,f))$ with respect to ***k*** is:

$$\frac{\partial l(g:k,f)}{\partial k} = \sum_m \frac{\partial}{\partial k} \left\{ (g_m \ln(km + Hf)_m - (km + Hf) - \ln(g_m!)) \right\} \tag{2.21}$$

Similarly, the differentiation is formed as:

$$\frac{\partial l(g:k,f)}{\partial k} = \sum_m \left\{ \frac{g_m m}{Hf + km} - m \right\} \tag{2.22}$$

Then the iterative algorithm of the linear gradient of particles random movements ***k*** yields to:

$$k^{(p+1)} = k^{(p)} \frac{\sum_m \frac{g_m m}{Hf^{(n)} + km}}{\sum_m m} \tag{2.23}$$

Where $\boldsymbol{k^{(p+1)}}$ is the gradient to maximize $l(g:k,f)$.

2.4.2 Evaluation Approaches

Three evaluation approaches have been used to assess the inversion method. One is to describe the absolute area error between the true particle size distribution and reconstructed particle size distribution. A goodness-of-fit parameter $\boldsymbol{\epsilon}$ is defined as the absolute area error, which is shown in the form of:

$$\varepsilon = \sum_{i=0}^{N} \left| f_i^{(0)} - f_i \right| . \Delta R \tag{2.24}$$

where $\boldsymbol{N}$ is the number of points of the distribution and ΔR is the spacing between these points. $\boldsymbol{f_i^{(0)}}$ and $\boldsymbol{f_i}$ are the normalised true and reconstructed particle size distribution values. For an ideal fit, $\boldsymbol{\varepsilon}$ is equal to zero; for completely non-overlapping distributions, $\boldsymbol{\varepsilon}$ is equal to two.

A second evaluation criterion is to compare the mean value of the true particle sizes and the mean value of the recovered particle sizes. The mean value determines the averaged reconstructed particle sizes. A third evaluation approach is to determine the standard deviation of the recovered particle size distribution to analyse the fluctuation of the particle sizes.

2.4.3 An Example of a Reconstructed Particle Size Distribution by the Maximum Likelihood Inversion Method

Figure 2.7 displays a simulated example of the reconstructed particle size distribution by Maximum Likelihood inversion applied for PMDD. The Particle Movement Displacement Distribution (PMDD) is shown on the left, and the reconstructed particle size distribution based on PMDD is shown on the right. **Table 2.2** lists some relevant simulation parameters. More details of the simulation carried out will be given in Chapter 3.

Particle radius	100nm with 20nm standard deviation
Temperature	20^{o}C
Dynamic viscosity (water)	0.001pa.s
Number of frames	300
Frame time interval	1s
Particle concentration	5 x 10^{6}/ml

Table 2.2: Simulation parameters.

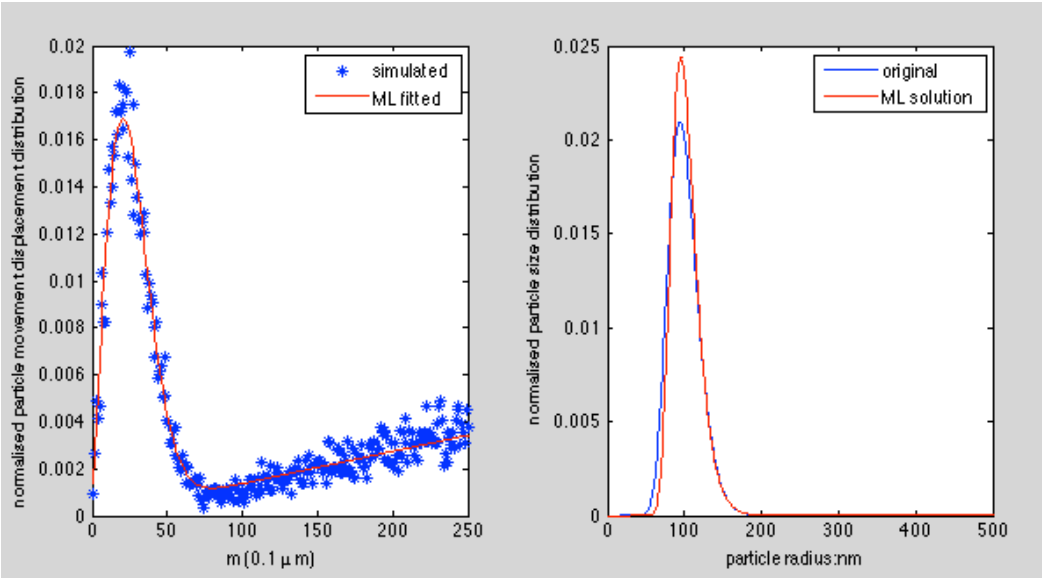

Figure 2.7: The reconstructed particle size distribution with ML algorithm. The recovered mean radius is 102.7nm compared with the actual mean radius of 100nm and with a recovered 19.9nm standard deviation compared with an actual value of 20nm. The area error (defined I equation (2.24)) is 0.14.

It should be noted that the simulation used to generate the data in **Figure 2.7** was quite idealised, in that no photon or detector noise was included and the optics was modelled as diffraction limited. A comprehensive analysis of the accuracy of this method under different noise and distorting conditions is provided in the next chapter. A comparison of the accuracy in recovering particle size distributions compared with a particle tracking method (based on the NTA method developed by NanoSight Ltd.) is given in Chapter 4.

2.5 Summary

An alternative method to measure a particle size distribution called Particle Movement Displacement Distribution (PMDD) of processing multiple images of

particles undergoing Brownian motion has been described in this chapter. It shows a histogram of the vectors connecting the centres in each frame with all the centres in the subsequent frame. Some further details about PMDD can be found in the paper (57). Some relevant knowledge about Brownian movement and the particle centre finding method known as the image moment method are discussed briefly. Maximum Likelihood inversion procedure is applied to PMDD data distribution to yield a particle size distribution in **Section 2.5**. Three evaluation approaches to assess the inversion method have been discussed and an example of the reconstructed particle size distributions is illustrated in **Figure 2.6**. The effectiveness of the PMDD method will be presented in the next chapters with simulation and experimental results.

3 Optimising and Assessing the Influence of the Parameters in the PMDD Method

3.1 Introduction

The basic principles of Particle Movement Displacement Distribution (PMDD) and a Maximum Likelihood data inversion algorithm have been discussed in Chapter 2. Chapter 3 will concentrate on further investigations on the PMDD method. Section 3.2 describes the imaging arrangement that is simulated and the computational steps used in the simulation to produce the results presented in this chapter. Section 3.3 investigates the influence of the various parameters based on the simulation results, including the time interval, exposure time, noises (Poisson noise, quantisation noise and background noise) and sample concentration. Finally, it considers the complicated optics aberration effects. Section 3.4 presents simulation results when combining all of the optimised experimental parameters and considering noise conditions. Finally, section 3.5 is a brief summary of the work carried out in this chapter.

3.2 Simulated Setup

The schematic setup of the PMDD method is illustrated in **Figure 3.1**. Laser light is applied as the light source and a cylindrical lens is employed to generate a narrow monochromatic coherent light sheet passing through the glass cell. The particles are suspended in water in this cell. A two-lens system is used to collect and focus the

scattered light from the particles. A CCD camera is implemented to capture photons and form images.

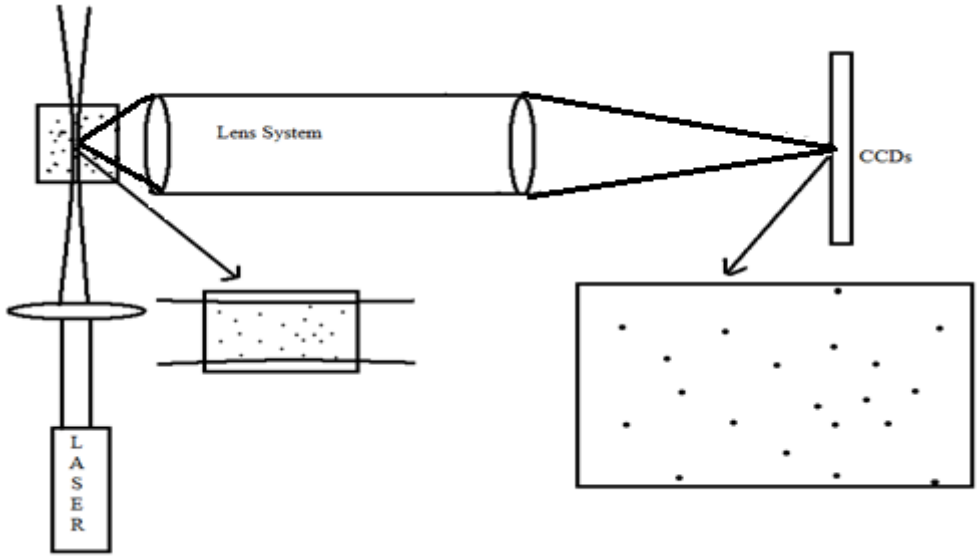

Figure 3.1: Schematic of the simulated PMDD setup.

In the simulation:

(1) The number of particles in the cell is calculated based on the specified particle density/concentration.

(2) Each particle is assigned a radius, and an initial random position with the cell; these are the particle positions used for frame one.

(3) For the subsequent frames, based on the specified temperature and viscosity, each particle is moved to simulate Brownian motion using equations (2.1) and (2.2).

(4) To form an image, firstly, the total scattered light, expected to reach the detector from each particle is calculated; this calculation depends on the particle properties, its position within the illuminating beam, the intensity profile of the illuminating beam,

the collection angle of the imaging lenses. The calculation is detailed in Appendix II(a).

(5) Secondly, the form of the intensity pattern resulting from each particle is calculated; this depends on the focal position of the particle, any aberrations of the imaging lens system, the system magnification and diffraction effects. Details of the calculation are given in Appendix II(b).

(6) Thirdly, the normalised form of the intensity pattern calculated in step (5) is multiplied by the intensity calculated in step (4) to give the resultant contribution from a single particle.

(7) Steps (4) to (6) are repeated for every particle within the cell and the intensities are added together to produce an overall image.

(8) Based on the quantum efficiency of the detector, the expected number of electrons in each pixel can be calculated from the result of step (7).

(9) The steps (4) to (8) are then repeated for each subsequent frame with the particles undergoing simulated Brownian motion as outlined in step (3).

(10) For each frame of data, the detector noise is then included by adding to the expected number of electrons in each pixel: (i) a constant value to simulate the effect of background noise, arising from thermal events in the camera and stray ambient light, (ii) a further constant value to simulate the effect of readout noise, which originates in the amplifier that converts the electrons to a voltage level. The calculation of these constants is detailed in Appendix (3). Then, the detected number

of electrons is simulated by calling a random number from a Poisson distribution with the expected value as the mean.

(11) Finally, the quantisation process of the analogue to digital conversion process is simulated by using an electron to count conversion factor (3.2 electrons per count was used as that was the specified value for the camera used in the experimental work) that is used to simply multiply the simulated detected electron counts before rounding the values to the nearest quantisation level.

(12) As the background and readout noises add a statistically uniform level to the images, this level may be subtracted before the particle centroiding process is carried out.

It should be noted that for some simulation results, not all the noise factors are included in the simulation; this is so as to enable the influence of particular variables to be studied more effectively without the masking effect of all the different sources of noise.

For the simulated results in this chapter, the wavelength of the laser is 532nm, the laser beam diameter is 0.6mm, but focussed by the cylindrical lens (focal length 50mm) to a diameter of 25 micrometres (diameter measured between the $1/e^2$ points in the Gaussian intensity profile) in the sample cell and the laser power is 25mW. The sample cell is 10mm x 10mm x 40mm, the temperature of the water is 20 degrees centigrade and the dynamic viscosity of the water is 0.001Pa.s. The focal length of the first lens is 10cm and the focal length of the second lens is 67cm so the system magnification is 6.7, and the numerical aperture of the first imaging lens was set to 0.4 as these values were those of the experimental setup described in chapter 4.

An example of a single simulated frame including all the camera noise effects is shown in **Figure 3.2**, the conditions are given in the figure caption. It may be noted that the simulated image shown here has a similar general appearance to frames captured from the experimental setup e.g. as shown in **Figure 4.2**.

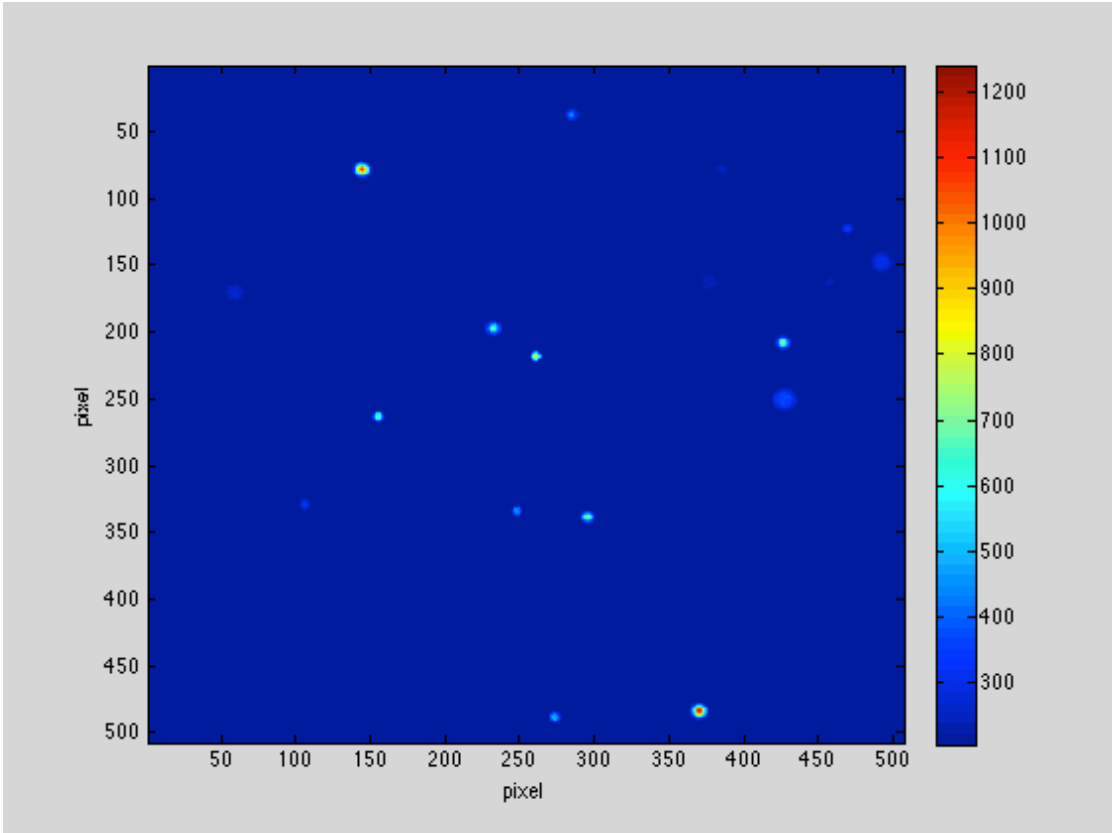

Figure 3.2: A simulated image of 100nm mean radius particles with 20nm standard deviation, with a density of $5*10^6$ particles per millilitre imaged according to the parameters stated above.

3.3 Optimising the Experimental Parameters in PMDD

This section examines, through computer simulations the effect of varying the various parameters that define a PMDD experiment in order to determine optimum values or to assess the importance of their influence on the quality of the results obtained.

3.3.1 Time Interval

Time interval is the time period between the start of two consecutive frames. Time interval is a crucial parameter during the experiment because the time interval affects how far the particles move within the period under Brownian movement. If the interval is large, the displacements of the particles will be larger. However, although it is easier to measure the displacements in this situation, fewer frames will be obtained in a set experimental time and fewer ***class I*** pairings will be measured. When the time interval becomes small, the movements of particles are small. If the displacement is around pixel size, it is quite difficult to measure the movements of particles. This is more of a problem for larger particles which move smaller distances under Brownian motion than smaller particles. As the time interval is such a fundamental parameter, it is explored first in the absence of noise effects, so as to see the dependence on this parameter alone. Hence, the different interval times and some relevant parameters in this simulation are given in **Table 3.1**.

Temperature / viscosity	20^{o}C/ 0.001 Pa.s
Particle size distribution: mean / standard deviation	100nm/20nm
Simulation time	5 minutes
Image size/pixel size	500 x 500 pixels /3.35microns
Exposure time	0.05s
Magnification	6.7
Movement histogram interval	0.1 microns
Time interval	0.1s, 0.5s, 1s, 2s, 3s

Particle concentration	5 x 10^6 /ml
Poisson noise	No
Quantisation noise	No
Background noise	No

Table 3.1: Simulation parameters used in the simulation to assess the effect of changing the time interval.

In order to examine the effect of changing the time interval in isolation from other effects, the particles are assumed to be still during the exposure time, and as mentioned above no noise is considered. The following **Figures 3.3**, **3.4, 3.5, 3.6** and **3.7** display the particle movement displacement distributions (PMDD) based on 5 minute simulation time and the reconstructed particle size distributions are inverted by the Maximum likelihood method at different time intervals 0.1s, 0.5s, 1s, 2s and 3s respectively. In the following figures, the original distribution is a lognormal distribution with a mean size (radius) of 100nm and 20nm standard deviation. It is represented in the blue line. The recovered particle size distribution is displayed as the red line.

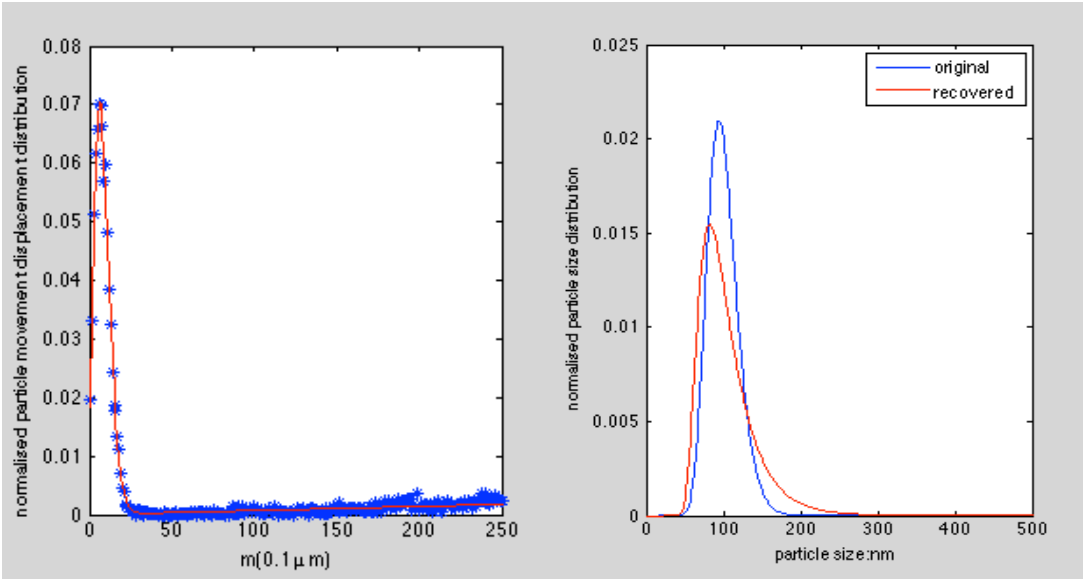

Figure 3.3:The normalised particle movement displacement distribution and the normalised recovered particle size distribution when the time interval is 0.1s, and other simulation parameters are given in Table 3.2.

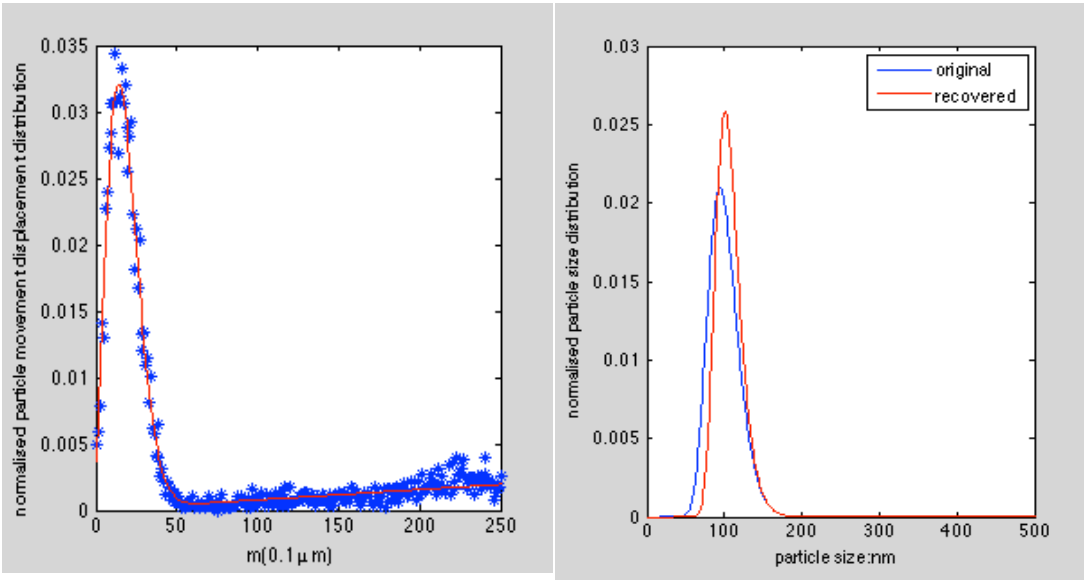

Figure 3.4: The normalised particle movement displacement distribution and the normalised recovered particle size distribution when the time interval is 0.5s, and other simulation parameters are given in Table 3.2.

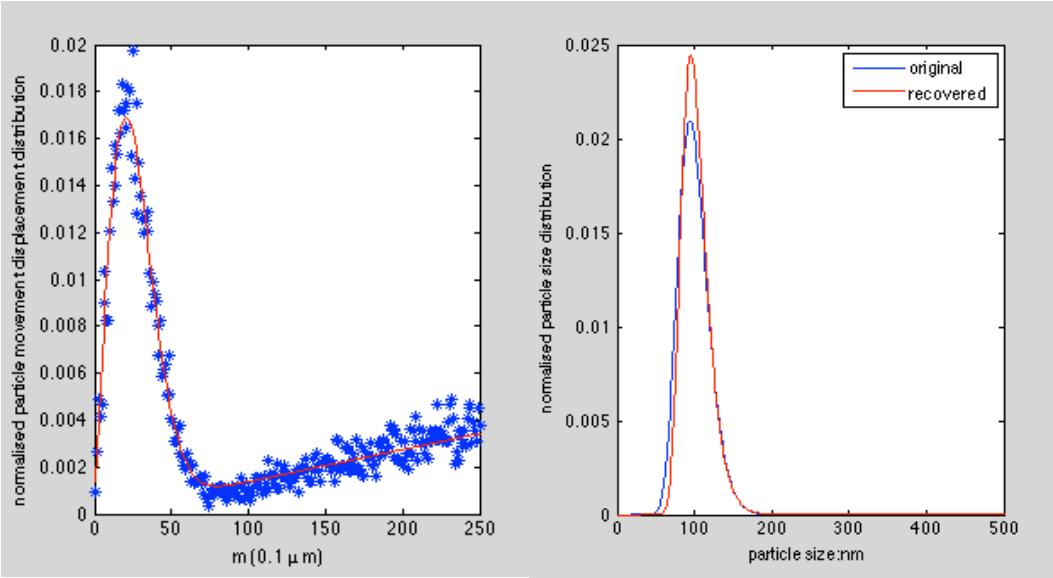

Figure 3.5: The normalised particle movement displacement distribution and the normalised recovered particle size distribution when the time interval is 1s, and other simulation parameters are given in Table 3.2.

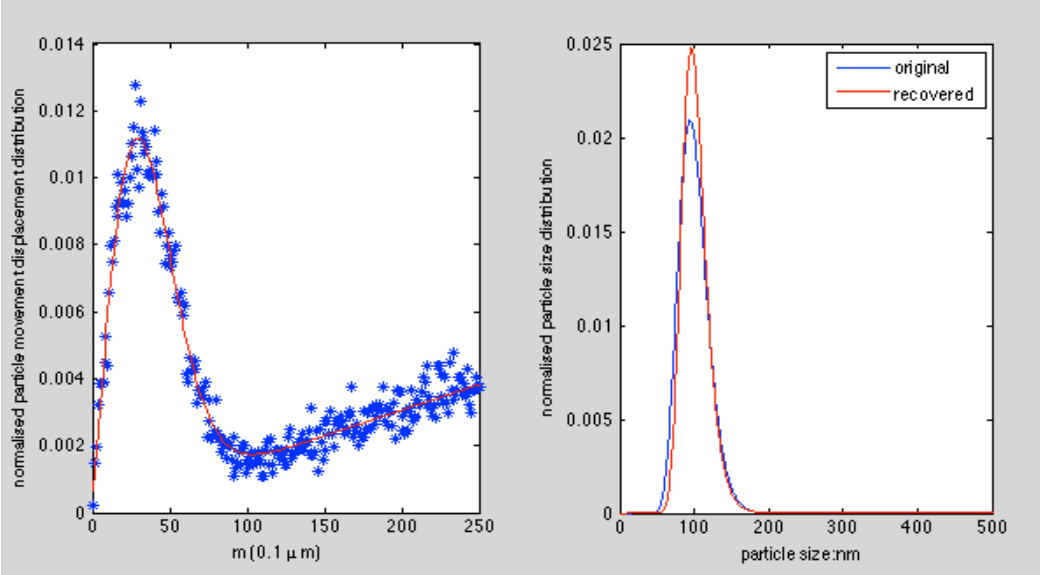

Figure 3.6: The normalised particle movement displacement distribution and the normalised recovered particle size distribution when the time interval is 2s, and other simulation parameters are given in Table 3.2.

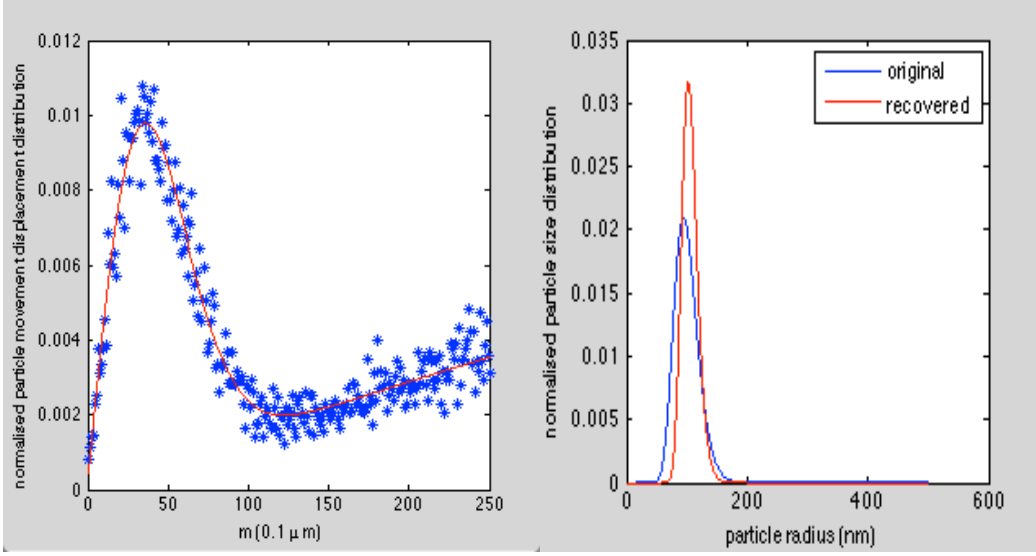

Figure 3.7: The normalised particle movement displacement distribution and the normalised recovered particle size distribution when the time interval is 3s, and other simulation parameters are given in Table 3.2.

The expected behaviour in the normalised particle movement displacement distribution can be observed in **Figures 3.3** to **3.7**. Firstly, as the time interval increases, the width of the peak is seen to increase as the particles move further in the longer times. Secondly, the distributions become noisier; this is a consequence of the reduction in the number of frames (for the fixed experiment time used) and therefore a reduction in the number of displacements is measured. Thirdly, it may be seen that the linear ramp part of the distribution (arising from the class II pairings) increases in proportion to the peak part of the distribution (arising from the class I pairings). This occurs because for the longer intervals it is more likely that the particles present in one frame will not be also present in the next frame.

The first effect (increased peak width) is of benefit as errors in the width due to finite accuracy of the particle centroiding will be less significant. However, the other two

effects will both lead to an expected reduction in accuracy of the recovered particle size distribution.

To quantify the effect of varying the time interval, the three criteria discussed in section 2.4.2 can be utilised to evaluate the results. **Figure 3.8** shows the mean values and the standard deviations of (i) the mean of the particle radius distribution, (ii) the standard deviation of the particle radius distribution, and (iii) the area error function defined in eqaution (2.24) for different time intervals based on ten independent simulations.

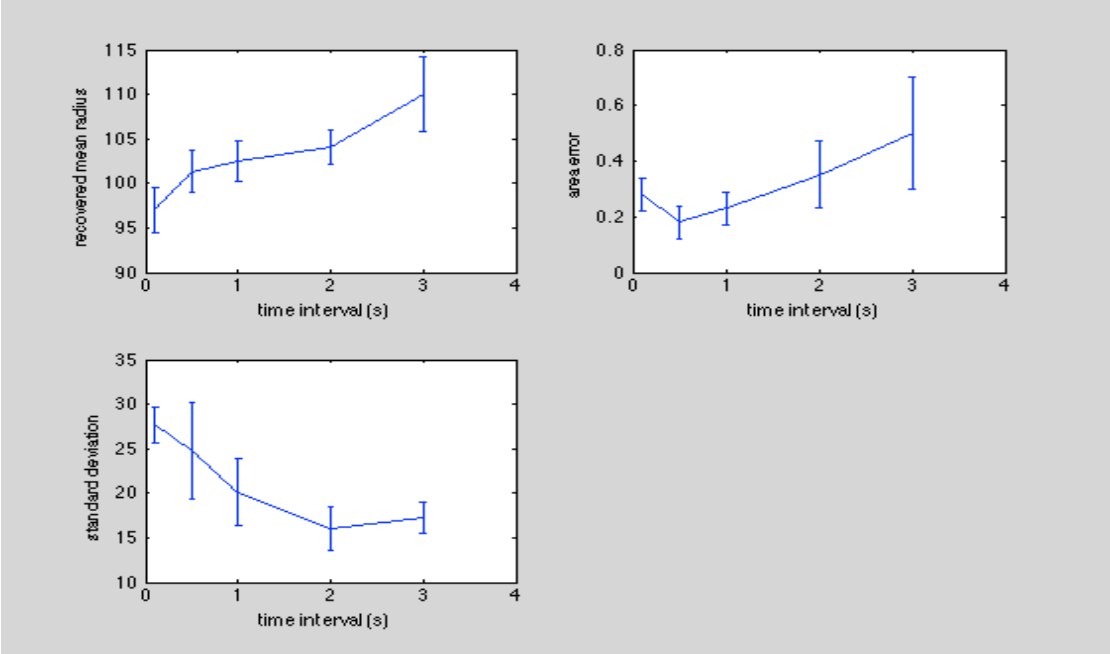

Figure 3.8: Area errors, mean radii and standard deviation of the particle size distributions for ten independent simulations at different time intervals: 0.1s, 0.5s, 1s 2s and 3s. The particle mean radius is 100nm and the standard deviation is 20nm.

As discussed above, it is expected as the time interval is increased, the increased width of the PMDD will have a beneficial effect but that the other two effects (increased noise and higher proportion of class II contributions) will have a detrimental effect on the recovered particle size distribution. Thus it would be

expected that both very short and very long time intervals would both be worse than some intermeditae value. This is broadly what is observed in **Figure 3.8** .

In the area error graph, it can be seen that the mean area error is worse at both the small and large ends compared with 0.5s and 1s time interval results. Compared with 0.32 for DLS, the area error is smaller with 0.5s and 1s time intevals, but the area error is around this value with 0.1s time interval and larger than this value when the time interval is 2s or 3s. The standard deviation (which is a measure of the repeatability of the expected results) is seen to be very much worse for the time intervals larger than 1s.

The increase in area error at 0.1s may be attributed to the narrowness of the PMDD compared to the accuracy of the particle positions. The increase in area error and in its variance above 1s may be attributed to the reduced number of class ***I*** pairings in the data set.

Similar patterns are observed for the reovered mean particle size, where it may be seen that the best value (close to 100nm) is obtained for 0.5s; the result for 1s is slightly worse but those for smaller and larger times are all significantly worse.

The results for the recovered standard deviation, show a similar pattern, here the best value (close to 20nm) is obtained for 1s with worse results for the smaller and larger times.

Based on these results, 1s is chosen as a suitable time interval in the subsequent simulations and experiments.

3.3.2 Exposure Time

Exposure time of the camera is another important factor to influence the simulation results. In photography, exposure time is the effective length of time a shutter is open; the total exposure is used to calculate the light reaching to the film or image sensor. When optimising the time interval, it was assumed the particles are still during the exposure time. In practice, due to the continuous random Brownian motion of particles, the particles move slightly during the exposure time. That suggests the smaller the exposure time is, the better result will be obtained. However, dark images are generated in the absence of light due to the short exposure time. Thus, it is difficult to form a clear image. In contrast, the longer the exposure time, the greater will be the signal to noise ratio, but the particle images will be blurred due to the continuous Brownian motion. In this section, the effect of the small Brownian movements of particles during the exposure time will be examined. **Figure 3.9** presents the effects of small Brownian movements of particles during the exposure time.

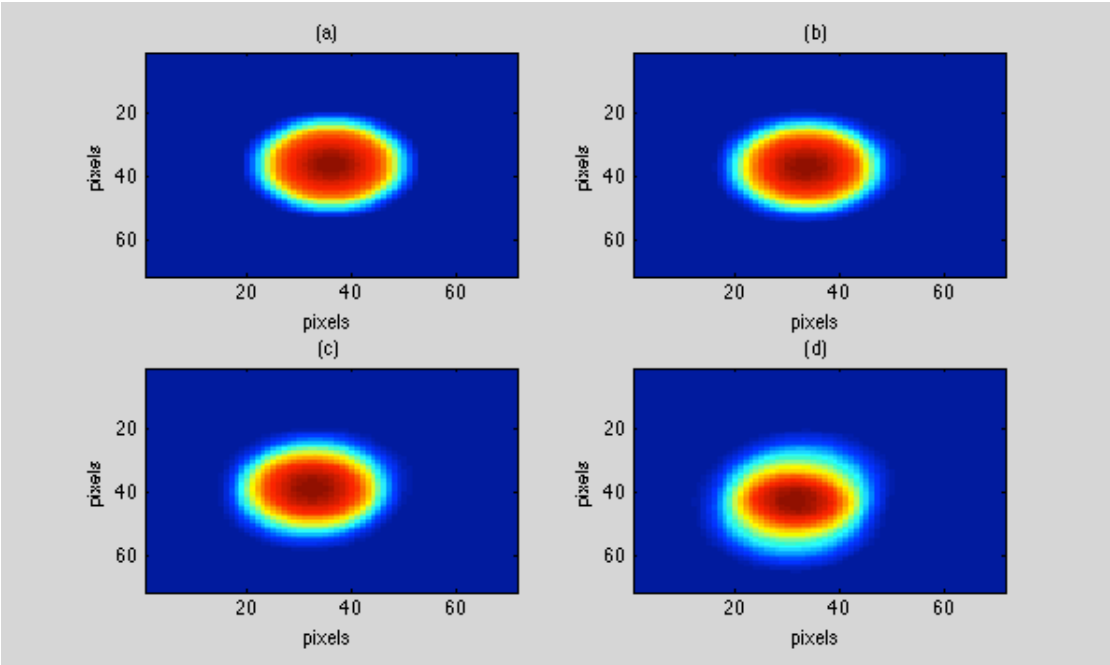

Figure 3.9: The effect of small Brownian movements of particles during the exposure time for a particle of 100nm radius imaged using the parameters listed in **Table 3.2**. (a): particle image with 20ms exposure time. (b): particle image with 50ms exposure time.(c): particle image with 100ms exposure time. (d): particle image with 200ms exposure time.

In **Figure 3.9**, it can be seen that as the exposure time increases the size of the resulting image increases and the circular symmetry deceases, both these effects lead to a decrease in the accuracy of the particle centroiding algorithm described in section 2.2.

In order to find an optimum time, it should be large enough to present a bright image, and also it should minimise the errors caused by the existing Brownian movements. Although, in general, changing the exposure time has two effects (image brightness and image quality). In this section only the image quality effect will be examined. The reason is that the Poisson noise signal to noise ratio varies as the square root of the light level; thus at low light levels (low numbers of photons contributing to the image) any increase in light level has a significant effect on the signal to noise ratio in the image whereas at higher light levels any increase in light level will have only a small increase in signal to noise ratio. Thus, to isolate the effects of the image quality degradation due to the exposure time, photon noise is neglected in this section.

In section **3.3.1**, 1s has been chosen to be the suitable time interval, and therefore, four exposure times 0.02s, 0.05s, 0.1 and 0.2s are considered to simulate the results. Some relevant simulation parameters to examine the effect of exposure time are listed in **Table 3.2**. An example of the reconstructed particle size distributions based on different exposure times is displayed in **Figure 3.10.** It considers the small Brownian movements of particles during the exposure time.

Temperature /viscosity	20^{o}C/0.001 Pa.s
Particle size distribution: mean / standard deviation	100nm/20nm
Number of frames	300
Image size/pixel size	500 x 500/3.35microns
Exposure time	0.02s, 0.05s, 0.1s, 0.2s
Magnification	6.7
Movement histogram interval	0.1 microns
Time interval	1s
Particle concentration	5 x 10^{6} /ml
Poisson noise	No
Quantisation noise	No
Background noise	No

Table 3.2: Simulation parameters used in the simulation to assess the effect of changing the exposure time.

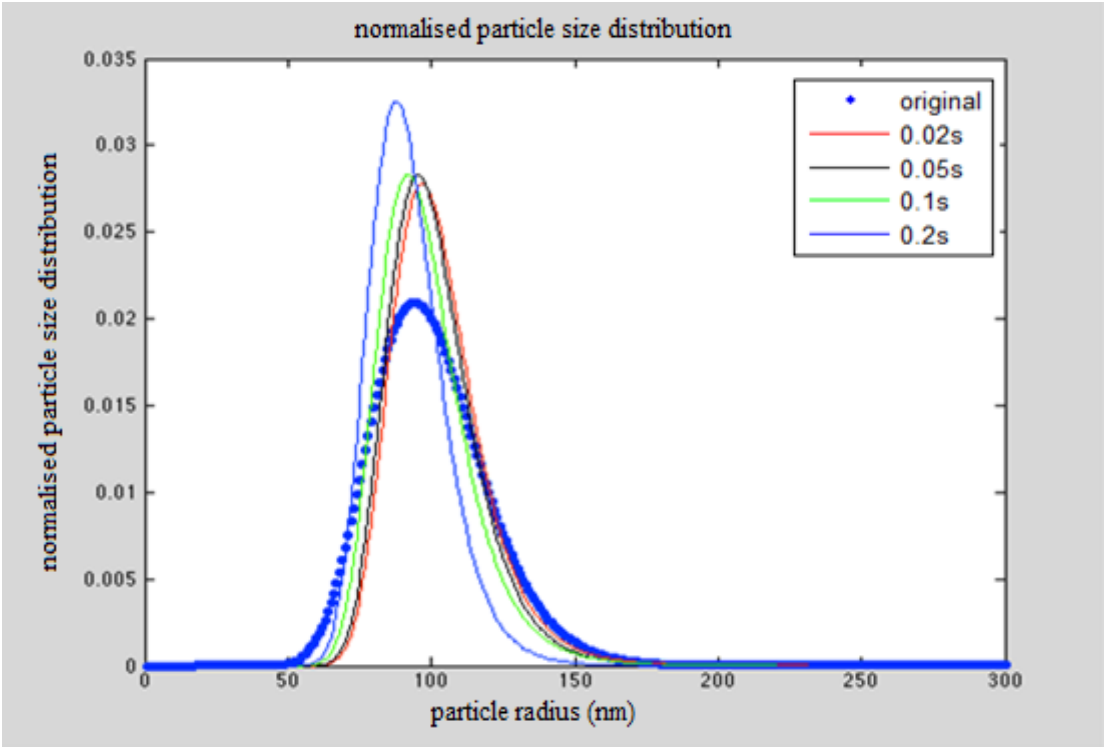

Figure 3.10：An example of the normalised reconstructed particle size distributions when the exposure times are 0.02s, 0.05s, 0.1s and 0.2s respectively. The original mean radius of particles is 100nm. It has a lognormal distribution with 20nm standard deviation.

It may be seen in **Figure 3.10**, that as the exposure time is increased the recovered distribution loses accuracy, when the exposure time is 0.2s, the reconstructed particle size distribution is worse than the others. The recovered mean radii of the example are 100.47nm, 98.72nm, 96.69nm and 90.88nm respectively with the exposure time increasing. The results of a series of simulations to compare the different exposure time are shown in **Figure 3.11**. The mean radii, area errors and standard deviation of the particle size distributions from ten independent data sets are presented in **Figure 3.11**.

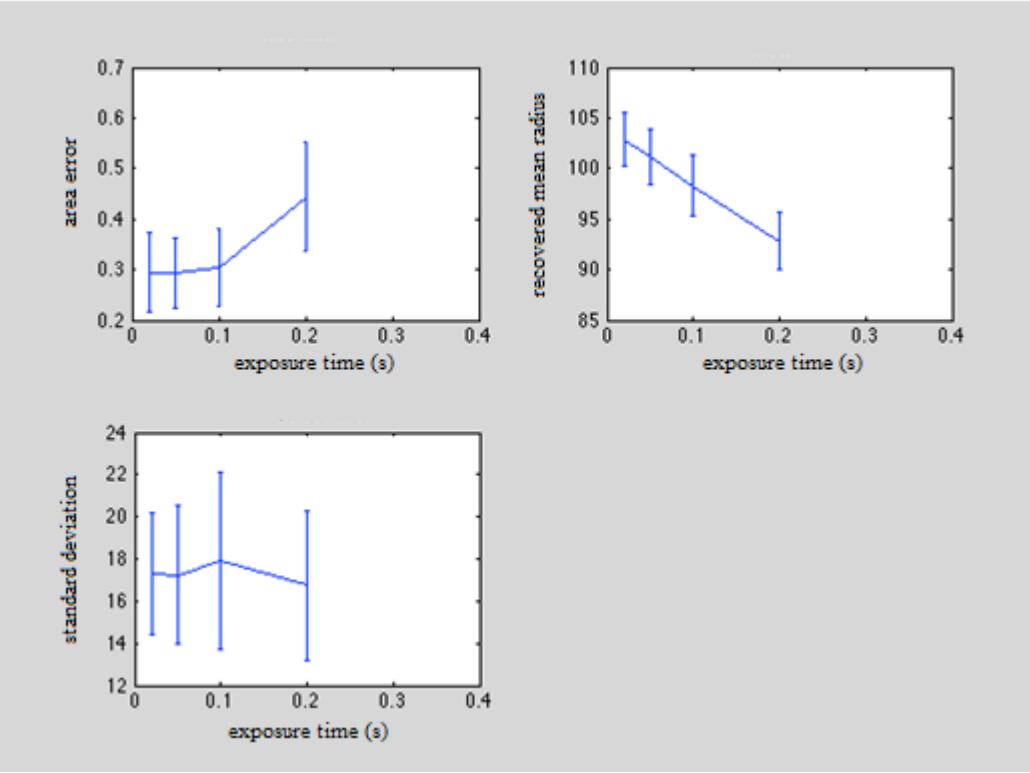

Figure 3.11: Area errors, mean radii and standard deviation of the particle size distributions for ten independent simulations at different exposure times: 0.02s, 0.05s, 0.1s, and 0.2s. The particle mean radius is 100nm and the standard deviation is 20nm.

According to the comparisons in **Figure 3.11**, an exposure time between 0.02s and 0.05s performs better results than the longer exposure times (0.1s and 0.2s). When the exposure time is up to 0.2s, the recovered mean value and area error become worse compared with the shorter exposure times. The area error is around 0.3 when the exposure time is less or equal to 0.1s, which is smaller than 0.32 for DLS, but the area error increases to 0.4 with 0.2s exposure time. That can be explained by the movements of particles during the exposure time.

In these simulations, an increase in exposure time above 0.1s is seen to lead to a decrease in the recovered mean of the particle size distribution. As the exposure time increases two effects occur (100), firstly for an ideal centroiding algorithm, a 'particle

smearing' effect leads to the measurement of shorter particle movements (which appear therefore as larger particles) but secondly the accuracy of the centroiding algorithm will decrease which leads to the measurement of longer particle movements (which appear as therefore as smaller particles). For the conditions of these simulations it is evident that the second effect is dominant.

The results of **Figure 3.11** indicate that the blurring effects are quite minor for exposures time below 0.05s, although practically, one exposure time applied for all size particles is impossible, because large particles scatter much more light than the small ones. The light intensity may exceed the scale limit of the CCD camera from large particles, whilst the intensity may too faint to distinguish for the small particles. Because these simulations are based on 100nm size particles, if necessary, the exposure time may vary for some particular size particles.

3.3.3 Poisson Noise Effects on the PMDD Method

In practice, Poisson noise arising from the random detection of photons is a crucial factor which cannot be ignored. This type of noise changes with the sensitivity of the camera, length of the exposure, temperature, and even varies amongst different camera models. Poisson noise is a fundamental noise in the optical device. It will give rise to detectable fluctuations in the measurement. It is determined by the mean number of detected photons which follow a Poissonian process in an integration time or exposure time of the camera. The Poisson probability distribution is shown in formula **(3.1)** with μ being the expectation value, which is equal to the mean of the photon counts (if a number of similar exposures were made). The Poisson distribution

has the property that its variance σ^2 is equal to its mean μ. Therefore, the signal to noise ratio (SNR) with Poisson noise can be determined by formula (**3.2**).

$$p(n) = \frac{e^{-\mu}\mu^n}{n!} \tag{3.1}$$

$$SNR = \frac{\mu}{\sigma} = \sqrt{\mu} \tag{3.2}$$

The signal to noise ratio is proportional to the square root of the mean value. Therefore, a brighter light source, long exposure time etc. can reduce the Poisson noise effects. In contrast, if a weaker light source or if the exposure time is too short, Poisson noise will dominate the experimental data.

In simulation, an image corrupted by noises (Poisson noises, background noises and quantisation noises) can be simulated by applying equation **(3.3)** and **(3.4).** A derivation of these expressions can be found in Appendix **III**.

$$I_{noise} = round[\frac{P(N_e)}{g} + b - \frac{r^2}{g}] \tag{3.3}$$

where,

$$N_e = g\frac{I}{I_{\max}}\alpha + r^2 \tag{3.4}$$

where ***P(x)*** is a function to generate Poisson random numbers with mean ***x***; ***g*** is the amplifier gain conversion coefficient; ***r*** is the readout noise; ***b*** is the background noise of the CCD camera; and ***α*** is the Poisson noise factor which is determined by the intensity above the background achieved in experiments for a particular particle size.

Because, as explained above the number of photons detected in an image depends on a large number of factors, in these simulations the Poisson noise is described by a single parameter referred to as the Poisson noise factor. Poisson noise factor represents the mean number of photons in the brightest pixel in the data set that reaches the CCD in one exposure time.

The simulation parameters are listed in **Table 3.3**. **Figure 3.12, 3.13, 3.14** and **3.15** present an example of the particle size distributions with different Poisson noise factors of 10, 100, 1000 and 10000 respectively.

Temperature	20^{o}C
Particle size distribution: Mean/standard deviation	100nm/20nm
Number of frames	300
Image size/pixel size	500 x 500/3.35microns
Exposure time	0.05s (particles are still during the exposure time)
Magnification	6.7
Movement histogram interval	0.1 microns
Time interval	1s
Particle concentration	5×10^{6} /ml
Poisson noise	Yes
Quantisation/background noise	No/No

Table 3.3: Simulation parameters used in the simulation to assess the effect of Poisson noise.

Figures 3.12 to **3.15** show the simulated example images and the original and recovered particle size distributions.

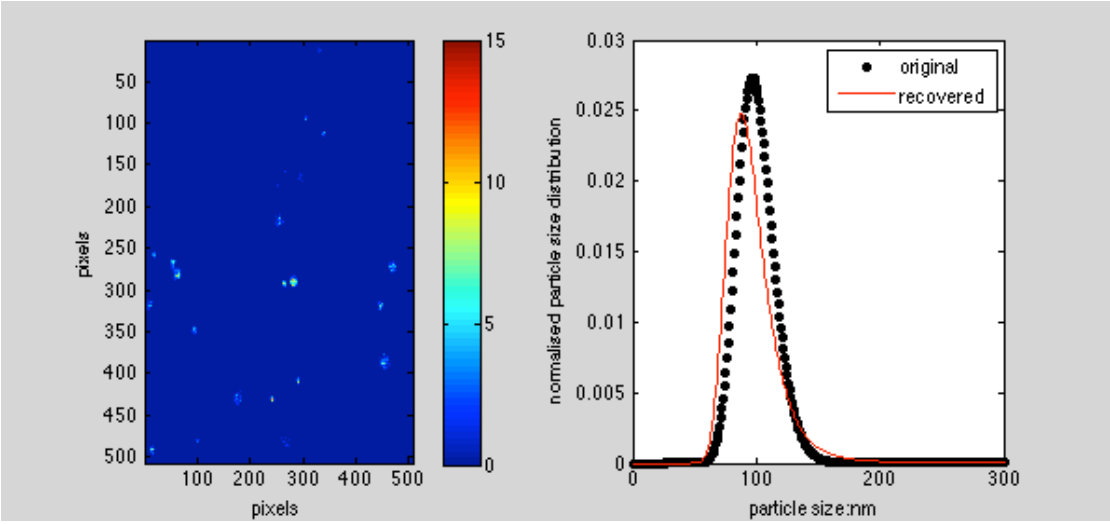

Figure 3.12: An example image when the Poisson noise factor is 10, and the original and reconstructed distributions for particle mean size of 100nm and deviation of 20nm. The area error, mean radius and standard deviation are 0.4, 96.94nm, and 24.92nm respectively.

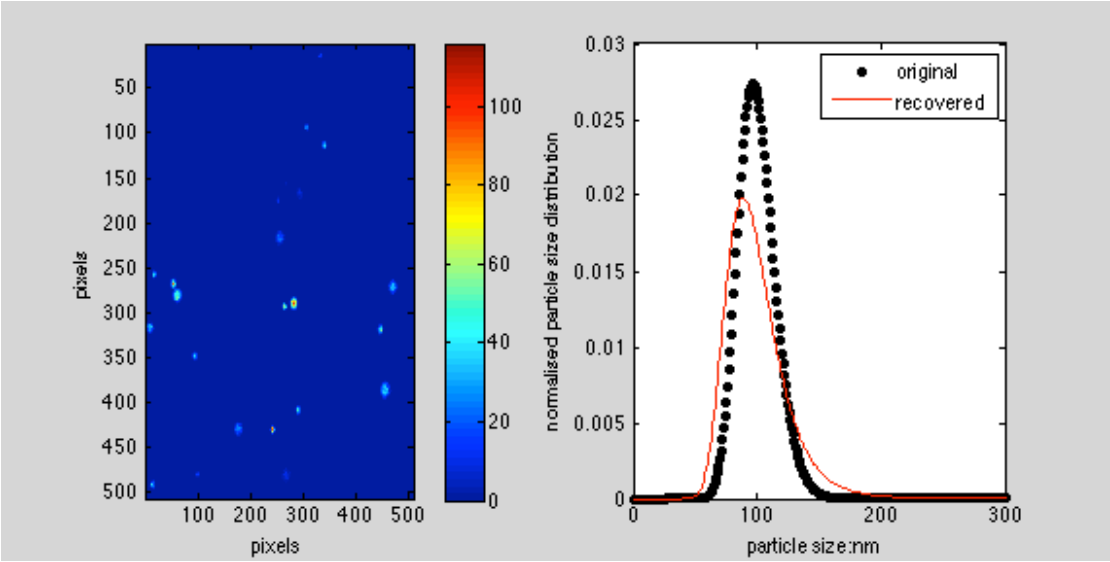

Figure 3.13: An example image when the Poisson noise factor is 100, and the original and reconstructed distributions for particle mean size of 100nm and deviation of 20nm. The area error, mean radius and standard deviation are 0.43, 99.62nm, and 28.82nm respectively.

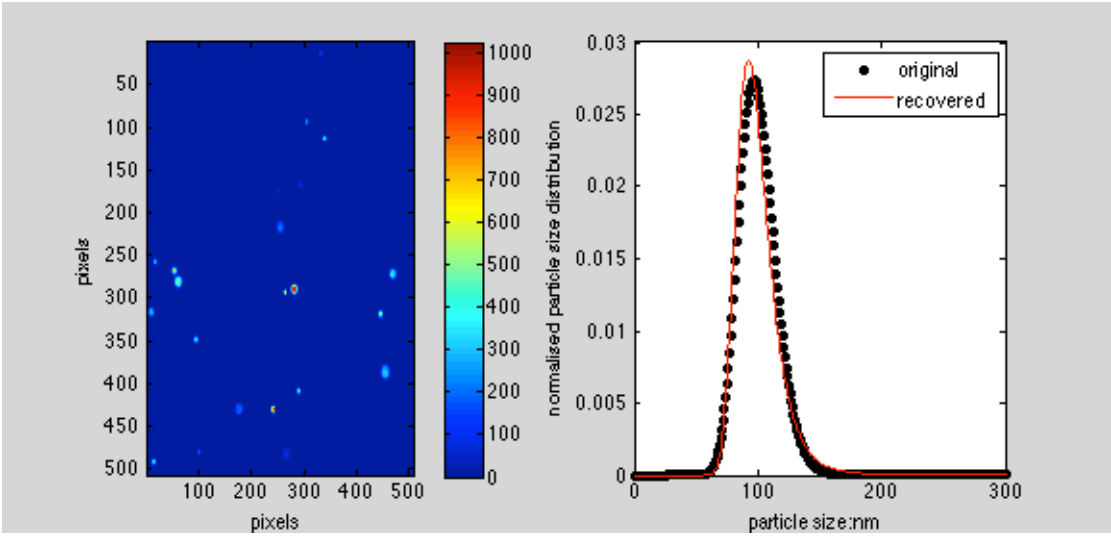

Figure 3.14: An example image when the Poisson noise factor is 1000, and the original and reconstructed distributions for particle mean size of 100nm and deviation of 20nm. The area error, mean radius and standard deviation are 0.17, 99.83nm, and 22.96nm respectively.

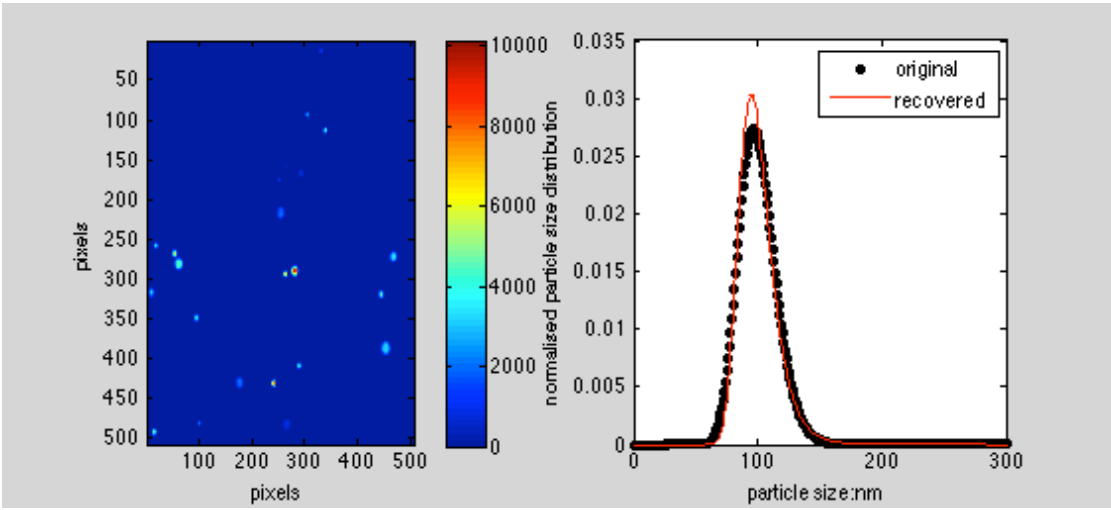

Figure 3.15: An example image when the Poisson noise factor is 10000, and the original and reconstructed distributions for particle mean size of 100nm and deviation of 20nm. The area error, mean radius and standard deviation are 0.12, 100.42nm, and 20.45nm respectively.

It may be seen in **Figures 3.12** to **3.15** that, as expected, the general accuracy of the recovered distributions improves as the Poisson noise factor increases. To provide a statistical analysis, **Figure 3.16** presents the standard deviations of the three criteria evaluations according to ten independent simulations.

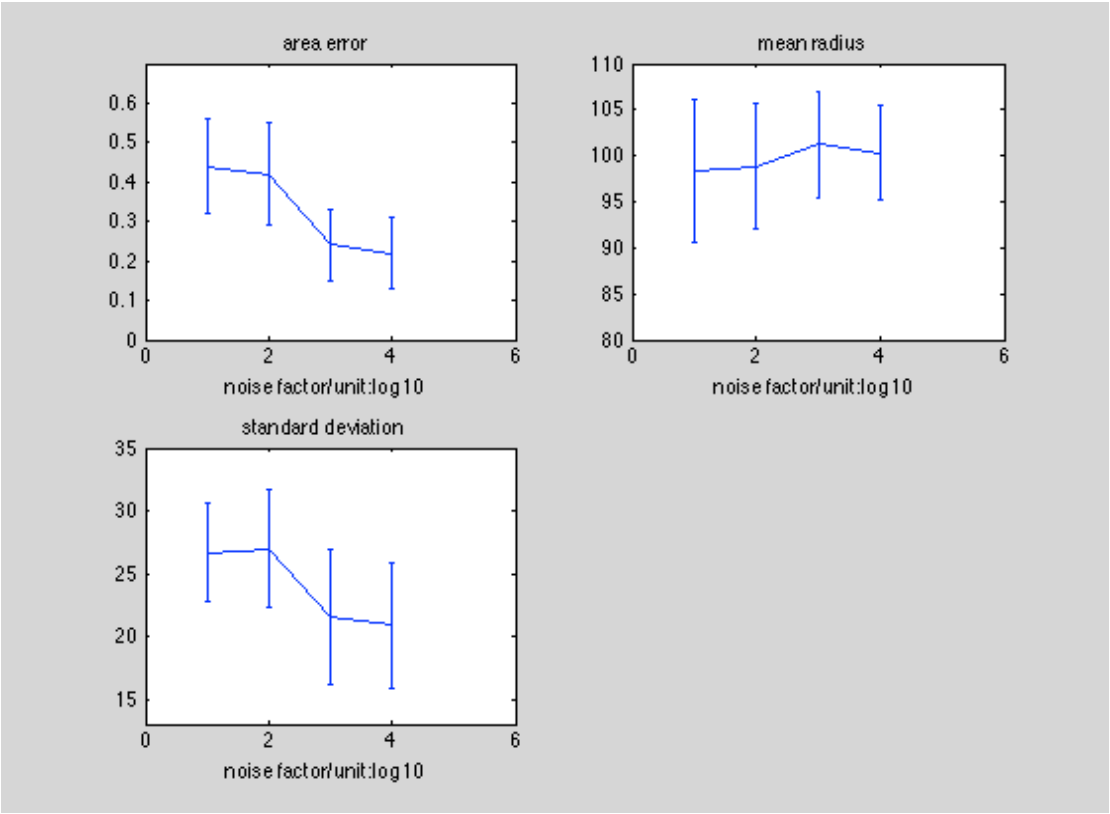

Figure 3.16: Area errors, mean radii and standard deviations of the reconstructed particle size distributions from ten independent simulation data in the Poisson noise simulations.

In summary, the results become better in the ascending order of the Poisson noise factor. When the Poisson noise factor is less than or equal to 100, it gives a larger area error (above 0.4) and a wider recovered distribution (around 27nm) compared with the results recovered when the Poisson noise is larger than or equal to 1000 (around 21nm). If the Poisson noise factor is above 1000, the area errors are less than 0.3 (compared with 0.32 for DLS), and the recovered mean is about 5% shifted from the original distribution. That is because a larger signal to noise ratio (SNR) is obtained with a large Poisson noise factor.

These results indicate that in an experiment, the source brightness, exposure time etc. should be chosen to give a Poisson noise factor larger than or around 1000. In the

experimental work report in the next chapter, values greater than 1000 were generally achieved.

3.3.4 Quantisation Noise and Background Noise of the CCD

For digital images, some noise can significantly degrade image quality. Poisson noise has been discussed in the previous section. However, the results indicated that a very large Poisson noise factor was not needed. There are still some other noises of the system to be taken into account in this section, including quantisation noise and background noise. Because the read out noise of the CCD camera is about 8 RMS electrons, which is very small compared with the other two noises, it will be ignored.

Firstly, consider quantisation noise only. Quantisation noise arises from the discrete nature of sampling/conversion process of the AD converter (65, 66). Normally, the camera is able to render 4096(2^{12}) steps into a useable digital output. Three different numbers of quantisation levels, 4096(2^{12}), 1024(2^{10}) and 256(2^{8}), are considered in the simulations. Theoretically, the smaller number of the levels, the worse the result is. The larger the number of the levels, the better it will be able to capture signal in the image without saturating the highlights, but a high number of quantisation level needs a good quality CCD camera.

The simulation parameters used to investigate the effects of background and quantisation noise are listed in **Table 3.4**.

Temperature	20^{o}C
Particle size distribution: Mean/standard deviation	100nm/20nm
Number of frames	300
Image size/pixel size	500 x 500/3.35microns
Exposure time	0.05s (particles are still)
Magnification	6.7
Movement histogram interval	0.1 microns
Time interval	1s
Particle concentration	5 x 10^{6} /ml
Poisson noise factor	4000
Quantisation levels	Yes (256, 1024, 4096) steps
Background noise	No

Table 3.4: Simulation parameters used in the simulation to assess the effect of quantisation levels.

Figure 3.17 compares an original image (un-quantised) with a set of example images with various quantisation levels, 4096, 1024 and 256.

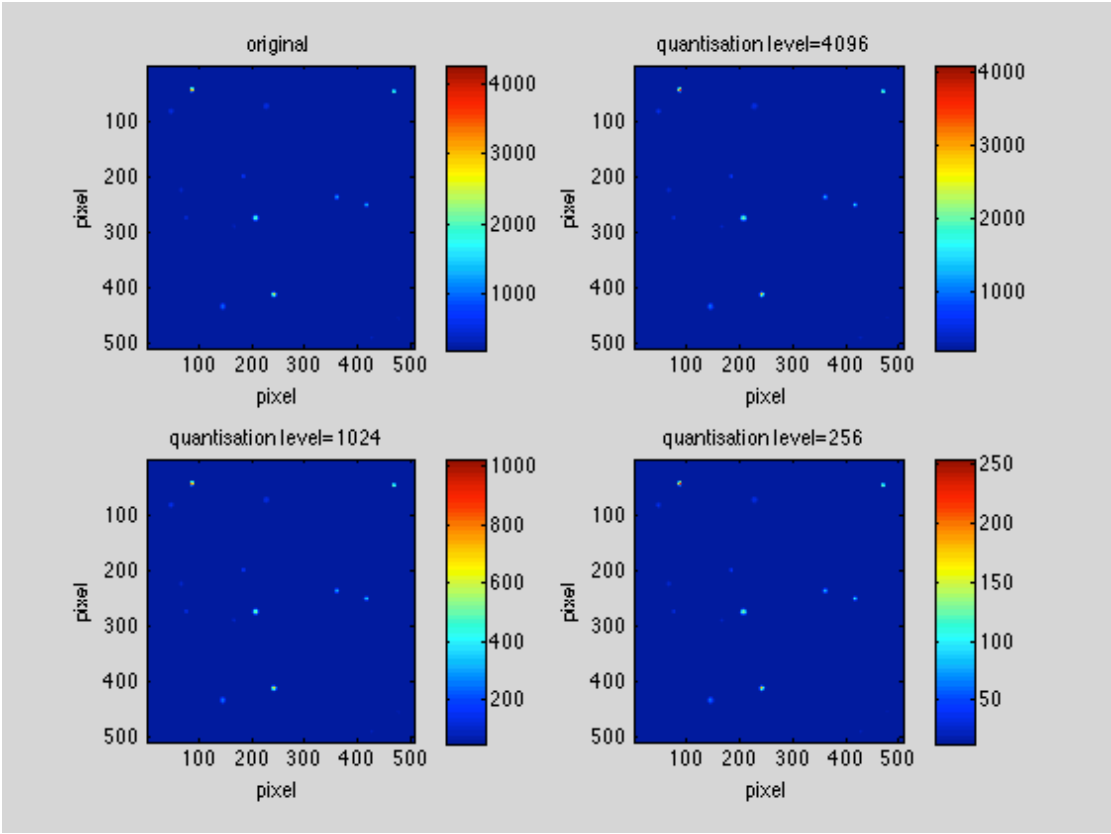

Figure 3.17: Simulated example images with different quantisation levels, 4096, 1024, and 256.

All the images in **Figure 3.17** have very similar appearance although, of course, the images with the smaller numbers of quantisation intervals are measured less accurately.

Figure 3.18 show a simulated example of the recovered particle size distributions with various quantisation levels. The red, black and blue line represent the quantisation level are 4096(2^{12}), 1024(2^{10}) and 256(2^{8}), respectively.

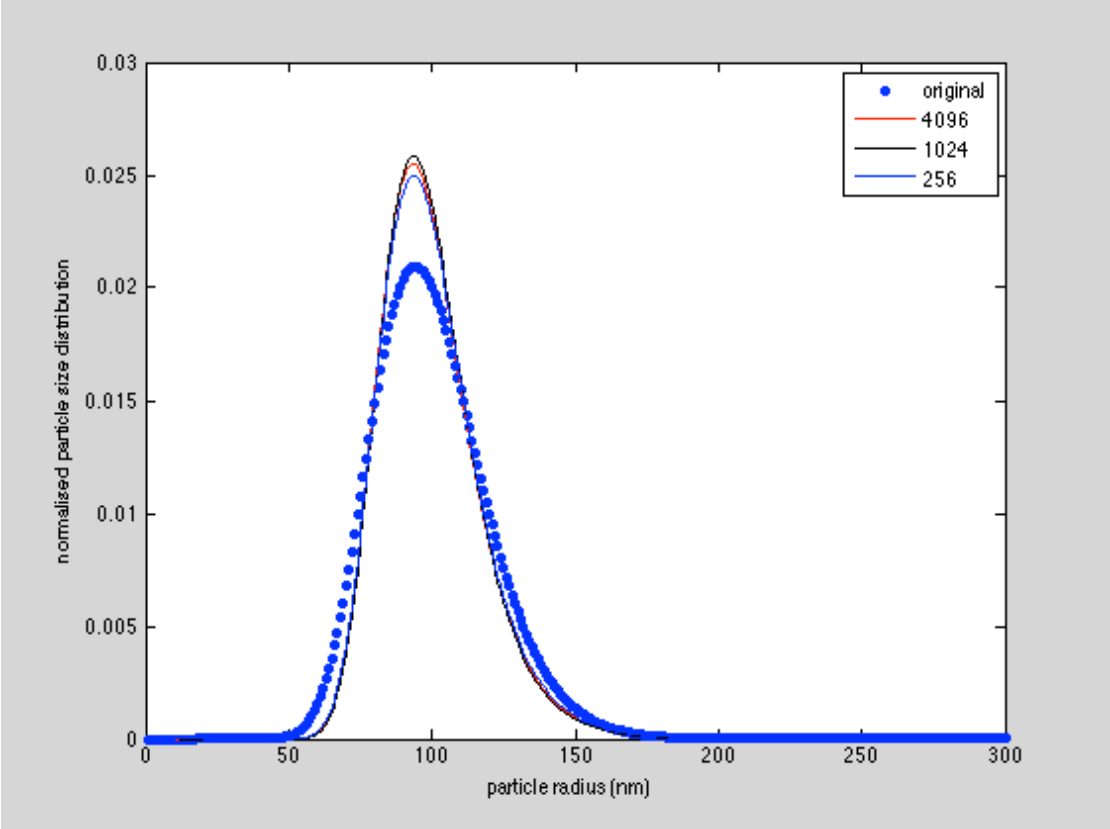

Figure 3.18: recovered particle size distributions with various numbers of simulated quantisation levels.

The reconstructed particle size distributions in **Figure 3.18** with different numbers of quantisation levels match the original distribution very well no matter which number of quantisation levels is used.

To obtain some statistical results, these simulations were repeated in ten times. The standard deviations of these three evaluation criteria are shown in **Figure 3.19**.

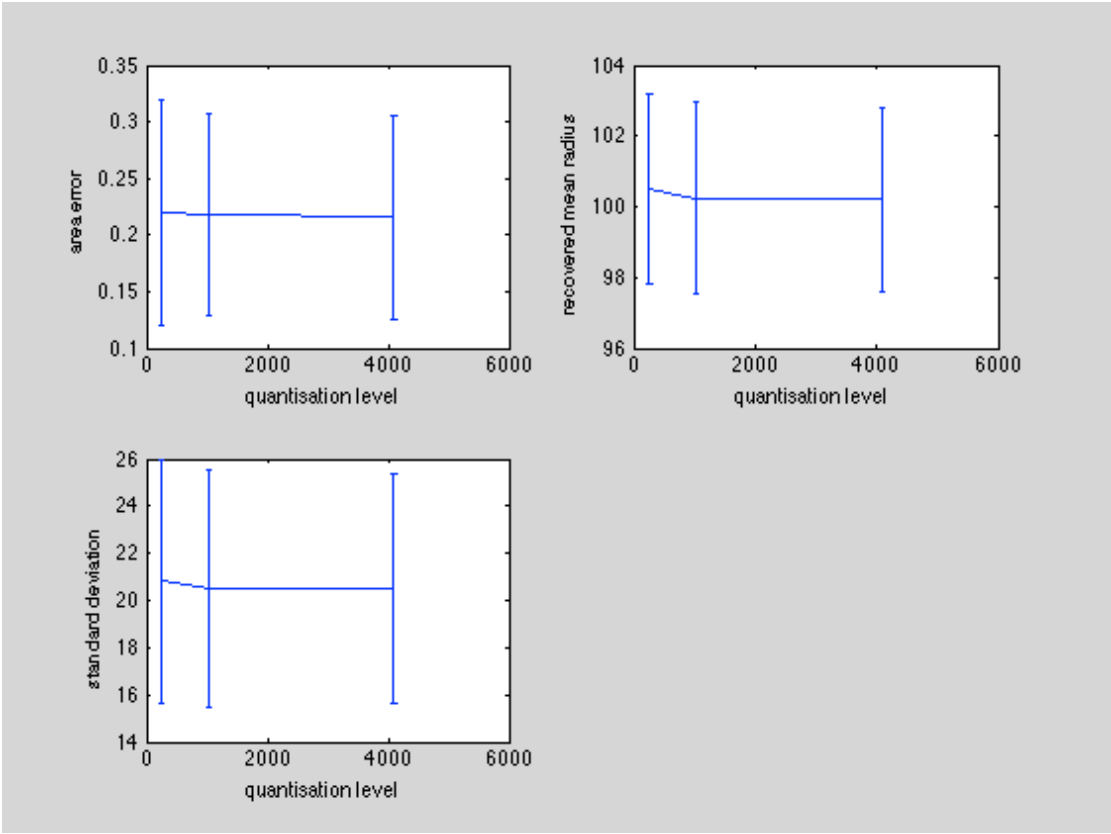

Figure 3.19: Area errors, mean radii and standard deviations of the reconstructed particle size distributions in ten independent simulations when the number of quantisation levels is 256, 1024 and 4096 respectively.

As may be seen in **Figure 3.19**, the three evaluated criteria are very similar for all three different numbers of quantisation levels and significantly the area error is less than the DLS value of 0.32 in each case. The number of quantisation levels determines the number of photons that comprise each level in the image. In order to represent subtle intensity differences in a digital image, it is necessary to discriminate as many levels as possible. That is to say, the number of quantisation levels does not change the brightness of the image; it only rounds values to some unit of precision. If the signals do not saturate the dynamic range of a CCD, the number of quantisation levels becomes insignificant when ignoring the background noise in **Figure 3.19**.

Secondly, quantisation noise and background noise are considered simultaneously. The background noise arises from two possible sources (i) statistical variation in the number of electrons thermally generated within the silicon structure of the CCD, which is independent of photon-induced signal, but highly dependent on device temperature and (ii) from any stray light that enters the detector from sources other than the scattering particles. The generation rate of thermal electrons at a given CCD temperature is referred to as dark current. The real image quality is susceptible to the background noise. Considering the background noise, it appears as random speckles in the image instead of a smooth background. During the simulation process, different mean background levels are taken into account. The levels that were simulated were based around the values encountered using the Hamamatsu camera used in the experimental work, which exhibited thermal background noise levels of around 200 quantisation levels in 12-bit operation but less than 20 in 8–bit operation. In theory, if the ratio of the number of quantisation levels and the background noise is small, signals above the background noise are difficult to distinguish, and the image quality will be strongly affected.

Table 3.5 presents the different simulation parameters when considering the background noise and quantisation noise simultaneously. The other parameters are kept the same as **Table 3.4** except for the noises.

Poisson noise	No
Quantisation levels	Yes, 4096
Background levels	Yes (50, 200, 400)

Table 3.5: Simulation parameters used in the simulation to assess the effect of background levels when the number of quantisation levels is 4096, and the background noise varies from 50 to 400.

Figure 3.20 presents a group of example images with different background noise when the number of quantisation levels is 4096. It compares the original image with the noisy images. Visually, it is difficult to see the effects of background noises in the images.

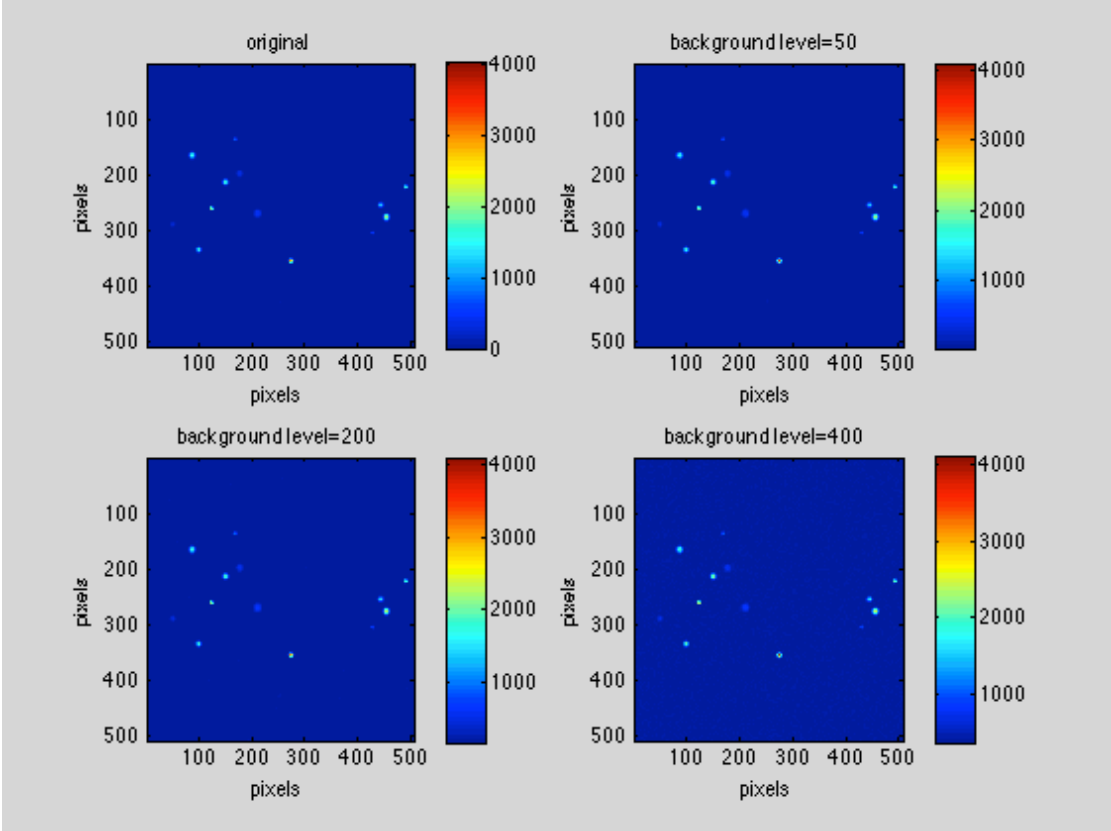

Figure 3.20: Example images with different background levels when the number of quantisation levels is 4096.

Figure 3.21 reconstructs a simulated example of the particle size distributions with different background noise levels. The real mean size (radius) is 100nm and the standard deviation is 20nm. The red, black and blue lines represent the reconstructed particle size distributions with the increment of the background noises respectively.

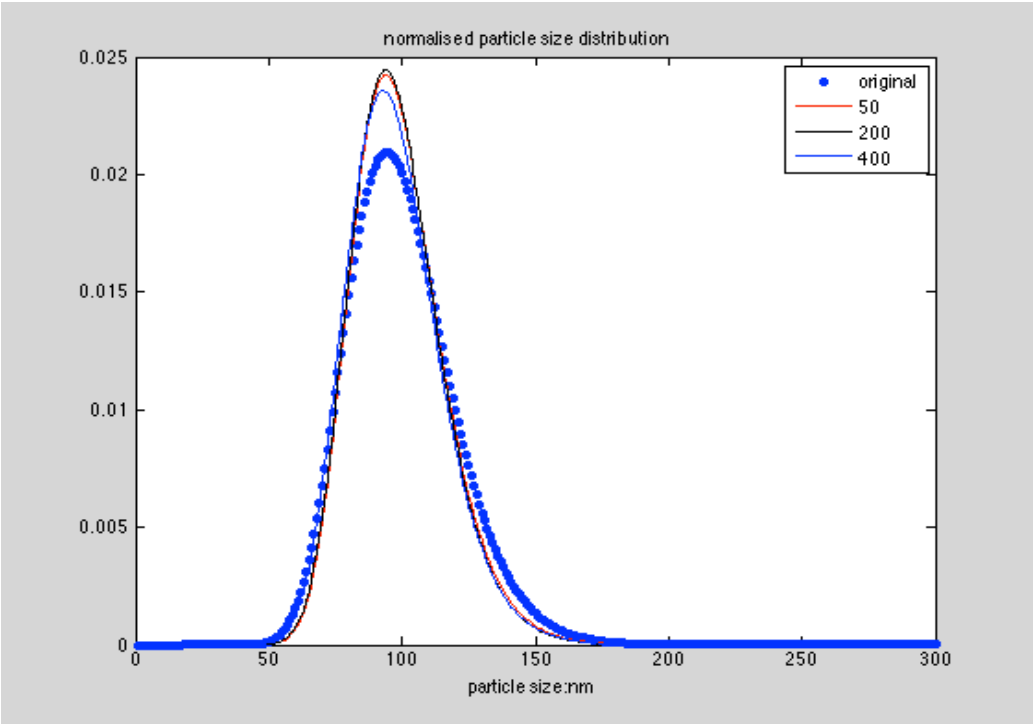

Figure 3.21: The recovered particle size distributions with various background noises when the number of quantisation levels is set to be 4096 steps. The mean radius of the original particle size distribution is 100nm, with 20nm standard deviation.

As may be seen in **Figures 3.21**, when the number of quantisation levels is 4096, the recovered example particle size distributions are all very similar to each other. Ten independent simulation data are recorded to statistically examine the background noise effects. **Figure 3.22** presents the area errors, mean radii and standard deviations of the recovered particle size distributions with various background levels for ten independent simulations when the number of quantisation level is 4096.

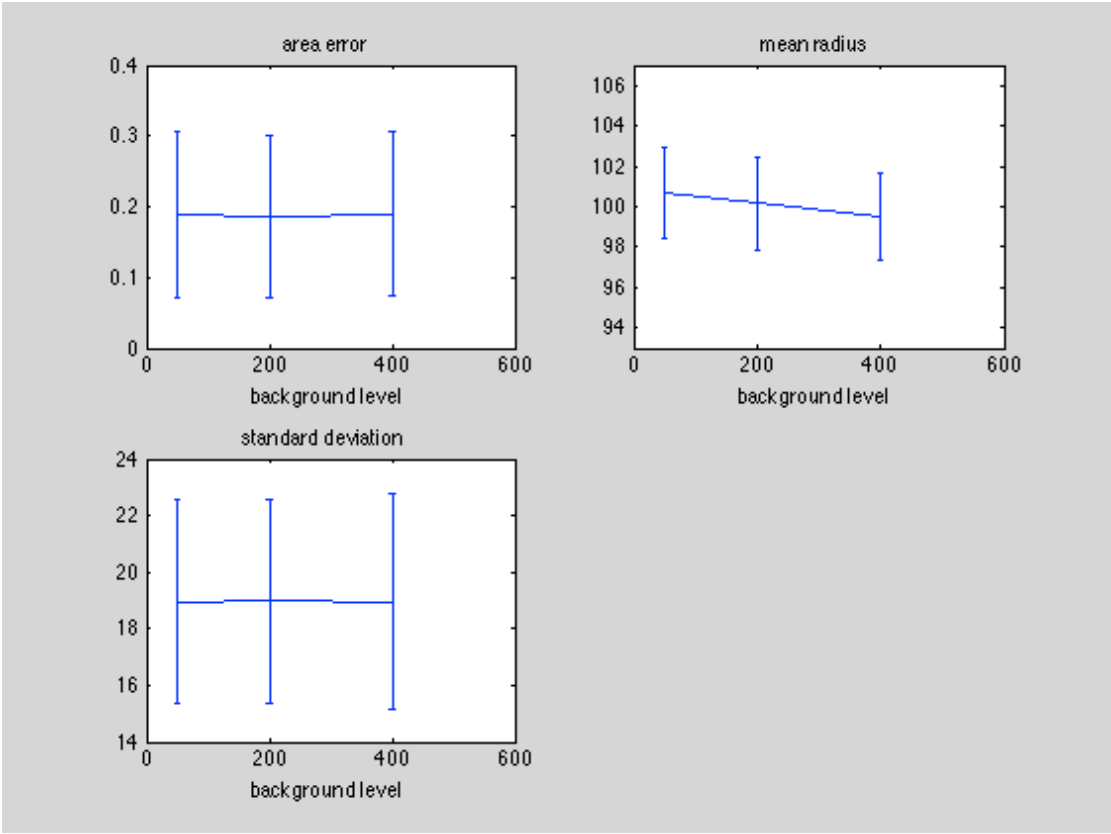

Figure 3.22: Area errors, mean radii and standard deviations of the recovered particle size distributions with various background noise levels in ten independent simulations when the number of quantisation levels is 4096.

As can be seen from **Figure 3.22**, when the number of quantisation levels is 4096 (2^{12}), and the background level is up to 400, the recovered mean radius and the standard deviation are still very similar to the original distribution. It may also be seen that the area error does not change significantly and is less than the DLS value of 0.32 in each case. That is because the image has a sufficiently high signal to noise ratio (SNR) to clearly separate the image information from the background noise.

The lower number of quantisation levels 1024 is investigated in the following **Figure 3.23** and **3.24. Table 3.6** presents the different noise parameters from **Table 3.4**, whilst the other parameters are the same.

Poisson noise	No
Quantisation levels	Yes, 1024
Background levels	Yes (12.5, 50, 100)

Table 3.6: Simulation parameters used in the simulation to assess the effect of background levels when the number of quantisation levels is 1024, and the background level varies from 12.5 to 100.

Figure 3.23 compares a group of images with different background levels (12.5, 50, 100) when the number of quantisation levels is 1024.

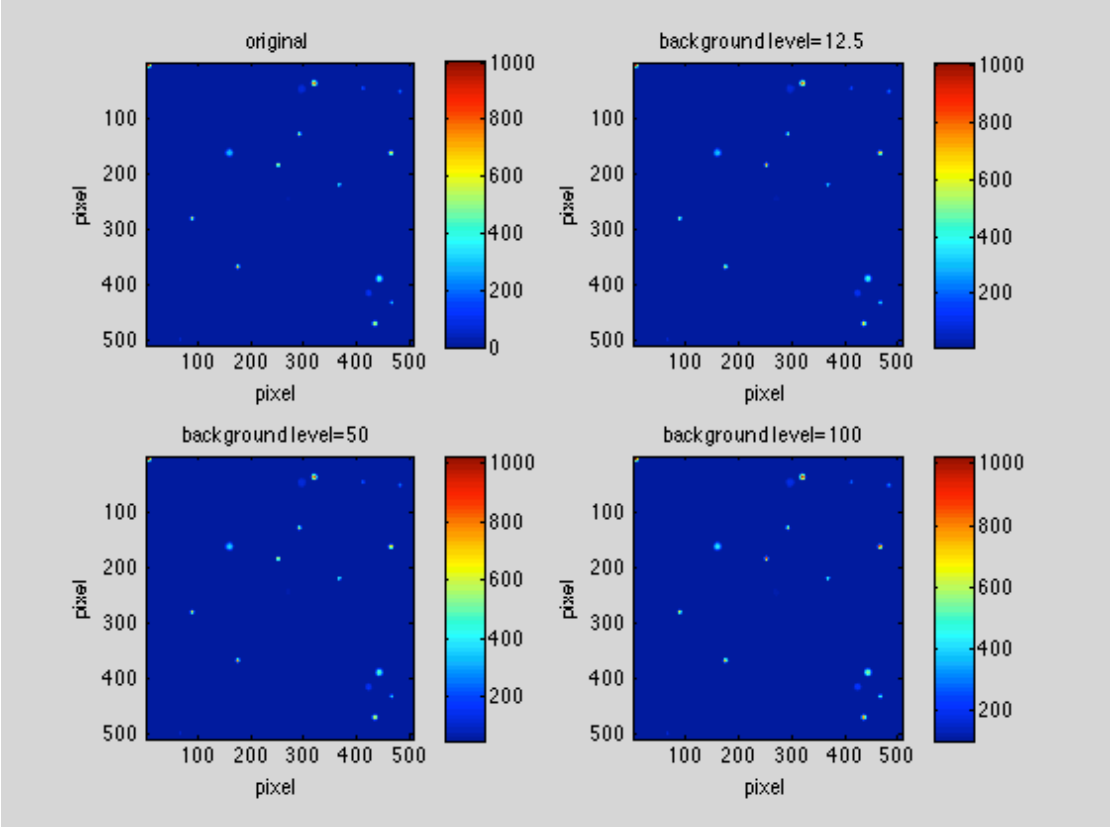

Figure 3.23: Example images with different background levels (12.5, 50, 100) when the number of quantisation levels is 1024.

Figure 3.24 is a simulated example of the recovered particle size distributions with different background levels when the number of quantisation levels is 1024.

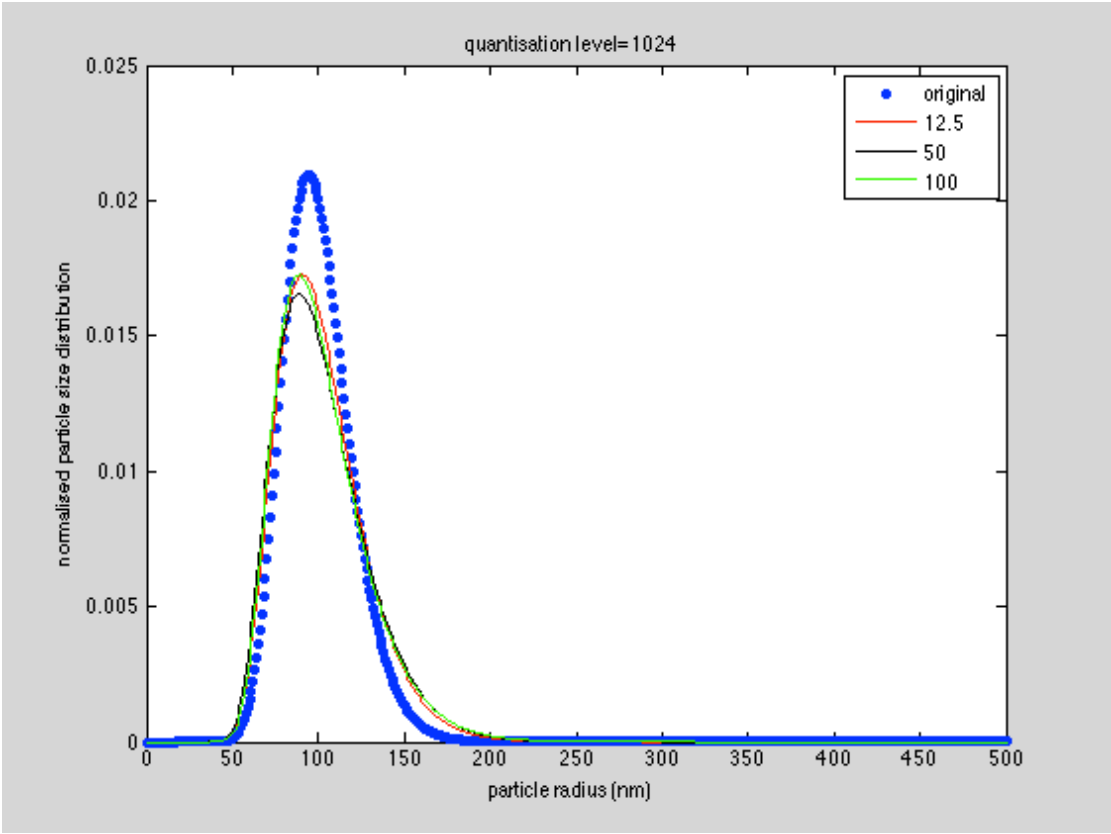

Figure 3.24: The recovered particle size distributions with various background levels when the number of quantisation levels is 1024 steps. The mean radius of the original particle size distribution is 100nm, with 20nm standard deviation.

Generally, the smaller the background noise level is, the better the recovered distribution is. Ten independent simulation data are recorded in **Figure 3.25** to show the fluctuations of the area errors, mean radii and standard deviations of the recovered distributions.

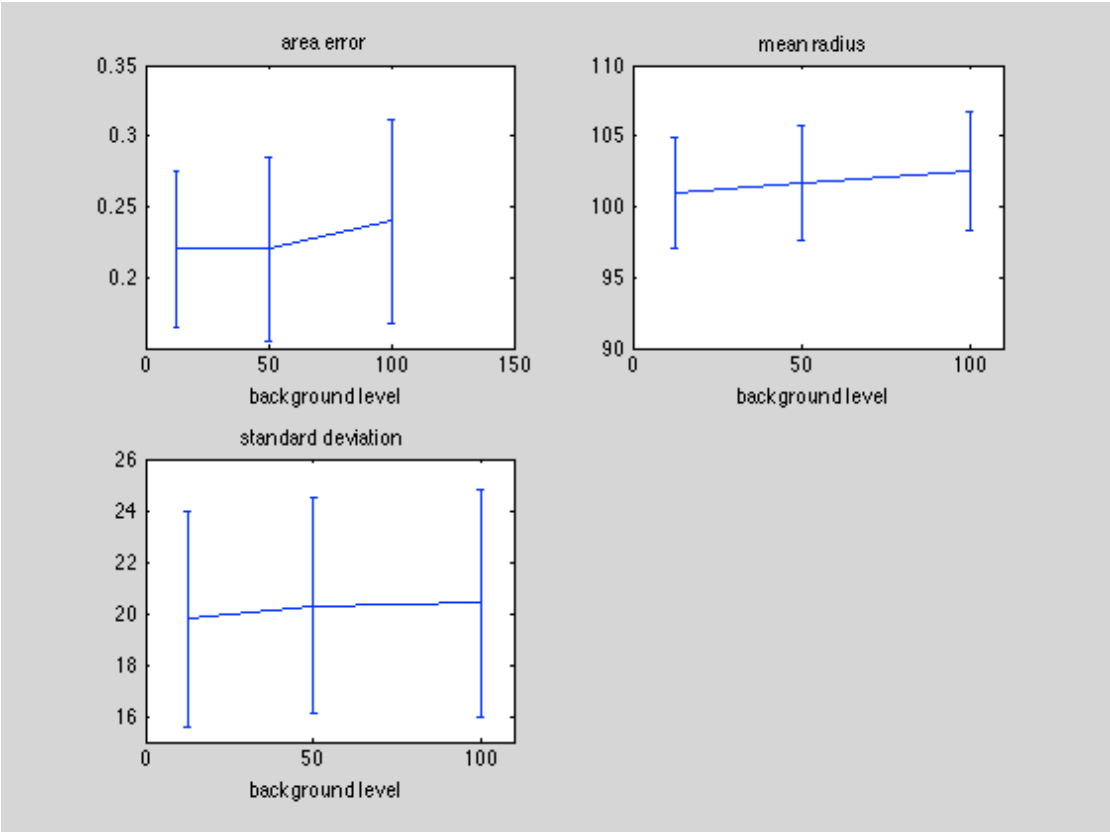

Figure 3.25: Area errors, mean radii and standard deviations of the recovered particle size distributions with various background noise levels in ten independent simulations when the quantisation level is 1024.

For the results shown in **Figure 3.25**, when the number of quantisation levels is 1024 it may be seen that the results are very slightly worse for the background level of 100 than for the lower two background levels. The recovered mean radius varies from around 101nm to around 103nm compared with the simulated value of 100nm. The area error is around 0.22 for background level of 12.5 and 50 but increases to around 0.24 for a background level of 100. Importantly all these values are significantly lower than the DLS value of 0.32. These results indicate that when the number of quantisation level is $1024(2^{10})$ and the background level is less than 100, the image has a sufficiently high signal to noise ratio (SNR) to clearly separate the image information from the background noise.

Figure 3.26 and **3.27** show example images and recovered size distributions when the number of quantisation levels is 256 (2^8), and the background level is 3, 12.5 and 25 counts respectively. **Table 3.7** presents the different noise parameters from **Table 3.4**, whilst the other parameters are the same.

Poisson noise	No
Quantisation levels	Yes, 256
Background levels	Yes (3 12.5 25)

Table 3.7: Simulation parameters used in the simulation to assess the effect of background levels when the number of quantisation level is 256, and the background level varies from 3 to 25.

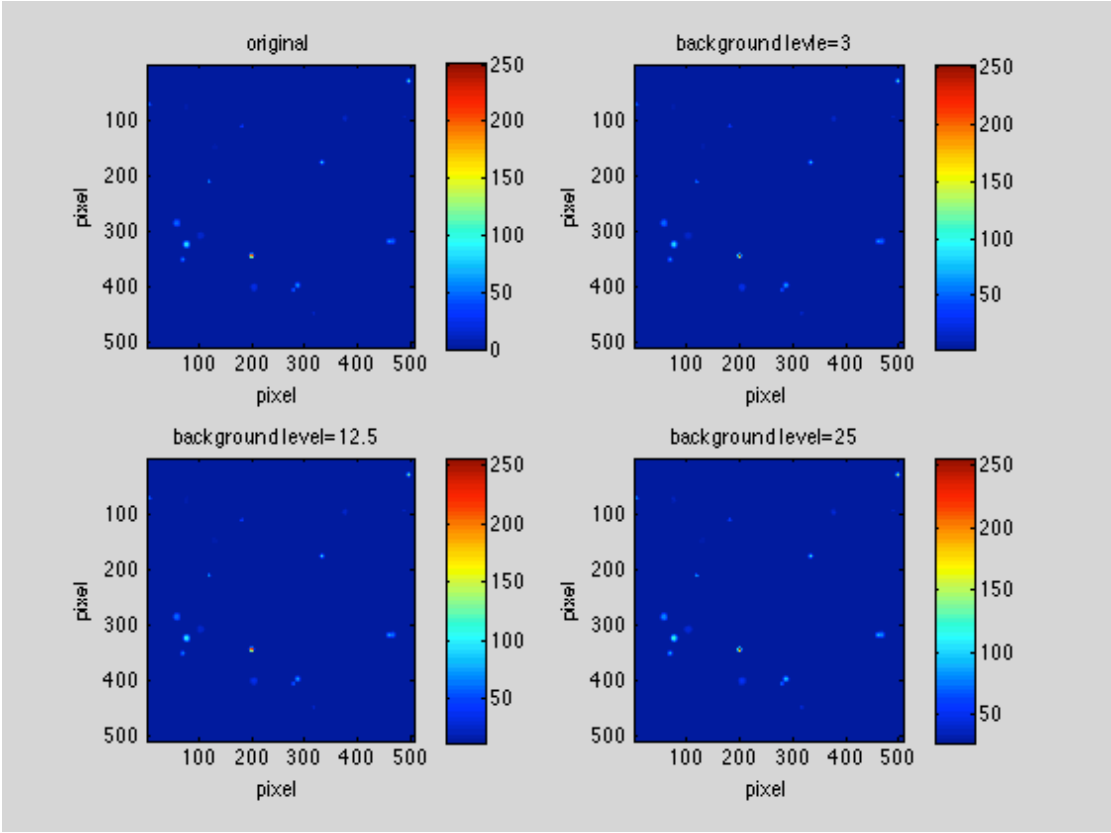

Figure 3.26: Example images with different background levels when the number of quantisation levels is 256.

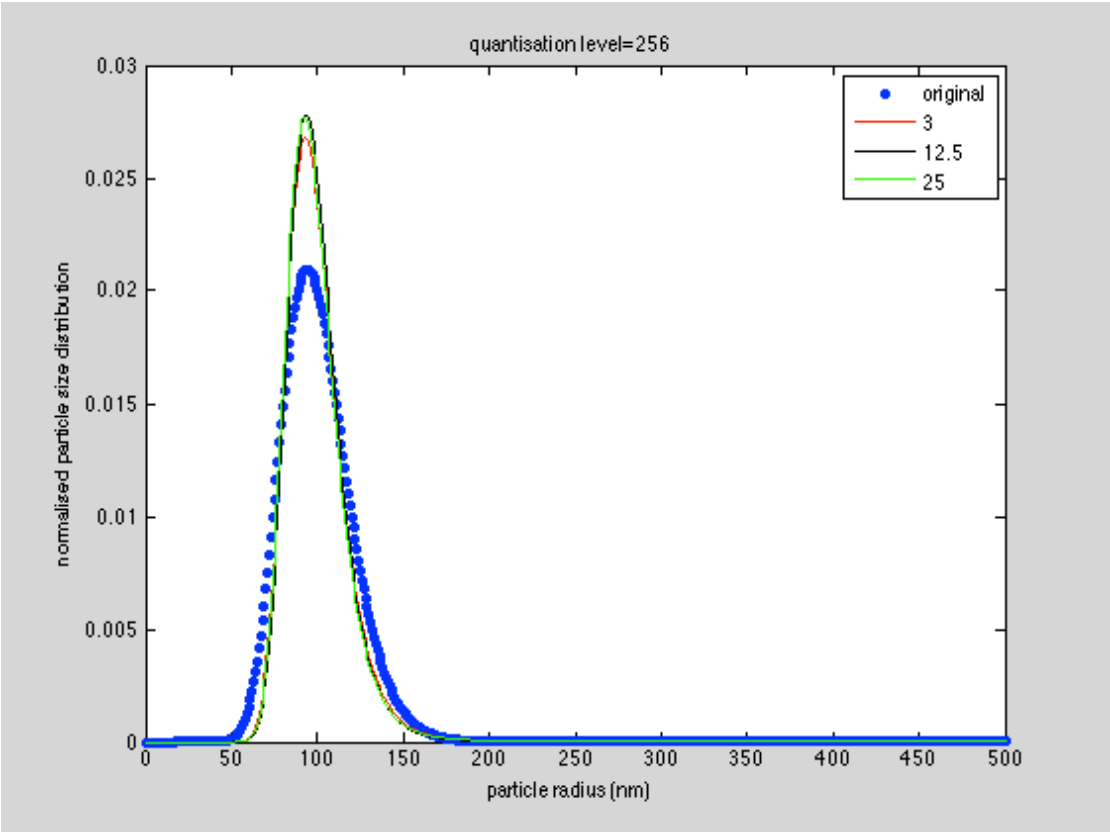

Figure 3.27: The recovered particle size distributions with various background levels when the number of quantisation levels is 256 steps. The mean radius of the original particle size distribution is 100nm, with 20nm standard deviation.

In **Figure 3.27**, when the background level is less than or equal to 25, the recovered distributions are quite similar.

Figure 3.28 shows the standard deviations of the three criteria (area error, recovered mean radius, and standard deviation) based on ten independent simulations.

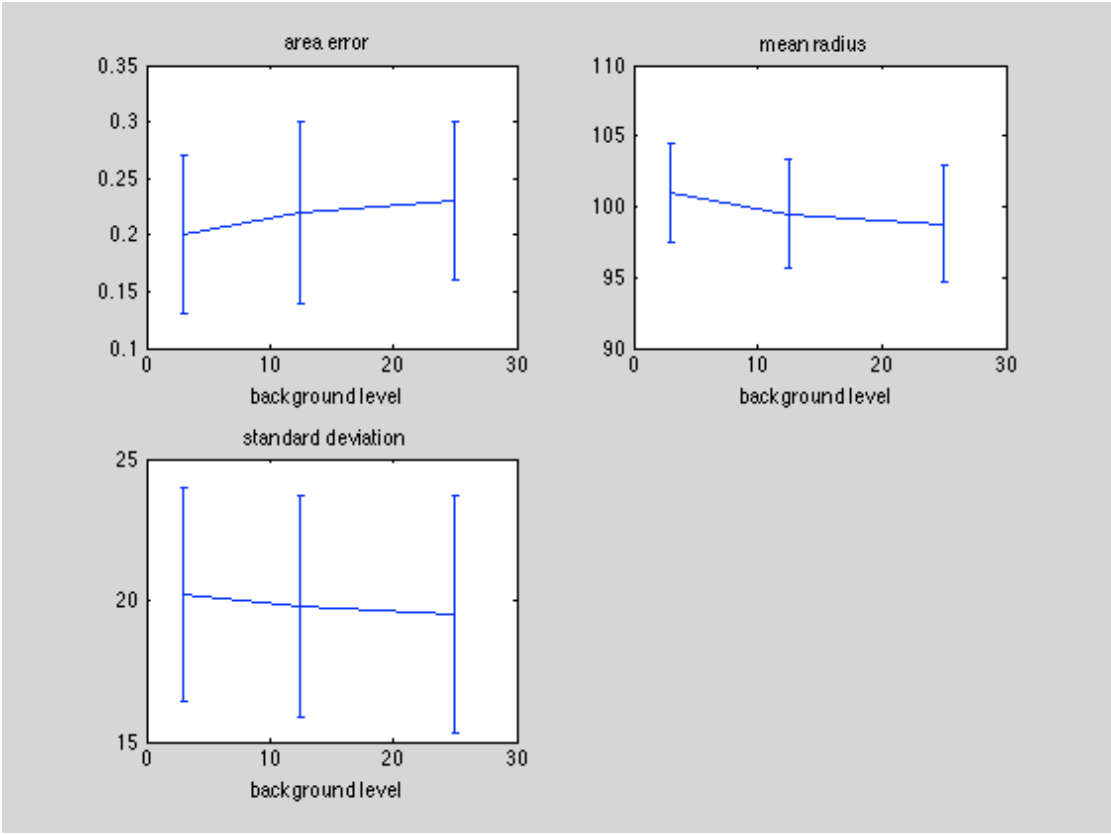

Figure 3.28： Standard errors of area errors, mean radii and standard deviations of the recovered particle size distributions with various background noise levels in 10 random times when the number of quantisation levels is 256.

Inspection of **Figure 3.28** shows that when the background level is less than or equal to 25, the area error is smaller than 0.3, and the recovered mean radius is 5% different from the original value. This result is very similar to **Figure 3.22 and 3.25**. Therefore, when the number of quantisation level is 256(2^8), the background level is less than or equal to 25, the image is not influenced by the background noise significantly.

In summary, this section considered different background levels with different numbers of quantisation levels. When the background level is around 200 in a 12-bit operation, and the background level is less than 20 in a 8-bit operation, the recovered mean radius has a 95% accuracy compared with the original value, the area error is less than 0.3 (compared with 0.32 for DLS) and the standard deviation is similar to

the original standard deviation 20nm. That means the background noise in the real Hamamatsu camera used in the experimental work does not influence the results seriously.

3.3.5 Sample Concentration

Sample concentration influences the image properties in a number of ways. If the sample concentration is too low, there will be few particles captured in the image, even none of them. Because the basic idea of the PMDD method is to find the relationship of particles centres between two consecutive frames, if there are no particles in one frame, it should be eliminated as a bad frame. In this situation, more frames will be needed in order to generate a precise result. Thus, it extends the experimental time. Likewise, low concentration samples may bring in large errors. For instance, if there are two peaks recorded in the frame, but one of them from dirt, then it leads to large errors. In the same condition, if there are twenty peaks recorded in the frame, the errors become much smaller. In contrast, there will be many particles within the field of view if the sample concentration is too high. The particles overlap with each other, and thus it gives rise to errors and produces a bad result. In this section, a suitable concentration range will be investigated.

Table 3.8 lists the simulation parameters used in the sample concentration optimising.

Temperature	20^{o}C
Particle size distribution Mean radius/standard deviation	100nm/20nm
Number of frames	300
Image size/pixel size	500 x 500/3.35microns
Exposure time	0.05s (particles are still during this time)
Magnification	6.7
Movement histogram interval	0.1 microns
Time interval	1s
Particle concentration	10^5, 10^6, 10^7, 3 x 10^7, 5 x 10^7 /ml
Poisson noise	No
Quantisation noise	No
Background noise	No

Table 3.8: Simulation parameters used in the simulation to assess the effect of sample concentration.

Figure 3.29 illustrates an example image captured by the CCD and the resulting reconstructed particle size distribution when the sample concentration is $\mathbf{10^5}$/ml. The recovered particle size distribution is based on 300 frames. In **Figure 3.29**, there is only one particle measured in the illuminated region or the field of view. Sometimes, it captures a black image without particles in this low concentration.

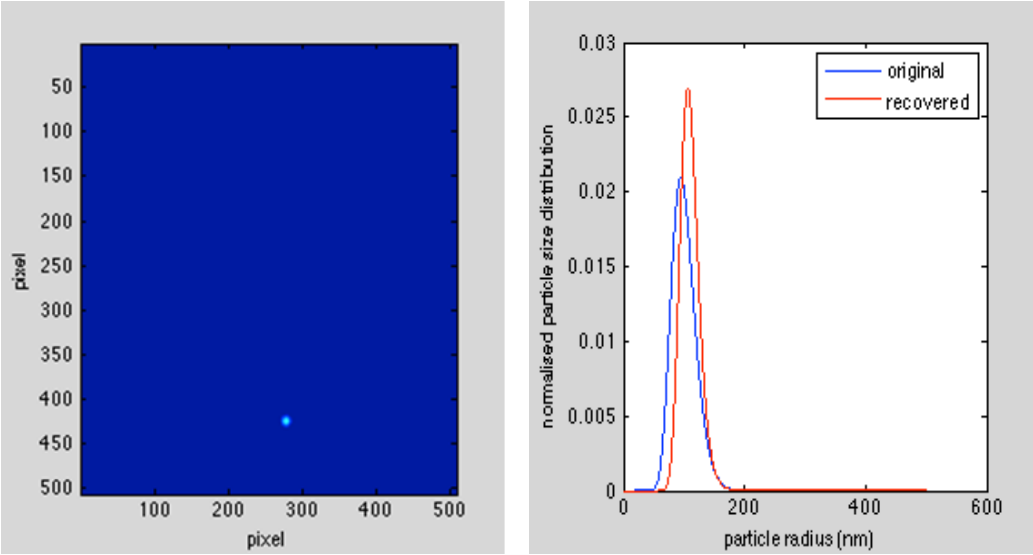

Figure 3.29: An example simulated image and the recovered particle size distribution when the sample concentration is 10^5/ml. The area error, mean radius and standard deviation are 0.49, 105.27nm and 16.68nm respectively.

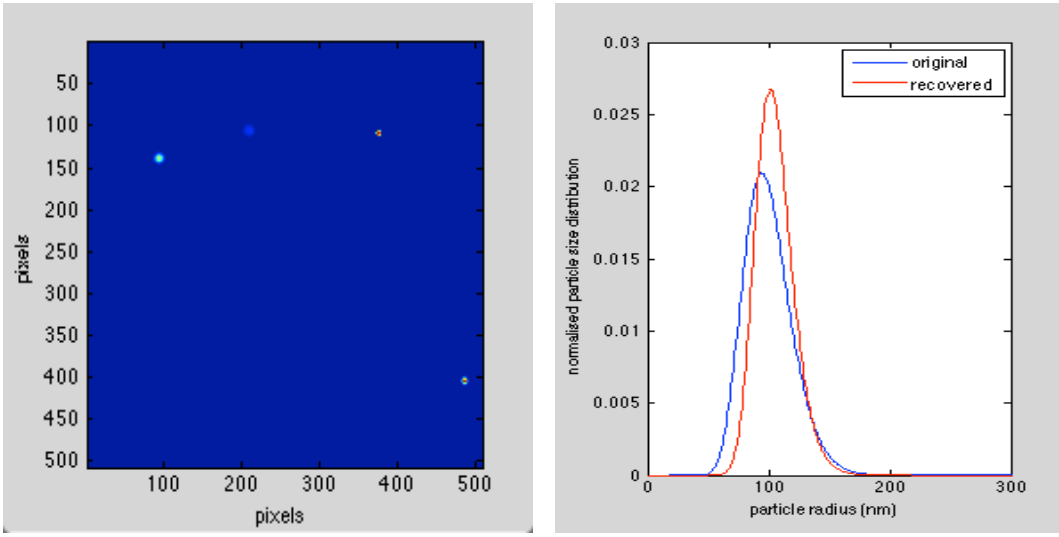

Figure 3.30: An example simulated image and the recovered particle size distribution when the sample concentration is 10^6/ml. The area error, mean radius and standard deviation are 0.40, 104.21nm and 17.80nm respectively.

It may be seen that there are four particles in the field of view in Figure **3.30** when the particle concentration is $\mathbf{10^6}$/ml.

Keeping the other conditions the same, **Figure 3.31** increases the concentration to **1x10^7**/ml.

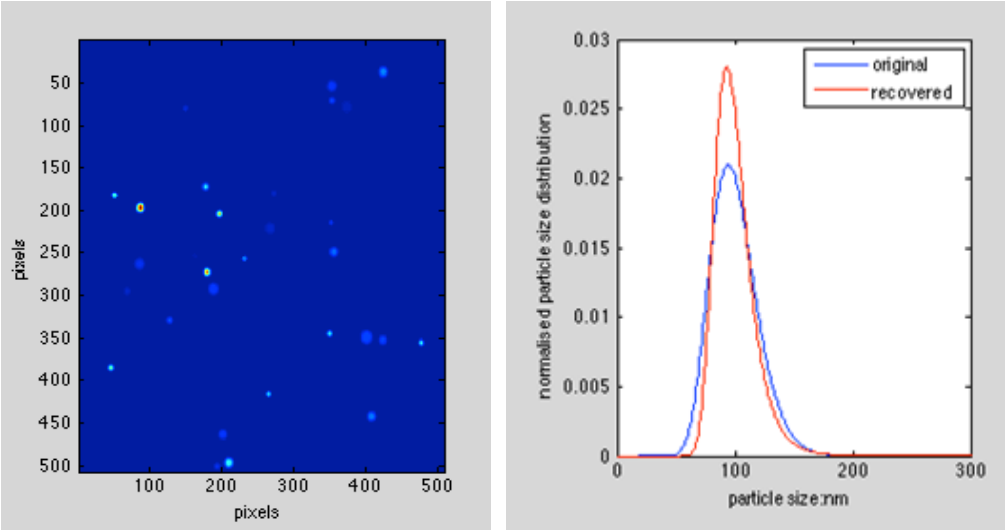

Figure 3.31: An example simulated image and the recovered particle size distribution when the sample concentration is 1x10^7/ml. The area error, mean radius and standard deviation are 0.29, 100.32nm and 18.54nm respectively.

Figure 3.32 shows another example when the sample concentration changes to 3x10^7/ml. There are many more particles in this figure compared with **Figure 3.30** and **Figure 3.31**. Due to the presence of a number of overlapping particle images, the quality of the reconstructed particle size distribution has become worse compared with the simulations performed at lower concentration.

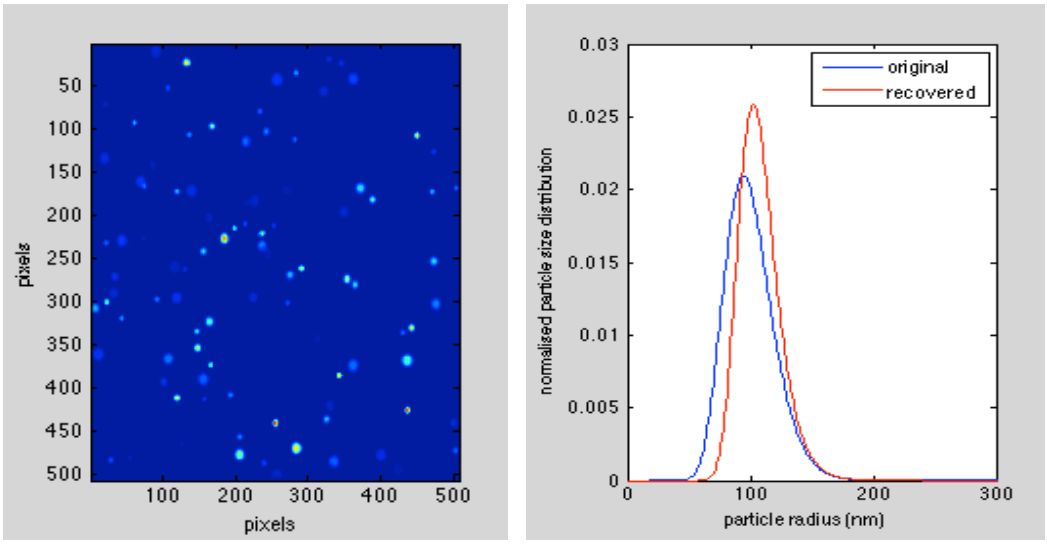

Figure 3.32: An example simulated image and the recovered particle size distribution when the sample concentration is $3x10^7$/ml. The area error, mean radius and standard deviation are 0.48, 107.89nm and 17.03nm respectively.

Finally, **Figure 3.33** increases the sample concentration up to **$5x10^7$**/ml.

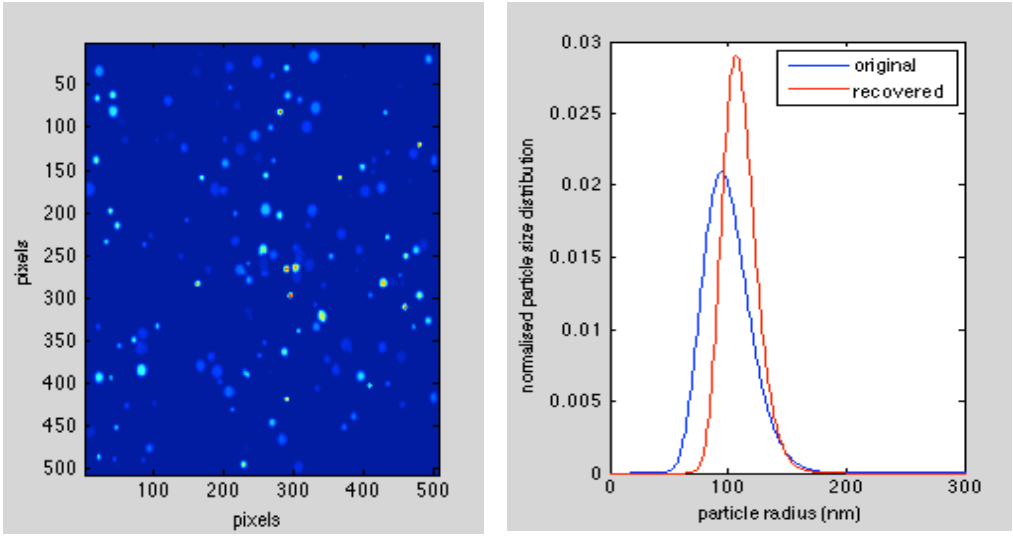

Figure 3.33: An example simulated image and the recovered particle size distribution when the sample concentration is $5x10^7$/ml. The area error, mean radius and standard deviation are 0.72, 111.62nm and 15.97nm respectively.

It is seen that two or more particle images are often superposed in **Figure 3.33**. The errors introduced by this have caused the particle size distribution to have a larger

mean than the original one. The recovered mean radius shifts about 10nm (10%) from the original radius, and the area error is large (0.7) compared with the values obtained at small particle concentration.

Ten independent simulations were performed to statistically examine the effect of sample concentration; the Area errors, mean radii and standard deviations of the recovered particle size distributions are presented in **Figure 3.34**. The standard errors of the three criteria show the fluctuations of the recovered distributions.

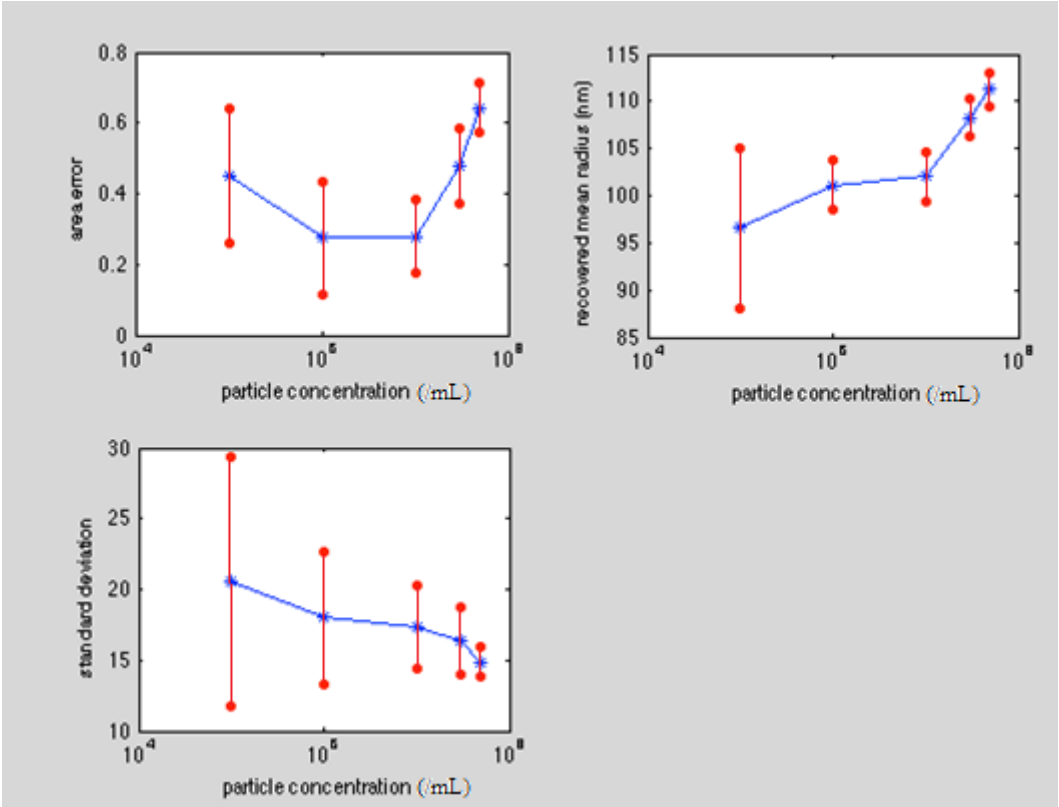

Figure 3.34: Area errors, mean radii and standard deviations of the recovered particle size distributions with different particle concentrations.

In a conclusion, this section compares the reconstructed particle size distributions with five different sample concentrations. When the sample concentration is $\mathbf{10^5}$/ml, sometimes, there is no particle in the field of view or in the illuminated region, which

means in the same experimental time, few particles are recorded. That explains the large fluctuations of the recovered mean radius and large area error compared with the samples with concentration of $\mathbf{10^6}$/ml. When the sample concentration is between $\mathbf{10^6}$/ml – $\mathbf{10^7}$/ml, the recovered mean radius has a high accuracy (95%), and the area error is small, around 0.3 compared with 0.32 for DLS. The area error is larger than 0.4 with the other densities. When the sample concentration increases to $\mathbf{5x10^7}$/ml, the mean radius of the recovered particle size distribution changes 10%-15% from original data and the area error increases to 0.6 that is because some particle images may overlap each other. Thus for the illumination and imaging conditions simulated, the best suitable particle concentration range is between $\mathbf{10^6}$/ml and $\mathbf{10^7}$/ml.

3.3.6 Optics Aberrations

Due to any imperfections of the optical components, aberrations occur in the real imaging system in practice. Optical aberration is very complicated subject. Typically, lenses suffer from these common aberrations: spherical, chromatic, curvature of field, and astigmatism (63). When the rays originate in a single point (**Figure 3.35**) ***O***, each one at a different angle ***u***, if the medium is homogeneous (has the same refractive index everywhere and the lens is perfect), the wavefront in the object space is a sphere. In this situation, all the rays will intersect at a single point in the image space and an ideal image will be formed. However, in most situations, when the rays pass through an imperfect lens, then the real wavefront is not spherical in the image space. In other words, the rays of different angles such as ***u1*** and ***u2*** in Figure **3.35** from the same single point ***O*** converge into different points ***O'*** and ***O1***. Thus, it causes the image to appear hazy or blurred.

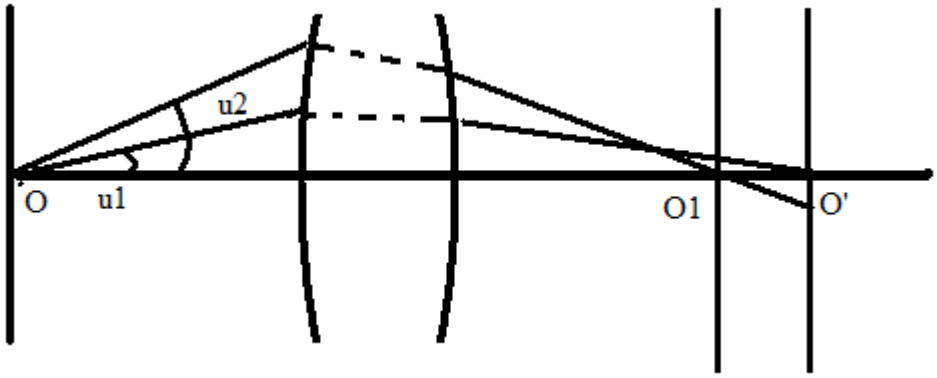

Figure 3.35: Real image formation based on optical aberrations.

It is complicated to show any equations to describe optical aberrations due to the complicated nature of the whole system. The most serious aberration is spherical aberration which occurs mostly on the interface of the cell wall (glass) and the surrounding air in the experiment. In order to investigate this complicated process, an optical design software package, WinLens 4.4 LINOS library (64) is applied to model the real system and simplify the optics performance.

The experiment setup from WinLens is shown in **Figure 3.36**. Lens1 and lens2 are thin lenses with 10mm and 80mm focal length. Objects are suspended in a water cell; a laser beam passes through the cell 2mm away from the 1mm thick glass wall. The field of view of this model is 0.5mm x 0.5mm x 25 μm approximately.

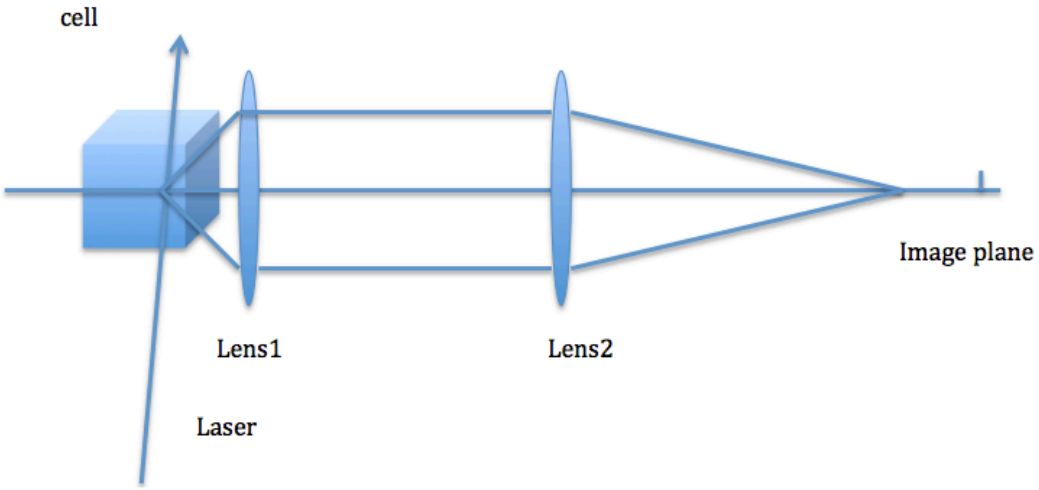

Figure 3.36: Illustration of the optical arrangement modelled by the Winlens LINOS optics library.

Assuming there is a perfect point object, and it is perfectly on focus and on-axis. The laser beam is 2mm away from the glass wall. **Figure 3.37** displays the spot diagrams of the system. It compares the point source on focus and out of focus situations, and the on axis and off axis situations.

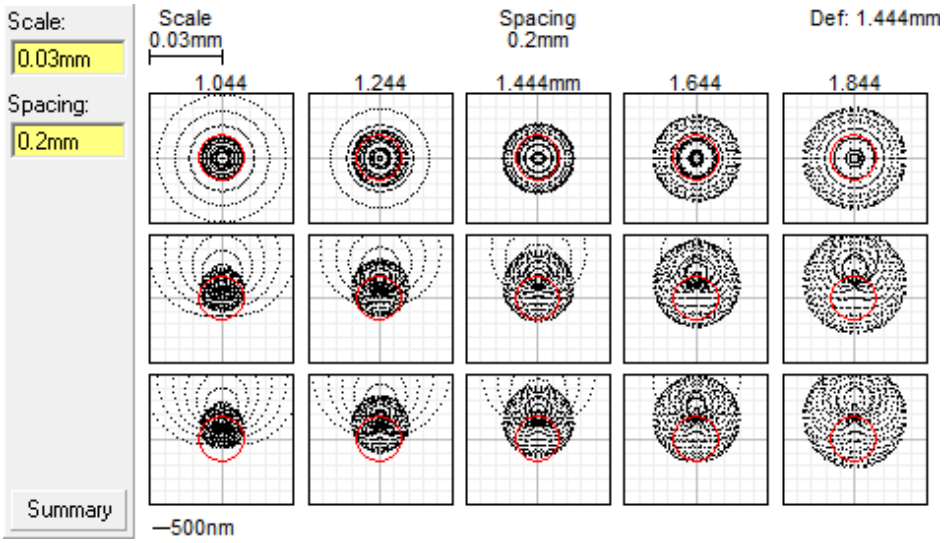

Figure 3.37: Spot diagrams. First row images represent object on-axis; second row images represent an object 0.1mm off-axis; whilst the third row images represent an object 0.2mm off-axis.

The spot diagrams in **Figure 3.37** show that the best image plane is 1.444mm away from the auto-calculated image plane if the laser beam is 2mm depth away from the glass wall. In the diagram, it is clear to see that the radius of the Point Spread Function (PSF) is slightly larger than the Airy disk. The red circle represents the Airy disk. The middle column is the case where the object is on focus, whilst the other columns represent the object is +(-) 0.2mm out of focus by step. The first row in **Figure 3.37** represents that a point object is on axis and the second row images show that a point object is 0.1mm off axis; whilst the third row images represent a 0.2mm off-axis object.

The size of the blurred circle is related to the object position. Considering the spot diagram in the same row, the smallest circle occurs when the point object is on focus. When the point object is out of focus, the blurred spot becomes larger. Comparing the images in the same column, it is found the radii of the spots are different when the object is positive off-axis and negative off-axis. However, most of the strong illuminations are nearly the same and only the peripheral rings become larger but weak. In general, to simplify the analysis of optics aberration, it is assumed the radii of the blurred circles approximately keep the same when the object is off axis and the radius of the blurred circle is mainly affected by defocus.

In order to investigate how strongly the image quality is affected by aberrations, **Figure 3.38, 3.39** and **3.40** display the spot diagrams in three different situations when the laser beam is 1mm, 2mm and 3mm depth away from the glass wall respectively.

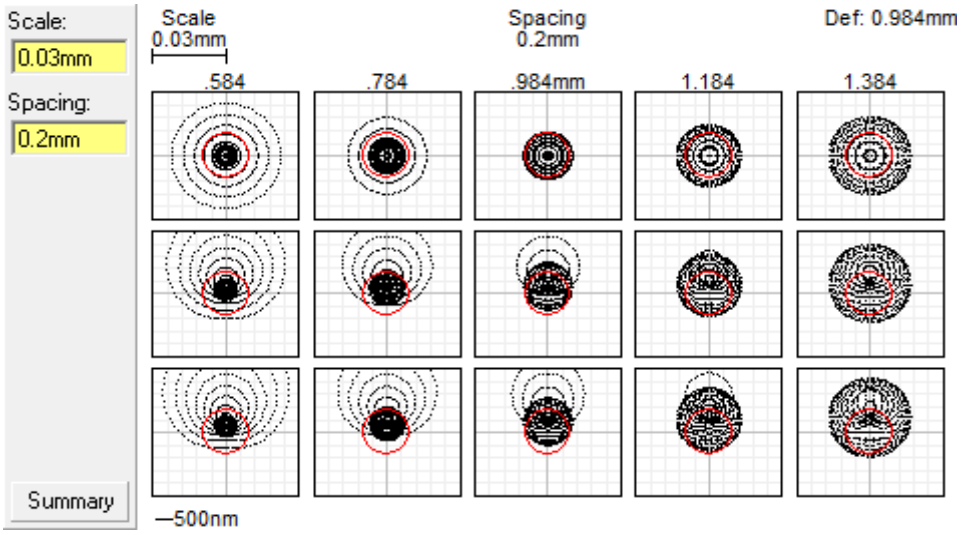

Figure 3.38: Spot diagrams from LINOS optics library. The laser beam is 1mm away from glass wall. Every row in one diagram represents the object on-axis, 0.1mm off-axis and 0.2mm off-axis respectively.

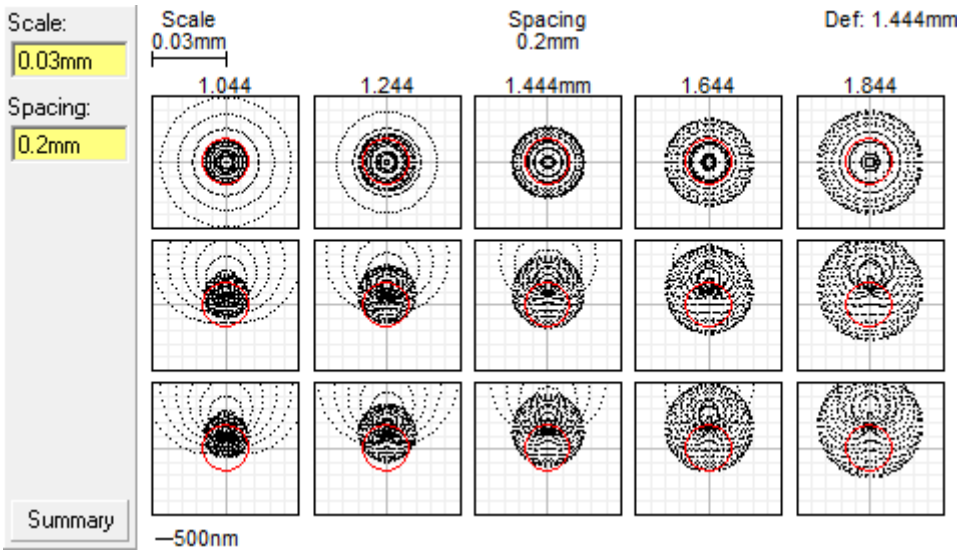

Figure 3.39: Spot diagrams from LINOS optics library. The laser beam is 2mm away from glass wall. Every row in one diagram represents the object on-axis, 0.1mm off-axis and 0.2mm off-axis respectively.

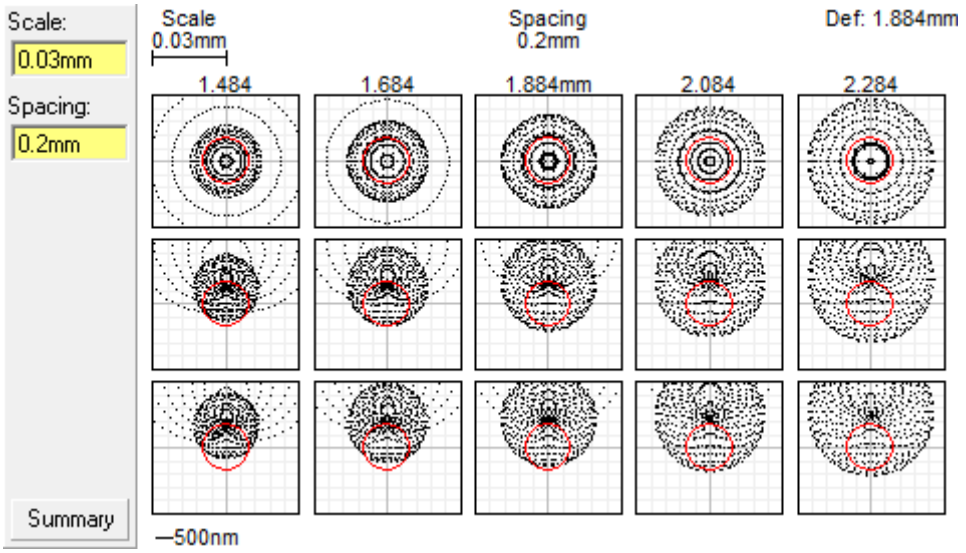

Figure 3.40: Spot diagrams from LINOS optics library. The laser beam is 3mm away from glass wall. Every row in one diagram represents the object on-axis, 0.1mm off-axis and 0.2mm off-axis respectively.

Based on these spot diagrams, only considering the defocus effect, it may be deduced that to a good approximation a simple equation can be used to describe the complicated aberrations.

$$radius = centre\_rays + \Delta \times particle\_position \qquad (3.5)$$

where the ***radius*** and ***centre_rays*** are the radius of the PSF when the point object is out of focus and the radius of the PSF when the point object is on focus, Δ is the gradient of the change in radius when the point object is out of focus comparing with the object on focus, ***particle_position*** is the real object position in the experiment.

For instance, when the laser beam is 1mm away from the glass wall, the rays can be expressed as:

$$radius = 0.018e^{-3} + 0.015 \times particle\_position \ \ (+) \qquad (3.6)$$

where the object is positive off-axis, and

$$radius = 0.018e^{-3} + 0.03 \times particle\_position \text{ (-)} \quad (3.7)$$

where the object is negative off-axis.

Table 3.9 shows the simulation parameters used in a series of simulations to assess the effects of aberrations.

Temperature	20^{o}C
Particle size distribution: Mean/standard deviation	100nm/20nm
Number of frames	300
Image size/pixel size	500 x 500/3.35microns
Exposure time	0.05s (particles are still during this time)
Magnification	6.7
Movement histogram interval	0.1 microns
Time interval	1s
Particle concentration	5 x 10^{6} /ml
Poisson noise	No
Quantisation noise	No
Background noise	No

Table 3.9: Simulation parameters used in the simulation to assess the effect of optics aberration.

Figure 3.41, **3.42** and **3.43** displays the example images and the recovered particle size distributions when the laser beam is 1mm, 2mm and 3mm away from the glass wall respectively.

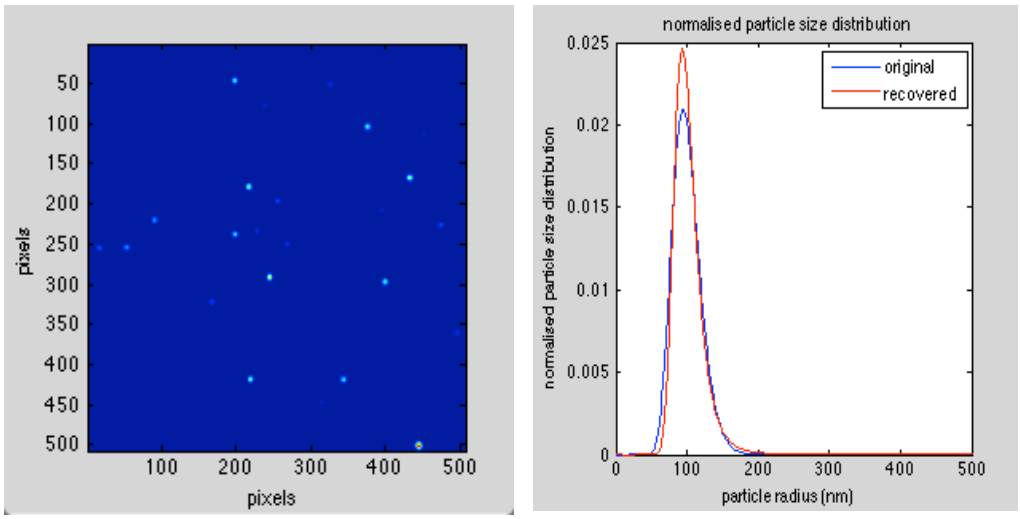

Figure 3.41: Example image and recovered particle size distribution when the laser beam is 1mm away from the glass wall.

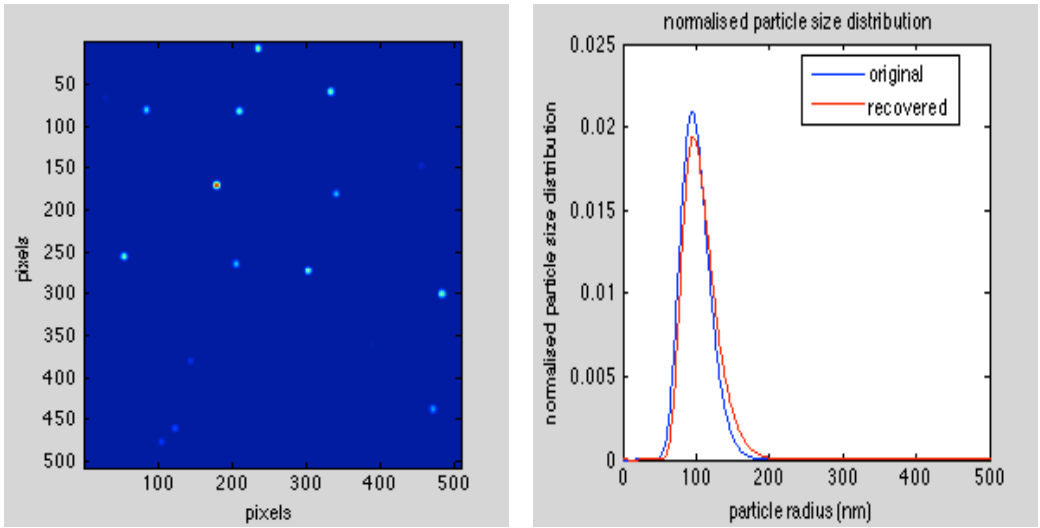

Figure 3.42: Example image and recovered particle size distribution when the laser beam is 2mm away from the glass wall.

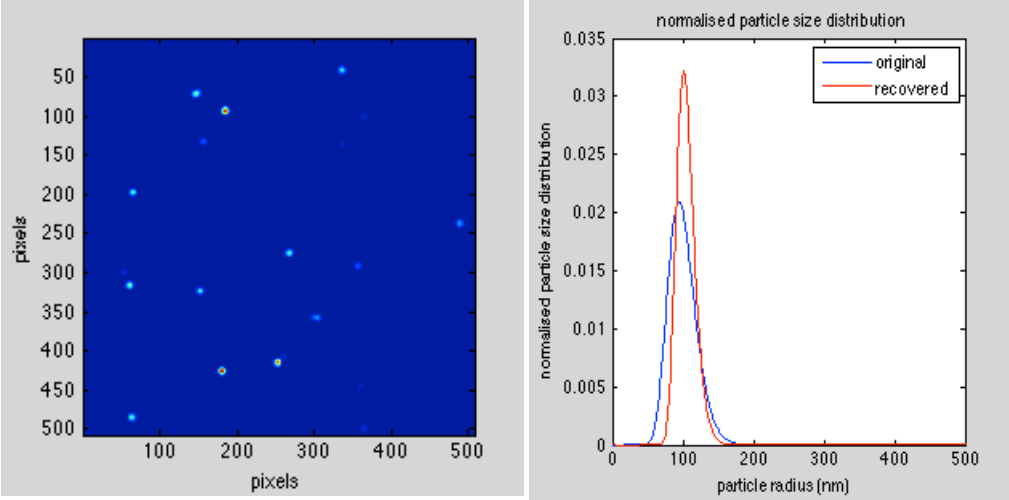

Figure 3.43: Example image and recovered particle size distribution when the laser beam is 3mm away from the glass wall.

It may be seen in **Figures 3.41** to **3.43** that the further the distance between the laser beam and the glass wall is, the larger the blurred spot is; for the largest distance, the example recovered distribution is worse than for the others. To provide a statistical analysis, **Table 3.10** compares the area errors, mean radius and standard deviations of recovered distributions in these three different conditions.

Laser position	Area error	Mean radius	Standard deviation
1mm	0.16	102.41	22.36
2mm	0.20	103.59	23.03
3mm	0.52	104.38	13.18

Table 3.10: Area errors, mean radii and standard deviations of the recovered particle size distributions when the laser beam is in different positions.

In general, comparing with the three criteria in **Table 3.10** and the reconstructed particle size distributions in **Figure 3.41**, **3.42** and **3.43**, the radius of the particle images becomes larger when the beam is further away from the glass wall, but optics aberrations do not strongly influence the final reconstructed particle size distributions. The recovered particle size distributions agree with the real distribution for the simulations conducted for the illumination beam 1 and 2 mm away from the cell wall, and the area errors (0.16 and 0.2) are much smaller than 0.32 for DLS. However, the area error is 0.52 if the illumination beam is 3mm away from the cell wall. Of course, the closer the beam is to the glass wall, the better the recovered distribution is. Therefore, it is necessary to keep the laser beam as close as possible to the glass wall in the experiments. However, as aligning the beam to be less than 2mm away from the cell wall is quite easily achieved in a real experiment, in the following simulations, lens aberration affections will be neglected.

3.4 Combined Effects Simulation Results

Section **3.3** established optimum values for some experimental parameters individually, including the time interval, exposure time, and particle concentration. It also assessed the importance of the noise conditions, including Poisson noise, different numbers of quantisation levels and different background levels. In this section, simulation results are presented which combine all the best experimental parameters, and considers Poisson noise, background noise and quantisation noise simultaneously. The simulation parameters are presented in **Table 3.11**.

Temperature	20^{o}C
Particle size distribution: Mean/standard deviation	100nm/20nm
Number of frames	300
Image size/pixel size	500 x 500/3.35microns
Exposure time	0.05s (particles moves)
Magnification	6.7
Movement histogram interval	0.1 microns
Time interval	1s
Particle concentration	5 x 10^{6} /ml
Poisson noise	Yes (Poisson noise factor = 1000)
Quantisation /background level	Yes (1024)/50

Table 3.11: Simulation parameters used in the simulation to assess the combined effects simulation results.

Figure 3.44 shows an example image simulated according to the experimental parameters in **Table 3.11**.

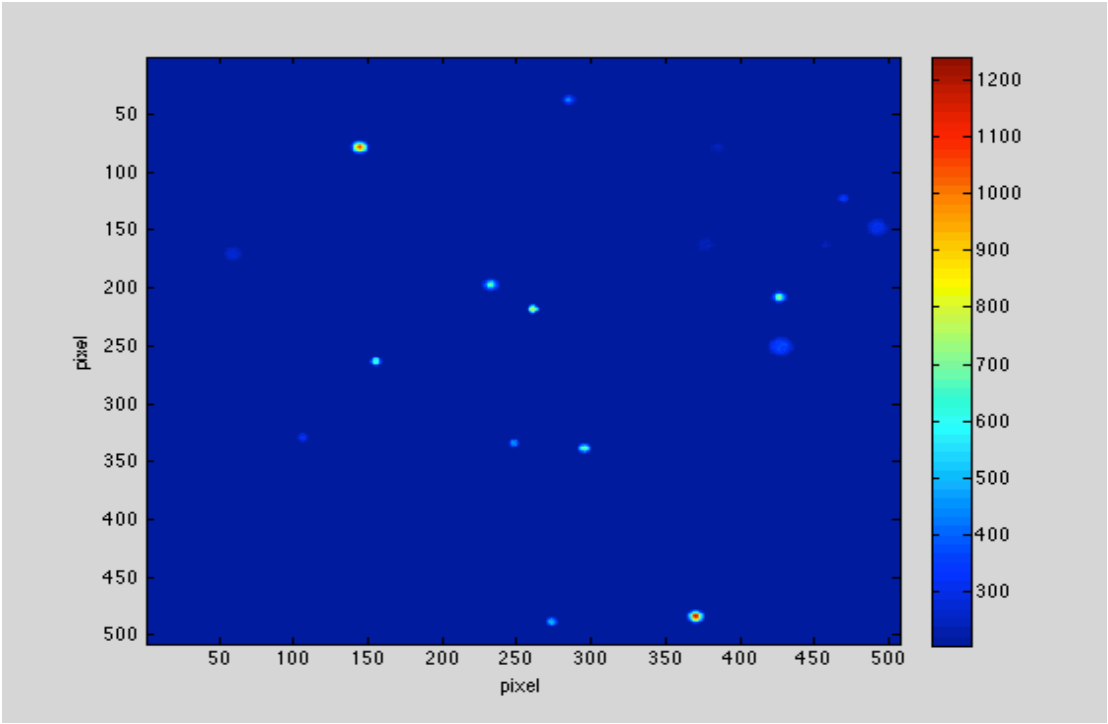

Figure 3.44: An example image simulated according to the experimental parameters in Table **3.11**.

Figure **3.45** is an example of the recovered particle size distribution.

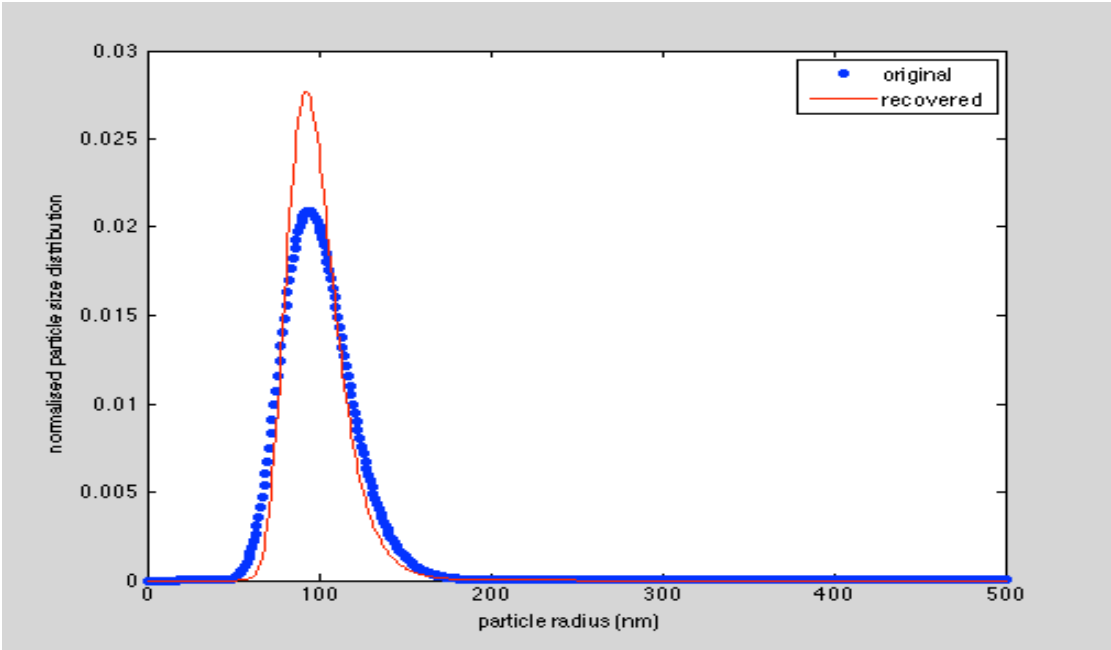

Figure 3.45: An example of the recovered particle size distribution. The area error, mean radius and standard deviation of the distribution are 0.25, 98.79nm, and 16.7nm respectively.

Ten independent data sets are recorded to statistically examine the recovered distribution. **Table 3.12** records the mean values and standard errors of these three criteria according to the ten independent simulations.

	Mean	Standard error
Area error	0.29	0.12
Mean radius	101.14nm	4.7nm
Standard deviation	19.30nm	5.1nm

Table 3.12: Mean values and standard errors of these three criteria based on 10 independent simulations.

These simulation results considered the combined effects of particle movements during the exposure time, Poisson noise, background noise and quantisation noise. Based on ten independent simulations, the area error is 0.29 (smaller than 0.32 for DLS), the recovered mean radius is 103.14nm, and the standard deviation is 19.3nm. These results demonstrate that the combination of effects and noise sources does not produce errors significantly different to the errors due these effects and noise sources acting alone.

3.5 Summary

Chapter **3** optimises and assesses the influence of the various parameters in the PMDD method used in experiments. It was found that 1s is the most suitable time interval. However, for some particularly large or small particles, the optimum time interval may vary depending on the particle sizes. The results indicated that exposure

time should be chosen from 0.02s to 0.05s to achieve enough light to form a bright image with small photon error. An exposure time of 0.05s is chosen to be the suitable exposure time in the simulation in order to minimise the Poisson noise effects whilst still minimise the blurring effect of the particle movements. Sections 3.3.4 and 3.3.5 considered the effects of Poisson, background and quantisation noise. Generally a high signal to noise ratio (SNR) will produce better results. When the background level is around 200 in a 12-bit operation, and the background level is less than 20 in an 8-bit operation, the recovered mean radius has a 95% accuracy compared with the original value, and the area error is smaller than the DLS value of 0.32. That means the background noise in the real Hamamatsu camera used in the experimental work does not influence the results seriously.

The results in section 3.3.5 showed that to obtain the most accurate results, the sample concentration should be restricted between $10e^6$/ml and $10e^7$/ml. The results in section 3.3.6 indicated that to minimise the effects of optics aberrations occurring at the edge of glass wall, the laser beam should be kept as close to the glass wall as possible, although the effects were almost negligible as long as the illuminating beam was within 2mm. With careful alignment, this distance is quite easy to achieve in practice.

In a final simulation, the optimum values of time interval, exposure time and particle concentration were used in conjunction with typical experimental values for the Poisson, background and quantisation noises, to assess whether the combined effect of all these effects was worse than the individual effects studied earlier and to estimate the likely outcome of an experimental implementation. The results are summarized in **Table 3.12** where it can be seen that the mean resulting area error has a value of 0.29 and that both the mean radius and the standard deviation are measured

with good accuracy. The area error of 0.29 compares favourably with simulated results for DLS for which the best area error was around 0.32-0.34 (see discussion in (21, 22)). This suggests that the PMDD method is capable of producing more accurate (in terms of area error) than DLS for the sort of particle size distributions examined in the two studies.

4 Comparisons of PMDD with a Tracking Method, Experimental Results and Simulation Results for Bi-modal Distributions

4.1 Introduction

Chapter **3** compared some different simulation results to find the optimised parameters in the experiment. This chapter will take into account the real data from the experiment. Firstly, in section **4.2**, it compares some simulation results from the PMDD method and a tracking method based on the NTA technique. Secondly, section **4.3** presents some experimental results recovered from both methods. The experimental data are obtained by Nam Trung Huynh (81) for several particle sizes. The reconstructed particle size distributions from the real data are important in demonstrating that the method produces particle size distribution results for real experimental data as well as for simulated data as demonstrated in the previous chapter. Section **4.4** continues by showing simulation results for a number of bi-modal distributions. Finally, a summary of the work carried out in this chapter is made.

4.2 Comparisons of a Tracking Method Based on NTA and PMDD in Simulation

The theory of NTA has been discussed in Chapter **1**. In this chapter, a particle tracking method is examined and the results of this method are compared to those obtained with the PMDD method.

The basis of and the inspiration for the tracking method used here is a description of the NTA method provided in (68, 97) although the implementation is not the same as that method. The tracking method used on the simulated and experimental results operates as follows. The experimental setup of the tracking method is the same as the PMDD method in **Figure 3.1**, and the original data set used to compare the techniques is the same set of recorded images. The particle positions in each image are then estimated using the centroiding algorithm described in Chapter 2. For the PMDD method these particle positions are the data used to form the PMDD histogram. For the tracking method, an attempt is made to identify particle positions in one frame with particle positions in the next frames, which arise from the same particle. For the tracking method employed here, this is performed simply by setting a threshold radius (4 pixels) around each particle.

If a single particle position was measured in the first frame, and there was only one particle found within this radius in the next frame, it may be identified as the same particle as the first frame. The movement of individual particles can be followed through the image sequence and the mean squared displacement is determined for each particle for as long as it is visible. The lifetimes of the displacement should be sufficiently long to ensure statistically accurate results, eg. over 5 or 10 frames, so that the estimation of diffusion coefficient is statistically accurate.

The equation to find the estimated radius from the mean squared displacement is:

$$R = \frac{2K_t T \Delta t}{3\pi\eta\bar{s}} \tag{4.1}$$

$$s = m^2 \tag{4.2}$$

where $\boldsymbol{R}$, $\boldsymbol{K_t}$, $\boldsymbol{T}$, $\boldsymbol{\Delta t}$, $\boldsymbol{\eta}$, and $\boldsymbol{m}$ represent the particle radius, Boltzmann's constant, the room temperature, the time interval between the frames, the viscosity of the liquid and the movement of an individual particle respectively .

Using the estimated R value from each particle track, it is then possible to generate an estimate for the particle size distribution.

The parameters used in the simulations are listed in **Table 4.1**.

Particle radius/ standard deviation	100nm/20nm
Number of frames	100, 300, 500, 1000, 3000
Image size/pixel size	500 x 500/3.35microns
Exposure time	0.05s
Magnification	6.7
Movement histogram interval	0.1 microns
Time interval	1s
Particle concentration	5 x 10^6 /ml
Minimum number of steps in a track	5/10 frames

Table 4.1: Simulation parameters used in the simulation to assess the PMDD method and the Tracking method.

Figure 4.1 presents some simulation results by both methods in different conditions (different number of frames, different minimum number of steps in a track).

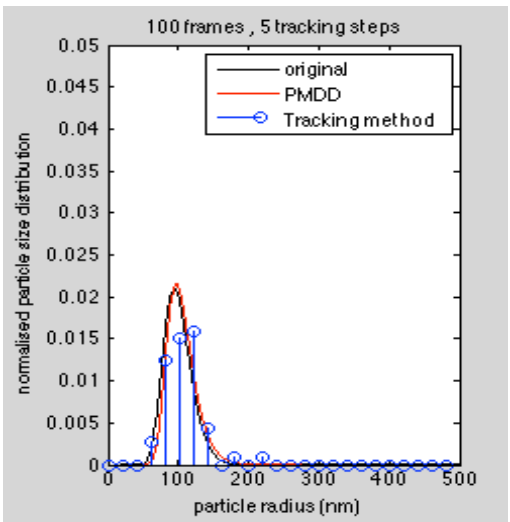
100 frames , 5 tracking steps
original
PMDD
Tracking method
normalised particle size distribution
particle radius (nm)

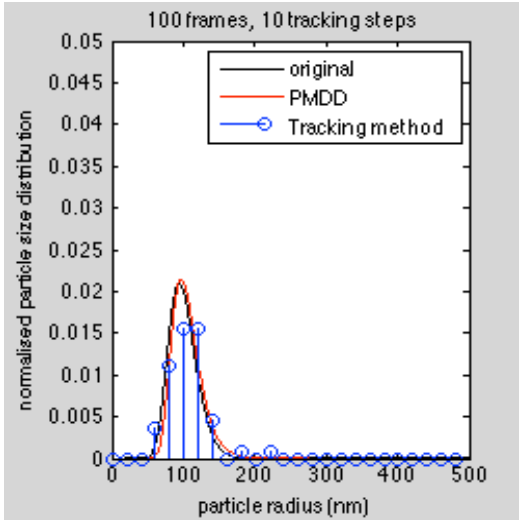
100 frames, 10 tracking steps
original
PMDD
Tracking method
normalised particle size distribution
particle radius (nm)

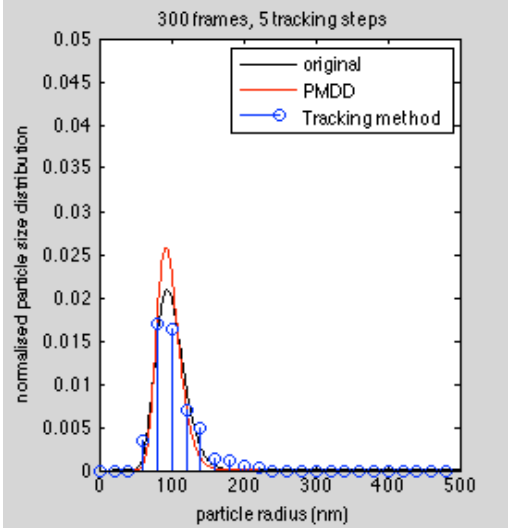
300 frames, 5 tracking steps
original
PMDD
Tracking method
normalised particle size distribution
particle radius (nm)

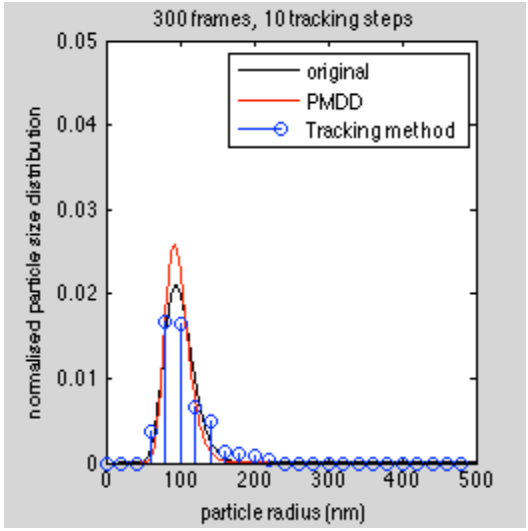
300 frames, 10 tracking steps
original
PMDD
Tracking method
normalised particle size distribution
particle radius (nm)

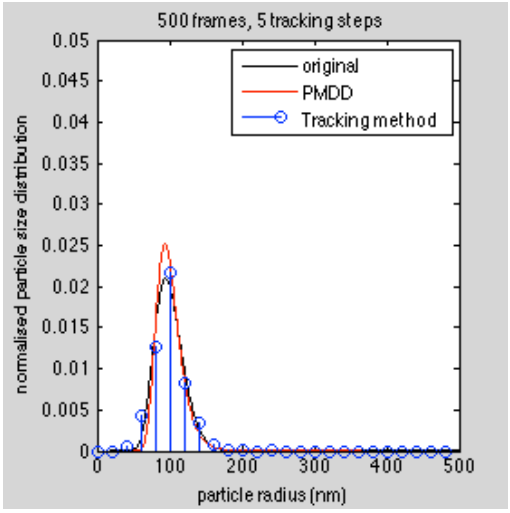
500 frames, 5 tracking steps
original
PMDD
Tracking method
normalised particle size distribution
particle radius (nm)

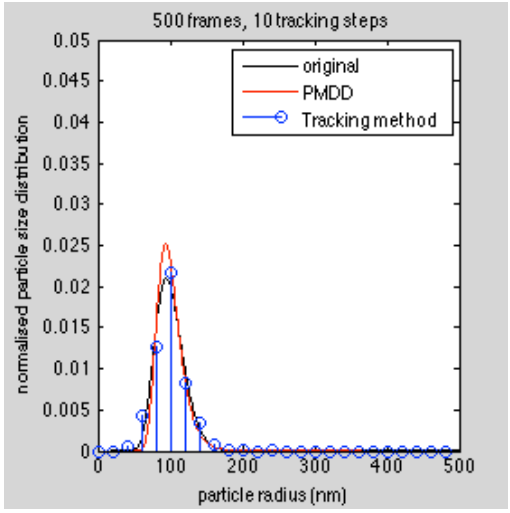
500 frames, 10 tracking steps
original
PMDD
Tracking method
normalised particle size distribution
particle radius (nm)

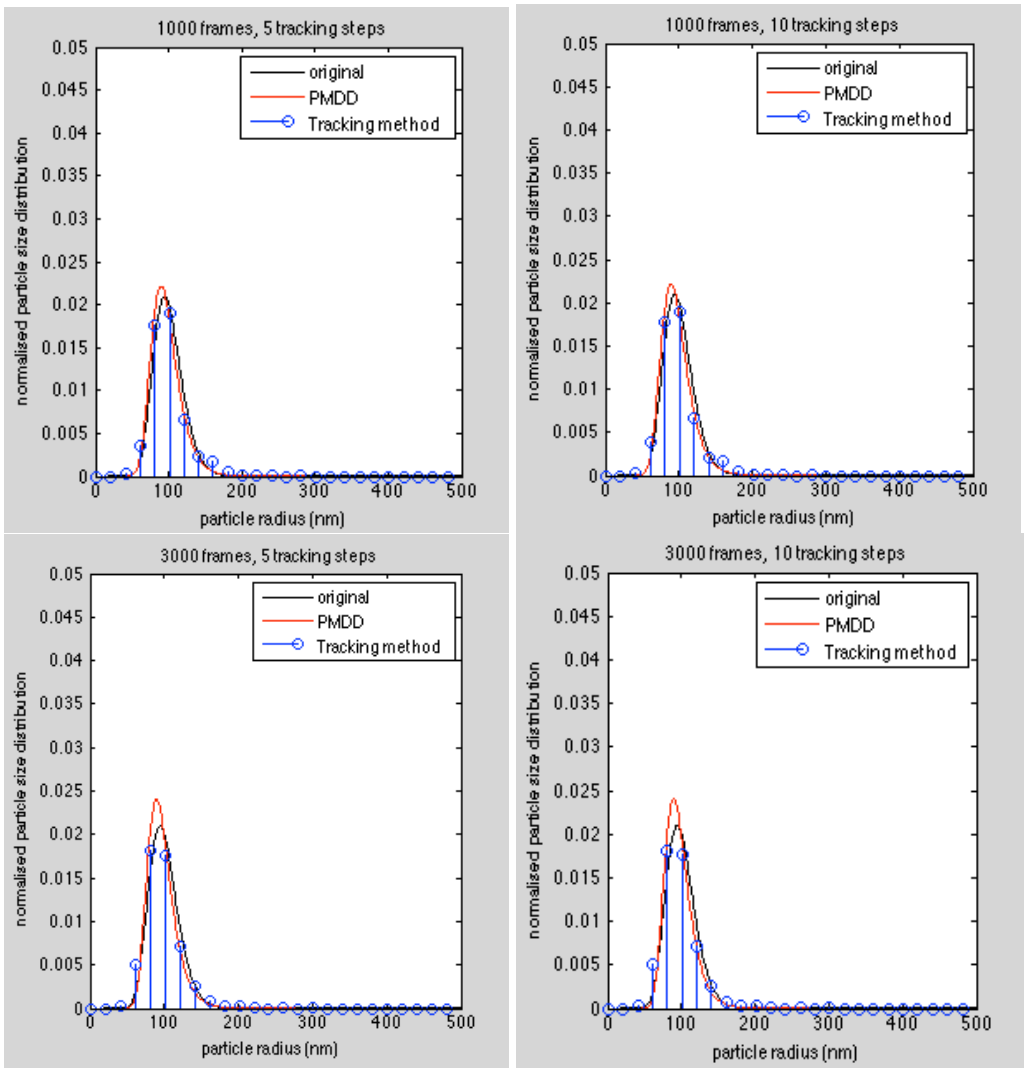

Figure 4.1: Recovered particle size distributions from tracking method and PMDD in different simulation conditions. The original mean radius is 100nm with 20nm standard deviation.

As may be seen in **Figure 4.1**, both methods can recover particle size distributions, and both of the recovered distributions are very similar to the original distribution when the minimum number of steps in a track is over 5. The mean radius, area error and standard deviation of the particle size distributions in every condition are listed in **Table 4.2**.

Tracking steps		5			10		
Frames	Method	Mean	Area error	dev	Mean	Area error	dev
		(nm)		(nm)	(nm)		(nm)
100	PMDD	105.46	0.19	21.18	105.46	0.19	21.18
	Tracking	107.48	0.58	27.5	107.06	0.56	27.12
300	PMDD	98.71	0.20	16.87	98.71	0.20	16.87
	Tracking	102.44	0.49	28.64	102.35	0.49	29.14
500	PMDD	100.57	0.16	19.23	100.57	0.16	19.23
	Tracking	98.93	0.34	23.73	99.2	0.34	23.81
1000	PMDD	98.35	0.16	21.0	98.35	0.16	21.0
	Tracking	99.1	0.35	26.64	98.89	0.35	26.58
3000	PMDD	98.03	0.19	19.58	98.03	0.19	19.58
	Tracking	97.68	0.38	24.22	97.86	0.38	24.13

Table 4.2: Mean values, area errors and standard deviations of PMDD and the tracking method in different simulation conditions.

As may be seen in **Table 4.2**, in general, both methods can recover good results (i.e. area errors similar to or less than a value of around 0.32 in DLS). When the number of frames is over 300, the recovered mean value is less than 5% different from the original data for both methods, but the tracking method has a slightly wider distribution than the PMDD method and the area error is slightly larger for the tracking method in the same condition. If there are only 100 frames tracked, the recovered mean value is not as good as the others (more frames). The more frames are, the more statistically accurate the result is.

4.3 Experimental Results

The 3000 series polystyrene Nano-spheres from Brookhaven Instruments Limited were employed in the experiment. Four different sample groups were used with the nominal radius of 50nm, 75nm, 100nm and 200nm, and the standard deviations of every single sample are 5.2nm, 4.3nm, 4.7nm and 7.3nm respectively (these figures are quoted from the manufacturers data sheets for the supplied samples). For each sample, a set of 300 contiguously grabbed frames with a time interval of 1 second between frames was collected.

Figure 4.2 is an example of a frame of the raw data captured using 12 bit digitisation, and obtained using an exposure time of 25 milliseconds and a sample of polystyrene particles with a nominal (spherical) radius of 200nm (The image may be too bright with 50ms). A 256 by 256-pixel region of the camera was used and the camera pixels were 6.7 by 6.7 micrometres. Because the camera's magnification factor is 6.6, the corresponding effective pixel in the sample region is about 1 micrometre.

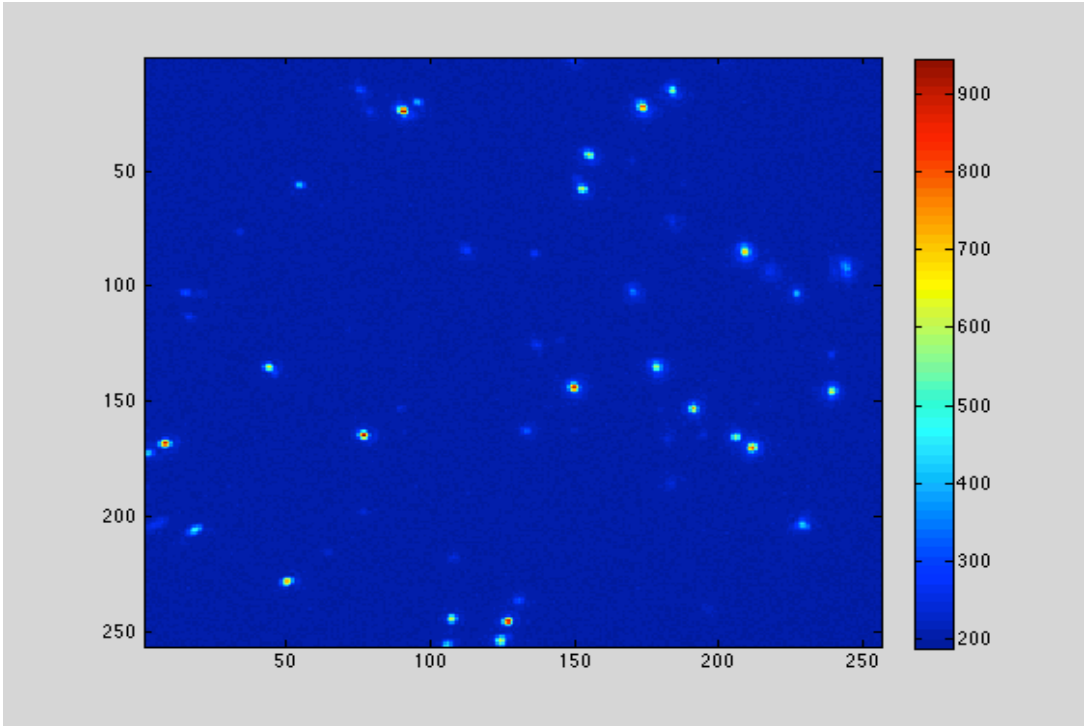

Figure 4.2: An image of 200nm radius polystyrene particles in a 10mm x10mm glass cell illuminated with a thin sheet of light (~25μm x 500μm) from a solid state laser ($\lambda = 532\text{nm.}$) focussed into the sample using a 50mm cylindrical lens and imaged with a 0.4 NA long working microscope objective.

Figure 4.3 - 4.6 show the recovered distributions with the PMDD method and the tracking method from the different real data groups respectively.

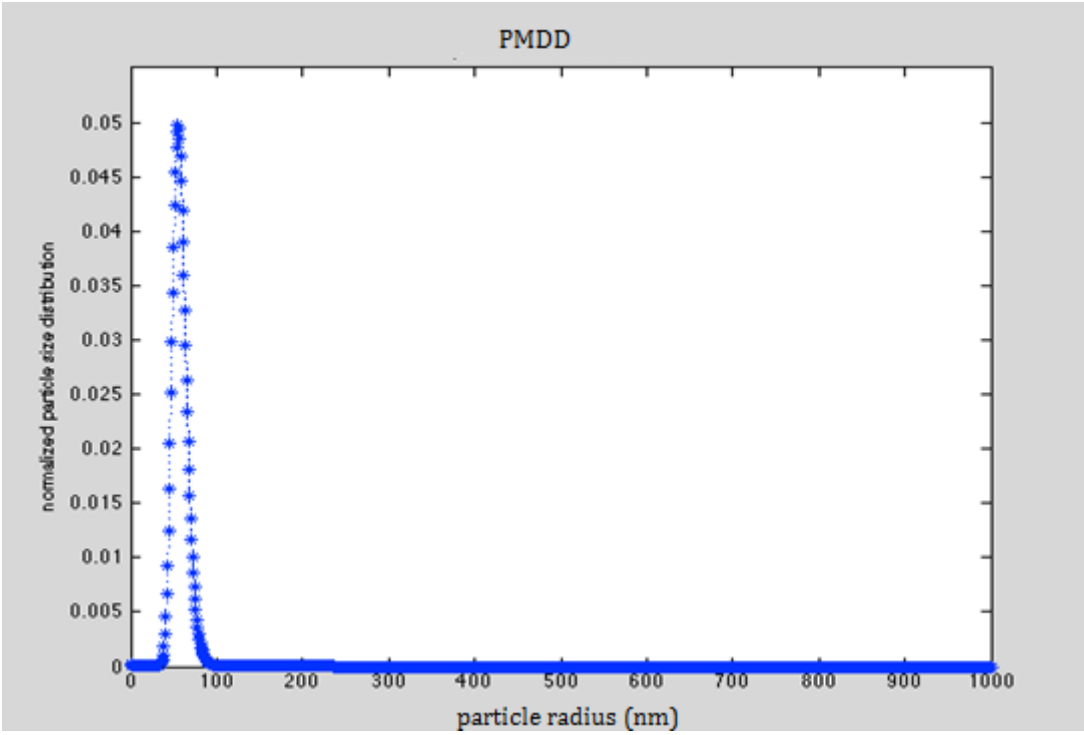

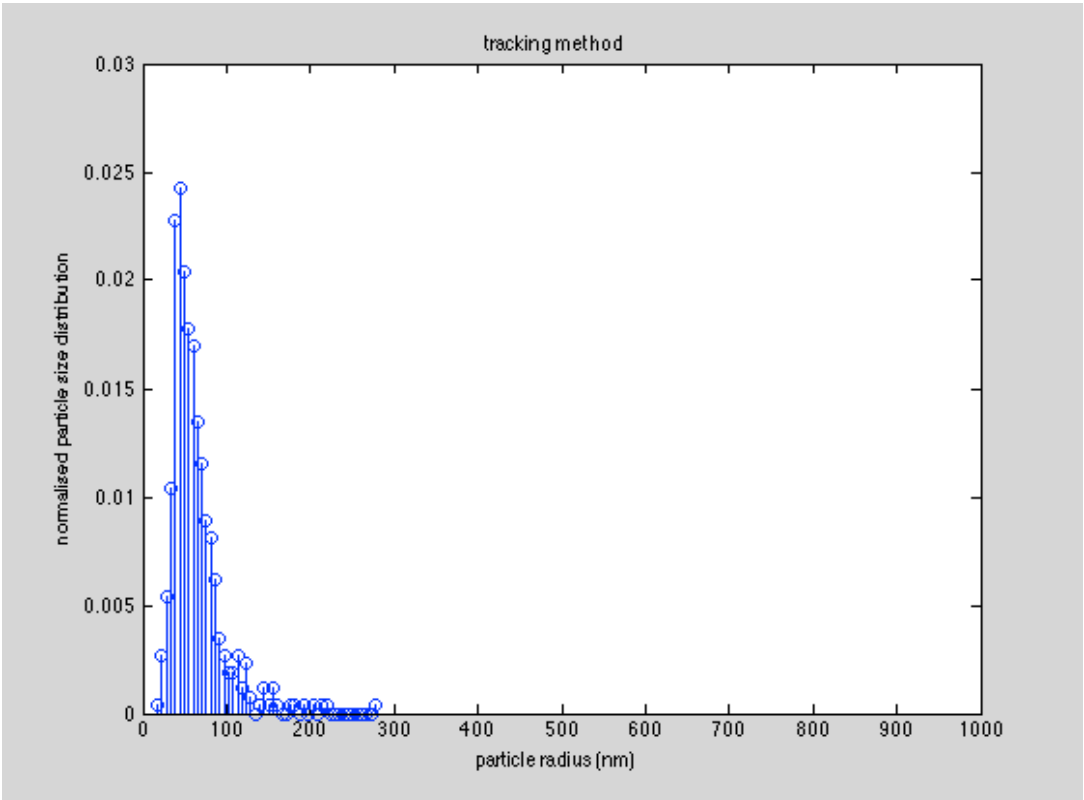

Figure 4.3: Recovered particle size distributions based on PMDD and tracking method. The real particle radius is 50nm, and standard deviation is 5.2nm.

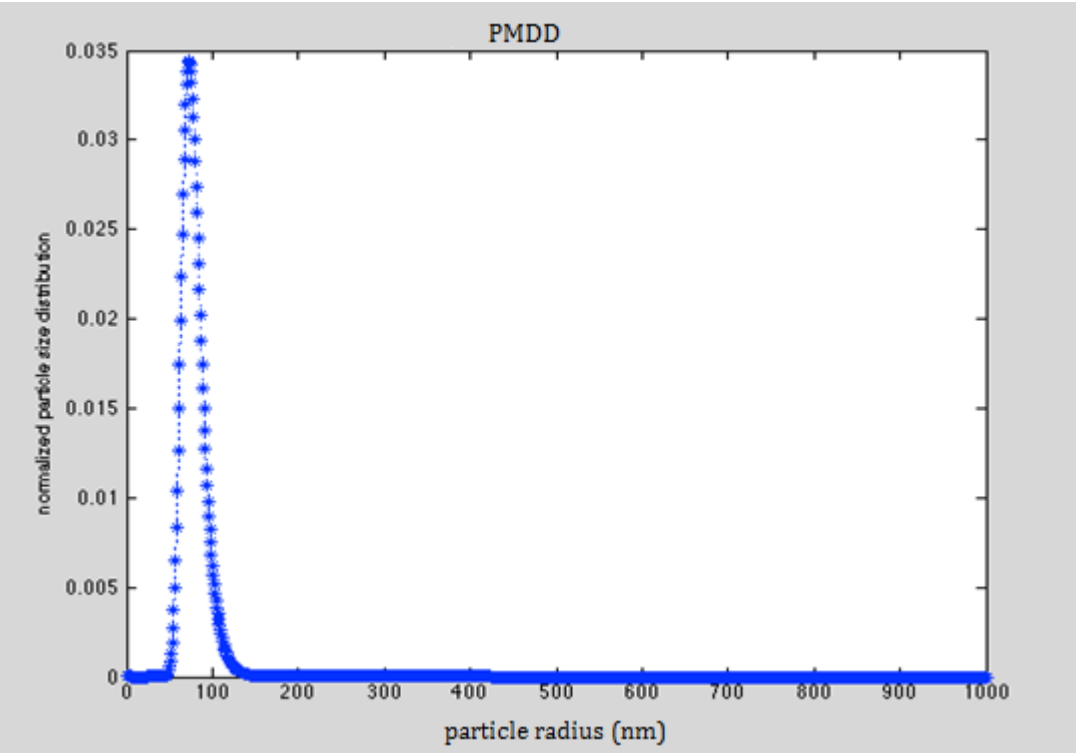

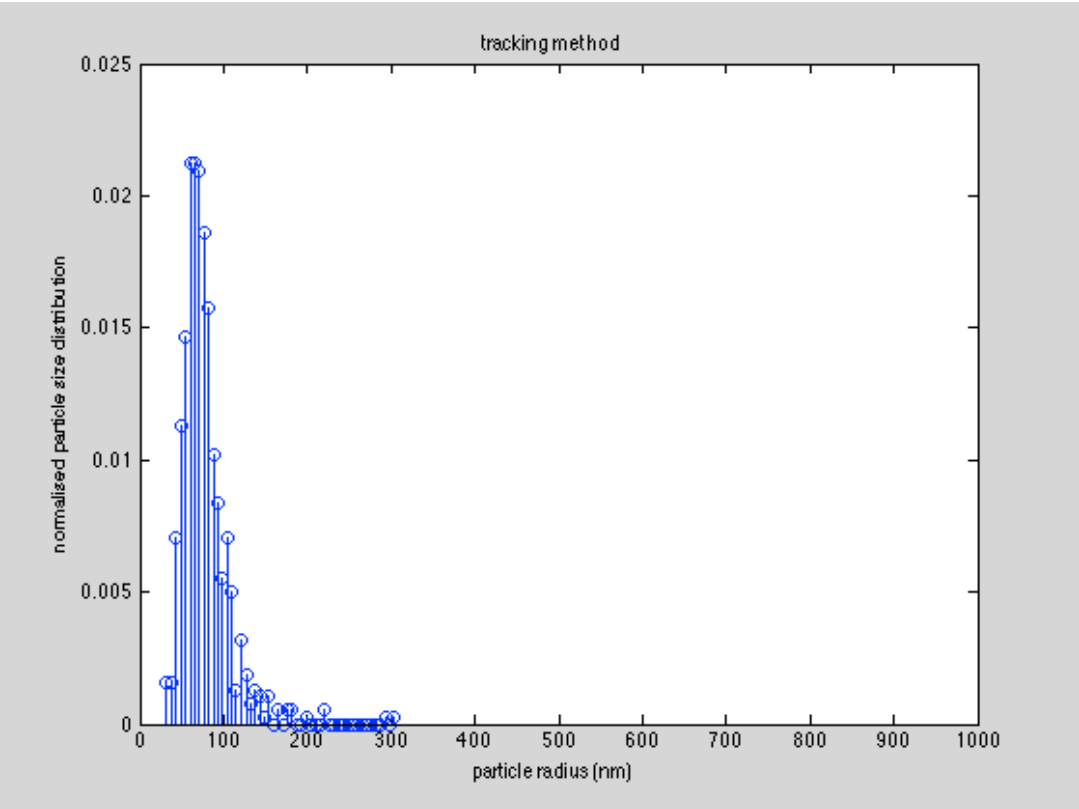

Figure 4.4: Recovered particle size distributions based on PMDD and tracking method. The real particle radius is 75nm, and the standard deviation is 4.3nm.

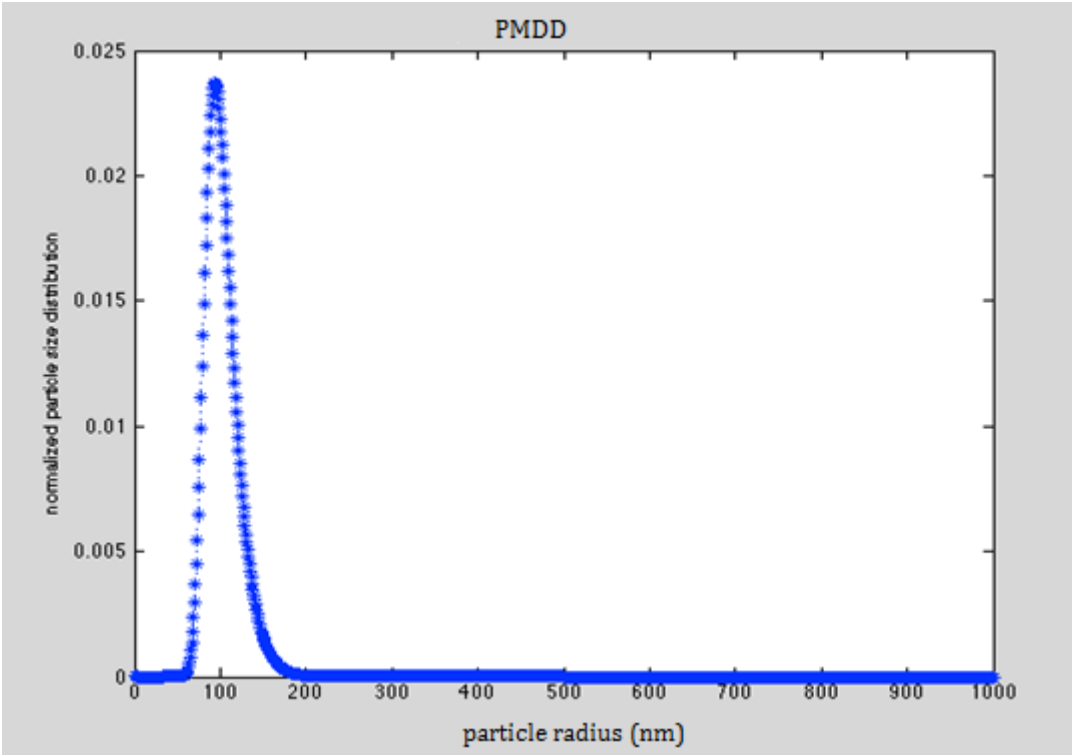

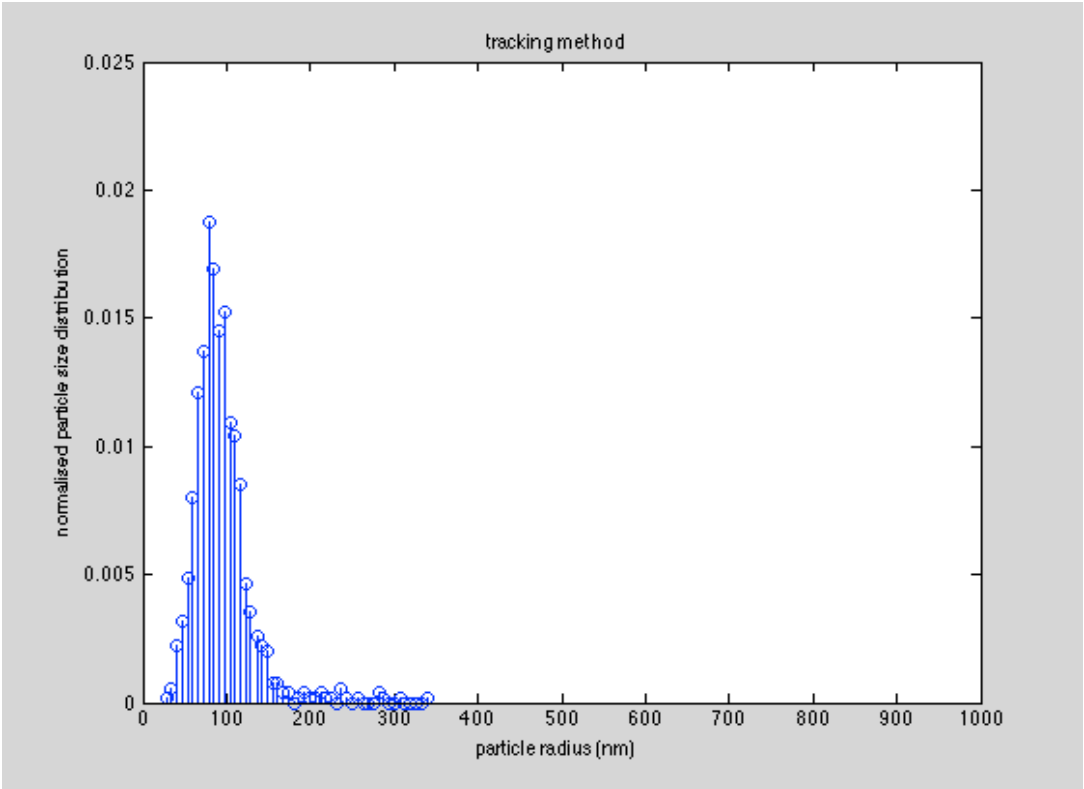

Figure 4.5: Recovered particle size distributions based on PMDD and tracking method. The real particle radius is 100nm, and the standard deviation is 4.7nm.

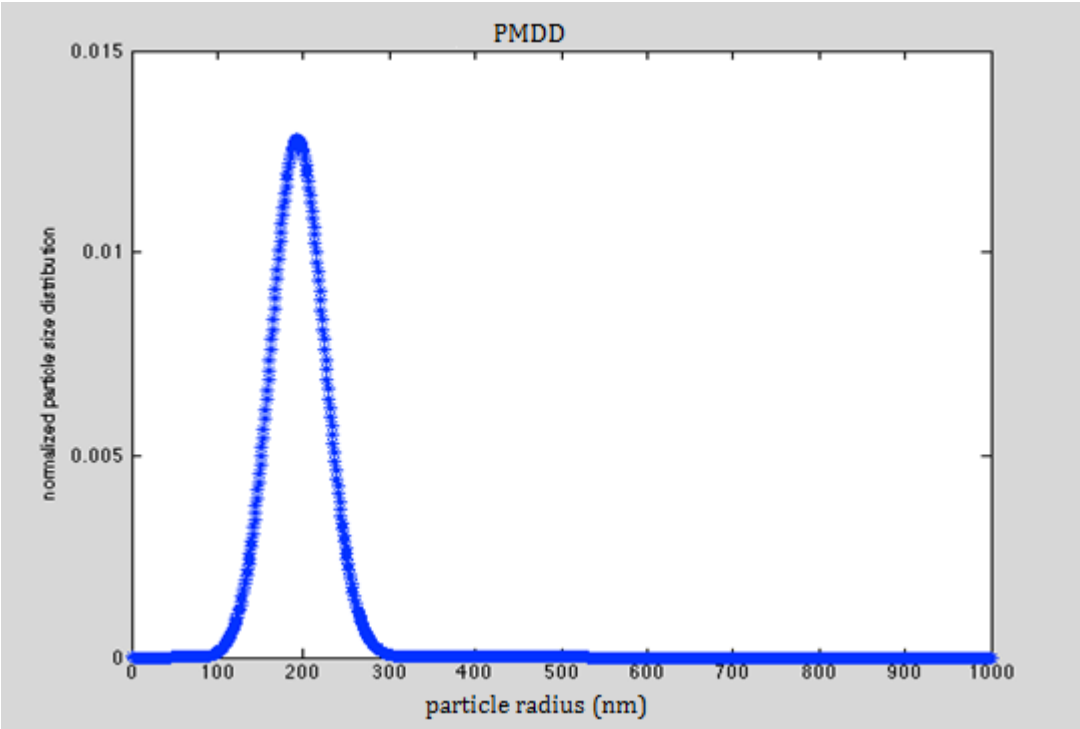

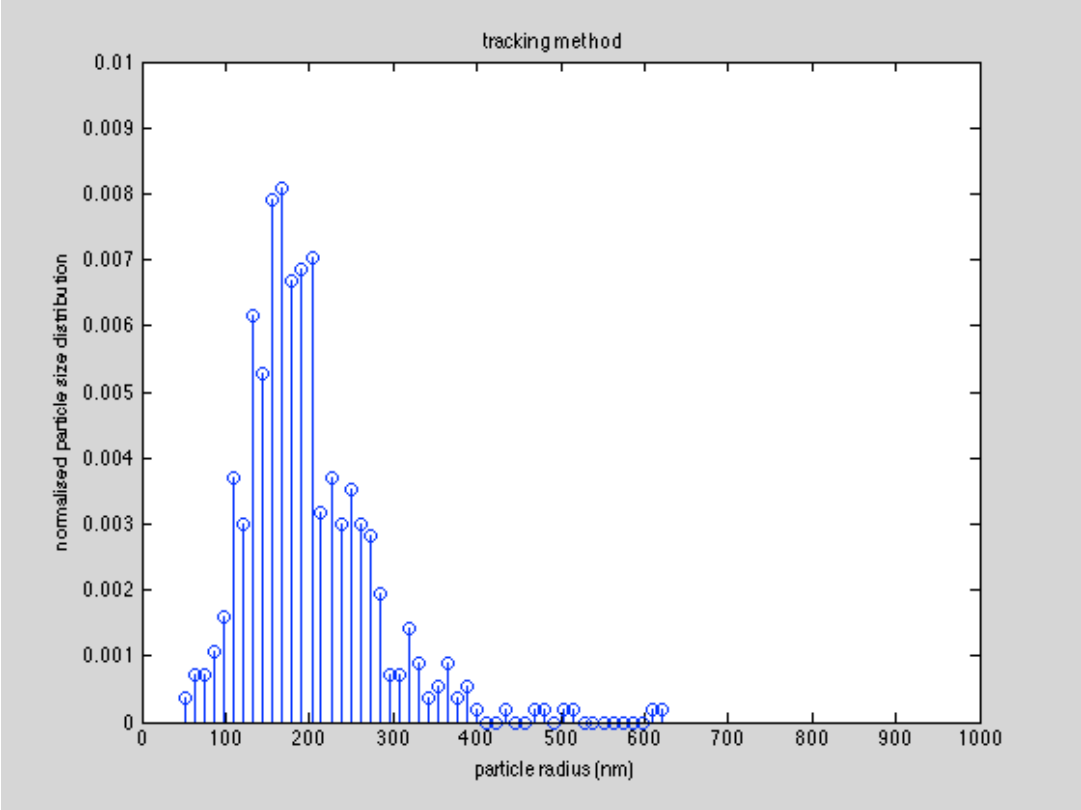

Figure 4.6: Recovered particle size distributions based on PMDD and tracking method. The real particle radius is 200nm, and the standard deviation is 7.3nm.

It may be seen that for each nominal particle size, the PMDD method has produced a narrower distribution than the corresponding tracking method result. **Table 4.2** compares the recovered mean radii and standard deviations in these four different sizes with both methods. In the processing of this data, a temperature of 20^{o}C and a dynamic viscosity of 10^{-3} Pa.s were used. In the experiments the temperature/dynamic viscosity of the sample was not measured accurately, so the results produced may have an incorrect scaling in the radii axis. However, this scaling would be the same for both PMDD and the tracking method, so the comparisons made below are still interesting despite this uncertainty. It is also worth noting that the recovered mean radii values for the 75, 100 and 200nm nominal radius particles are in good agreement with the nominal radius values, suggesting that the assumed temperature/dynamic viscosity was not in error by more than a few percent.

	Tracking Method		PMDD	
Real radius	Mean	Standard deviation	Mean	Standard deviation
50nm	62.41nm	30.14nm	57.39nm	8.16nm
75nm	76.9nm	28.28nm	76.13nm	12.98nm
100nm	93.00nm	33.37nm	101.21nm	23.89nm
200nm	196.99nm	75.04 nm	197.28nm	30.26nm

Table 4.3: Comparisons of mean values and standard deviation between tracking method and PMDD on mean values and standard deviations with four different particle sizes.

According to **Table 4.2**, the PMDD method and the tracking method present good performances when the particle radius is 75nm, 100nm, and 200nm, but the tracking

method has a broader distribution than the PMDD method. When the nominal radii of particles are 50nm, the recovered distribution is not as good (in terms of giving a mean value close to the nominal radius) as the others in both methods. The recovered mean radius is more than 10% different from the real radius in each method for the 50nm sample. That can be explained by the weak scattering of particles and the stronger relative background noise. In addition, two or more particles superposing together may result in bad results. With the nominal radius increasing, the particle size distribution becomes wider. The large fluctuations arise from the slow Brownian movements of large particles. When calculating the displacements of particles, large errors occur due to the small displacements.

4.4 Bi-modal Sample Simulation Results

Because of the good simulation results presented in Chapter 3 and the encouraging experimental results presented in section 4.4, it is worth investigating further the performance of the PMDD method. The results shown so far have all been for mono-modal distributions. Some bi-modal size distributions are examined with the PMDD performance in the following examples. **Figure 4.7(a)**, and **(b)** show the samples with single particle size distribution: mean radius 60nm, 20nm standard deviation; mean radius 100nm, 20nm standard deviation respectively; Figure **4.7 (c)** shows the samples with bi-modal particle size distribution: 50% mean radius 60nm, 20nm standard deviation; 50% mean radius 100nm, 20nm standard deviation.

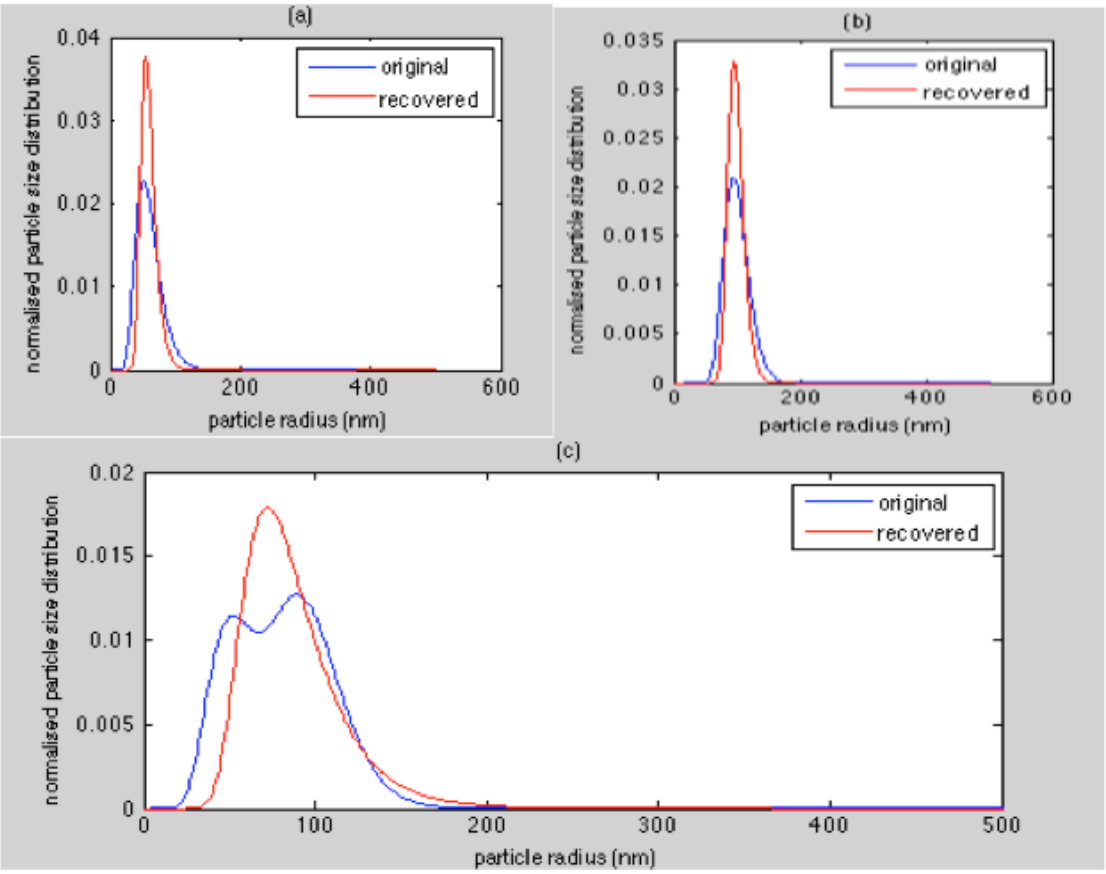

Figure 4.7: (a) Recovered single particle size distribution with 60nm mean radius and 20nm standard deviation; the recovered mean radius is 59.65nm, area error is 0.49, standard deviation is 14.9nm. (b) Recovered single particle size distribution with 100nm mean radius and 20nm standard deviation; the recovered mean radius is 98.67nm, area error is 0.41, standard deviation is 13.00nm. (c) Bi-modal sample: 50% mean radius 60nm, dev 20nm; 50% mean radius 100nm, dev 20nm; the recovered mean radius is 87.23nm, standard deviation is 43.34nm.

It may be seen in **Figure 4.7** that each of the single-peaked distributions has been recovered well but the recovered bi-modal particle size distribution has only one peak in **Figure 4.7 (c)** which is different from the original distribution with two peaks.

Figures 4.8 and **4.9** show some other bi-modal samples respectively.

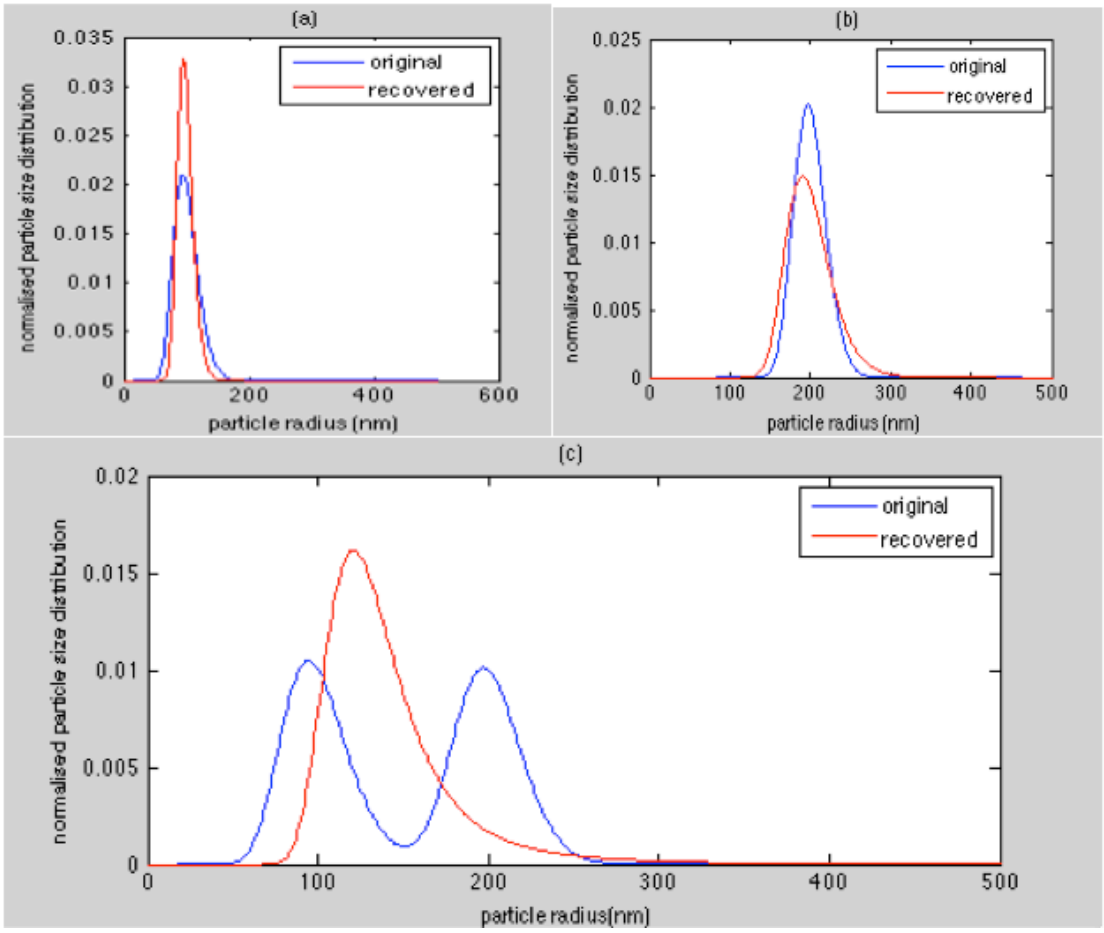

Figure 4.8: (a) Recovered single particle size distribution with 100nm mean radius and 20nm standard deviation; the recovered mean radius is 98.67nm, area error is 0.41, standard deviation is 13.00nm. (b) Recovered single particle size distribution with 200nm mean radius and 20nm standard deviation; the recovered mean radius is 200.03nm, area error is 0.35, standard deviation is 29.55nm. (c) Bi-modal sample: 50% mean radius 100nm, dev 20nm; 50% mean radius 200nm, dev 20nm; the recovered mean radius is 144.87nm, standard deviation is 59.45nm.

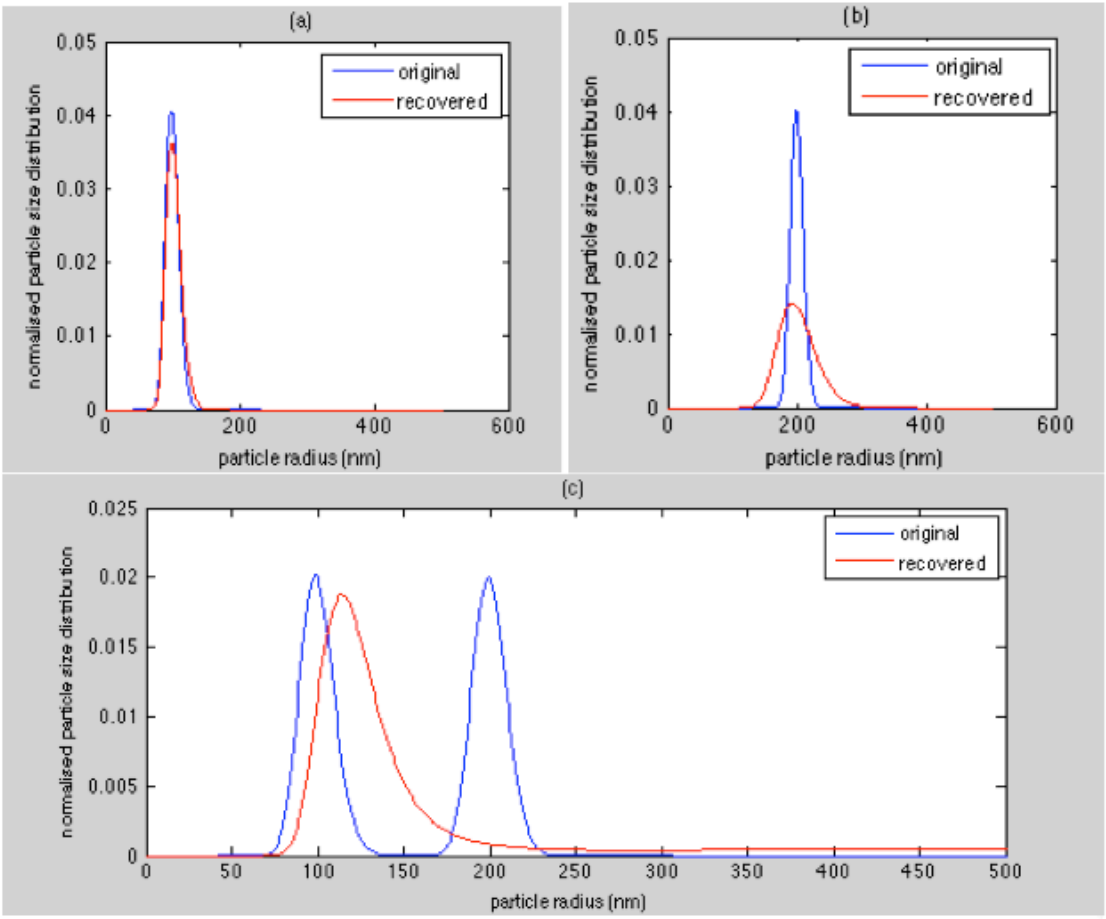

Figure 4.9: (a) Recovered single particle size distribution with 100nm mean radius and 10nm standard deviation; the recovered mean radius is 102.58nm, area error is 0.17, standard deviation is 11.7nm. (b) Recovered single particle size distribution with 200nm mean radius and 10nm standard deviation; the recovered mean radius is 201.88nm, area error is 0.94, standard deviation is 29.61nm. (c) Bi-modal sample: 50% mean radius 100nm, dev 10nm; 50% mean radius 200nm, dev 10nm; the recovered mean radius is 157.01nm and the standard deviation is 89.02nm.

It may be seen in both **Figures 4.8** and **4.9** that the original bi-modal distributions are recovered as single peak distributions for the mixtures i.e. similar to the result in **Figure 4.7**. This failure to recover two peaks is related to the way that the PMDD method measured the displacements between different particles. For two size populations in the mixtures, the movement displacements from **class *I*** parings is wider compared with a single size distribution, but it does not separate into two

distinct PMDD peaks, and thus it is difficult for the ML inversion method to distinguish two size populations in a mixture with the PMDD method.

Although the PMDD method gives good performance to recover single particle size distribution, it is difficult to recover bi-modal particle size distributions (**Figure 4.7-4.9**). This is the drawback of the PMDD method. According to (69), the NTA method was able to resolve and distinguish the two size populations: 60+100nm, 100+200nm, 200+400nm, 400+1000nm, and 100+400nm in the mixtures and yielded accurate size estimations.

4.5 Summary

In this chapter, the PMDD method and a tracking method were compared. In the simulation, it considered different number of frames, and different minimum number of steps in a track. Both methods can recover particle size distribution very well (compared with the best values (area error) of around 0.32 for DLS) when the number of frames is over 300 and the minimum number of steps in a track is over 5. However, the tracking method gave slightly larger area error and standard deviation than the PMDD method. In the experiment, both methods give good performances when the particle radius is 75nm, 100nm and 200nm. However, when the particle radius is 50nm, the recovered distribution is not as good as the others. Both methods give wider distributions than the manufacturers quoted values. In each case, the tracking method has a wider distribution than the PMDD method; this result is consistent with the computer simulation results of section 4.2. As there is no ‘gold standard’ method to give a true particle size distribution and the amount of contamination and/or

aggregation present in the sample is not known, it is not possible to say which method is giving a better result.

Simulations were also performed for bi-modal size distributions. For bi-modal distributions, the PMDD method gave poor performance, and it can only reconstruct one peak in two size populations in a mixture. This is a drawback of the PMDD method, which arises from the use of an inversion algorithm to construct the final particle size distribution (similar problems are seen when using inversion algorithms in DLS (21)). So, the PMDD method suffers from an inability to reconstruct accurately bi-modal distributions, whilst the tracking method can reconstruct bi-modal distributions but generally gives wider distributions due to the limited accuracy of each estimated R value.

The work in the next chapter is an attempt to develop a sizing method that does not need an inversion algorithm, and also does not suffer from the statistical uncertainty arising from measuring the random movements from Brownian motion.

5 Angular Dependent Intensity for Individual Particle Sizing

5.1 Introduction

Chapters 2 to 4 introduced the PMDD method, which gave good performance for single particle size distribution, but poor performance for bi-modal distributions. Chapter 5 develops another novel approach to size particles which is based on image intensity, a form of this approach was first published in the thesis of Nam Trung Huynh (81), the work in chapter 6 assesses, develops and improves the method he implemented.

Particles scatter light in all directions, and the illuminations are determined by particles characteristics and the scattered angles. In other words, the intensities are angular dependent. The new approach developed in this chapter is similar to the SLS technique, but it combines angular dependent intensity method and individual visualisation together to recover particle sizes. In SLS, the light intensity is measured as a function of angle but for light scattered by a collection of many particles, in this situation the large particles can dominate the collected light, and the small particles may become invisible in the traditional SLS technique. The approach investigated here attempts to measure the angular intensity variations for individual particles, which helps to overcome the domination by large particles.

The proposed imaging system is illustrated in **Figure 5.1**. Laser light is applied as the light source and a cylindrical lens is employed to generate a narrow monochromatic coherent light sheet passing through a cell which contains many suspended particles in a certain liquid (normally water). A two-lens system is employed to condense and focus scattered light from particles. A mask with some apertures (such as four apertures in **Figure 5.2**) is inserted between these two lenses to split the scattered light into different angles and then a multi-angle image system is formed. Behind the mask, wedge prisms are introduced to tilt the scattering light from different apertures and form an image in a certain position on the CCD.

The apertures are positioned in the back focal plane of the first lens and thus they act like angle dependent detectors for each scattering particle; however the actual detection cannot take place in this plane as, if it did, the measured light would come from all the illuminated particles. To separate the light from different particles the light leaving the apertures is refocused to an image plane; but for each particle the light from each aperture is imaged to a different spatial position by the bending effect of the prisms. Thus, the final image contains light from different particles, which are spatially separated but also angular scattering intensity information as each particle now forms multiple images, each of which contains light scattered into the different angles defined by the apertures.

The number of apertures determines the number of selected scattering angles. The arrangement of the wedge prisms defines the patterns of the groups of the bright peaks. The brightness of these peaks is normalised to compare with the look-up table of predicted data to find the most suitable particle size. This technique is investigated in detail in the following sections. The image captured on the CCD is composed of

many groups of bright peaks. Depending on the various patterns of the groups, two kinds of approaches will be described in detail in the following sections, which are Multiple Image Technique (MIT) and Separated Multiple Image Technique (SMIT).

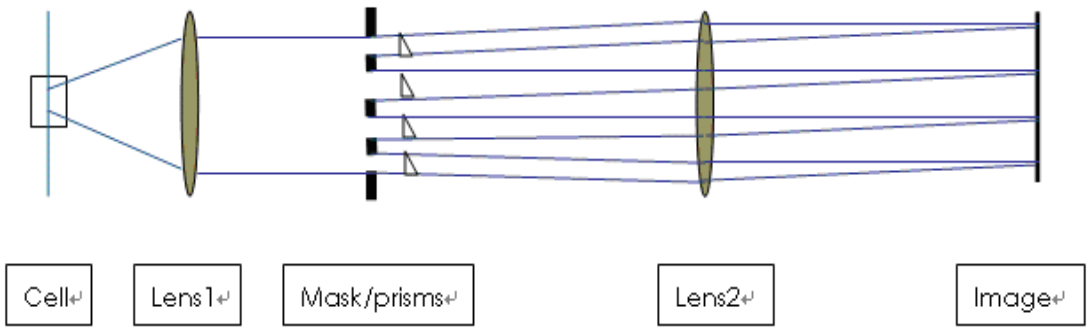

Figure 5.1: The proposed imaging system for particle sizing.

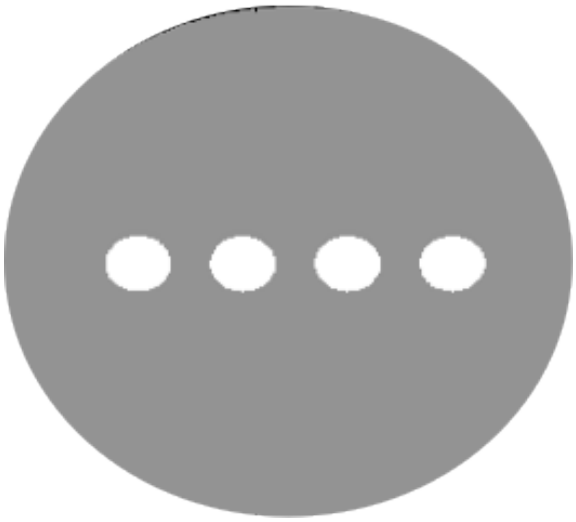

Figure 5.2: A mask with four apertures in a line. Four apertures have the same shape and the space between every two apertures is the same as well.

Section **5.2** presents some useful background information for image intensity technique. It explains the image formation system which is based on 'Fourier Optics' theory. Section **5.3** describes two kinds of image intensity techniques; one is Multiple Image Technique (MIT), whilst the other is Separated Multiple Image Technique

(SMIT). Some further investigations between these two approaches are compared in section **5.4**. It considers different sizes particles, and the comparisons of bi-modal particles distributions are presented in this section as well. Section **5.5** optimises the experimental parameters, including the number of apertures, noise factors and sample concentration. Section **5.6** optimises the laser beam position to form a sharp image. Section **5.7** continues with some improvements of the SMIT method. It combines the SMIT method with Brownian motion information to size particles. It also considers the total intensities of particles from different angles in the SMIT method to improve the simulation results. Finally, section **5.7** is a brief summary of the work carried out in this chapter.

5.2 Image Formation Arrangement and Analysis

5.2.1 Image Formation Equation

According to the "Fourier Optics" approach to imaging (79, 80), the image system employs the ***4-f*** setup as shown in **Figure 5.3**.

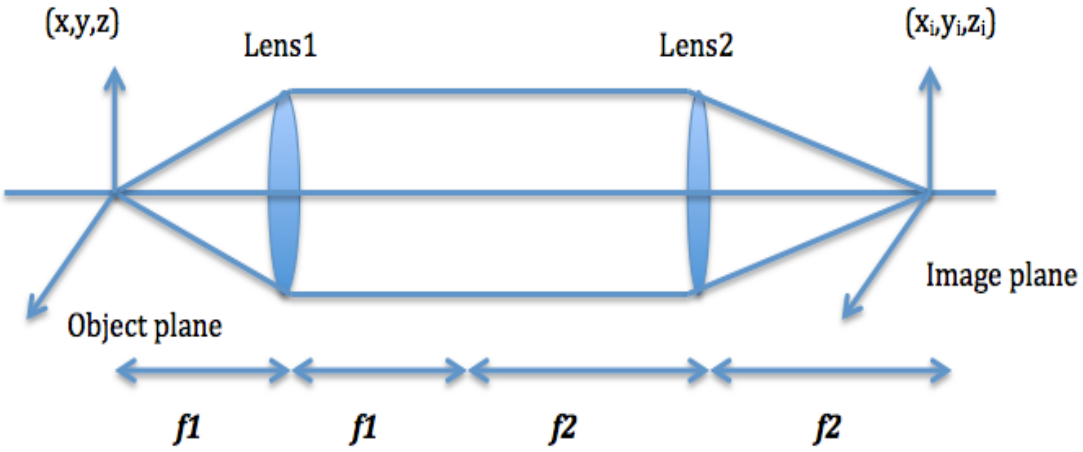

Figure 5.3: A 4-f system setup.

Lens1 performs a Fourier transform of the field distribution on its front to its back focal plane. Lens2 then inverts the field function from frequency domain back to the space domain. As particle positions are very close to the front focal point, the light behind lens1 can be assumed to be parallel. According to (79, 80), the approximate field at the Fourier plane of lens1 for a single particle can be determined by applying equation (5.1) as follows:

$$H(X,Y)=A(X,Y;R_N,n).\exp\left(-j\frac{k}{f_1}(x_0X+y_0Y)\right).\exp\left(-j\frac{kz_0}{f_1^2}(X^2+Y^2)\right).\exp(jkz_0).\exp\left(-\frac{x_0^2}{L_x^2}-\frac{z_0^2}{L_z^2}\right) \quad (5.1)$$

where (x_0,y_0,z_0) is the particle position on the object plane, k is the wave number, and $A(X,Y;R_N,n)$ is the angular dependent field amplitude of the scattered light of the particle size R_N, and n is the particle refractive index. When the laser beam is illuminated along the y axis, L_x and L_z are the laser beam width in the x and z directions.

The first exponential term in the equation represents the Fourier transform field by the object on the front focal plane of lens1, and the second exponential term represents the phase curvature due to the out of plane objects. The third term is the phase differences of the on-axis objects, whilst the last term shows the Gaussian beam effect on the field amplitude. The further detail can be found in (79, 80).

Finally, the complex field on the image plane of the system can be expressed as:

$$U_i(x_i,y_i)=\int_{-\infty}^{+\infty}\int H(X,Y)\phi(X,Y)P(X,Y).\exp\left(-j\frac{k}{f_2}(x_iX+y_iY)\right)dXdY \qquad (5.2)$$

where f_2 is the focal length of lens2, $\phi(X,Y)$ is the phase delay by the wedge prisms, and $P(X,Y)$ represents the mask term which is defined as formula (**5.3**). It allows light at certain angles to go through, and the wedge prisms alter the phases of the light from different apertures of the mask.

$$P(X,Y)=\begin{cases} 0 & if \quad (X,Y)\notin aperture \quad area \\ 1 & if \quad (X,Y)\in aperture \quad area \end{cases} \qquad (5.3)$$

Figure 5.4 compares the image formations from the Fourier Optics with the image formations based on the lens geometrical properties as described in Section **3.3**. The left image is formed according to the geometrical optics properties, whilst the right image is formed according to Fourier Optics. In general, they form two similar images on the same condition with these two methods.

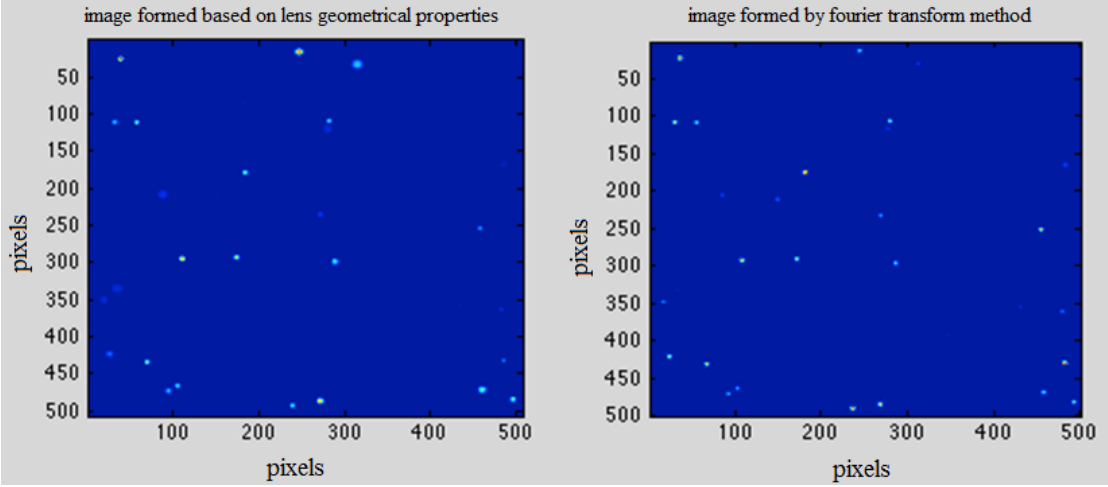

Figure 5.4: Image formations according to two different methods.

5.2.2 Predicted Intensities Data

The basic idea of the angular dependent intensity method is to measure the intensities at different angles and analyse them with the look-up table of the predicted data to find the most suitable particle sizes. The predicted intensities data are derived from the Mishchenko Code described in Chapter ***1*** (38).

Figure 5.5 displays the normalised predicted intensity ratios in four different conditions. (a) shows an example of the normalised predicted intensity ratios from two different angles (80^o and 100^o), whilst (b) shows the results from three different angles (80^o, 90^o and 100^o). (c) and (d) show the different results with four (74^o, 85^o, 95^o and 106^o) and six(75^o, 81^o, 87^o, 93^o, 99^o and 106^o) angles. Note that the range of angles considered here is within the range 70^o to 110^o as this represents a typical range of angles that can be imaged with a long working distance microscope objective.

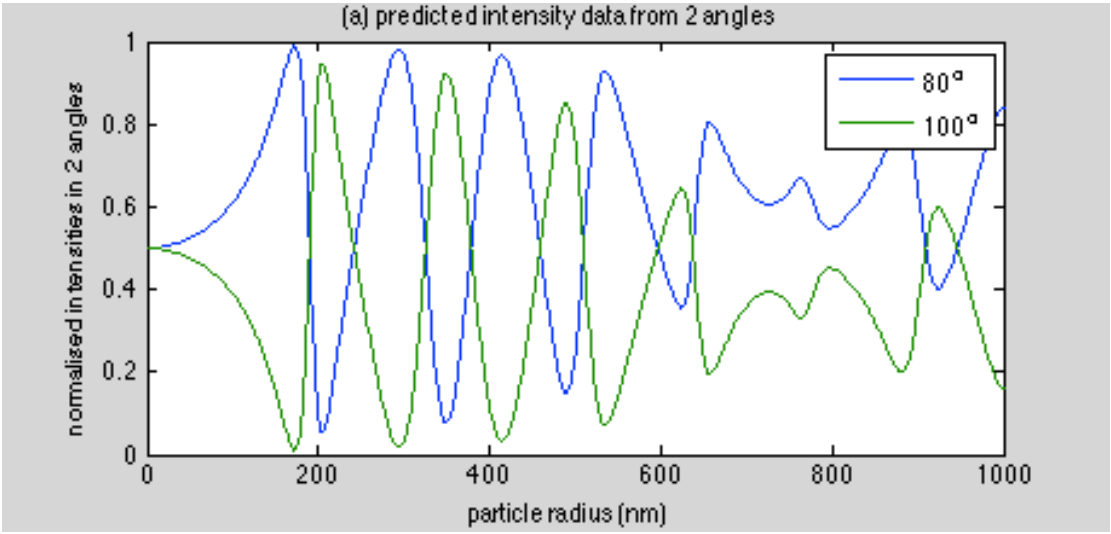
(a) predicted intensity data from 2 angles
normalised intensities in 2 angles
particle radius (nm)
80°
100°
0
0.2
0.4
0.6
0.8
1
0
200
400
600
800
1000

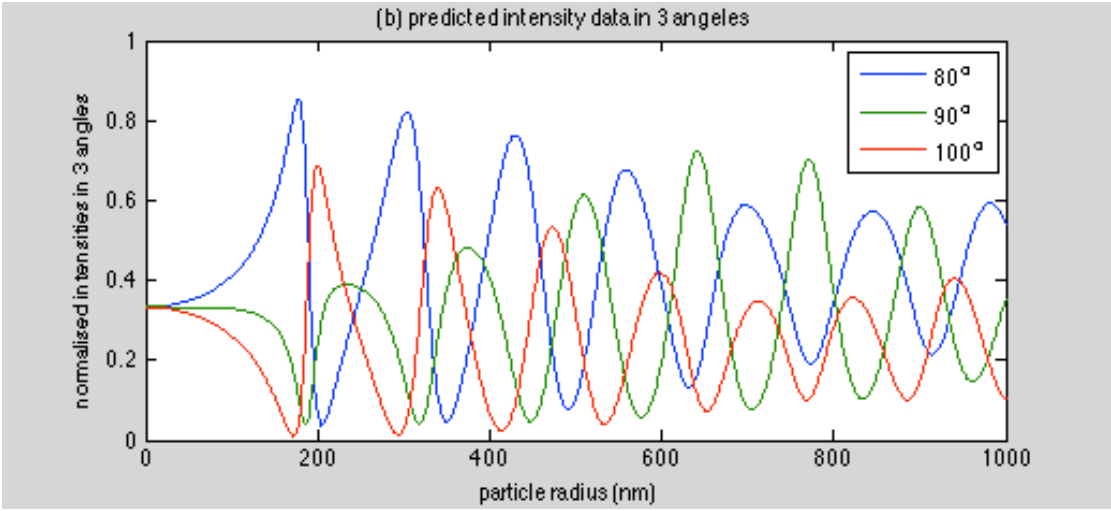
(b) predicted intensity data in 3 angeles
normalised intensities in 3 angles
particle radius (nm)
80°
90°
100°
0
0.2
0.4
0.6
0.8
1
0
200
400
600
800
1000

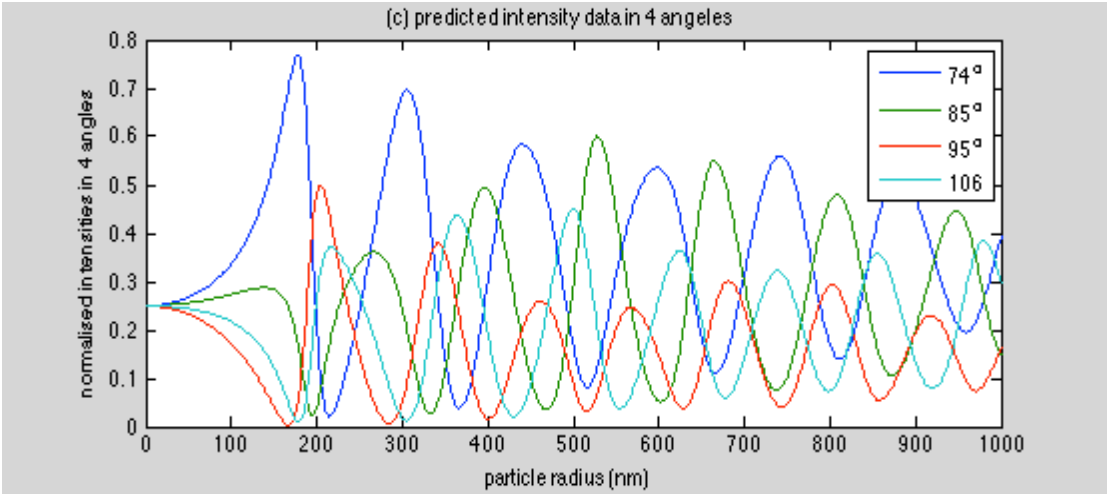
(c) predicted intensity data in 4 angeles
normalised intensities in 4 angles
particle radius (nm)
74°
85°
95°
106
0
0.1
0.2
0.3
0.4
0.5
0.6
0.7
0.8
0
100
200
300
400
500
600
700
800
900
1000

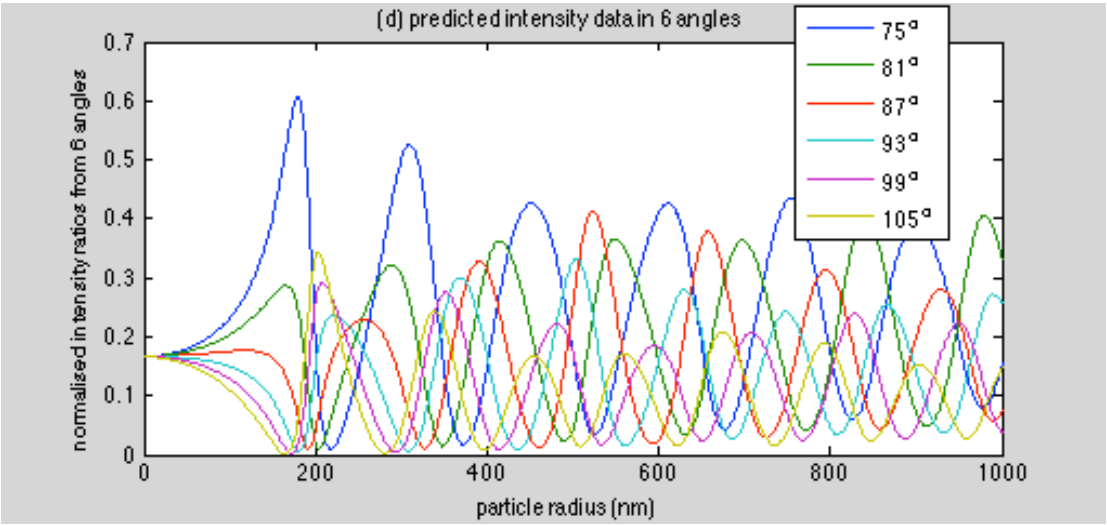

Figure 5.5: The normalised predicted intensities data in different angles. (a) shows an example of the predicted intensity ratios from two different angles (80^o and 100^o); (b) shows the results from three different angles (80^o, 90^o and 100^o); (c) and (d) show the different results with four (74^o, 85^o, 95^o and 106^o) and six(75^o, 81^o, 87^o, 93^o, 99^o and 106^o) angles. Particle radius varies from 1nm to 1000nm.

In **Figure 5.5(a)**, obviously, there are many different particle sizes which have a very similar normalised predicted intensity ratio; for example an intensity ratio of one is obtained for particles of radius around 195nm, 230nm, 350nm etc. Therefore, when comparing the normalised intensity ratio in the simulation or the experiment with the predicted data, it is difficult to give unambiguous accurate results.

Figure 5.5(b) considers three different angles to find the unique normalised intensity ratios, but it still has some ambiguities. For example, when the particle radii are around 280nm or 420nm, they have similar normalised intensity ratios (around 0.65: 0.3: 0.05) from 80^o, 90^o and 100^o. Even for four different angles in **Figure 5.5(c)** when the particle radii are around 160nm or 285nm, they have similar normalised intensity ratios (0.64:0.28:0.07:0.01) from 74^o, 85^o, 95^o, and 106^o. It can be seen that, in general, if more angles are used then the possibility of obtaining a false result will be reduced. However using a larger number of angles (i) adds complexity to the

experimental setup, (ii) reduces the light level of the individual images formed and (iii) increases the area occupied by the sub-images thus making overlap of images more likely. Thus in the following assessments, four apertures were usually employed as a compromise between complexity and image problems and possible ambiguities in determining particle radius.

5.3 Multiple Image Technique (MIT) and Separated Multiple Image Technique (SMIT)

In this section two novel optical arrangements are described to form images suitable for determining the radii of individual particles; these differ from the method implemented by Nam Trung Huynh (81) who used the aberration introduced by the glass/air interface to separate the images from a single particle.

5.3.1 Multiple Image Technique (MIT)

Multiple Image Technique forms an image by the setup in Figure **5.1**. Because aberrations are present in the real experiment, at the cell (water)/glass (air) boundary, it will form some groups of peaks in a straight line if there are no wedge prisms behind the apertures. N. T. Huynh (81) simulated some patterns with diamond shape, but the slightly out of focus particles often appear in distorted patterns, even when using a narrow sheet of light to illuminate the particles. For an out of focus particle, the line group pattern only changes in length whilst the group pattern may be totally different for a diamond pattern. Therefore, detecting line groups is much more convenient.

Nam Trung Huynh (81) made a simple set up for the MIT method which is the same as **Figure 5.1**, but without prisms. He tried to use three small apertures to form an image and compared the normalised intensity ratios with the predicted data. However, the results are poor due to the similar ratios of some different particles. There are many errors in the recovered distribution.

Figure **5.6 (a)** shows simulated results for some line groups of particles with four apertures. Four apertures may improve the simulation results in theory, but the sample concentration should be small to form images with no overlap of the groups of images.

Due to the different illumination power at different focal positions and optics aberrations, these groups appear different. Some of them are bright, whilst some of them are faint and the line group pattern changes in length.

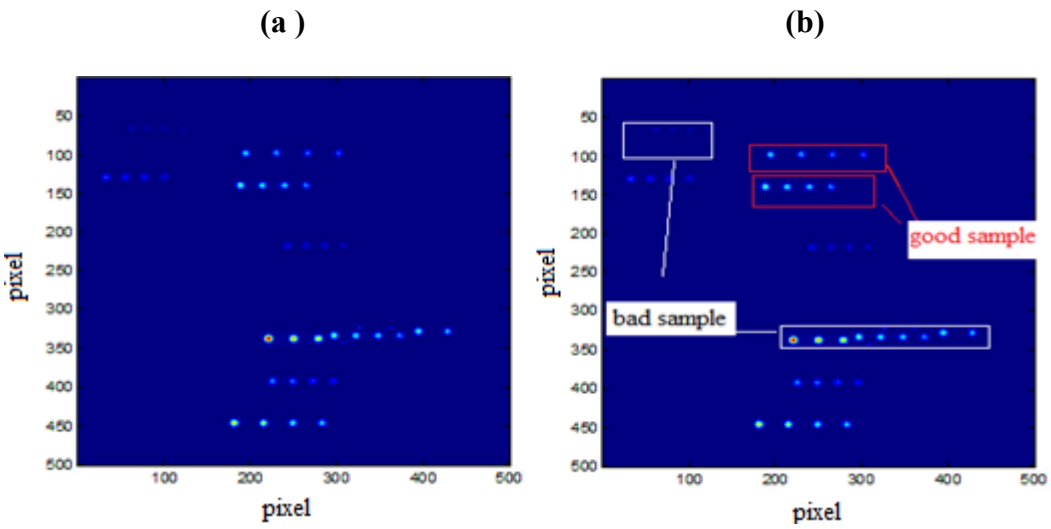

Figure 5.6: Images captured by the MIT method from four different scattering angles.

As may be seen in the images in **Figure 5.6**, some of the line groups have overlapped with those from neighbouring particles or are very faint. These groups could give

false results so it is necessary to set a criterion to find the good groups and bad groups. A good group of peaks is considered to have the following properties:

(1) The group of peaks from a single particle should not be too far from each other (eg: the displacement between every two consecutive peaks should be smaller than 50 pixels);

(2) The group of peaks should not be too faint to detect (based on the background level and quantisation level, a threshold is set to eliminate faint groups. For the results presented here, the threshold is set at 10% of the difference between the maximum measurable level and the background level);

(3) The group of peaks from a single particle should not overlap with those from other particles (if it finds more than four peaks in a line group pattern, such as the lower bad sample in **Figure 5.6 (b)**, this line group pattern will be eliminated as overlapping groups).

Thus, the good groups will be recorded whilst the bad groups will be eliminated. In the simulations described here and in the experimental work this process was automatically applied in software. Figure **5.6 (b)** gives some examples of the bad groups and good groups. The faint group and the overlapping groups are recorded as bad groups. Consequently, the data processing algorithm compares the intensities of good samples with the predicted intensities data to find the best matching sizes.

To test the effectiveness of this angular intensity approach to individual particle sizing, computer simulations were carried out. The simulation parameters are listed in **Table 5.1**. A set of 100 independent frames is recorded to recover a particle size distribution.

Particle radius/ standard deviation	100nm/15nm
Number of frames	100
Image size/pixel size	500 x 500/0.9microns
Exposure time	0.1s
Particle concentration	1 x 10^6 /ml
Poisson noise factor	4000
Background /Quantisation noise	No
Magnification	1

Table 5.1: Simulation parameters used in the simulation.

In previous chapters, three criteria evaluations have been utilised to examine the accuracy of the recovered particle size distribution. However, sometimes it is difficult to show the accuracy of the recovered distributions from the MIT method with these three criteria. In the MIT method, because it compares the normalised intensity ratios with the predicted data, just as shown in **Figure 5.5**, sometimes, different particle sizes may have similar normalised intensity ratios, and therefore some ambiguities and some small number of falsely recovered large radius particles could significantly enlarge both the mean values and the standard deviations.

The area error criterion is also not suitable for the MIT method. This criterion was suitable for a method such as PMDD which produces a smooth highly-sampled distribution. The MIT method however produces individual particle sizes, which are then combined into a histogram to give an estimate of the particle size distribution. It

is found that the area error value depends on the histogram bin sizes, so is not suitable for the present method.

Another criterion is employed for the image intensity technique. For an original mean radius of the distribution of X, and a standard deviation of y, if the total number of the particle radii measured by the MIT method is A, then it can approximately calculate the fraction of particles around the original distribution by equation (5.4):

$$P = \frac{B}{A} \tag{5.4}$$

where *B* is the number of the measured particle radii between ***(X-2y)*** and ***(X+2y)***.

Based on some simulation code, the P value can be calculated automatically.

Figure 5.7 shows a reconstructed particle size distribution by the MIT method based on 100 random frames.

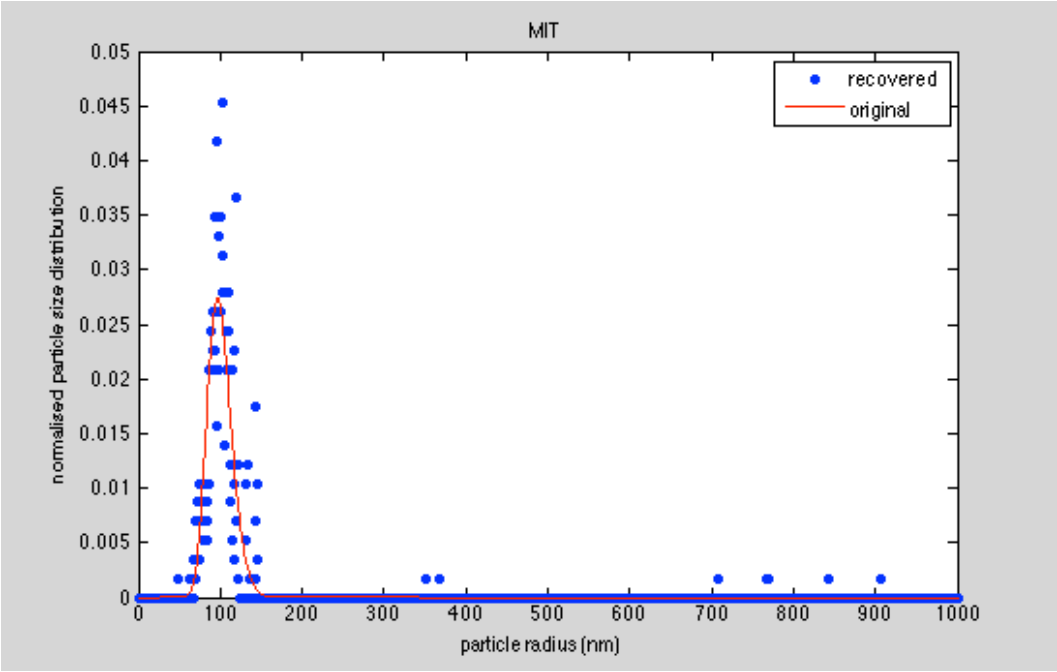

Figure 5.7: The particle size distribution reconstructed by the MIT method. The mean radius is 100nm and the standard deviation is 15nm. The recovered mean radius is 109.59nm with 73.98nm standard deviation, and the area error is 0.46. 91% particles are between 70nm and 130nm.

Inspection of **Figure 5.7** illustrates that a majority of the measured particle radii are around 100nm. A small number of false results appear at around 350nm and 700nm to 900nm. These are due to the ambiguity problem discussed in section 5.2.2. If some prior knowledge about the particle sizes was available then the range of the lookup table could be restricted to avoid some of these ambiguities. Two methods to attempt to include some form of prior knowledge are investigated in sections 5.7

Around 91% of the measured radii are in the range of 70nm to 130nm. However, it may be seen that there are errors in the peak of the recovered distribution around 100nm. The look up table used was sampled with a resolution of 1nm. So these errors are not due to under sampling of the look up table but rather due to the Poisson noise in the images and hence in the measured intensity ratios.

In general, the MIT method recovers a good particle size distribution. Further investigations on the MIT method, to compare its performance with the SMIT method will be described in the following section **5.4**.

As outlined above (in the discussion after **Figure 5.6**) there are problems with the MIT method having bad groups of peaks. One of the difficulties that can arise is if a group of three peaks is detected (from a four aperture experiment) then there will be an ambiguity as to which peaks arises from which aperture. In the next section an alternative optical arrangement is investigated with the potential to overcome this difficulty.

5.3.2 Separated Multiple Image Technique (SMIT)

Compared with the MIT method, there are some differences on the image formation system of the SMIT method. Figure **5.8** displays the image formation system of the SMIT method. A field aperture is inserted between the first and second lenses to keep the field of view small and avoid images overlapping on the CCD. A mask with four apertures and wedge prisms are applied behind lens2. The wedge prisms tilt the scattering light into different positions. The key difference between this SMIT arrangement and the MIT method is that in MIT one particle generates a closely spaced set of peaks within a single image. In SMIT four separate images are produced and each particle contributes a peak to each of these images (such an image is shown below in **Figure 5.10**).

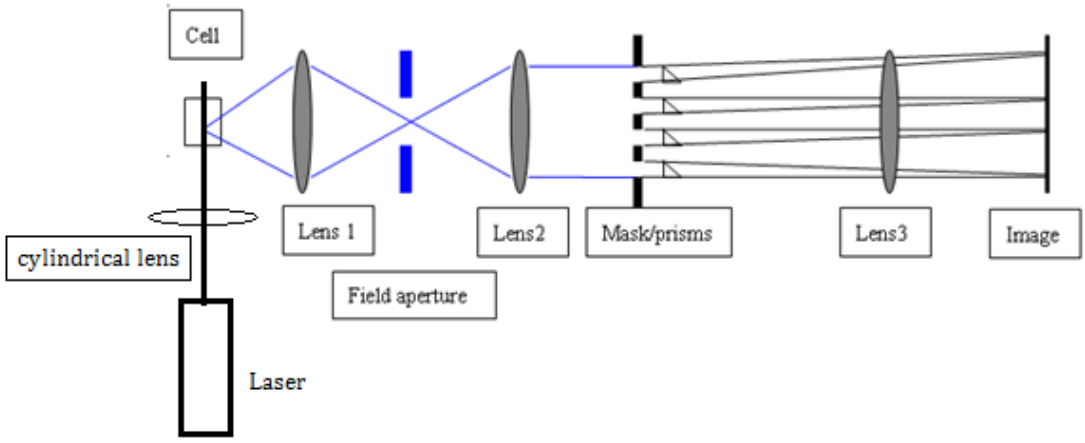

Figure 5.8: Image formation system of the SMIT method.

If there is a particle perfectly on focus, assuming the image plane is made up of four quarters (Figure **5.9**), the particle image from one aperture should be in the same position in each quarter image by the tilting of the wedge prism.

Figure 5.9: Four quarters of the image plane.

In other words, every quarter image plane forms an image of the particles in the field of view through one of the apertures.

Figure **5.10** shows an example of a simulated image captured by the SMIT method.

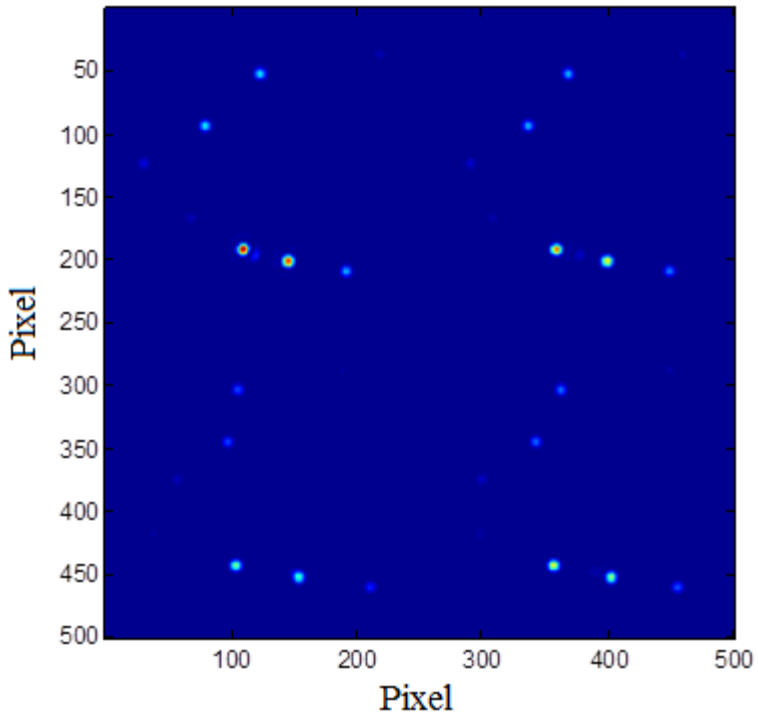

Figure 5.10: An example image captured by the SMIT method from four different scattering angles.

It is composed of four quarter-images. This four-quarter-image is formed through the apertures and wedge prisms at some different angles. These four quarter images

appear very similar, but the intensities of the peaks are different depending on the different scattering angles. If these four quarter images are superposed into one image, the centres of the perfectly on-focus particles will be exactly overlapped in the same position, but the centres of the out of focus particles shift a bit, and appear as a line pattern.

The simulation to compute the form of image produced by the SMIT optical arrangement is very similar to that used for the MIT method which was outlined in section 5.2.1, the only differences are (i) that the field aperture is simulated by excluding those particles that generate images outside the aperture from the image, and (ii) that the phase functions applied to simulate the effect of the wedge prisms are increased in magnitude so as to separate the 4 images into different regions of the detector plane.

The SMIT method also uses the same theory as the MIT method to look up for the best match size distribution, but the criteria are simpler. The SMIT method does not need to consider the first and second restrictions of the criteria used in the MIT method. Because the illuminations from different angles are formed in separate images, if the bright peaks positions in one quarter-image have been examined, the peaks positions in other quarter-images can be deduced, even for the very faint peaks from some particular sizes at particular angles.

The general idea of the SMIT method is also similar to the MIT method. Compare the intensities in the image with the theoretical data to find best matches sizes by the best-fit function in (**5.5**):

$$f(r)=\sqrt{\sum_{i}^{4}\left(I_i - I_i^{theory}(r)\right)^2} \tag{5.5}$$

where $\boldsymbol{I_i}$, I_i^{theory} are the normalised detected intensities and the predicted data from Mishchenko code respectively. The best-fit size r_0 is where the minimum value of function ***f(r)*** occurs.

Figure **5.11** represents four different best-fit functions of four different particles with nominal radius of 100nm. The minimum value of function ***f(r)*** occurs around 100nm in each diagram. Therefore, the minimum value in each diagram is selected to be the best match particle size.

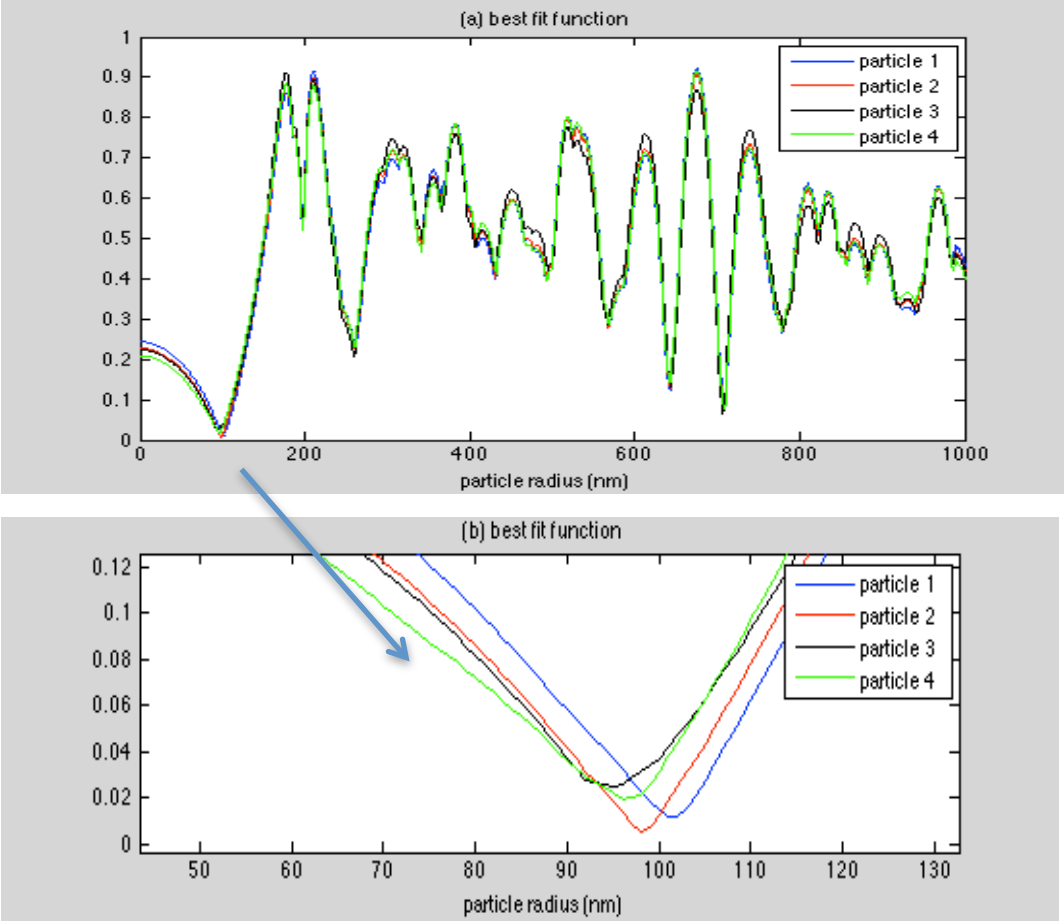

Figure 5.11: (a) Four different best-fit functions according to four different particles with nominal radius of 100nm. (b) Enlarged image of (a).

The simulation parameters used in the SMIT method (**Table 5.2**) are similar to the parameters in **Table 5.1** except for the sample concentration. The particle concentration in **Table 5.2** is four times larger than that in **Table 5.1** to keep the number of particles in the image nearly the same.

Particle size distribution: mean/ standard deviation	100nm/15nm
Number of frames	100
Particle concentration	4×10^6 /ml
Poisson noise factor	4000
Background /Quantisation noise	No/No

Table 5.2: Simulation parameters in the SMIT method.

Figure 5.12 displays an example of the reconstructed particle size distribution by the SMIT method.

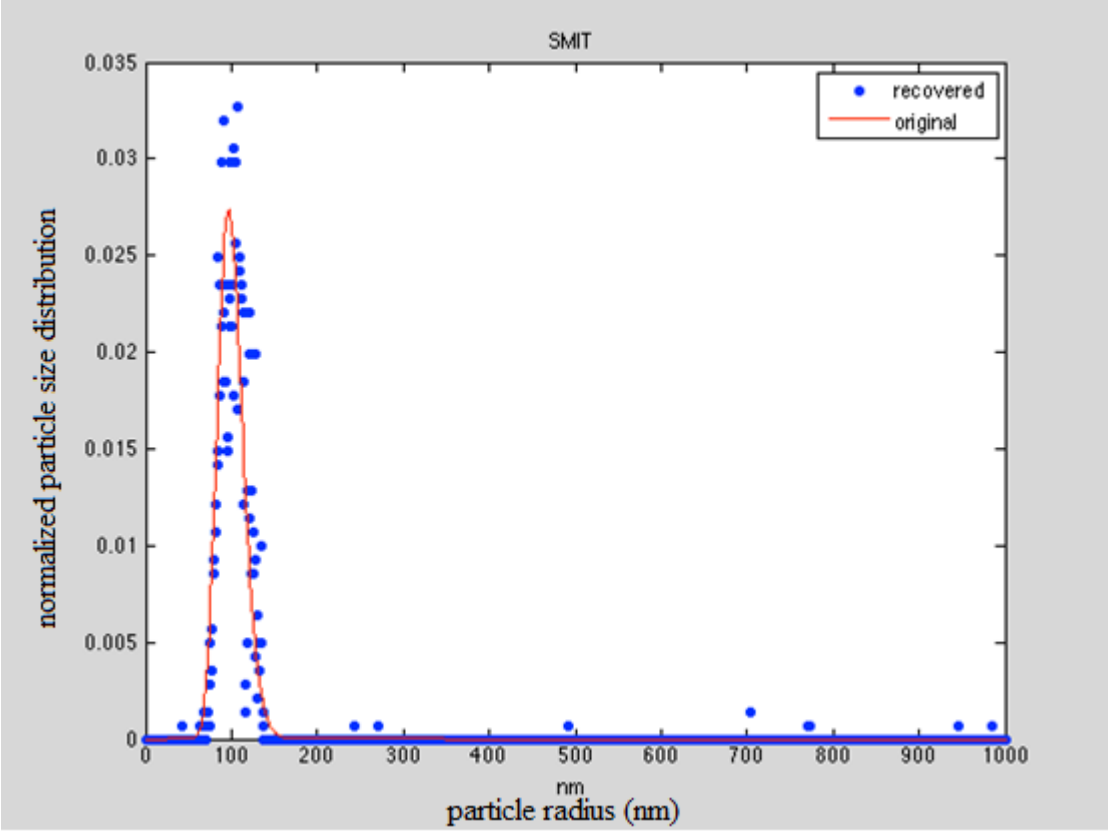

Figure 5.12: Recovered particle size distribution by the SMIT method. The mean radius is 100nm and the standard deviation is 15nm. The recovered mean radius is 106.77nm with 55.22nm standard deviation, and the area error is 0.36. There are 96% particles in the range of 70nm to 130nm.

The recovered distribution in **Figure 5.12** is acceptable, because a majority of particle sizes are around 100nm which is quite similar to the recovered distribution from the MIT method. Compared with the MIT method, there are more particles in the range of 70nm to 130nm, and the area error is smaller.

5.4 Comparisons between the MIT Method and the SMIT Method

In Section **5.3**, the basic ideas of the MIT and the SMIT method have been discussed. Both of these two approaches can reconstruct particle size distributions and the recovered results seem acceptable and reasonable when the particle mean radius is 100nm with 15nm standard deviation. Some more particle sizes distributions recovered from these two methods are compared in section **5.4.1**. Section **5.4.2** simulates bi-modal particle sizes distributions.

5.4.1 Different Particle Size Samples

Some other sizes of particles are examined in this section to verify whether these two approaches still work well. The simulation conditions keep the same as those in **Table 5.1** and **5.2**. It still records 100 independent frames for both methods. **Figure 5.13 - 5.17** compare the reconstructed particle size distributions by the MIT method and the SMIT method with five different sizes. The mean radii of the particles are 100nm, 200nm, 300nm, 400nm and 500nm respectively. The standard deviation is 15nm for all distributions. **Table 5.3** compares the area errors, mean radii, standard deviations and ***P*** in eq. (**5.4**).

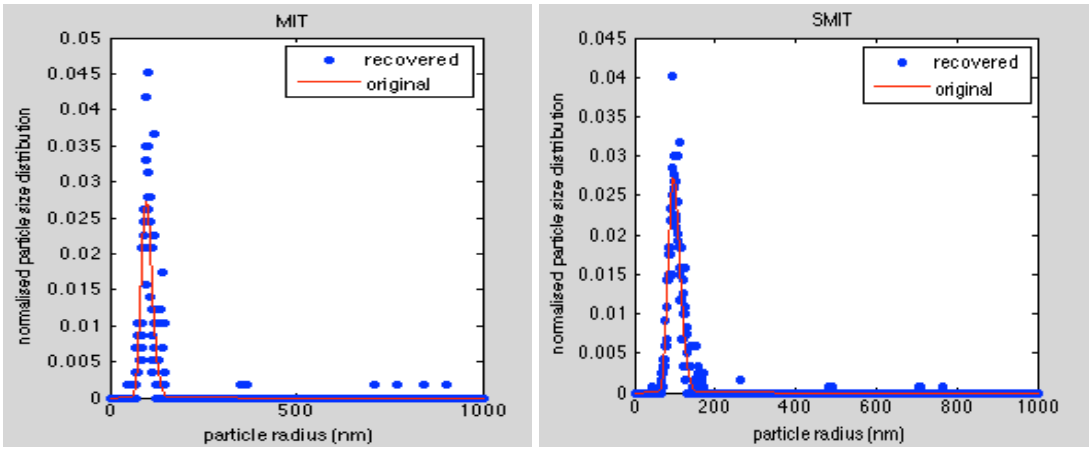

Figure 5.13: The reconstructed particle size distributions by the MIT method (left) and the SMIT method (right). The original particle radius is 100nm with 15nm standard deviation.

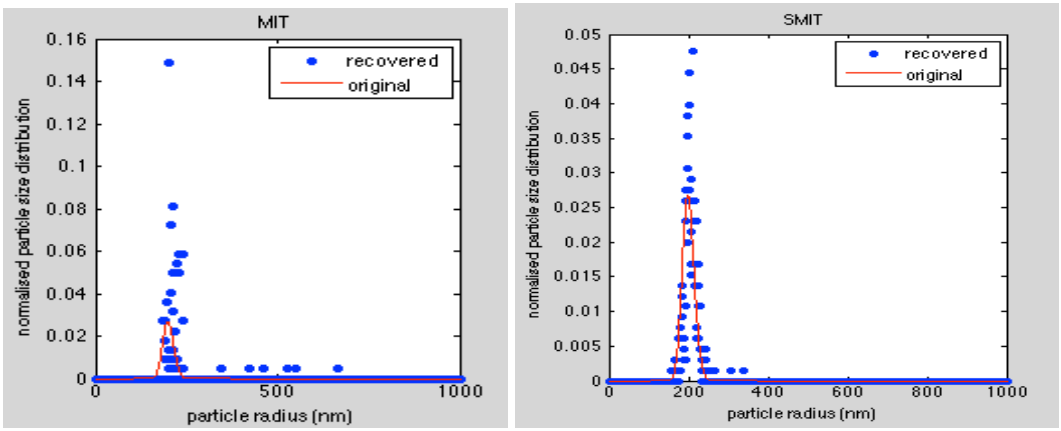

Figure 5.14: The reconstructed particle size distributions by the MIT method (left) and the SMIT method (right). The original particle radius is 200nm with 15nm standard deviation.

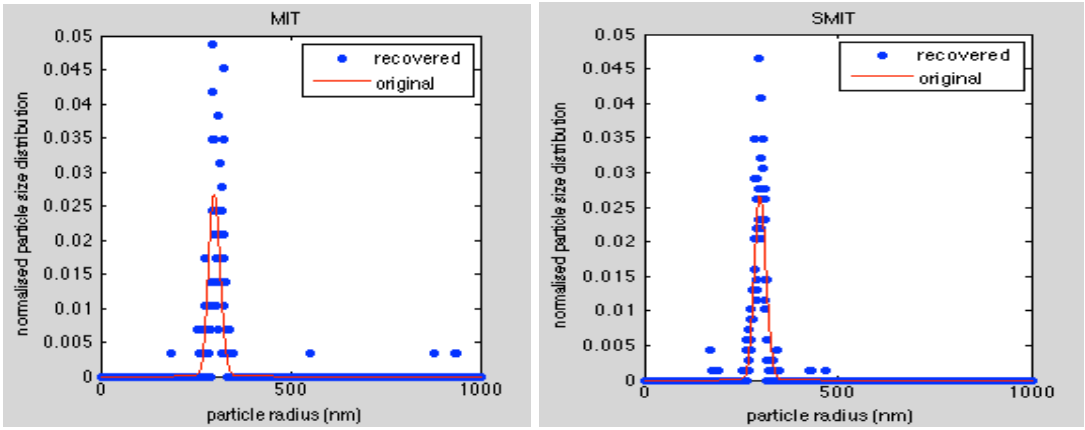

Figure 5.15: The reconstructed particle size distributions by the MIT method (left) and the SMIT method (right). The original particle radius is 300nm with 15nm standard deviation.

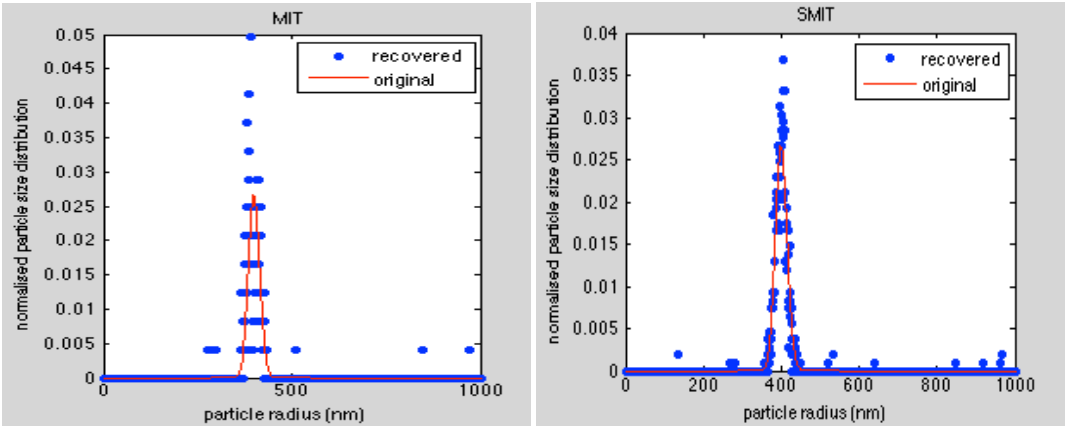

Figure 5.16: The reconstructed particle size distributions by the MIT method (left) and the SMIT method (right). The original particle radius is 400nm with 15nm standard deviation.

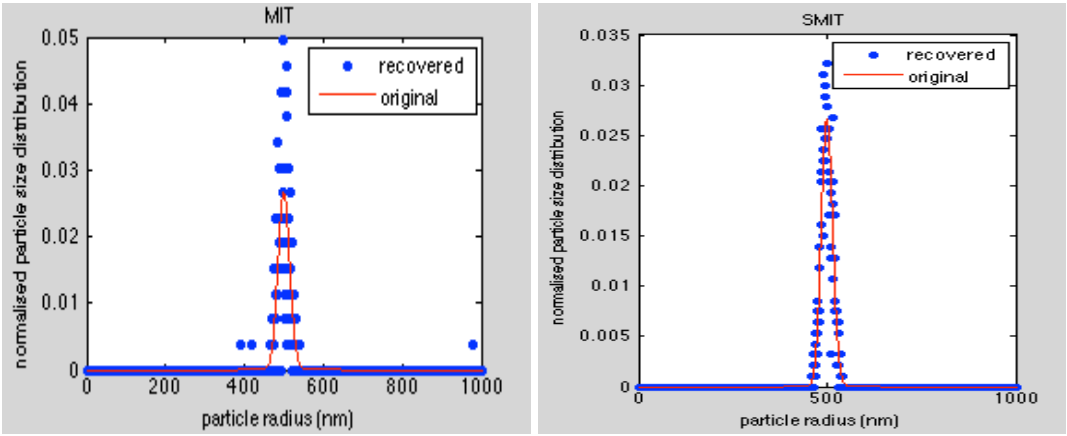

Figure 5.17: The reconstructed particle size distributions by the MIT method (left) and the SMIT method (right). The original particle radius is 500nm with 15nm standard deviation.

	Area error		Mean radius		Standard deviation		P (eq.(5.4))	
	MIT	SMIT	MIT	SMIT	MIT	SMIT	MIT	SMIT
100nm	0.46	0.36	109.59	106.77	73.98	55.22	0.91	0.96
200nm	1.2	0.45	220.44	206.15	51.43	15.88	0.87	0.95
300nm	0.68	0.39	314.54	296.99	75.59	21.38	0.92	0.95
400nm	0.53	0.29	400.26	407.70	51.18	52.27	0.94	0.95
500nm	0.52	0.24	500.02	499.12	33.94	14.77	0.95	0.96

Table 5.3: Area error, mean radius, standard deviation and ***P*** value in eq. (5.4).

Theoretically, both of these angular dependent intensity methods can reconstruct particle size distributions. A majority of particles are around the original distributions in both methods. According to **Table 5.3** and the figures above, the SMIT method performs better results than the MIT method in the same conditions. The area errors from SMIT are much smaller than those from the MIT method. It indicates that the recovered distribution from SMIT matches the original distribution better. In addition, the numbers of particles in every random frame for both methods are almost the same, but SMIT records many more particles than MIT. For instance, SMIT recorded 834 particles positions in 100 random frames when particle mean radius is 300nm, but MIT only tracked 226 particles. Because there are many limitations of the MIT method when looking for the good groups, some bad samples have been eliminated. Therefore, the recovered distribution by the SMIT method is more convincing than the MIT method in the same condition.

There are four spots in a group from the MIT method. In some situation, if some spots from one or two directions are too weak to detect, it encounters some troubles. It is difficult to know where the weak spots are, in front of the bright spots or after or in the middle (see **Figure 5.18**). **Figure 5.18** illustrates these error cases. Red dots represent the bright spots position on the image and black dots represent the very weak spots. For example, if three bright peaks in a group were detected in the image, it is difficult to decide where the fourth peak is. In addition, the particles in line patterns superpose each other much easier than the particles in separate image in the SMIT method. In these two situations, these groups should be recorded as bad samples and be eliminated. It explains why there are only a few particles reconstructed from the MIT method. In contrast, SMIT does not encounter this trouble. The positions of some weak peaks in certain direction can be deduced from

the other spots in other directions and then the intensities of the weak peaks can be estimated from the image.

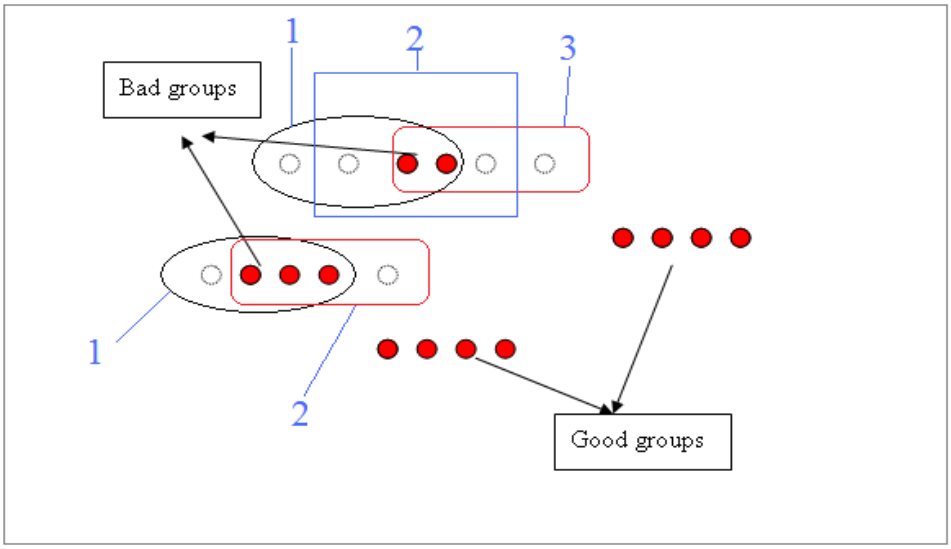

Figure 5.18: Confusions made by the MIT method. 1, 2 and 3 represent the confusion cases it may happen in the image plane.

It may be seen in **Figures 5.13** to **5.17** that one of the problems in both the MIT and SMIT method is the presence of false peaks in the recovered size distributions. One reason for these occurring has already been discussed in section 5.22 i.e. the ambiguity effect where two sizes of particles have very similar sets of intensity ratios. This can cause the look-up table data inversion procedure to fail occasionally. Another possible cause of these false peaks could be that two or more particles (of different sizes) are very close together in the sample and as a result contribute light to a single intensity peak in the image. This will lead to a false set of intensity ratios which the look-up table recovery procedure will interpret as a false radius. Inspection of the positions of the false radius peaks in the distributions in **Figures 5.13** to **5.17** indicates that it is the former issue which is responsible for the majority of the false results.

5.4.2 Bi-modal Particle Size Distributions Reconstructed by MIT and SMIT

In this section, the image intensity techniques (MIT and SMIT) are applied to some bi-modal particle size distributions. The simulation parameters keep the same as those in **Table 5.1** and **Table 5.2** for each method. The Poisson noise factor is 4000 and the background noise and quantisation noise are ignored. The original and reconstructed distributions for every sample are shown in the following figures.

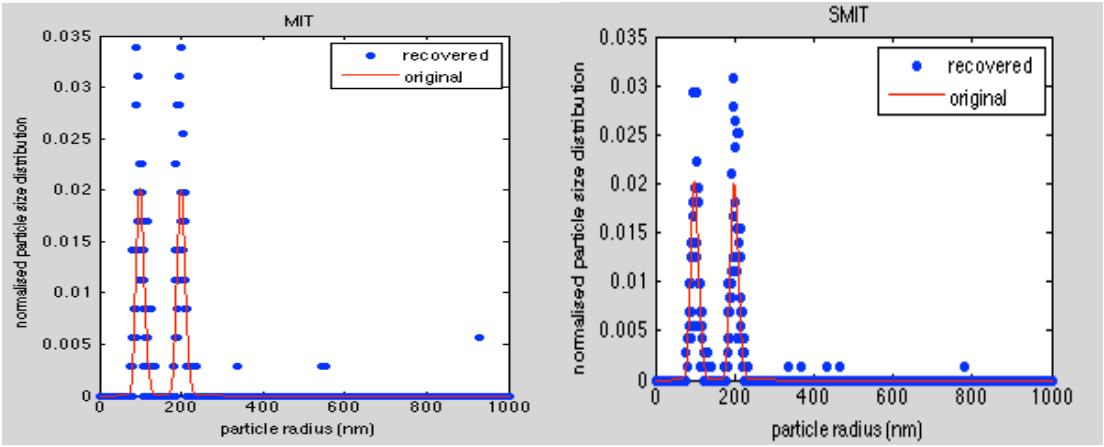

Figure 5.19: Original and reconstructed distributions for sample: 50% mean1=100nm, standard deviation1=10nm; 50% mean2=200nm, standard deviation=10nm. **P**(100nm)=47%, **P**(200nm)= 48% with the MIT method. **P**(100nm)=46%, P(200nm)=50% with the SMIT method.

Both MIT and SMIT succeed in measuring the mixture particle size distributions when 50% particles are 100nm and 50% particles are 200nm. The recovered distribution ratios are similar to the original ratios with both methods.

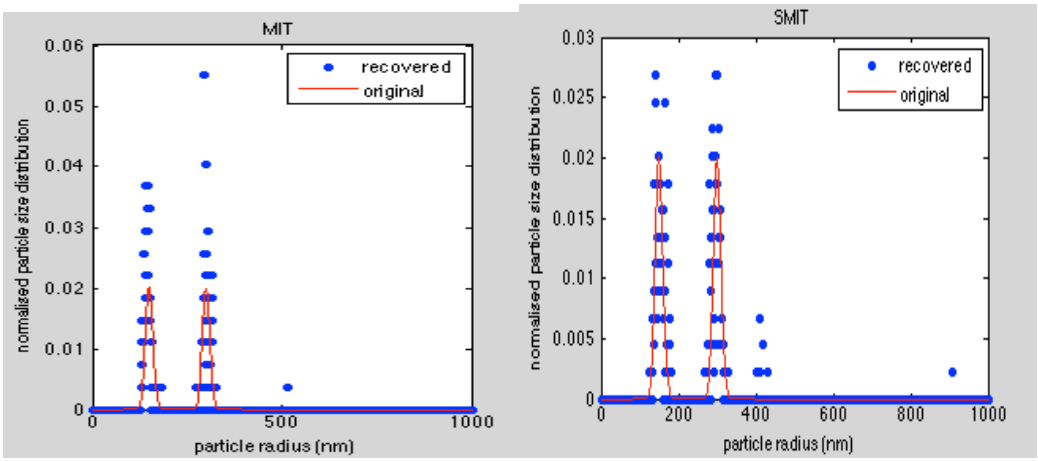

Figure 5.20: Original and reconstructed distributions for sample: 50% mean1=150nm, standard deviation1=10nm; 50% mean2=300nm, standard deviation=10nm. **P**(150nm)=51%, **P**(300nm)= 46% with the MIT method. **P**(150nm)=42%, P(300nm)=52% with the SMIT method.

Similarly, a simulation result in **Figure 5.20** shows that MIT and SMIT are able to evaluate bi-modal distributions. More particles are recovered around 150nm with the MIT method, since the illuminations from some particular angle are very weak to detect when the particles are around 300nm. For the SMIT method, since 300nm particles scatter more light than 150nm particles, their probability of detection is also higher. The recovered distribution ratio is acceptable.

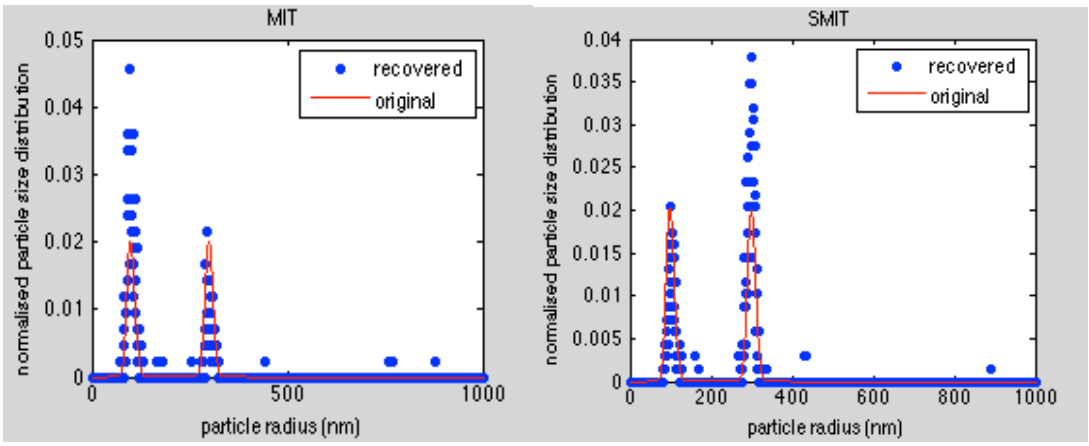

Figure 5.21: Original and reconstructed distributions for sample: 50% mean1=100nm, standard deviation1=10nm; 50% mean2=300nm, standard deviation=10nm. **P**(100nm)=70%, **P**(300nm)= 25% with the MIT method. **P**(150nm)=30%, P(300nm)=67% with the SMIT method.

Figure 5.21 shows another example of bi-modal distributions. Although both of the image intensity techniques can examine the bi-modal distributions, they fail in giving the distribution ratio correctly. Due to the limitations when looking up for good groups, a higher number of 100nm particles is observed from MIT. Because large particles scatter more light than small ones, a high ratio of 300nm particles is recovered from SMIT.

Another two narrow bi-modal simulations are examined in **Figure 5.22** and **5.23**.

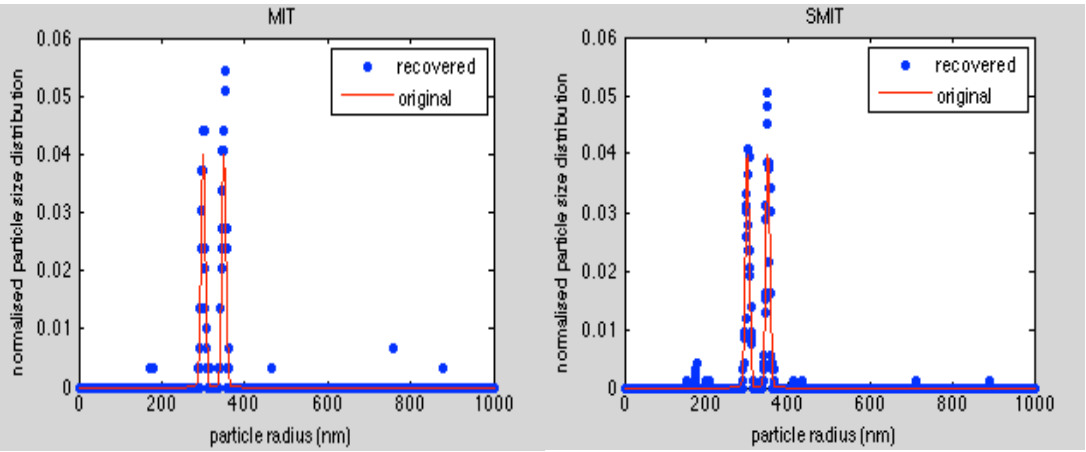

Figure 5.22: Original and reconstructed distributions for sample: 50% mean1=300nm, standard deviation1=5nm; 50% mean2=350nm, standard deviation=5nm. **P**(300nm)=41%, **P**(350nm)= 54% with the MIT method. **P**(300nm)=43%, P(350nm)=51% with the SMIT method.

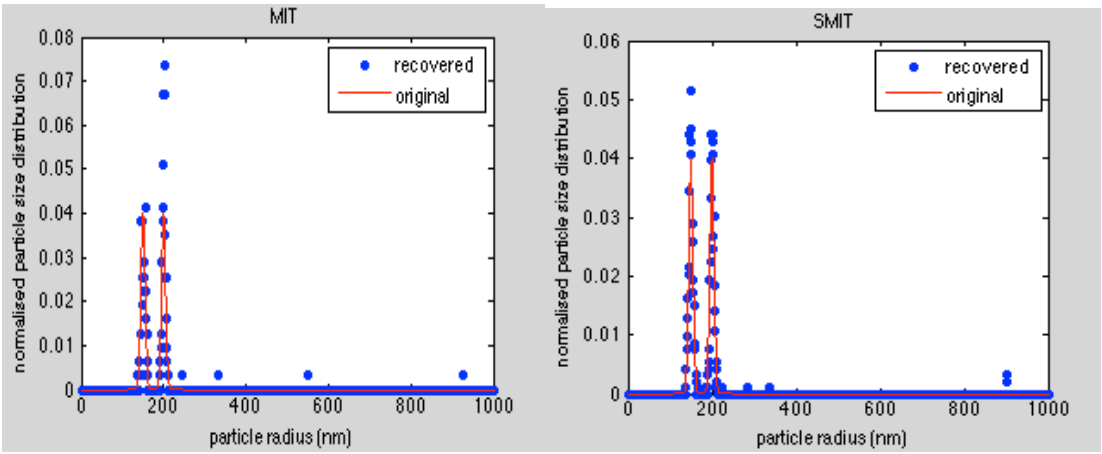

Figure 5.23: Original and reconstructed distributions for sample: 50% mean1=150nm, standard deviation1=5nm; 50% mean2=200nm, standard deviation=5nm. **P**(100nm)=38%, **P**(300nm)= 58% with the MIT method. **P**(150nm)=51%, P(300nm)=44% with the SMIT method.

Both MIT and SMIT are able to distinguish close bi-modal distributions. SMIT reconstructs a better distribution ratio than the MIT method.

In general, the MIT method is restricted by the limitations when looking up for good groups of samples both for single distribution and for bi-modal distributions. Some faint illuminations from some particular angles result in the wrong distribution ratio by the MIT method. For single size distribution, compared with the MIT method, the SMIT method obtains a more convincing result in the same situation. For the bi-modal size distributions, the recovered result from a close bi-modal distribution is acceptable with the SMIT method. If one size is much larger than the others, the large particles will dominate the distribution.

5.5 Optimising Experimental Parameters in the SMIT Method

5.5.1 Simulations Results by Six Apertures

Particles scatter light in every direction. Theoretically, the more illuminations from different angles are examined, the more accurate the result is. Occasionally, the normalised intensity ratios in some directions are very similar but the particle sizes are different. According to **Figure 5.5**, if there are two or three apertures, there are many different size particles examined with the similar intensity ratio. Thus, this section compares the simulation results with four and six apertures. **Figure 5.24** shows some ambiguities. It gives an example that when the particles are around 160nm and 280nm, the normalised intensity ratios from four angles (74^{o}, 85^{o}, 95^{o}, and 106^{o}) are very similar. Therefore, it will bring in some errors (wrong particle sizes) to recover particle sizes.

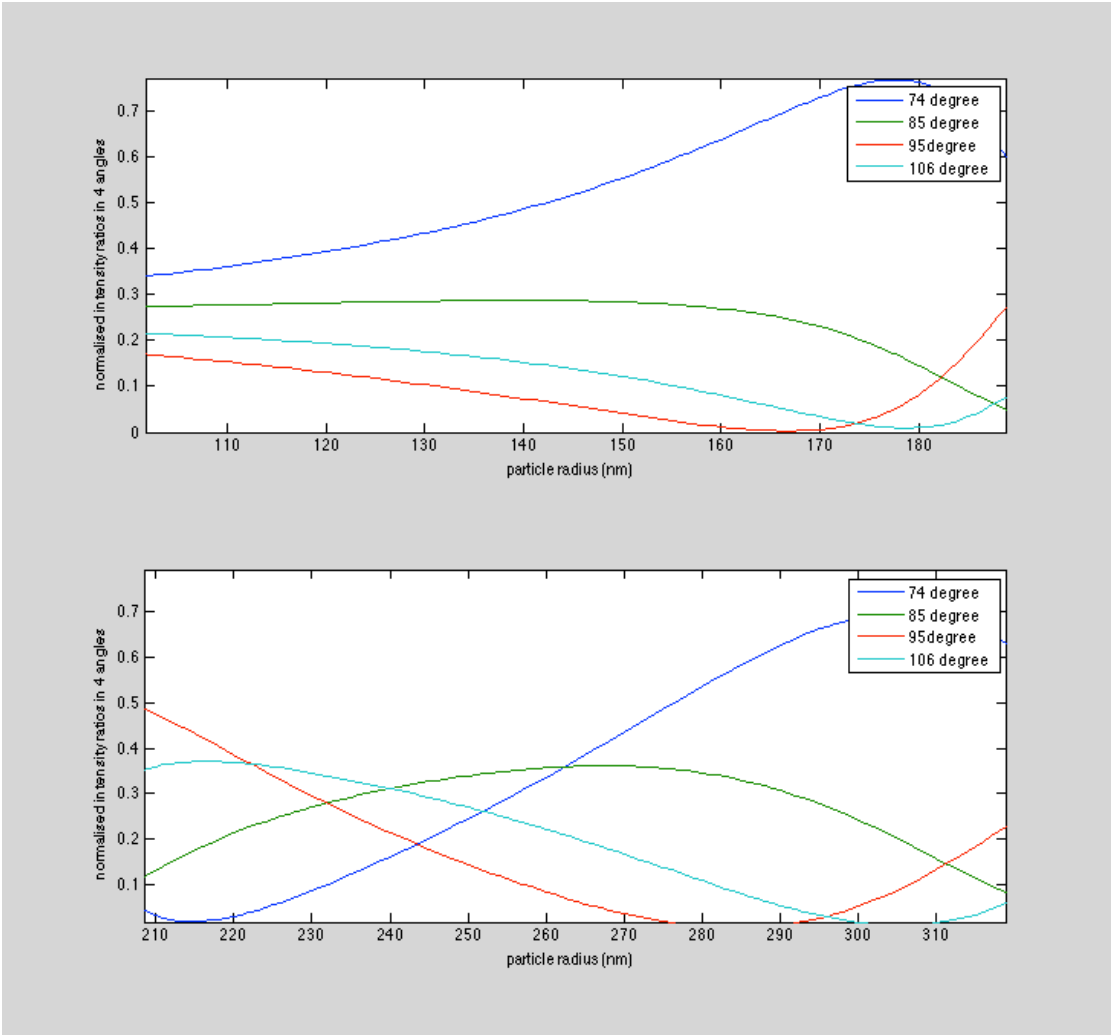

Figure 5.24: The normalised intensity ratios from four different angles with different particle sizes.

A six apertures mask is introduced in this section to minimise the ambiguities. According to Mishchenko code, a normalised predicted intensity data from six different angles is illustrated in **Figure 5.25**.

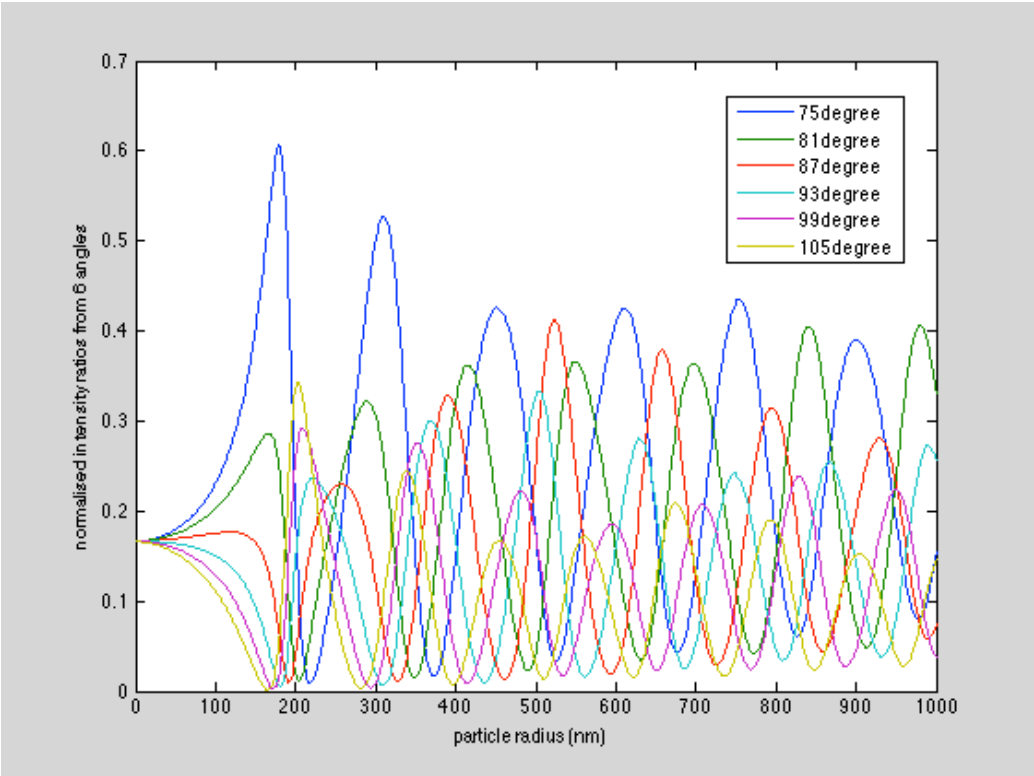

Figure 5.25: The normalised predicted intensity ratios from six different scattering angles (75^{o}, 81^{o}, 87^{o}, 93^{o}, 99^{o}, and 105^{o}). Particle sizes change from 1nm to 1000nm.

Figure 5.26, **5.27** and **5.28** compare the recovered distributions from four apertures in a mask and six apertures in a mask respectively with different particle sizes, 100nm, 200nm and 300nm respectively.

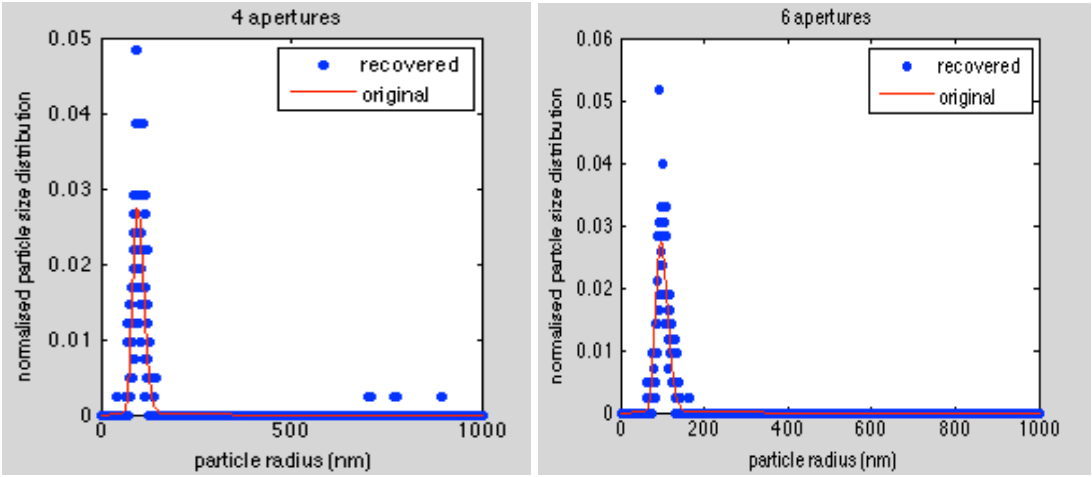

Figure 5.26: The recovered particle size distributions with four and six apertures in a mask. The original mean radius is 100nm, and the standard deviation is 15nm.

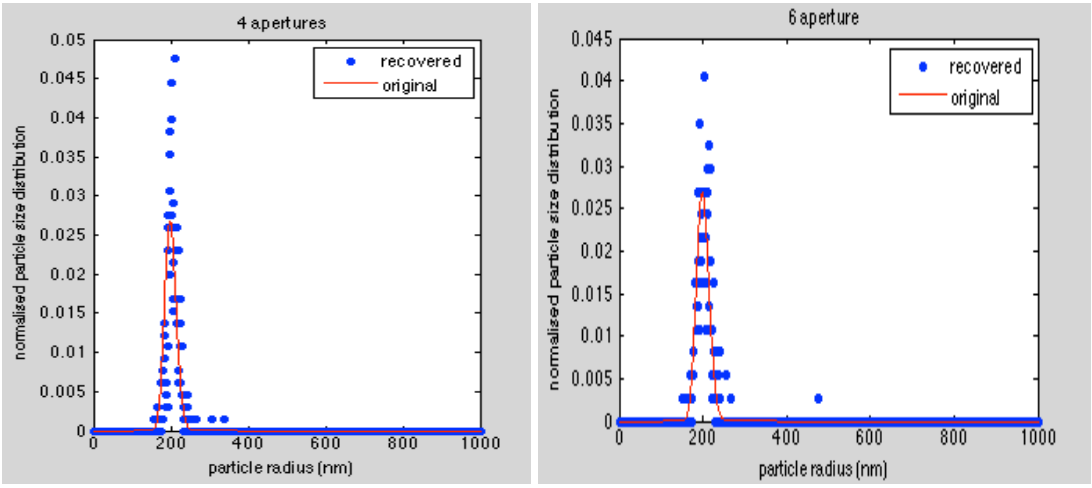

Figure 5.27: The recovered particle size distributions with four and six apertures in a mask. The original mean radius is 200nm, and the standard deviation is 15nm.

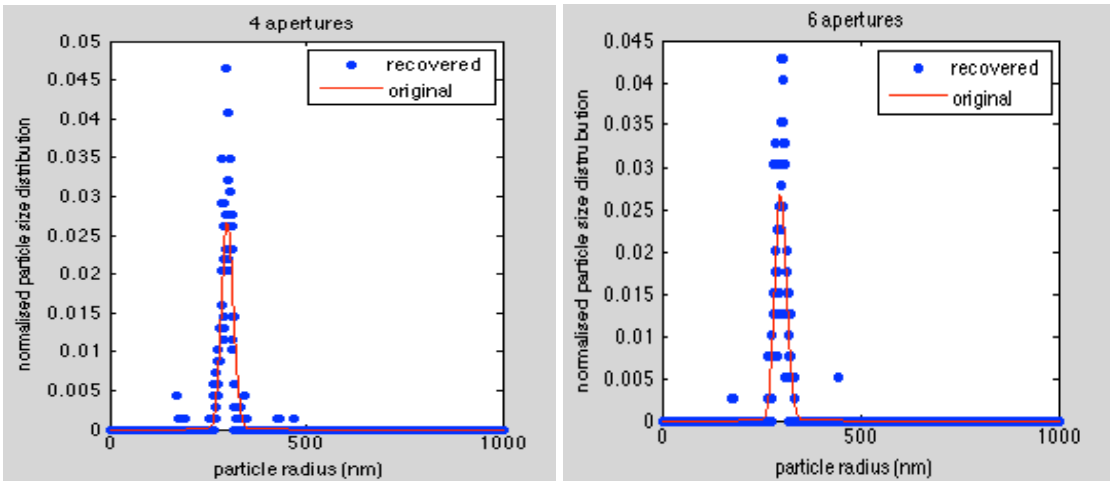

Figure 5.28: The recovered particle size distributions with four and six apertures in a mask. The original mean radius is 300nm, and the standard deviation is 15nm.

Table 5.4 compares the criteria evaluations in these two conditions.

	Area error		Mean radius (nm)		SD		P (eq.(5.4))	
	4	6	4	6	4	6	4	6
100nm	0.36	0.38	106.77	102.54	55.22	14.80	0.96	0.96
200nm	0.45	0.38	206.15	203.31	15.88	21.59	0.95	0.93
300nm	0.39	0.34	296.99	299.52	21.38	18.80	0.95	0.96

Table 5.4: Comparisons of the criteria evaluations with four and six apertures in a mask.

The recovered size distributions with six apertures are only slightly better than those with four apertures. Actually, in a real experiment, the more apertures in a mask, the smaller the aperture, the more complicated the experimental setup. Four apertures in a mask are easier than six apertures to realise in real experiment, and the results with four apertures are acceptable. Therefore, four apertures in a mask are employed in the experiment.

5.5.2 Simulation Results with Different Poisson Noise Factors

A discussion on detection program ability with several levels of Poisson noise factor is presented in this section. Poisson noise factor has been discussed in the PMDD method. Poisson noise is applied on the simulation images by using equations (**3.4**) and (**3.5**). The simulation parameters are the same as before. A set of 100 independent frames is captured. Particle images are corrupted by a Poisson noise factor of 100, 500, 1000 and 4000 respectively. Simulation results for two size distributions (100nm and 300nm) are illustrated in **Figure 5.29** and **5.30**. The criteria evaluations are compared in **Table 5.5** and **5.6** respectively.

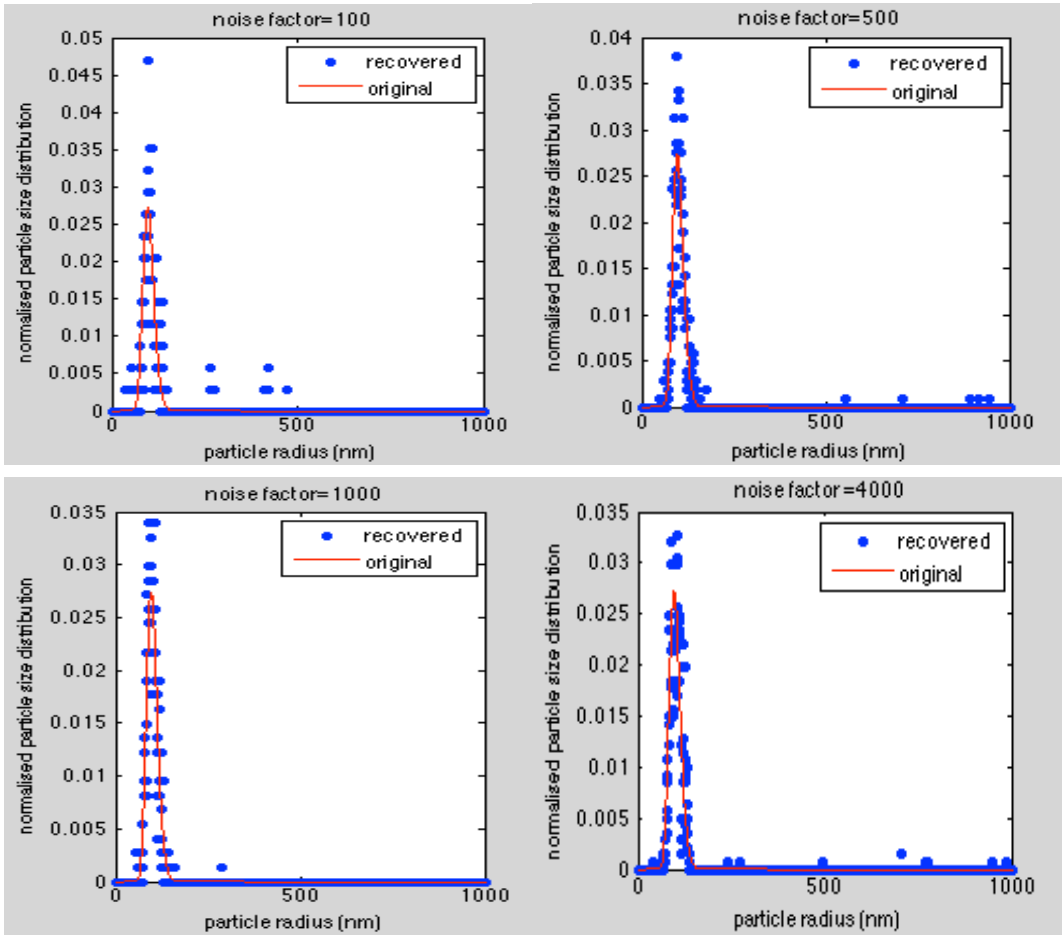

Figure 5.29: Reconstructed particle size distributions with different Poisson noise factors. The original mean radius is 100nm with 15nm standard deviation.

Noise factor	Mean radius	Standard deviation	Area error	P(eq.5.4)
100	110.25	47.16	0.48	0.86
500	104.90	51.82	0.29	0.93
1000	105.04	50.12	0.26	0.94
4000	106.77	55.22	0.36	0.96

Table 5.5: Criteria evaluations with different Poisson noise factors.

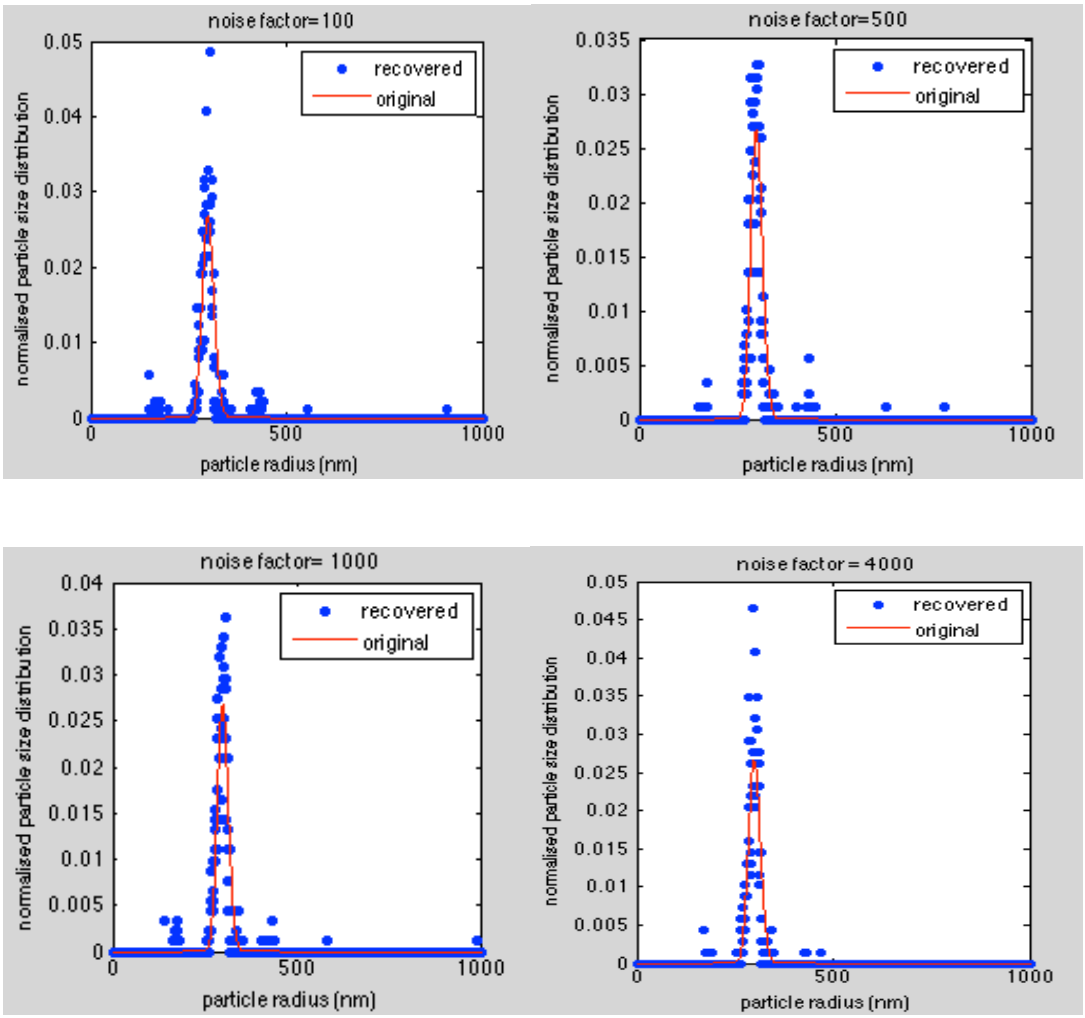

Figure 5.30: Reconstructed particle size distributions with different Poisson noise factors. The original mean radius is 300nm with 15nm standard deviation.

Noise factor	Mean radius	Standard deviation	Area error	P(eq.5.4)
100	297.77	38.25	0.41	0.91
500	297.97	32.01	0.41	0.93
1000	295.40	36.17	0.39	0.93
4000	296.99	21.38	0.39	0.95

Table 5.6: Criteria evaluations with different Poisson noise factors.

According to **Figure 5.29** and **5.30**, and the comparisons in **Table 5.5** and **5.6**, the detection process provides fairly consistent performance when Poisson noise factor is large than 500. This suggests that a very long exposure time is not necessary.

5.5.3 Simulation Results with Different Number of Quantisation Levels and Background Levels

Some examples on detection program ability with various quantisation levels and background noise levels are presented in this section. **Figure 5.31**, **5.32** and **5.33** display the recovered distribution with different number of quantisation levels, 4096, 2048 and 1024. In every image, it also considers different background noise levels 200 and 400. **Table 5.7**, **5.8** and **5.9** list the criteria evaluations of every figure.

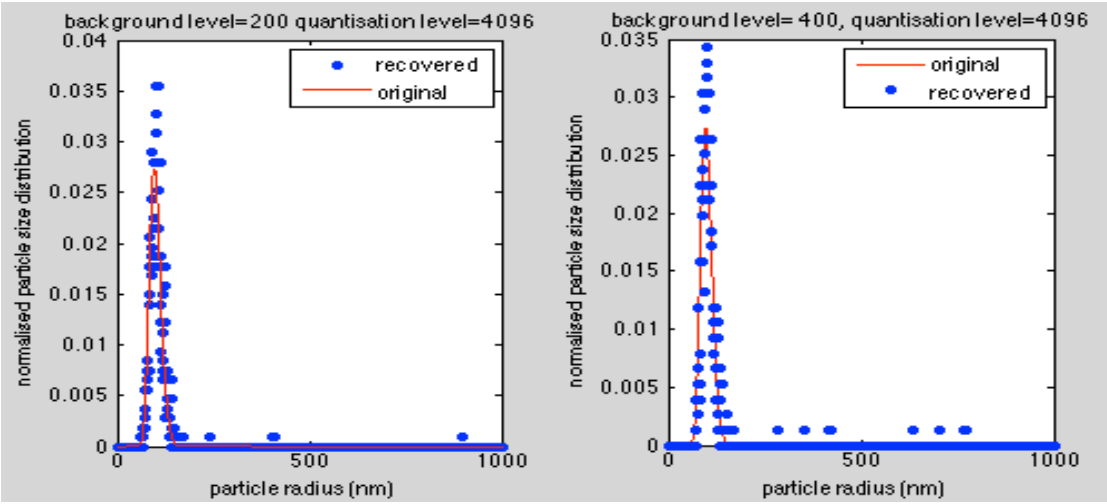

Figure 5.31: Reconstructed particle size distributions with different background noises when the quantisation level is 4096. The original mean radius is 100nm with 15nm standard deviation

Background noise levels	Mean radius	Standard deviation	Area error	P(eq.5.4)
200	104.45	32.04	0.3	0.94
400	107.70	52.27	0.29	0.94

Table 5.7: Criteria evaluations when the number of quantisation levels is 4096. The background noise levels are 200 and 400.

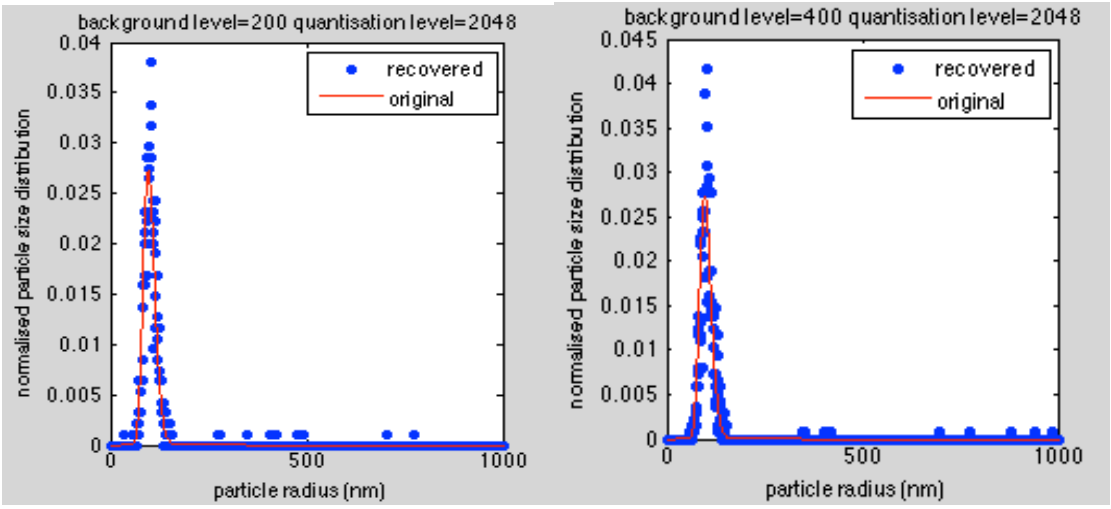

Figure 5.32: Reconstructed particle size distributions with different background noises when the quantisation level is 2048. The original mean radius is 100nm with 15nm standard deviation.

Background noise levels	Mean radius	Standard deviation	Area error	P(eq.5.4)
200	106.52	43.88	0.27	0.94
400	104.34	50.55	0.32	0.94

Table 5.8: Criteria evaluations when the number of quantisation level is 1024. The background noise levels are 200 and 400.

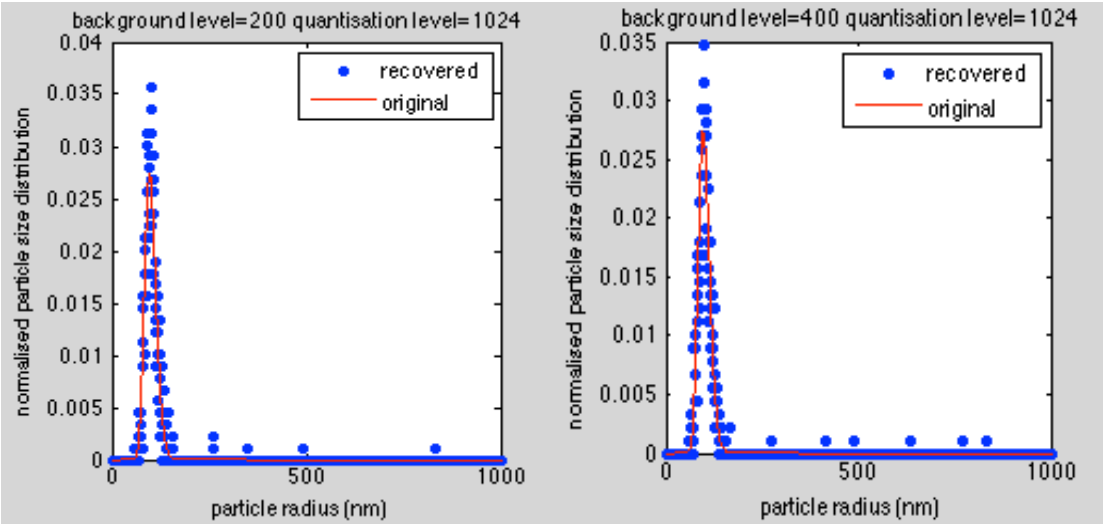

Figure 5.33: Reconstructed particle size distributions with different background noises when the number of quantisation level is 1024. The original mean radius is 100nm with 15nm standard deviation.

Background noise levels	Mean radius	Standard deviation	Area error	P(eq.5.4)
200	102.69	33.88	0.26	0.94
400	104.28	44.33	0.23	0.94

Table 5.9: Criteria evaluations when the number of quantisation level is 1024. The background noise levels are 200 and 400.

In general, the reconstructed particle size distributions are in good agreement with the original distribution when considering the background noise levels with different quantisation levels. This suggests that a very high number of quantisation levels is not necessary, and the background noise and quantisation noise do not influence the simulation results seriously.

5.5.4 Optimising Sample Concentration

This section will optimise the best sample concentrations range. The simulation parameters are the same as those in **Table 5.2**. Background noise and quantisation noise are ignored to simplify the simulations. A set of 100 random frames is captured to reconstruct the size distributions. **Figure 5.34** illustrates four reconstructed size distributions with various sample concentrations from 10^6/ml to 85 x 10^6/ml. **Table 5.10** compares the criteria evaluations with different sample concentrations.

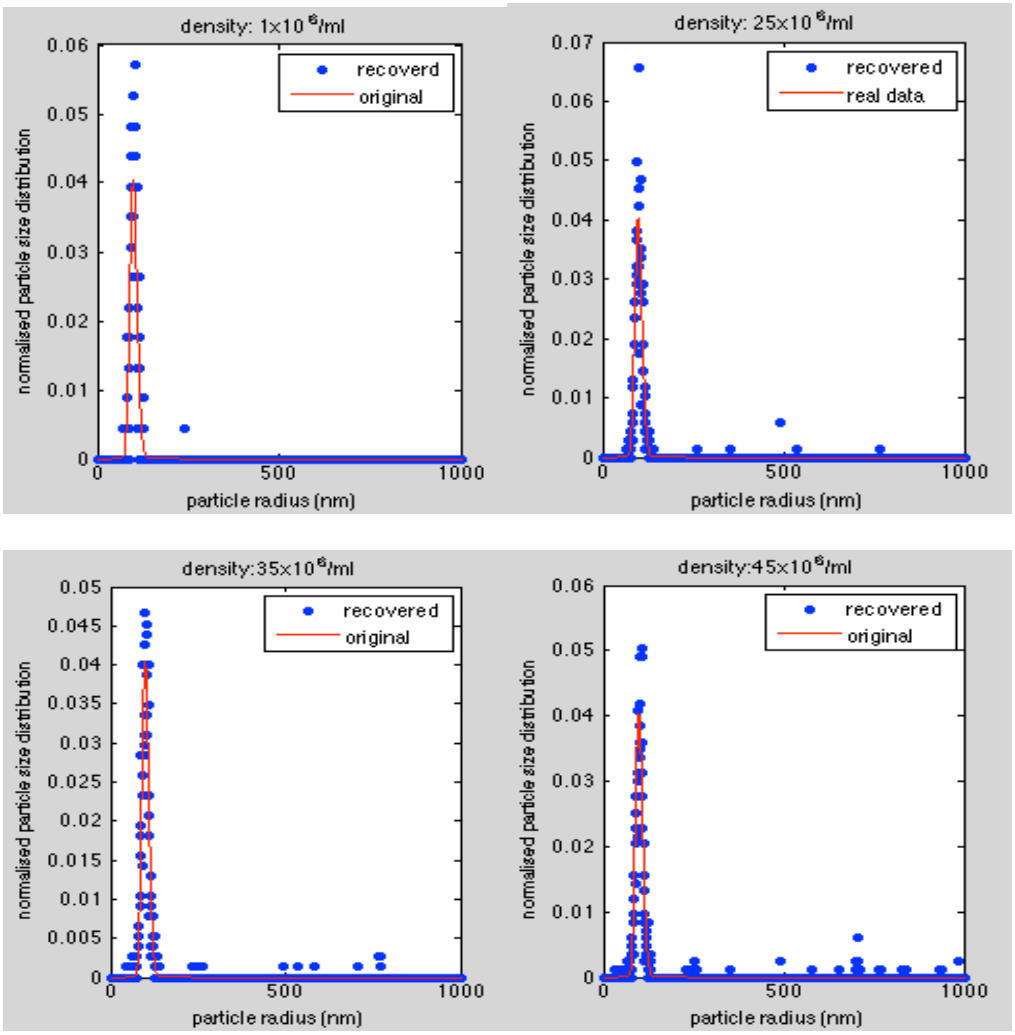

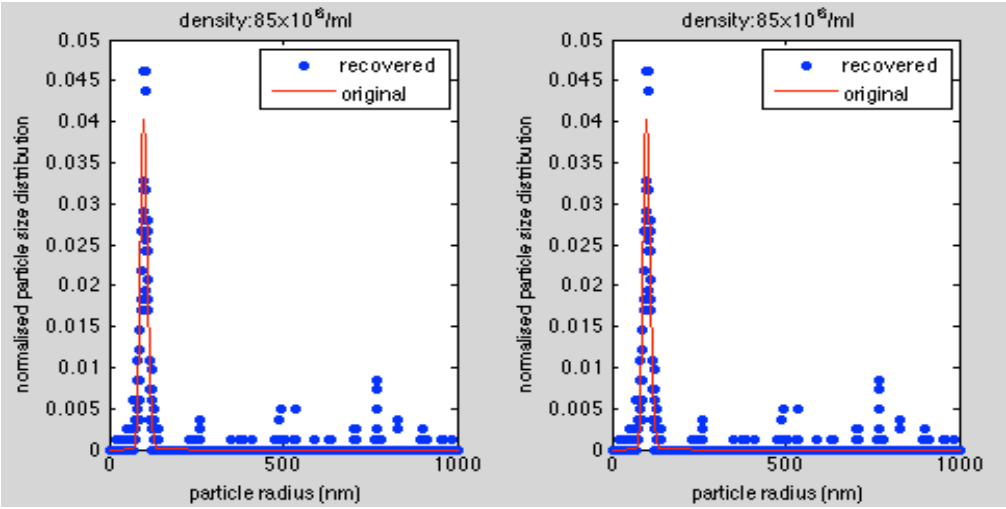

Figure 5.34: Reconstructed particle size distributions with different sample concentrations. The original mean radius is 100nm with 15nm standard deviation.

Concentrations/ml	Mean/nm	SD/nm	Area erro	P(eq.5.4)
$<10^6$	-----	-----	-----	-----
10^6	101.00	13.05	0.36	0.97
$25x10^6$	104.77	45.5	0.27	0.95
$35x10^6$	110.11	78.83	0.26	0.92
$45x10^6$	122.6	116.74	0.32	0.90
$65x10^6$	149.13	169	0.39	0.88
$85x10^6$	160.3	182.5	0.49	0.82

Table 5.10: Criteria evaluations with different sample concentrations.

Compared with the reconstructed distributions in **Figure 5.34** and the criteria evaluations in **Table 5.10**, when the sample concentration is less than $35x10^6$/ml, the recovered mean is reasonable and the standard deviation is not too large. Although a majority of particles are recovered around the original data, the mean radii and standard deviations are not as good as expected if the concentration is larger than

$35x10^6$/ml. More errors occur when the concentration is large due to the overlapping particles.

5.6 Optimising Laser Beam Position

When setting up the experimental devices, a good laser beam position can generate a high quality image. The knowledge of beam position is also important for one of the method discussed in section **5.7.2**. The centre of the laser beam should be at the focal length position (***O*** in **Figure 5.35**) in order to generate a high quality image. When the beam centre goes through the focal length position, most of particles in the field of view are in focus or almost in focus and then the scattered light from these particles is converged as much as possible to form sharp peaks in the image. If the laser light is far from the focal length which means most of the particles are out of focus, light will not be well converged and it will form blurred circles in the image. If the light is quite far from the focal length, it is difficult to detect the particles due to the weak scatterings.

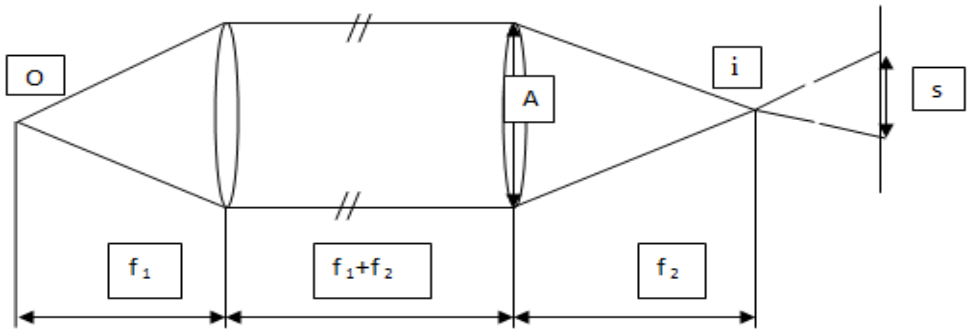

Figure 5.35: Simple image formation system. ***O*** is the ideal object position. ***i*** is the ideal image position.

It is necessary to find out the exact beam position. In this section, it will introduce two different approaches to optimise the beam position. The first one is based on image intensity method, whilst the other one depends on particle random movements.

5.6.1 Image Intensity Method to Detect the Beam Position

According to the SMIT method, the four-quarter image intensities can be represented by I_1, I_2, I_3 and I_4 respectively. Total intensity I is a summation of these:

$$I = I_1 + I_2 + I_3 + I_4 \tag{5.6}$$

If a particle is in focus or almost in focus, it forms a sharp impulse with high value, which is shown on the left in **Figure 5.36**. In contrast, if a particle is out of focus, the intensity becomes some blurred circles with small value (on the right in **Figure 5.36**).

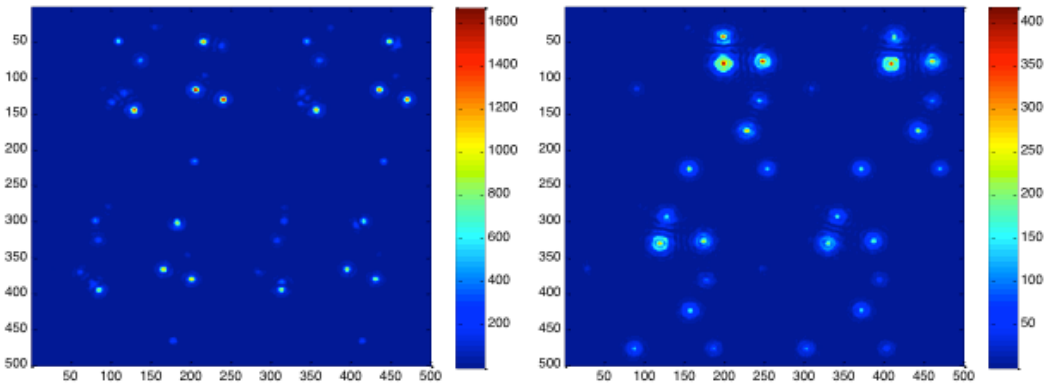

Figure 5.36: Comparisons of the total intensity image (500 pixels x 500 pixels) when particles are in focus and out of focus.

If summing four-quarter images, the total intensity of an on-focus or almost on-focus particle is a strong sharp impulse which is shown on the left in **Figure 5.37.** However, the total intensity image is not the same as every quarter image anymore for a particle

out of focus. The particle centres from every apertures shift a bit due to the out-of-focus effect. When summing these intensities, it forms an image on the right in **Figure 5.37**. It looks like some small consecutive pulses overlapping together.

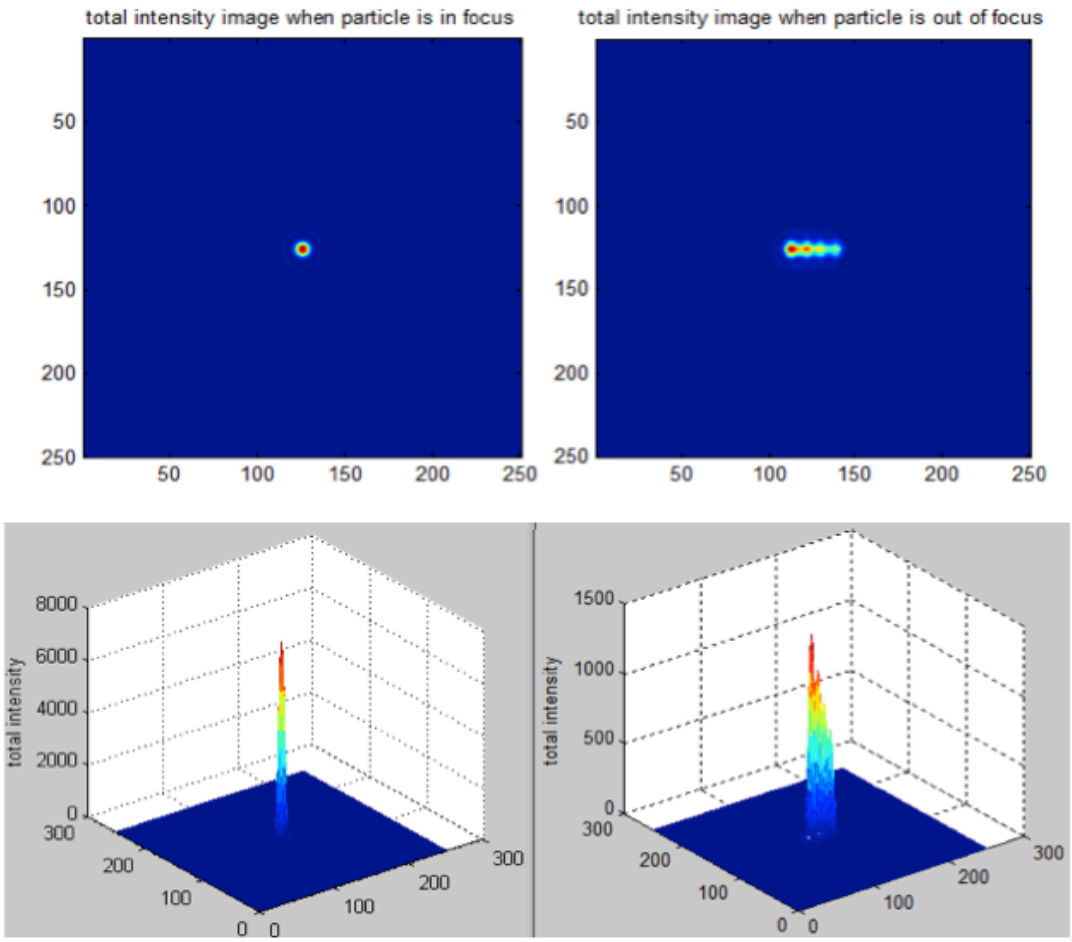

Figure 5.37: Total intensity image in 2-D and 3-D (250 pixels x 250 pixels): an in-focus particle (left) and an out-of-focus particle (right).

From the images above, it indicates that when particles are in focus or almost in focus, it will form a strong sharp column in the total intensity image, or else it will generate an irregular shape column in the total intensity image with small values. That means an in-focus particle dominates more brightness than an out-of-focus particle in the image. In other words, the in-focus particle takes more information compared with

the out-of-focus particle. Formula (**5.7**) explains the general idea of how to check beam position using the total intensity method.

$$q = \sum_{m,n} \left(\left(\frac{I}{\sum_{m,n} I} \right)^2 \right) \tag{5.7}$$

where ***I*** represents the summing intensity of the four quarter images, ***m*** and ***n*** represent the size of the summed intensity image, ***q*** is a summation of square of the normalised total intensity.

Hence, compare ***q*** value when the laser beam is in different positions, and the maximum ***q*** position is the best laser beam position. More particles in focus or almost on focus would provide a larger ***q*** value.

5.6.2 Simulation Results from Image Intensity Method

Figure 5.38, **5.39** and **5.40** compare the ***q*** value with different laser beam positions when the particle mean radii are 100nm, 200nm and 300nm respectively. '***0***' in x-axis represents the real focal length position '***O***'**,** and the beam shifts 125 microns away from '***O***' in **Figure 5.38**.

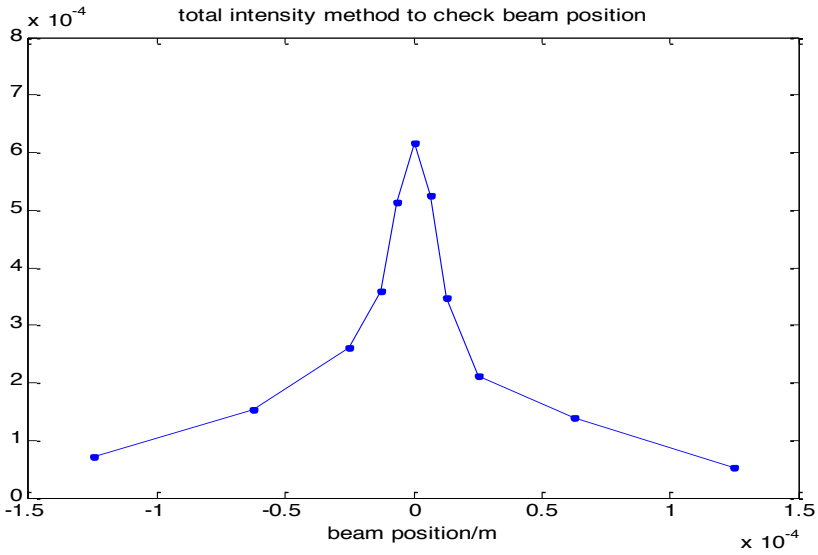

Figure 5.38: Y-axis represents ***q*** value in eq. (5.7) when the particle mean radius is 100nm with 0.1nm standard deviation.

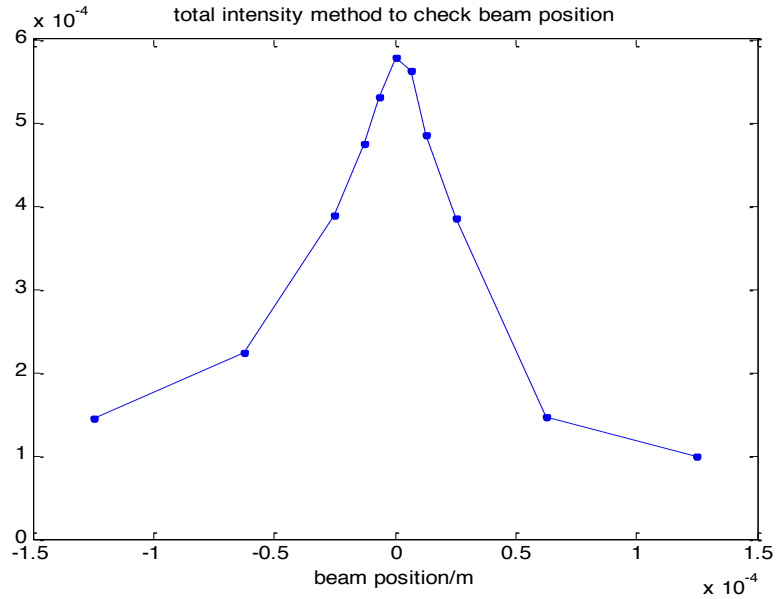

Figure 5.39: Y-axis represents ***q*** value in eq. (**5.7**) when mean particle radius is 200nm with 0.1nm standard deviation.

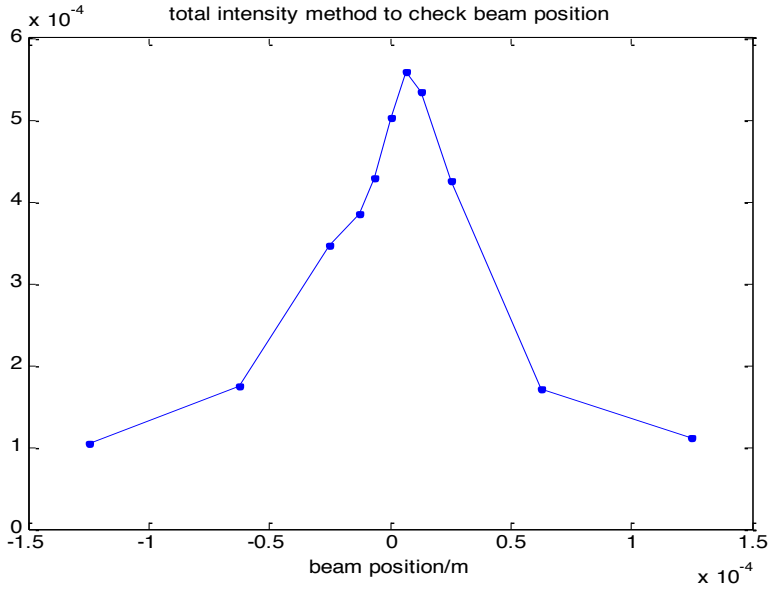

Figure 5.40: Y-axis represents ***q*** value in formula (**5.7**) when mean particle radius is 300nm with 0.1nm standard deviation.

Summarising these three graphs, when the laser beam is far away from position '***O***', ***q*** value has a sharp decline. The laser beam position can be restricted within 20 microns around the perfect focal length position. Within this range, it is difficult to compare the ***q*** value to obtain the perfect beam position. Further investigation should be done within this small range to find out the perfect beam position. Section **5.6.3** investigates another method which involves Brownian motion of particles to solve this problem.

5.6.3 Beam Position Checking Based on Particle Brownian Motions

In the previous section, the image intensity method makes a good performance when the laser beam is far from the ideal position, but it cannot distinguish the best laser

beam position when it is quite near the ideal position. The section will focus on a novel approach which is based on particle Brownian motions to solve this problem. Assuming the laser beam is at a certain position Z_B which is within 20 microns away from the ideal position. The intensity of a particle can be represented by the equations as follows:

$$I_1 = K.\exp\left(\frac{-2(Z_1 - Z_B)^2}{\alpha^2}\right) \tag{5.8}$$

$$I_2 = K.\exp\left(\frac{-2(Z_2 - Z_B)^2}{\alpha^2}\right) \tag{5.9}$$

where Z_1 and Z_2 represent two consecutive (1 and 2) positions of a particle with a certain time interval. K is scattering parameter which is relevant to particle size, particle shape, refractive index and etc. α is the laser beam width. The beam width is assumed as 25 microns in the simulations. I_1 and I_2 are the intensities of the particle in these two conditions respectively.

Within a short interval time, small displacement has been measured of the same particle. Z_1 and Z_2 record the particle positions respectively at different times. If positions Z_1 and Z_2 are known, and the particle intensities of each time can be detected, beam position Z_B can be deduced as a solution of equation (**5.8**) and (**5.9**).

$$Z_B = \frac{\frac{\alpha^2}{2}\cdot\log\left(\frac{I_1}{I_2}\right) - \left(Z_2^2 - Z_1^2\right)}{2\cdot(Z_1 - Z_2)} \tag{5.10}$$

In an optics system (**Figure 5.41**), if the scattering light from one particle passes through two apertures in parallel, and the distance between two apertures is ***A***, in the back focal length plane, it will form two peaks from these two different apertures with displacement of ***d***.

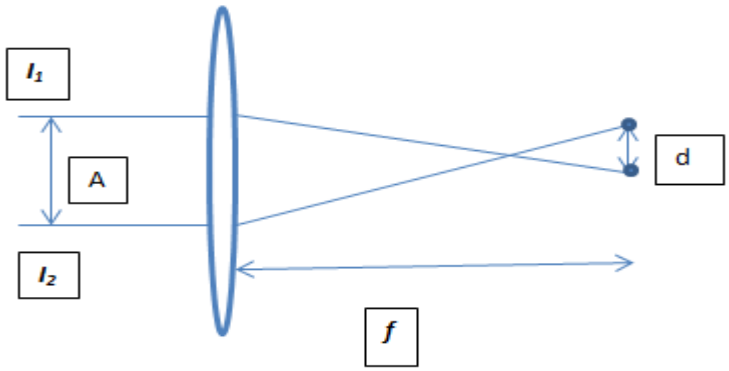

Figure 5.41: Image formation system from two apertures. The distance between two apertures is ***A***, and the displacement of the formed images on the image plane from these two apertures is ***d***.

Then, the particle position can be expressed as follows:

$$Z = \frac{df}{A - d} \tag{5.11}$$

where ***f*** is the lens focal length, ***A*** is the distance between two apertures on the mask, and ***d*** is the small displacement of the particle centres from these two apertures in the image plane.

There are a few steps to do this simulation to examine the accuracy of this method.

(1) The laser beam is not far from the ideal focal length '***O***', within 25 microns.

(2) Afterwards, choose one bright particle which can be any position in the image.

(3) According to **eq.** (**5.11**), the particle positions Z_1 and Z_2 can be calculated. Therefore, the beam position can be deduced by **eq.** (**5.10**).

(4) Finally, compare the beam position calculated in step**3** and the real beam position in step**1** to examine whether they coincide with each other.

In order to provide convincing and correct results, **Table 5.11** shows some simulation results in ten times when the mean radius is 100nm with 0.1nm standard deviation. The beam position is set at 25 microns away from '***O***'.

Beam position (μm)							
Particle position(μm)		0	5	12.5	15	20	25
Experiment	**1**	23.12	24.91	27.2	24.34	26.6	23.54
	2	24.91	25.32	25.7	24.9	24.4	28.19
Number	**3**	29.5	30.45	25.5	24.9	25.43	24.49
	4	28.95	24.7	25.2	24.74	24.31	24.69
	5	23.84	27.53	8	25.1	23.99	24.25
	6	25.72	24.05	24.8	24.84	25.57	22.27
	7	24.35	25.96	25.1	24.62	25.58	24.5
	8	23.7	24.54	25.4	25.35	24.04	24.74
	9	24.22	23.73	25.8	24.81	24.74	24.84
	10	28.91	21.6	24.73	24.66	23.07	24.77

Table 5.11: The beam position is set at 25 microns away from '***O***'. The beam positions are deduced with six different particle positions in ten independent simulations. The particle mean radius is 100nm with 0.1nm standard deviations.

According to **Table 5.11**, 59/60 results are in reasonable agreement with the ideal beam position 25μm except for the yellow marked number in **Table 5.11.** It is an inaccurate result which leads to the large standard deviation when the particle is 12.5 microns away from '***O***'. The inaccurate result is caused by the small random variance of (Z_1-Z_2). Z_B in eq. (**5.10**) is very sensitive to the variance between Z_1 and Z_2. **Figure 5.42** shows the standard errors of the beam positions according to 10 independent simulations. Ignoring the inaccurate result, the other simulations gave good results, and the beam position deduced is very similar to the real position.

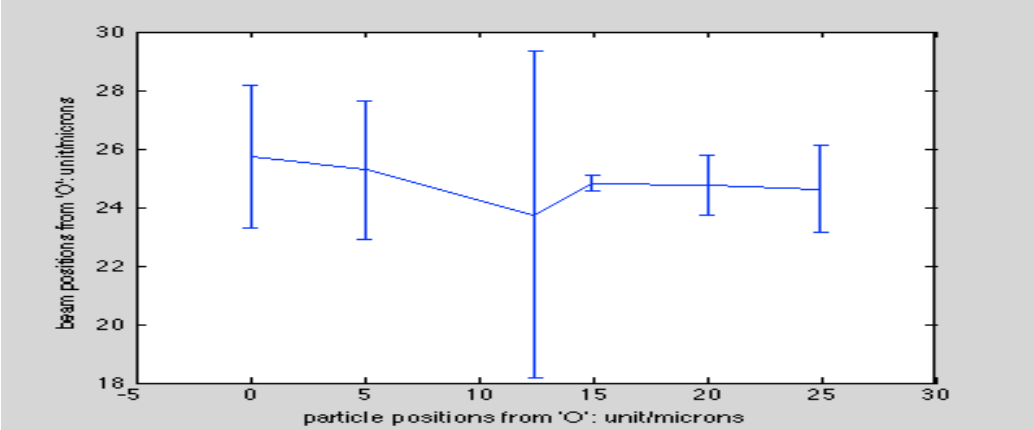

Figure 5.42: Standard errors of the beam positions when the particle positions are different. The real beam position is 25 microns away from '***O***'. The mean radius of particles is 100nm with 0.1nm standard deviation.

Table 5.12 and **Figure 5.43** compare another example when the real beam position is 12.5 microns away from '***O***' in ten independent simulations. The particle mean radius is 100nm with 0.1nm standard deviations.

Beam position (μm)							
***Particle position*(μm)**		-10	-5	0	5	10	12.5
Experiment	***1***	10.85	14.33	14.57	12.57	12.26	35.1
	2	16.73	11.87	12.6	12.44	12.36	12.5
Number	***3***	13.04	12.3	12.89	11.85	12.62	12.6
	4	12.38	12.03	12.56	12.25	13.87	12.2
	5	12.88	12.83	11.3	11.99	12.5	12.2
	6	11.45	19.92	12.67	11.03	12.71	12.4
	7	11.88	12.13	11.55	11.35	12.58	11.3
	8	10.63	11.06	12.6	11.62	12.16	13.3
	9	17.87	12.4	11.34	12.47	12.26	12.4
	10	13.77	12.32	11.76	12.44	11.86	12.1

Table 5.12: The beam position is set at 12.5 microns away from '***O***'. The beam positions are deduced with six different particle positions in ten independent simulations. The particle mean radius is 100nm with 0.1nm standard deviations.

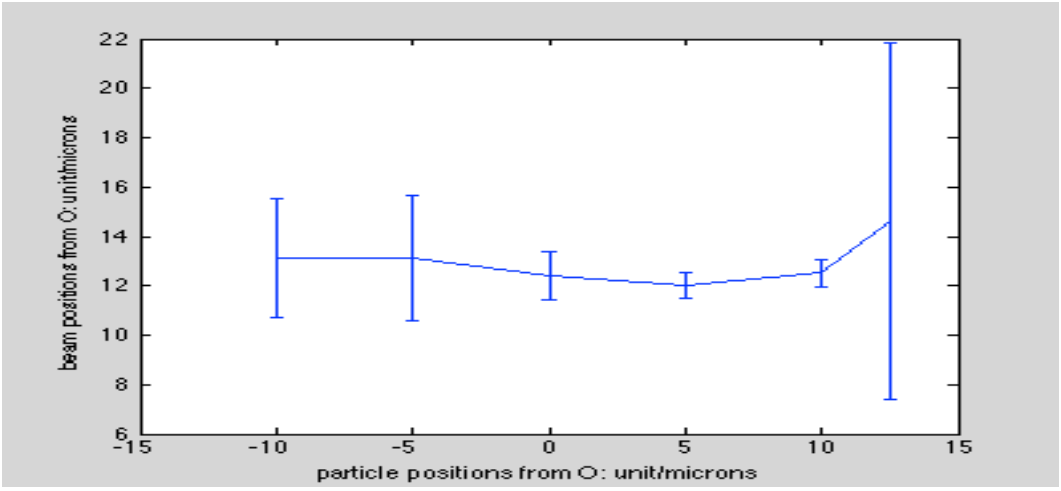

Figure 5.43: Standard errors of the beam positions when the particle positions are different. The real beam position is 12.5 microns away from '*O*'. The mean radius of particles is 100nm with 0.1nm standard deviation.

Table 5.12 and **Figure 5.43** show similar results as **Table 5.11** and **Figure 5.42**. 59/60 results are in the reasonable range of the ideal beam position 12.5μm expect for one yellow marked result in **Table 5.12**. Because the laser beam has a Gaussian distribution with 25 microns standard deviation, which is shown in **Figure 5.44**, in general, when a particle is within 25 microns away from the laser beam, it gives good results except for some ranges. The intensities appear very similar at the peak range, and it leads to an error which is yellow marked in **Table 5.12**. The intensity distribution slumps to some point, which is relevant to the standard deviation (25 microns) of the Gaussian function, and then the intensity is quite weak and comes to flat. Therefore, if the particles are within the sharp decline range, the result is better. The red marked ranges represent the error ranges.

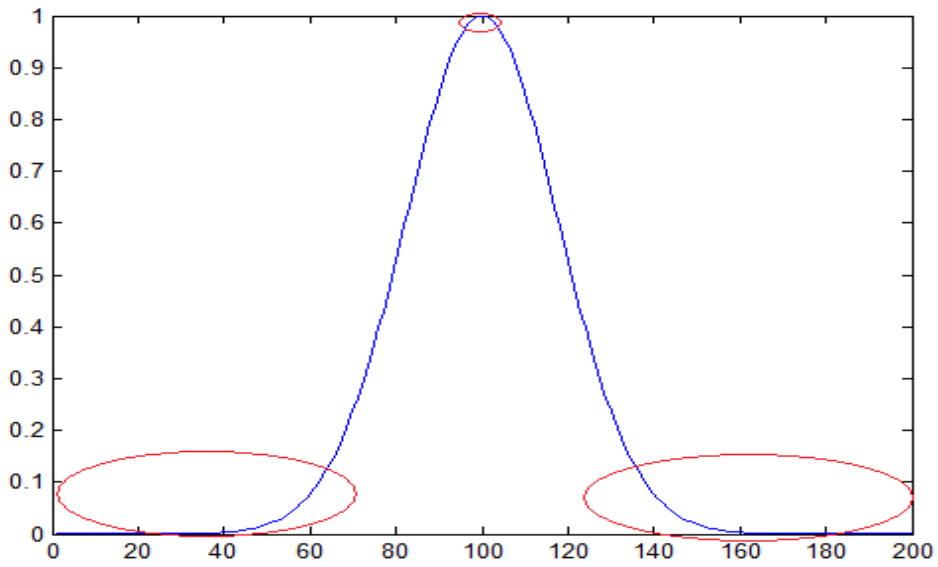

Figure 5.44: Gaussian function with 25 microns standard deviation. The red marked ranges are the error ranges.

Table 5.13 and **Figure 5.45** present ten independent simulation results when the nominal radius is 200nm with 0.1nm standard deviation, whilst **Table 5.14** and **Figure 5.46** compare the ten random simulation results when the nominal radius is 300nm with 0.1nm standard deviation.

Beam position (μm)							
Particle position (μm)		0	5	12.5	15	20	25
	2	25.85	24.13	24.3	23.43	23.86	24.49
	3	52.39	23.16	21.7	24.79	25.22	25.37
	4	24.23	24.49	16.4	24.82	24.59	29.89
	5	12.33	34.28	24.4	23.68	23.81	25.27
	6	22.76	26.59	12.3	24.87	24.3	25.71
	7	26.9	23.26	24.8	24.7	27.72	24.74
	8	27.03	22.86	24.9	26.02	24.93	23.89
	9	25.38	24.11	26.5	25.53	25.39	25.25
	10	23.97	21.93	25	26.**25**	25.34	24.82

Table 5.13: The beam position is set at 25 microns away from '***O***'. The beam positions are deduced with six different particle positions in ten independent simulations. The particle mean radius is 200nm with 0.1nm standard deviations.

55/60 results are in reasonable agreement with the ideal beam position in **Table 5.13**.

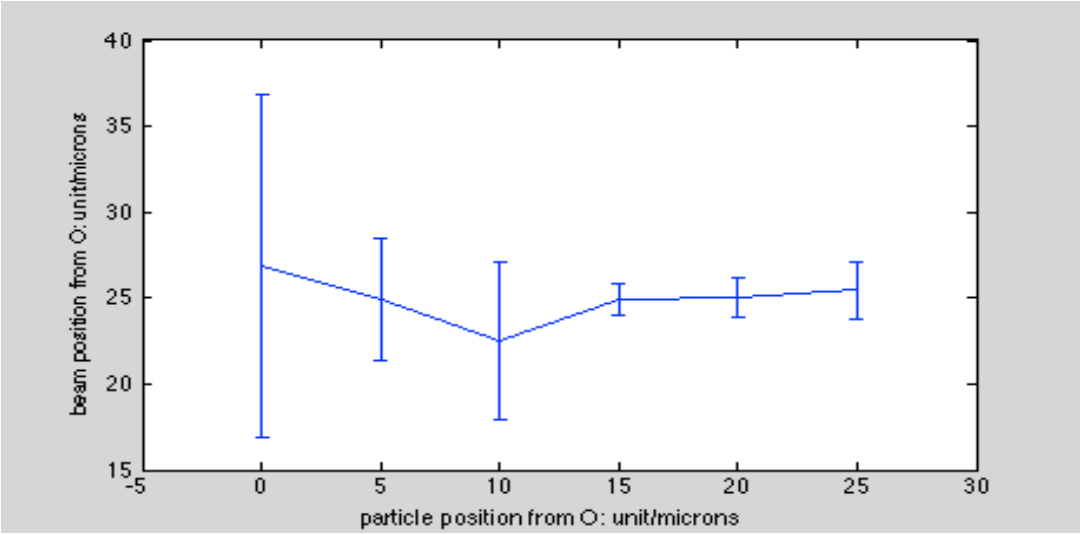

Figure 5.45: Standard errors of the beam positions when the particle positions are different. The real beam position is 25 microns away from '*O*'. The mean radius of particles is 200nm with 0.1nm standard deviation.

Beam position (μm)							
Particle position (μm)		0	5	12.5	15	20	25
Experiment	**1**	25.97	24.59	26.13	25.39	25.18	24.43
	2	24.78	23.62	23.72	24.57	26.28	24.9
Number	**3**	21.16	27.46	25.37	25.49	25.62	28.7
	4	28.38	24.9	24.53	23.93	24.78	28.43
	5	24.27	23.1	24.1	21.42	24.57	25.15
	6	26.13	26.61	24.9	25.02	24.86	26.31
	7	27.81	28.27	24.51	23.08	25.13	25.06
	8	22.92	20.74	26.02	27.34	24.9	24.83
	9	21.75	22.87	23.71	24.39	24.63	25.84
	10	23.23	24.26	23.09	24.91	25.1	30.26

Table 5.14: The beam position is set at 25 microns away from '***O***'. The beam positions are deduced with six different particle positions in ten independent simulations. The particle mean radius is 300nm with 0.1nm standard deviations.

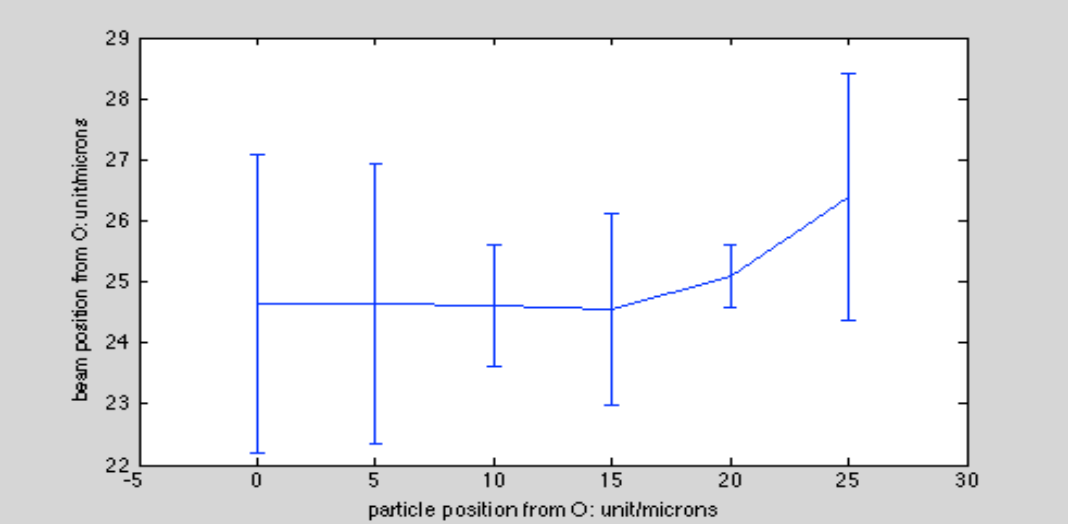

Figure 5.46: Standard errors of the beam positions when the particle positions are different. The real beam position is 25 microns away from '*O*'. The mean radius of particles is 300nm with 0.1nm standard deviation.

According to the figures and tables above, the beam positions can be deduced correctly in every situation. In summary, image intensity method can move the laser beam near to the ideal position, and then according to particles Brownian motions, the beam position can be deduced correctly.

5.7 Some Improvements on the SMIT Method

A majority of particles are reconstructed around the original data by the SMIT method. However, it still suffers from ambiguity in a look-up table. Figure **5.24** shows an example of the ambiguity. The normalised intensity ratios from four different angles at 160nm and 280nm are very similar, and therefore it is difficult to determine the size correctly. In this section, some improvements of the SMIT method are made to overcome this problem. Firstly, it considers Brownian motions of particles. Large particles move slower than the small ones. Combining the movement information

with the SMIT method, some ambiguities may be eliminated. Secondly, the total-ratio-intensity method, which is based on image intensity technique, is developed to improve the simulation results.

5.7.1 Combination of Brownian Motion Information with the SMIT Method for Particle Sizing

A novel approach is to combine the SMIT method and Brownian motion information together to size particles. According to the Brownian movement of particles, it is easy to find a range of particle sizes. The basic idea of the novel method is, for one single particle, to compare the particle size recovered by the SMIT method with the particle size ranges reconstructed from Brownian motion information.

There are a few steps to recover particle positions.

- In one frame, record the individual particle sizes recovered by the SMIT method.
- Track the individual particle Brownian movement. If the Brownian movement of a single particle is tracked more than 10 times, maximum 30 times with one-second time interval, calculate the particle size according to the averaged movement from the Stokes-Einstein relation.
- Because the Brownian movement is a random process, the particle size may vary from the size calculated in step2 in a range. Set up a range of this size from step2. If the recovered particle size in step1 is within the size ranges recovered from the movement information in step2, this sample will be

accepted; if not, this sample will be considered as a bad sample and removed from the size distribution.

Therefore, using movement information for particle sizing can eliminate some errors which are quite far from the real data. For example, when the original radius is around 100nm, there are some errors around 700nm or 800nm, and these errors, which are much larger than 100nm, will be eliminated in this condition.

Figure **5.47** compares two reconstructed distribution examples, 100nm and 200nm.

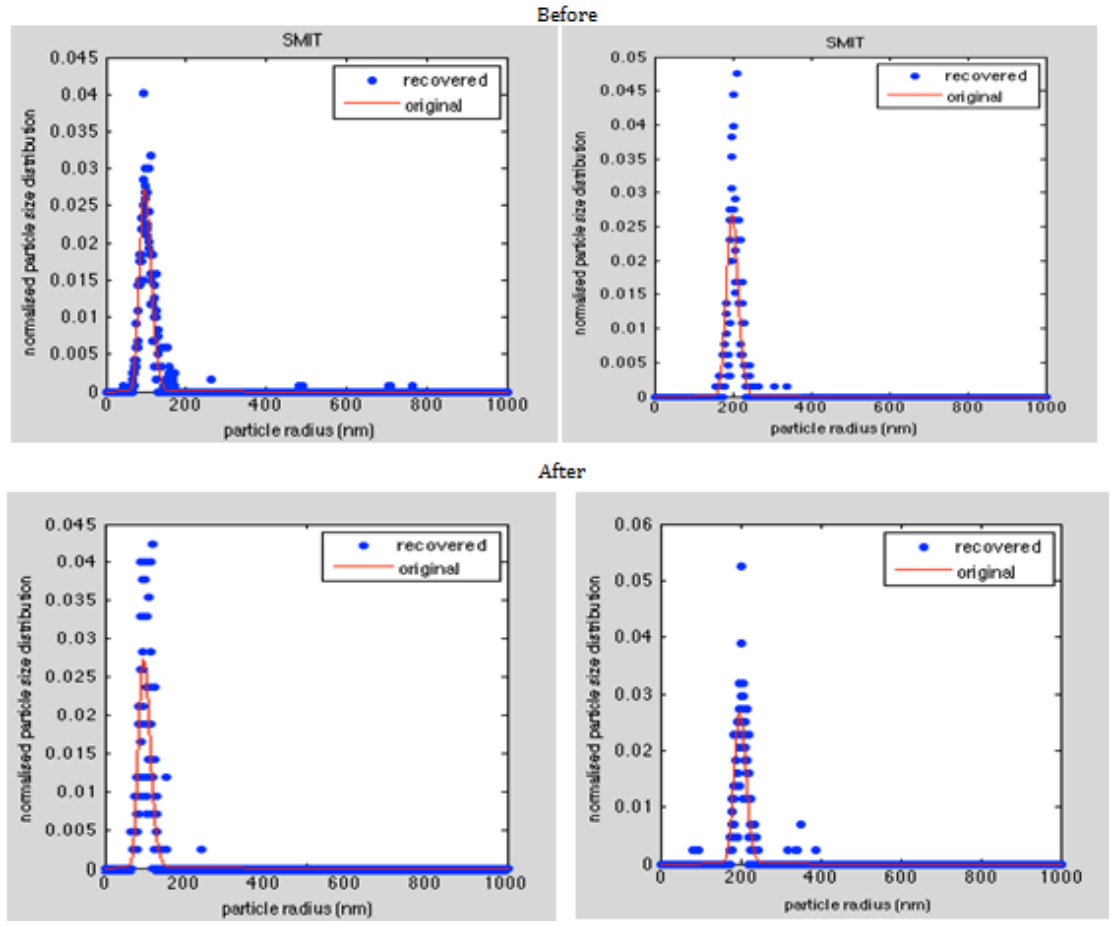

Figure 5.47: Comparisons of the reconstructed particle size distributions when the original radii are 100nm and 200nm respectively. The standard deviation is 15nm in each distribution.

The '**Before**' images are the recovered distributions by SMIT in step1, whilst the '**After**' images are the recovered distributions combined Brownian motion information with the SMIT method. The simulation parameters remain the same as those in **Table 5.2**.

Table **5.15** compares the criteria evaluations of the images in Figure **5.47**.

	Particle sizes	Mean radius (nm)	Standard deviation (nm)	Area error	P(eq.5.4)
Before	100nm	106.77	55.22	0.36	0.96
	200nm	206.15	15.88	0.45	0.95
After	100nm	102.54	17.86	0.45	0.96
	200nm	204.23	22.8	0.39	0.95

Table 5.15: Criteria evaluations of different reconstructed distributions.

The '**After**' images in **Figure 5.47** eliminate some errors, which are far away from the original size, and modify the results to approach to the original data. However, if the error size is near the original data, it is difficult to eliminate it, because Brownian motion is a random process and the random movement of similar size particles may be the same. Based on the Brownian motion information, the particle size can be restricted within a certain range but not a certain size. In addition, it records fewer particles in the recovered distribution due to the averaged movement check. Comparing the criteria evaluations in **Table 5.15**, mean radii and the standard deviations of the reconstructed distribution have been slightly improved, but the area error and **P** value are very similar. In summary, the additional Brownian motion information gives a slightly better distribution, but it takes much longer experiment

time and records fewer particles, and therefore it is not necessary to add Brownian motion information in the real experiment.

5.7.2 Total-Ratio-Intensity Method to Improve the Simulation Results

Section 5.3-5.5 presented the simulation results of the basic SMIT method. A majority of particles are reconstructed around the original data by the SMIT method. However, it still suffers from ambiguity in a look-up table. Just as mentioned in **Figure 5.24**, the normalised intensity ratios from four different angles at 160nm and 280nm are very similar, and therefore it is difficult to determine the size correctly. In section 5.7.1, it considers Brownian motions of particles. Although it improved the simulation results, it took quite long simulation times in order to examine the Brownian motions (30 times per particles) of particles. Therefore, in this section, the total-ratio-intensity method is introduced to improve the simulation results based on the basic SMIT method, and save simulation times.

The basic SMIT method compares the normalised intensity ratios from four different angles with the predicted data. This section considers the summed intensities from these angles as well. Because large particles scatter more lights than the small ones, the summed intensities from these four different angles vary with the particle sizes.

Figure 5.48 shows the summed intensities from four angles (74^{o}, 85^{o}, 95^{o}, and 106^{o}, same as before) based on Mishchenko code.

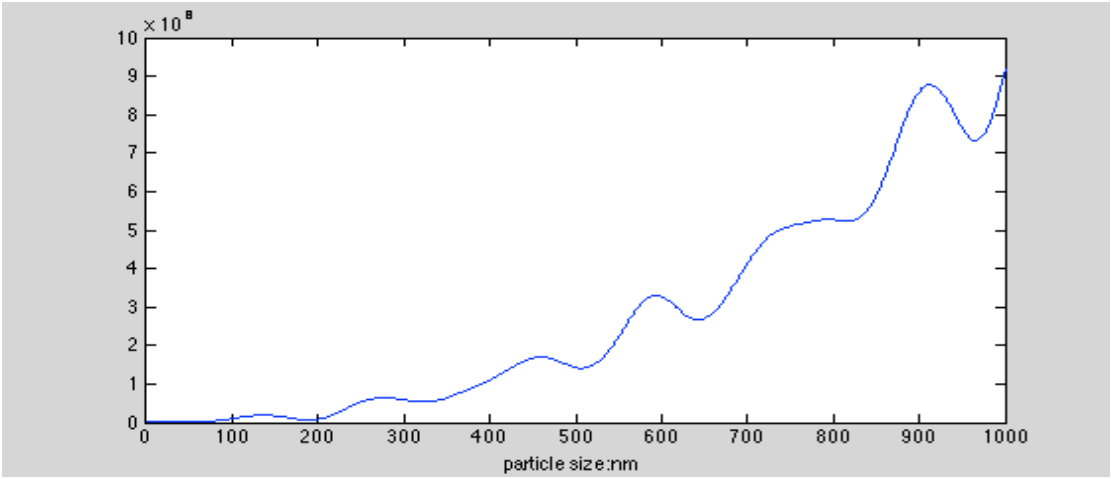

Figure 5.48: Summed intensities from four angles ((74^{o}, 85 ^{o}, 95 ^{o}, and 106 ^{o}).

This section considers the summed intensities with the normalised intensity ratios together to recover particle sizes. This new method is named as total-ratio-intensity method.

There are a few steps to recover particle sizes.

- Compare the normalised intensity ratios with the predicted data. The best-fit function in **eq. (5.5)** is illustrated in **Figure 5.49**. Set up a threshold ***T*** (such as 0.2) to record the troughs of the wave which are lower than the threshold. The positions of the troughs represent the suitable particle sizes.

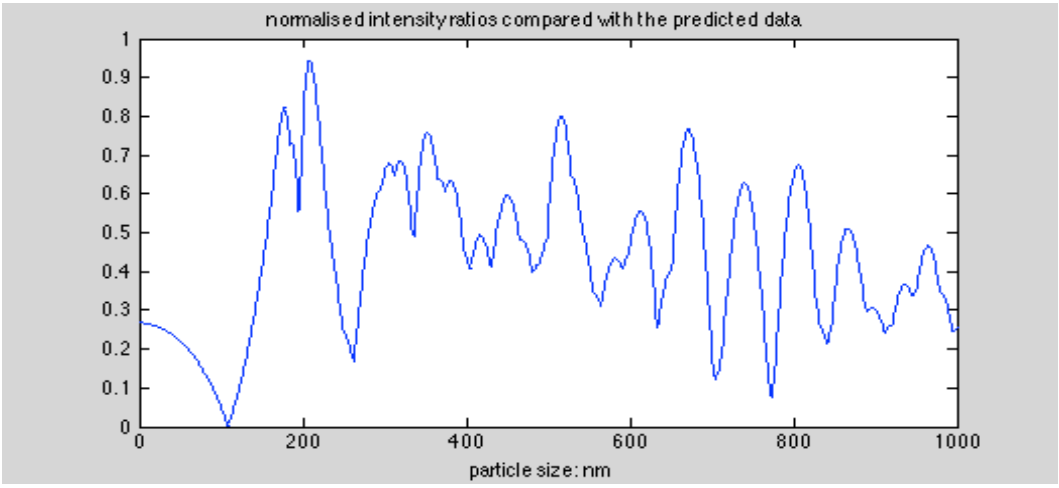

Figure 5.49: A best-fit function of **eq.**(5.5) of the normalized intensities from four angles.

- According to section 5.6, calculate the beam position and particle positions, and then deduce the summed intensities of the particles from these four angles. Subsequently, use **eq.** (**5.12**) to compare the summed intensities of the particles with the predicted data from Mishchenko code. **Eq.** (**5.12**) is another best-fit function for the summed intensities. **Figure 5.50** shows a best-fit function example of a particle.

$$\left| I g F_S - M \right| \tag{5.12}$$

where ***I*** is the summed intensity of the particles, F_S is the scattering factor, ***M*** is the predicted intensity data from Mishchenko code.

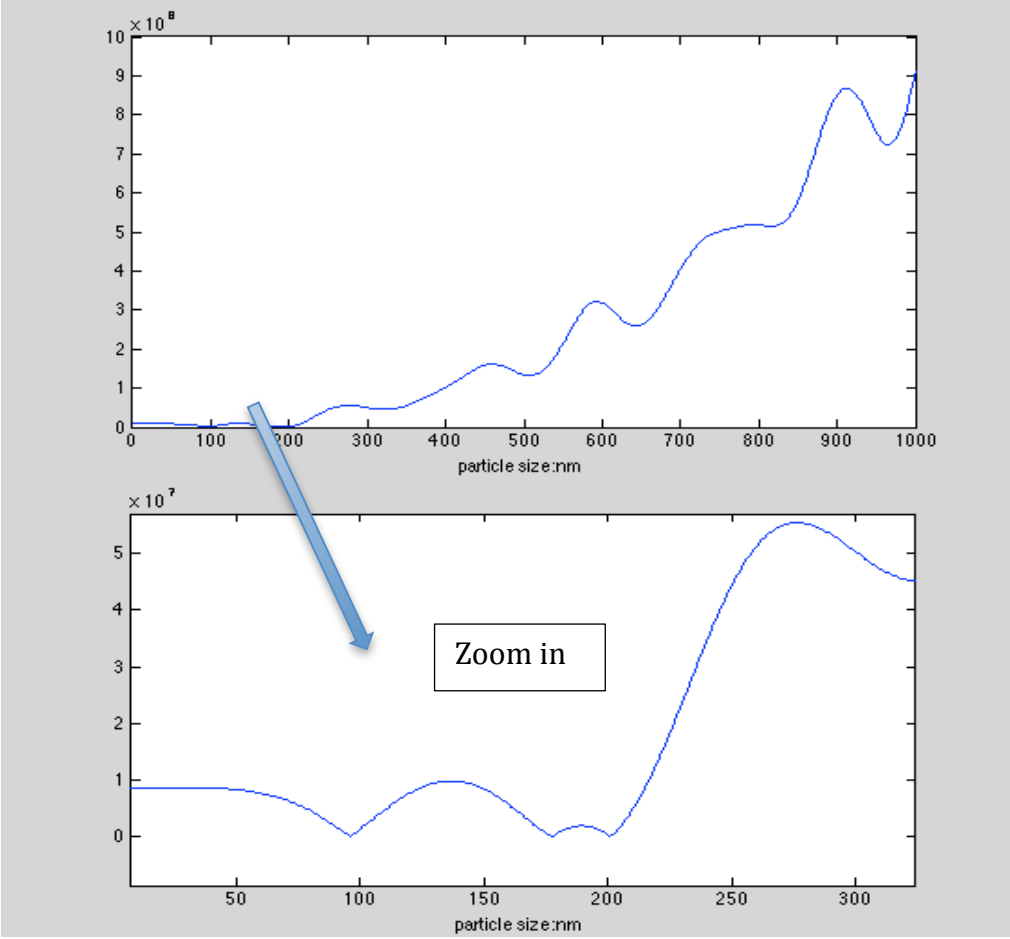

Figure 5.50: An example of the best-fit function of eq. (5.12) of the summed intensities. The bottom image is a zoom-in image of the top image.

- Set up another threshold to record the troughs of the wave in step2, which is lower than this threshold.
- Record the particle positions from step1 and step3. **Figure 5.51** shows an example. The blue dots represent the suitable positions from step1, whilst the red circles are the suitable positions recovered from step3. Comparing these positions, in most situations, one of the positions recovered from step1 is very similar to one of the positions from step3, and then this particle position will be recorded as the most suitable size. If there are no similar particle sizes from both methods recorded within a small range (such as 10nm), this particle will be eliminated as a bad sample.

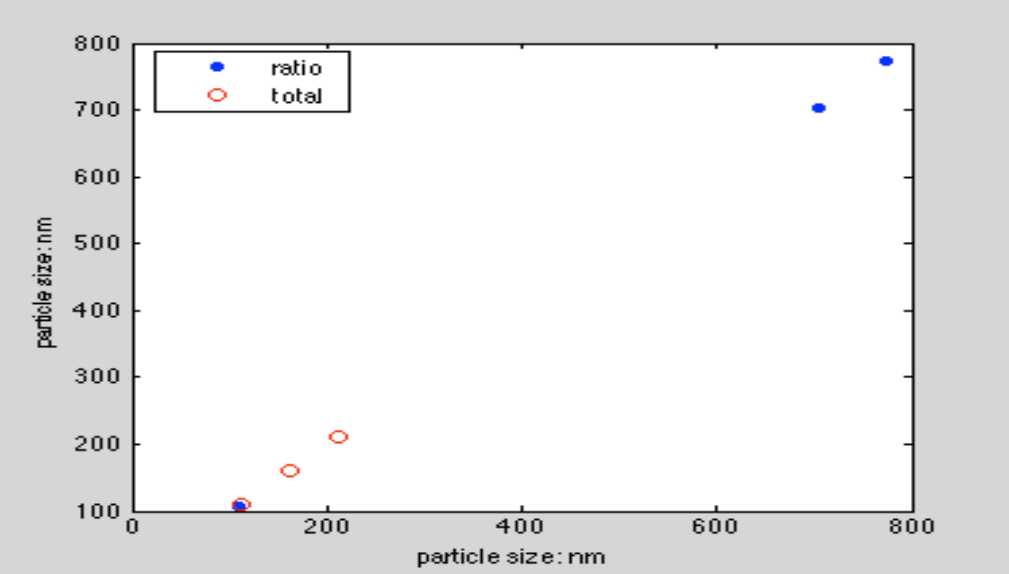

Figure 5.51: Comparisons of particle positions recovered by step1 and step2.

Figure 5.52 compares two recovered distributions. The simulation parameters are the same as before in **Table 5.2**. **Figure 5.51(a)** is a recovered distribution by the original SMIT method, whilst **Figure 5.51(b)** is a recovered distribution by the total-ratio-intensity method. **Table 5.16** lists the criteria evaluations by these two methods.

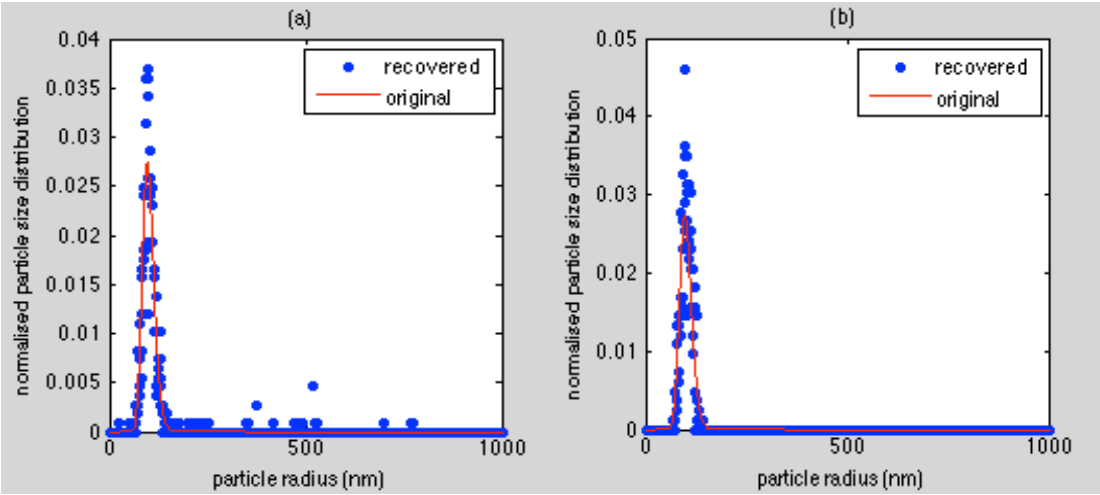

Figure 5.52: (a) Recovered particle size distributions by the original SMIT method. (b) Recovered particle size distributions by the total-ratio-intensity method.

Method	Mean radius	SD	Area error	P (eq.(5.4))
SMIT	109.86	60.32	0.37	0.93
Total-ratio	101.19	12.29	0.25	0.995

Table 5.16: Comparisons of the criteria evaluations between the original SMIT method and the total-ratio intensity method.

Obviously, the total-ratio-intensity method can recover a better size distribution than the original SMIT method in the same condition.

5.8 Summary

In this chapter, a novel approach was developed which is based on image intensity to size particles. Two imaging arrangements were investigated; these were named Multiple Image Technique (MIT) and Separated Multiple Image Technique (SMIT). A computer simulation was conducted to compare the performance of these two

arrangements. The results are summarised in **Table 5.3**. The SMIT method gave better results in terms of a smaller area error (with values in the range 0.24 to 0.45 for SMIT compared with 0.46 to 1.2 for MIT), giving a higher P value (defined in eq. 5.4)(0.95 to 0.96 for SMIT compared with 0.87 to 0.95 for MIT). The returned mean and standard deviation results were inconclusive because of the occasional presence of a false radius value due to the ambiguity problems present in both techniques. As the motivation for examining this intensity method was the failure of the PMDD method to accurately reconstruct bi-modal distributions, the ability of the SMIT method to do this was tested. It was found that it could reconstruct bi-modal distributions, even for very closely spaced pairs of peaks, which neither the PMDD method or the tracking method could have resolved. But for the widely spaced peaks, it was found that the ratio of the number of particles in each peak was measured with low accuracy in both the MIT and the SMIT method, for the reasons discussed under **Figure 5.21**. Subsequently, the noise effects for the SMIT method were studied. The study indicates that it is not necessary to use a long exposure time to give high Poisson noise factor (there was no significant improvement in the area error and P values for values of the Poisson noise factor above 500). Simulations to investigate the effect of using different sample concentrations were also conducted. In terms of minimising the area error, for the system studied a concentration of around 35 $x10^6$ particles per millilitre was found to be optimal.

The chapter also discussed two methods to determine the laser beam positions. One of these used the image intensity and the other was based on the Brownian motion of the particles. The image intensity technique was found to be able to give an approximate beam position (around 20 micron standard error) but over a wide range of initial beam positions (around 100 microns); whereas the ‘Brownian motion method could

measure the beam position more accurately (to a standard error of around 2 microns) but required the initial beam to be close to the focal position to within around 20 microns.

Finally, some improvements on the SMIT method were proposed in this chapter. It was shown that if Brownian motion information is combined with the SMIT method, it could improve the recovered results. In the simulations performed, it can be seen that the inclusion of the Brownian motion information can eliminate some ambiguities; this is evident in the simulation of 100nm particles shown in **Figure 5.47** and this has resulted in the measured standard deviation decreasing from 55.22nm to 17.86nm (the simulated standard deviation was 15nm). But for the 200nm particles, where there were not many ambiguities in the original distribution in **Figure 5.47**, the inclusion of the Brownian motion information has not led to an improvement but rather deterioration in the recovered standard deviation; for the original method the value recovered was 15.88nm but with the Brownian motion it was 22.8nm (the simulated standard deviation was 15nm). Also it can be seen in **Table 5.15** that the area errors did not show a consistent improvement. In addition, it should be noted that the use of Brownian motion records fewer particles and takes a longer experiment time.

In contrast, the total-ratio-intensity method gives a better result than the original SMIT method. It eliminates most of the ambiguities. For the original method the standard deviation recovered was 60.32nm but with the inclusion of intensity data reduced to 12.29nm and also the area error decreased from 0.37 to 0.25.

In summary, the SMIT method gives a good performance during the simulations and the results of combining the SMIT method with intensity data are sufficiently encouraging to investigate in a real experiment to improve the results.

6 Experimental Results with Separated Multiple Image Technique

This chapter concentrates on the experimental work of the SMIT method. Firstly, Section **6.1** presents the experimental setup. The simulation results in the previous chapter (results shown in **Figure 5.5**) showed that significant ambiguities will occur if fewer than 4 holes are used. A simulation comparison of using 4 or 6 holes (results shown in section 5.51) showed that there was no significant improvement in using 6 holes compared to 4 (see **Table 5.4**). Based on these results in the experiment a mask with 4 holes was constructed, the spacing of the holes was set to space the holes over the range of angles achievable with the long working distance microscope objective (Mitutoyo OBJ plan Apo 20x). Subsequently, section **6.2** gives some experimental results based on several particle sizes, 100nm, 150nm and 200nm respectively. Some modifications on the results are made on this section to improve the results. Section **6.3** continues with some results by introducing total-ratio-intensity method. Finally, Section **6.4** summarises the work carried out in this chapter.

6.1 Experiment Setup

Figure 6.1 shows the schematic and some pictures of the experimental setup.

(a)

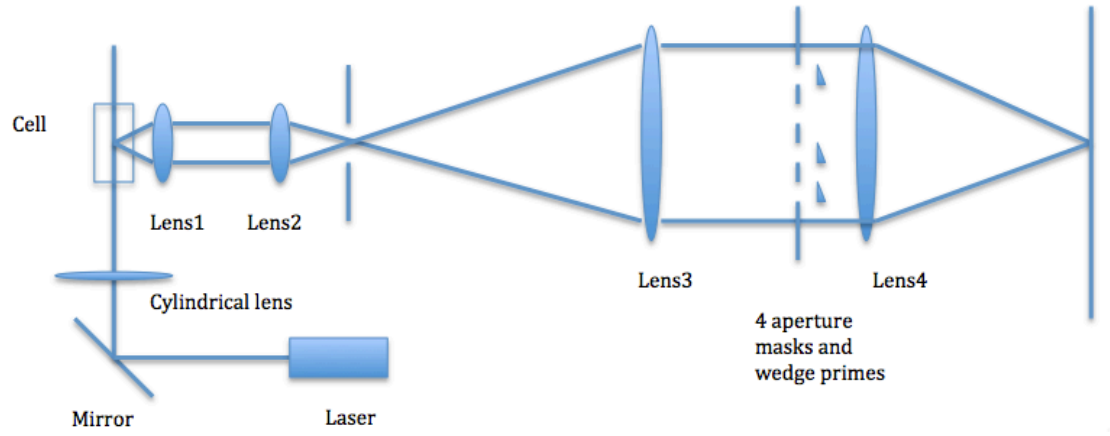

(b)

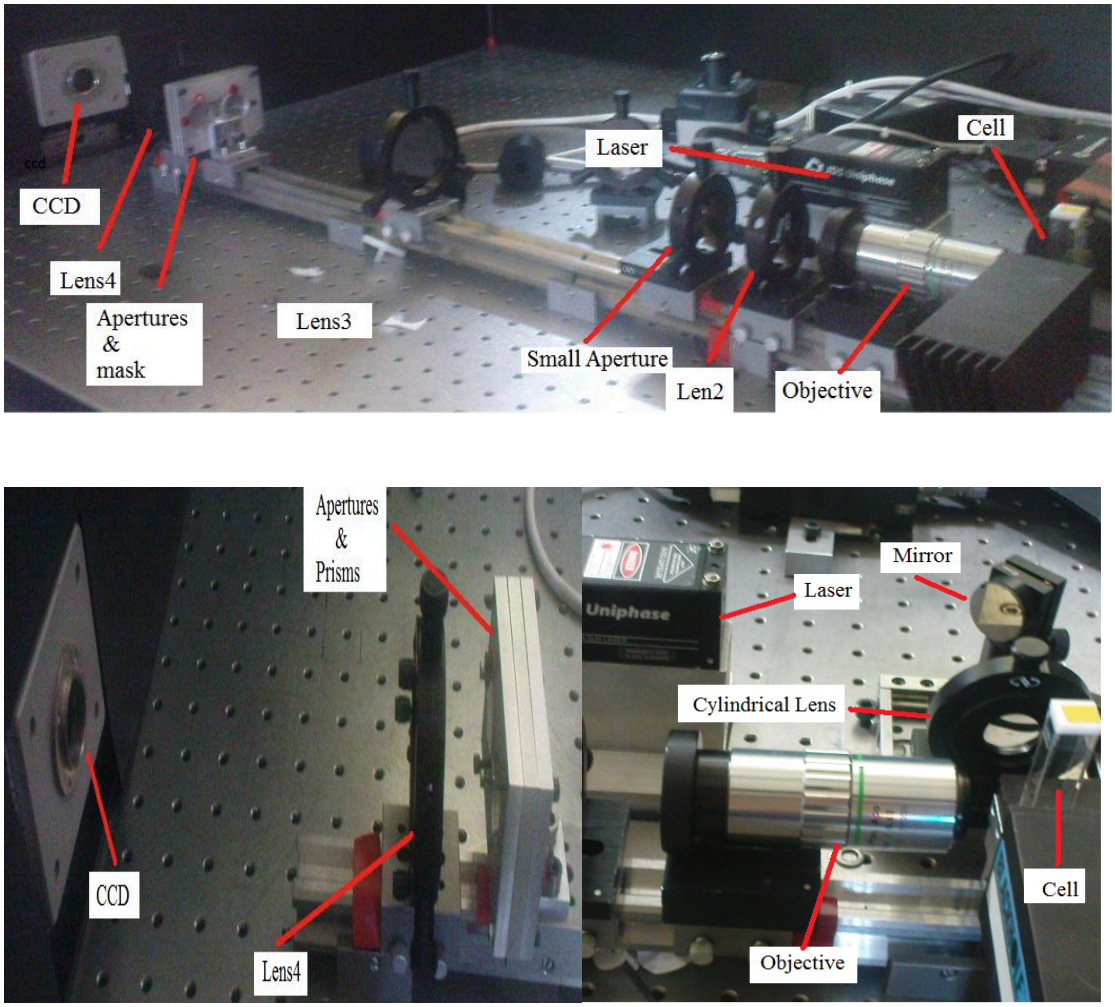

Figure 6.1: (a) A schematic; (b) Some pictures of real experiment setup.

The laser source (Uniphase 4611 series: uGreen SLM solid-state laser) has a wavelength of 532nm and a maximum power of 50mW emitted in a single TEM_{00}

mode and vertically polarized. The vertical plane of polarisation matches that used in the simulations of chapter 5. A cylindrical lens with 40mm focal length and 25mm diameter is employed to produce a sheet of laser light. A Mitutoyo OBJ Plan Apo 20X objective is used as lens1. Its focal length is 10mm. A plano-convex lens with 50mm focal length and 25mm diameter is utilised as lens2. A small aperture is used behind lens2 to stop some light and avoid image overlapping on the CCD. The CCD camera is manufactured by Hamamatsu, with series number of C4742-95-12NRG. Another two plano-convex lenses with 250mm ***f.l.*** x 50mm ***dia*** and 200mm ***f.l.*** x 40mm ***dia*** are used as lens3 and lens4 to focus the collimated beam on the CCD. A four-aperture mask and wedge prisms are placed between lens3 and lens4, which is shown in Figure **6.2**. The aperture mask and the prism holder are placed like a sandwich with the four aperture mask in the middle. Each aperture has a diameter of 5mm, and the space between each aperture is 3mm. The wedge prism has a diameter of 25mm with 1^{o} deviation, and it tilts the light to different positions on the 8-bit CCD.

(a)

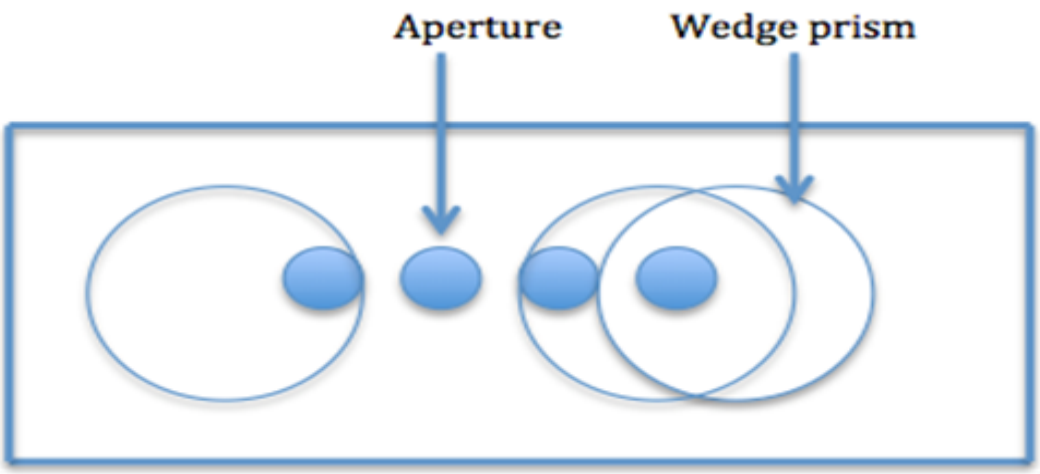

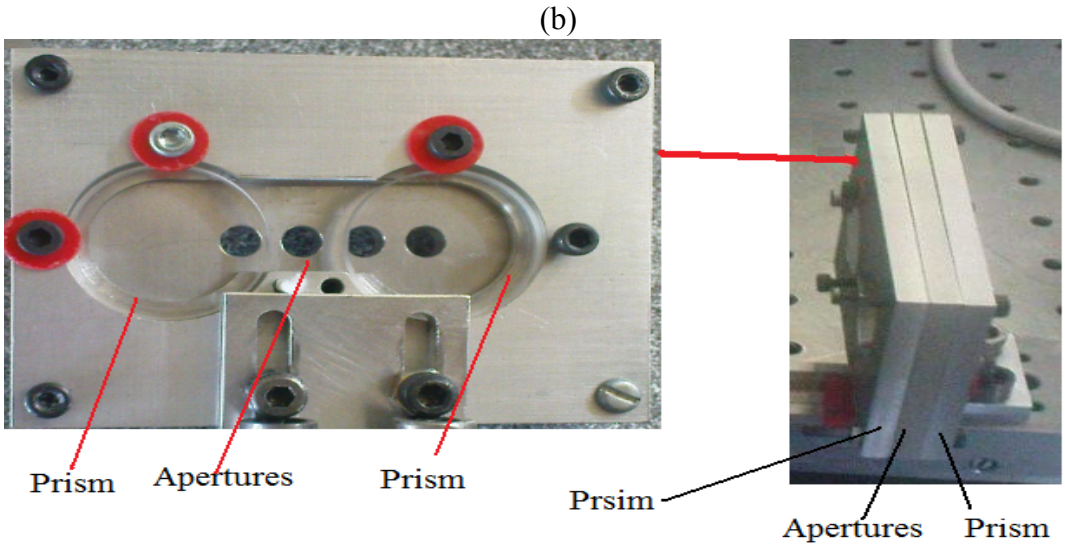

Figure 6.2: (a) A schematic of a four-aperture mask and wedge prisms. (b) Some pictures of the four-aperture mask and wedge prisms.

In order to position correctly the mask in the back focal plane (BFP), it was positioned centrally within the image of the physical back focal plane at the rear of the microscope objective. The particles do not scatter sufficient light to view this image, so the mask was positioned by directly illuminating the objective with the laser and inserting a scattering screen (lens tissue) over the microscope objective back focal plane aperture. This procedure generated a clear bright image to allow the mask to be aligned to an estimated accuracy of around 1mm which is small compared to the dimensions of the mask.

The sample preparation was conducted as follows. The water used was HPLC quality, CHROMASOLV® Plus, for HPLC from Sigma-Aldrich. The 3000 series polystyrene Nano-spheres from Brookhaven Instruments Limited are used as the particle samples.

The first stage was that the water was filtered through a filter specified to only allow particles with diameters smaller than 0.1-0.2μm to pass.

After dilution of the particle sample using the filtered HPLC water, the cuvette was placed in an ultrasonic bath for a period of 8 hours to vibrate the samples in order to reduce any aggregation of the particles.

The sample was then further diluted using the filtered HPLC water, to give a suitable particle concentration in the imaging cuvette.

It is not claimed that this procedure necessarily produces a sample with a known particle size distribution and as stated in Chapter 4 there is no 'gold standard' method to give a true particle size distribution with which to compare the results obtained.

Table **6.1** lists the experimental parameters.

Particle radius	100nm
Number of frames	60
Exposure time	0.1s
Laser power	50mW
Pixel size	6.7 microns
Magnification	4
Image size	1024 x 1280

Table 6.1: Experimental parameters.

Figure 6.3 presents an example of an image captured from the real experiment. The nominal radius of particles is 100nm. Four-quarter images from different apertures seem the same. The first quarter image is formed from the second aperture without wedge prism. The left bottom quarter image is formed from the first aperture with one wedge prism. The right top quarter image is captured from the third aperture with one

wedge prism, and the right bottom quarter image is from the fourth aperture with two wedge prisms which is shown in **Figure 6.2**.

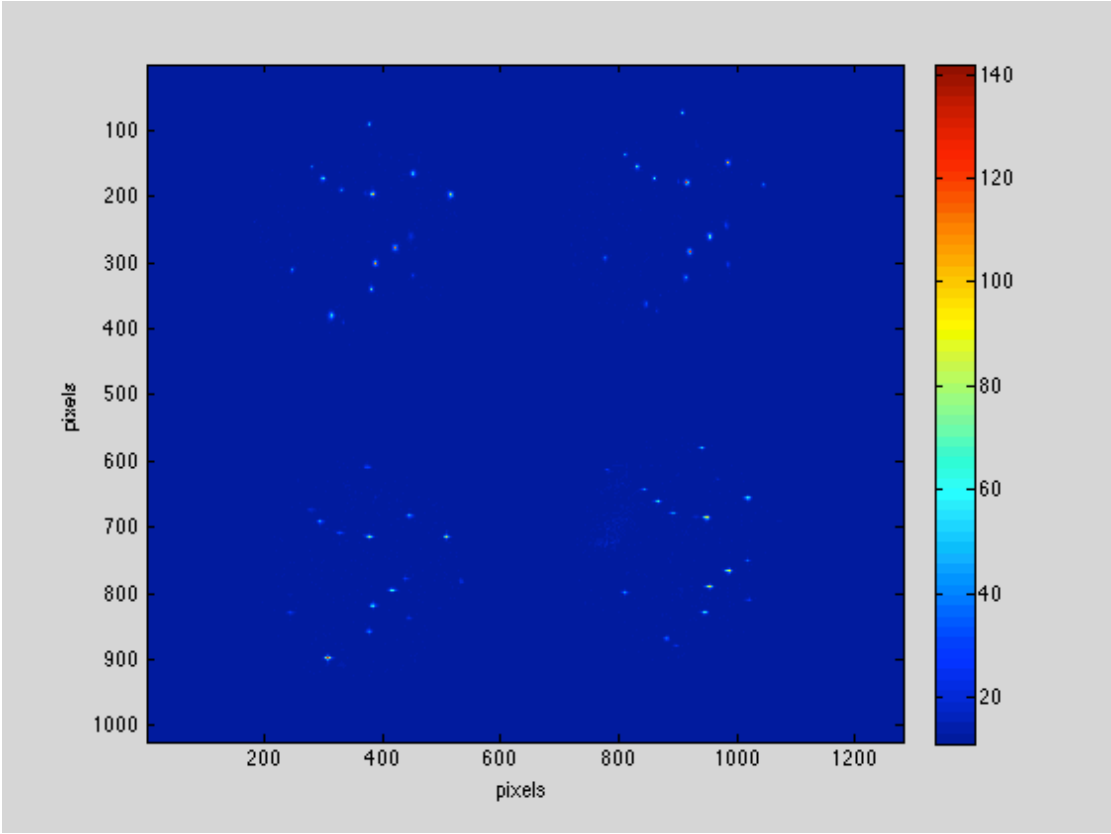

Figure 6.3: Image (1024 x 1280 pixels) of 100nm particles taken with a 4-aperture mask. The exposure time is 0.1s.

6.2 Experimental Results

The 3000 series polystyrene Nano-spheres from Brookhaven Instruments Limited are employed in the experiment. Their refractive index is 1.59 at 589nm wavelength. Some further specifications of the samples can be found in the company website (67). Three different sample groups are provided with the nominal radii of 100nm, 150nm and 200nm, and the standard deviation of every single sample are 4.7nm, 6nm, and

7.3nm respectively. Firstly, **Figure 6.4** compares the normalised intensities ratios from these four apertures when the nominal radius is 100nm in one frame. The red star is the real ratio from Mishchenko code, whilst the blue circles record the recovered ratios from the real frame.

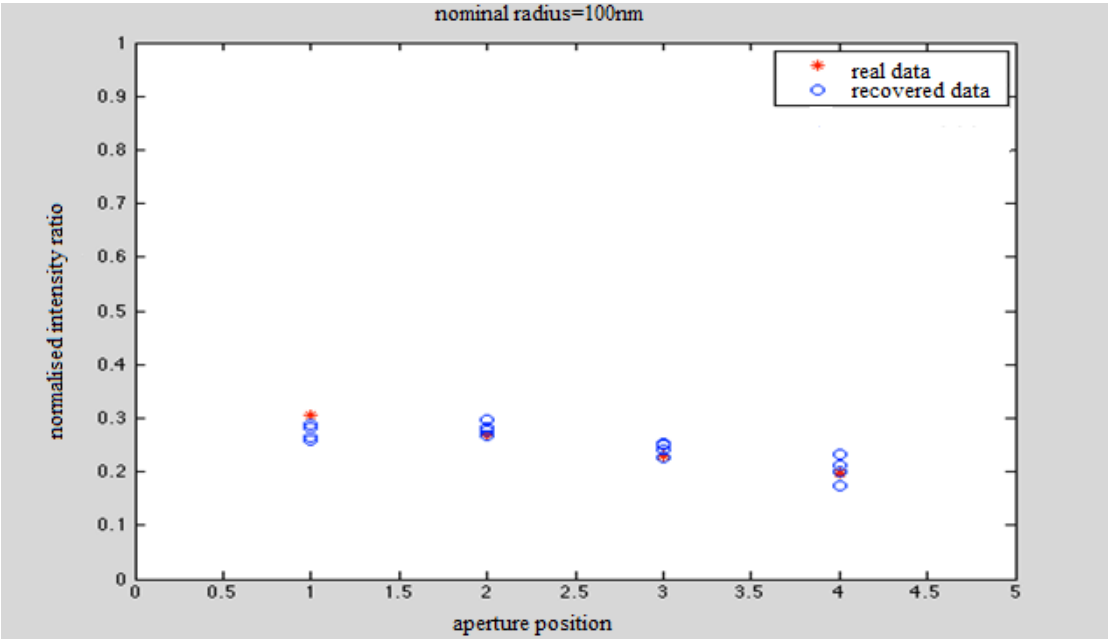

Figure 6.4: Comparisons of the normalised intensity ratios between the theoretical ratios from Mishchenko code and the recovered ratios from a real frame, in inverted order of apertures.

Figure 6.5 recovered the particle size distributions from the SMIT method. Unfortunately, it reconstructs a poor particle size distribution in **Figure 6.5**. Most of the particles are reconstructed around 245nm, which is different from the original radius 100nm.

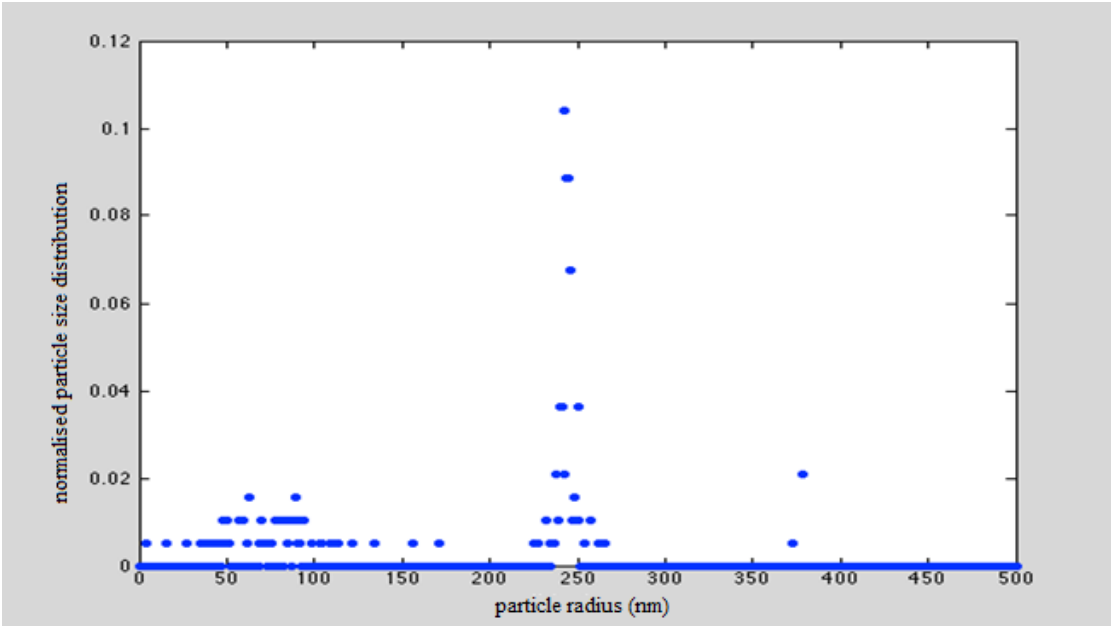

Figure 6.5: Recovered particle size distribution when the nominal radius is 100nm.

Figure 6.6 and **6.7** present the normalised intensity data and recovered particle size distribution when the nominal radius is 150nm, whilst **Figure 6.8** and **6.9** show another example when the nominal radius is 200nm. However, poor quality distributions are recovered in both situations.

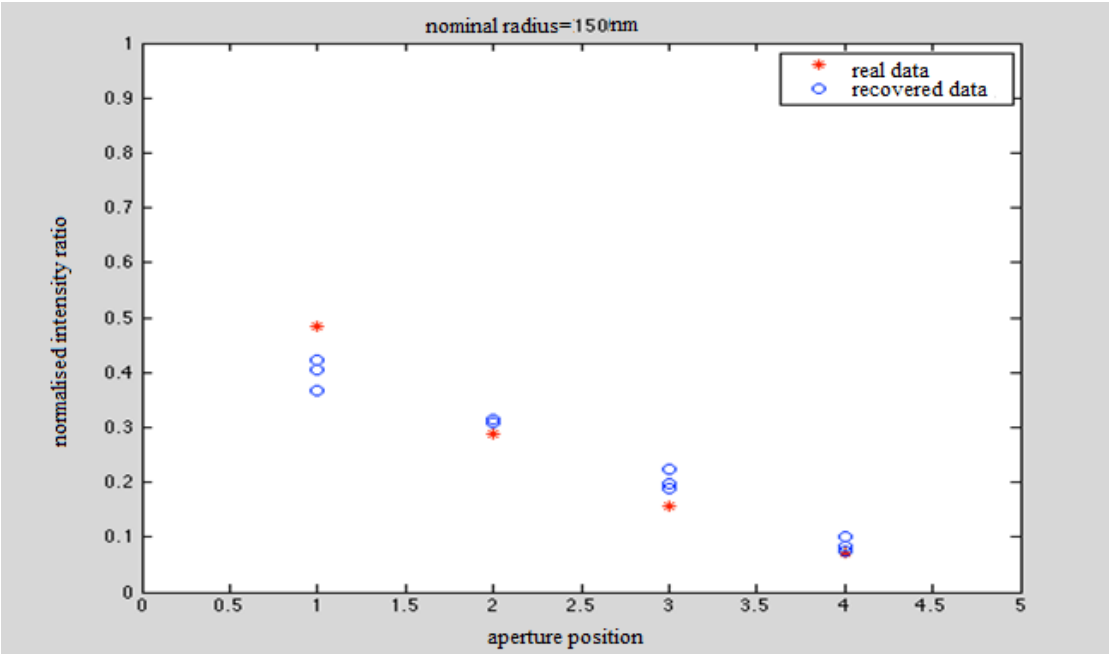

Figure 6.6: Comparisons of the normalised intensity ratios between the theoretical ratios from Mishchenko's code and the recovered ratios from real frames, in inverted order of apertures.

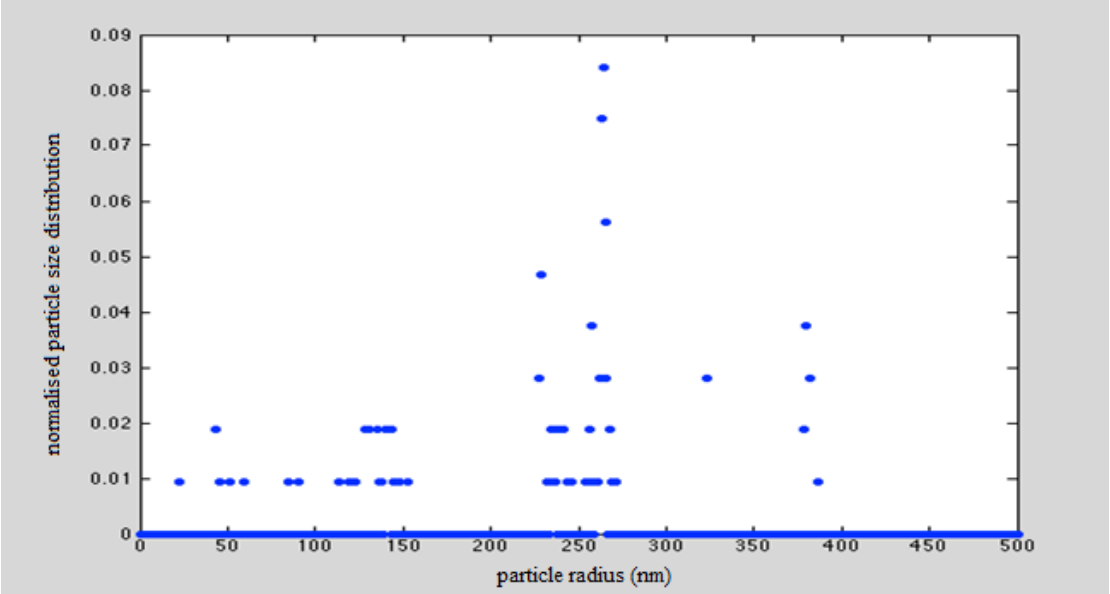

Figure 6.7: Recovered particle size distribution when the nominal radius is 150nm.

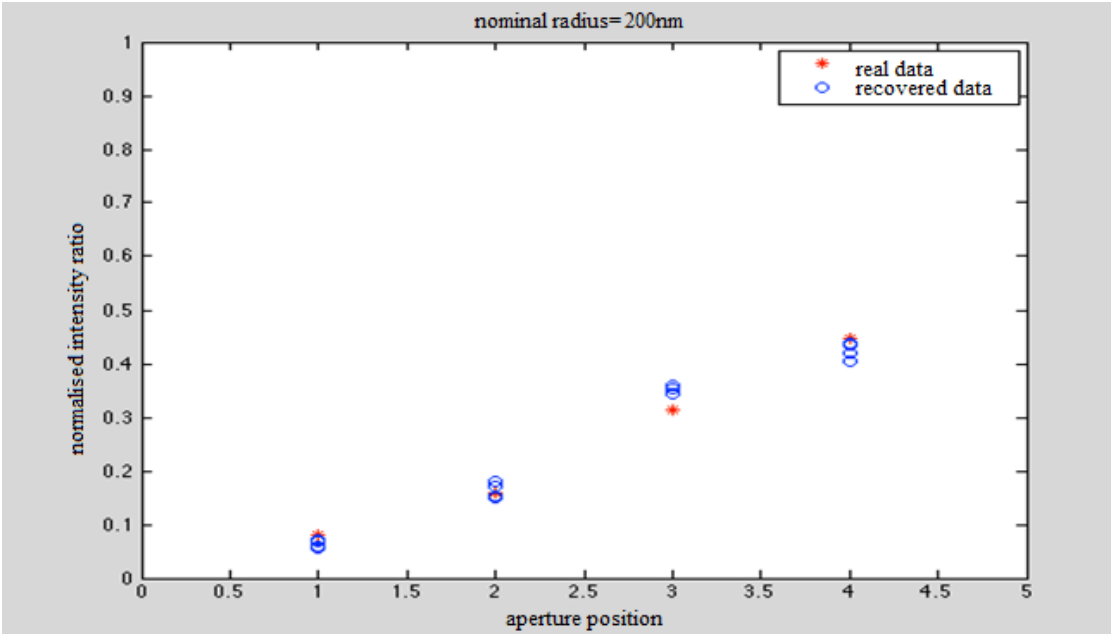

Figure 6.8: Comparisons of the normalised intensity ratios between the theoretical ratios from Mishchenko code and the recovered ratios from real frames, in inverted order of apertures.

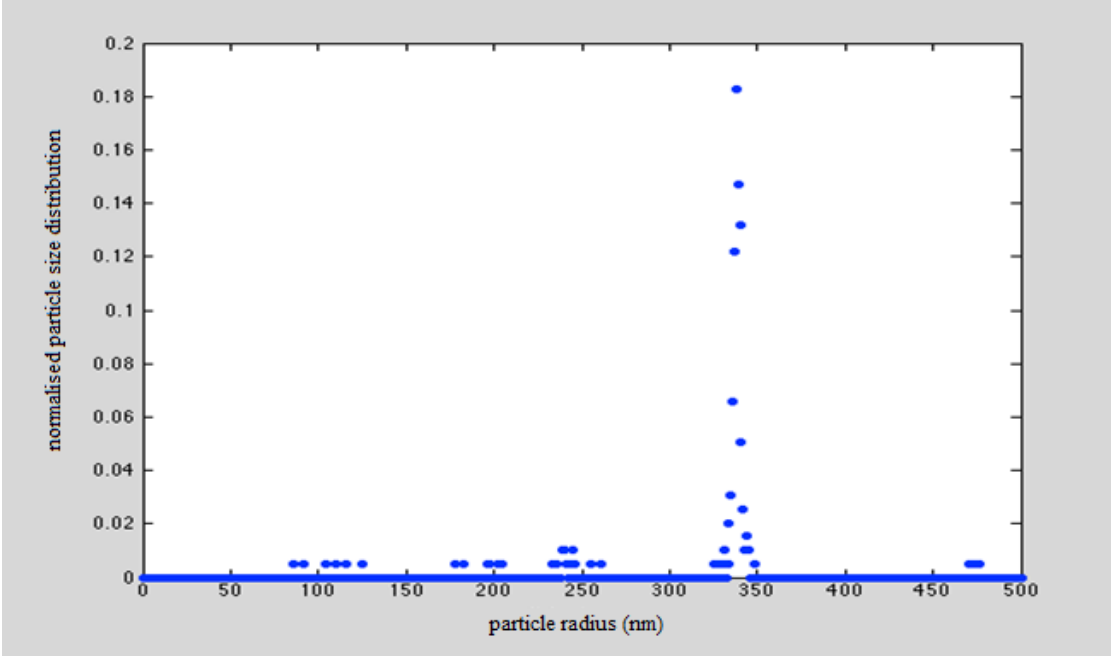

Figure 6.9: Recovered particle size distribution when the nominal radius is 200nm.

According to the figures above, it fails to reconstruct the particle distributions with all these samples, 100nm, 150nm and 200nm. When analysing the normalised intensities, it is found that the normalised intensity ratios are very similar when the particle radius

is 100nm and 245nm. **Table 6.2** compares the normalised intensity ratios at these two sizes.

Radius	Aperture4	Aperture3	Aperture 2	Aperture 1
100nm	0.3069	0.2664	0.2295	0.1972
245nm	0.2659	0.2918	0.2554	0.1869

Table 6.2: Comparisons of the normalised intensity ratios from these four apertures when the particle radii are 100nm and 245nm.

There are many reasons to explain why some of the ratios are smaller than the ideal data, whilst the other ratios are larger than the ideal data. Due to the reflection and refraction of the wedge prism, the recovered intensities using wedge prism should be smaller than the intensities recovered without wedge prism. In addition, due to the optics aberration and distortion, the image captured from the rays far from the optics axis may be defocused in comparison with the image captured from the rays closer to the axis. Therefore, when calculating the intensities from these four pupils, the faint peripheral rings of the defocused particle may be not included due to the background noise. It may results in small intensity ratios for the images captured from the peripheral rays. That explains why the recovered intensity ratios tilted by two prisms from the fourth aperture seem smaller than the theoretical data, whilst the recovered intensity ratios from the second aperture without prism are slightly larger than the theoretical data. When looking for the most suitable size, the intensity ratios from 245nm is more suitable than those from 100nm, and therefore most of the particles are recovered around 245nm when the ideal radius is 100nm in **Figure 6.5**. In this condition, some modifications on the normalised intensity ratios should be done to correct the recovered distribution.

It is difficult to calibrate the set up theoretically according to the optical properties of the components, as there might be errors in the refractive indices of the components and uncertainty in the exact properties of any anti-reflection coatings. It is also difficult to design an experimental approach in which light is directed at different angles into the optical system as this would not include the effect of the light of interest originating from particles at some (not precisely known) depth within the scattering cell. Thus in order to calibrate the experimental results, data from known particle sizes is used to calibrate the experimental set up.

There are some steps to do the modifications.

- Assuming the 100nm sample from Brookhaven Instruments Limited is known. Compare the normalised intensity ratios from the experiment with the theoretical ratios from the Mishchenko code. Correct the intensity ratios from the experiment by percentage. For instance, increasing the intensity ratio from the 2nd aperture by 10%. Normalise the corrected ratios.
- Use the corrected intensity ratios to form a new particle distribution.
- Use the same corrections by percentage in step1 on the other samples (150nm and 200nm), and normalise the corrected ratios. According to the new intensity ratios to form a new distribution.

Based on the 100nm sample, the intensity ratios from the 1st and 4th apertures are increased by 2% and 10%, whilst the intensity ratios from the 2nd and 3rd apertures are decreased by 5% and 11%. Then, normalise these four corrected ratios and form a new particle distribution in **Figure 6.10**.

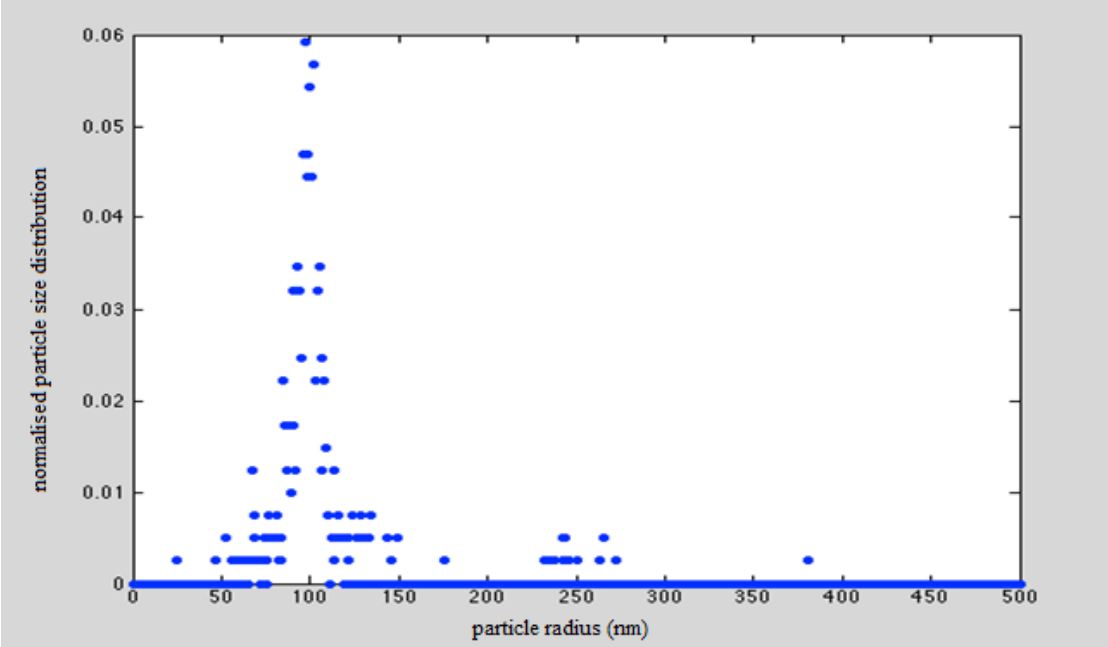

Figure 6.10: Recovered particle size distribution after correction when the nominal radius is 100nm. The main peak recovered is 98nm.

Compared with **Figure 6.5**, most of the recovered particles are around 100nm after correction in **Figure 6.10**, and the recovered distribution is further improved. However, there are still some errors in wrong positions.

In the same correction, the intensity ratios from the 1st and 4th apertures increased by 2% and 10%, whilst the intensity ratios from the 2nd and 3rd apertures decreased by 5% and 11%, **Figure 6.11** and **6.12** present another two corrected distributions. The nominal radii of particles are 150nm and 200nm respectively.

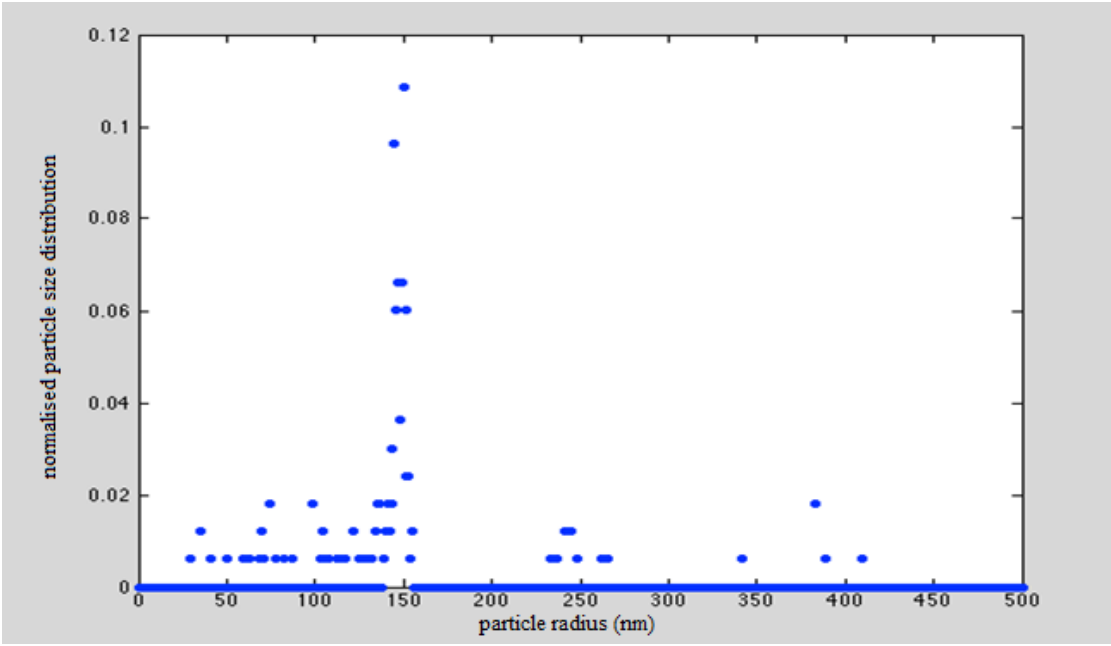

Figure 6.11: Recovered particle size distribution after correction when the nominal radius is 150nm. The main peak recovered is 150nm.

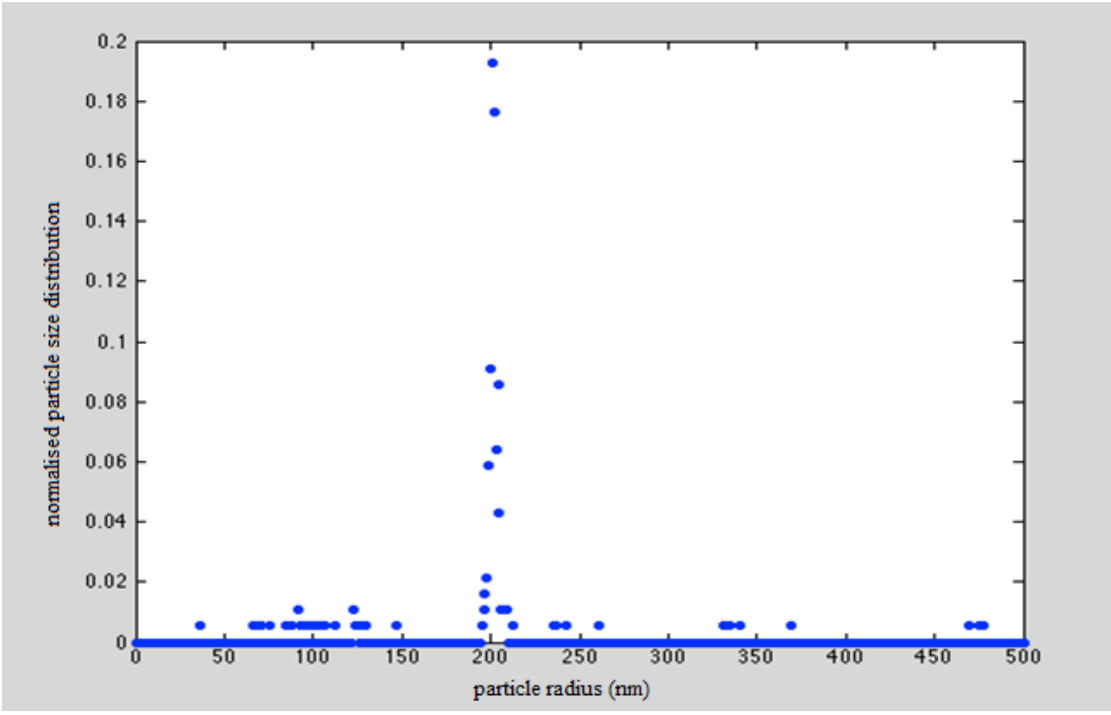

Figure 6.12: Recovered particle size distribution after correction when the nominal radius is 200nm. The main peak recovered is 202nm.

Figure 6.11 and **6.12** recover much better results than the distributions in **Figure 6.7** and **6.9** when the nominal radius is 150nm and 200nm respectively. A majority of

particles match the real sizes. This correction tends to the improvement of the recovered distributions. Although most of the recovered particles are in reasonable agreement with the real size, there are still some wrong sizes recovered in the distributions. These errors result from many factors.

- Some particles may stick together or overlap with each other or close to each other. In this situation, the intensity ratios of the double particles may be different from the ideal data from single particle.
- There are some impurities in the water. Although some filters have been used to minimise the impurities in the water, it cannot eliminate all of them. Some errors may result from these impurities.
- The background noise level is another limitation from the experiment. When the exposure time is 0.1s, for the 8-bit (255) camera, the background noise is up to 13 or 14. When analysing the intensities, the background noise should be subtracted. During this process, it may bring in some errors. If decreasing the exposure time, although the background noise decreases, the particle intensities are also decreasing at the same time and the signal-to-noise ratio is small. If increasing the exposure time, although it increases the signal-to-noise ratio, the signal may blow out the highlights and the background noise becomes large, and then the intensities measured may be not correct.
- The optics aberration is another limitation. The peripheral rays are bent more than the central rays. It therefore does not produce a perfect sharp image for all the four apertures at the same time. This effect may influence the measurement of the particle centre positions and their intensities.
- Distortion should be considered in geometric optics (53, 90, 91). In 'barrel distortion', the apparent effect is that of an image which has been mapped

around a sphere or a barrel. The peripheral image is not exactly the same as the central image. Thus, the images captured from the peripheral pupils may slightly shift.

- In every calculation process, there are some small deviations of the results, such as the image moment method for particle centre finding and particle intensity measurement. Sometimes, for the very similar particles, the small deviation may influence the experiment results.

Overall, the experimental performance of the SMIT method as applied (using a calibration set of data from a sample of assumed size) to samples containing nominally mono-modal particles can be summarized as producing distributions that have a clearly defined peak but that the peak is broader than would be expected for a sample of this sort. The method could be described as working well in giving a peak value in the distribution that is close to the nominal particle size (the main peak value in **Figure 6.10-6.12** is 98nm, 150nm and 202nm compared with a nominal radius of 100nm, 150nm and 200nm). However, all of the distributions exhibit broadening of the main peak and the presence of a number of false peaks, and in this respect the method could not be described as working well. The reasons for these effects are discussed above.

In view of this limited success, the method described in section 5.7.2 (which worked well in computer simulation) was investigated experimentally; this is described in the next section.

6.3 Experiment on the Total-Ratio-Intensity Method

The real experiment on the Total-Ratio-Intensity method is much more complicated than the simulation. There are a few steps to obtain the experimental results.

- A set of 30 consecutive frames with 1s time interval is captured. The nominal radius is 100nm.
- Based on the image moment method, particle centres captured from every aperture can be measured. Calculate the small displacements ***d*** in ***eq. (5.11)*** of every particle between two apertures.
- According to ***eq. (5.11)***, calculate every particle positions ***Z***.
- Calculate the summed intensities measured in the frame.
- For the next frame, track the same particles in the previous steps, and then repeat step**2** to **4**.
- According to ***eq. (5.10)***, for every particle, calculate the real beam position. Average the beam positions calculated from every particle, and set the averaged value to be the real beam position.
- Assuming one sample (100nm) is known, according to eq. **(5.12)**, find the relationship between the real intensities from experiment and the theoretical intensities from Mishchenko code. Use the scaling factor for the other two samples, and follow the steps in Section **5.7.2** to check the accuracy of the total-ratio-intensity method.

Unfortunately, it fails to give the right beam position. **Table 6.3** records the beam position based on 14 individual particles. The beam positions calculated from the real experiment change with different particles, and therefore it is difficult to determine

where the real beam is. One of them cannot provide any beam position, since this particle is assumed to be on focus, and the displacement ***d*** is 0.

Beam position	35.8	-46.7	20.3	109.5	87.3	32.6	-11.3
μm	12.3	30.1	-19.9	50.6	-3.7	NaN	57.8

Table 6.3: Beam position calculated from 14 individual particles.

Compared with the simulation results, there are a few limitations, which can lead to the wrong beam positions.

The major limitations come from the measurement errors of particle centre displacement ***d*** in eq. **(5.11)**. In the simulation, it forms the images from every pupil on every quarter of the image plane accurately. However, in the real experiment, it is difficult to form an image on the expected position. Therefore, it needs to choose a bright sharp peak, and assume it is on focus. Then, corresponding to this peak, move the quarter images to the equivalent position to calculate the small particle centre displacement ***d*** in **eq. (5.11)**. In the simulation, it is assumed in an ideal condition. Although noise conditions are considered, it still ignores many effects. The first image in **Figure 6.13** presents some groups of particle centre positions from every pupil in the simulation, whilst the second image in **Figure 6.13** records every group of particle centre positions in the real experiment.

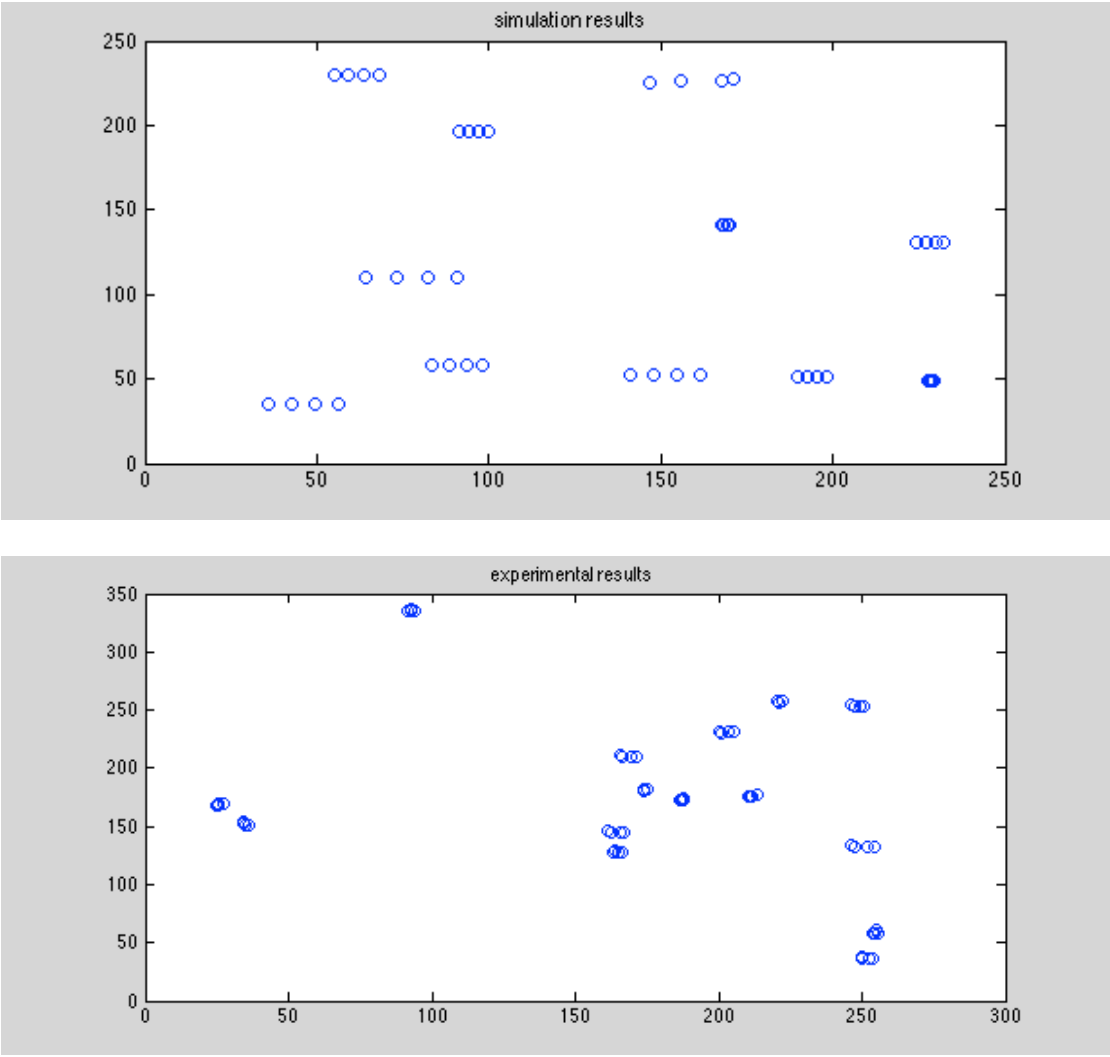

Figure 6.13: Comparisons of some groups of particle centres in the simulation and experiment.

Apparently, in the simulation, particle centre positions in one direction are almost the same, and ***d*** is only the movement of particle centres in the other direction. In addition, the displacements ***d*** measured between every two consecutive apertures are almost even in every group. Compared with the simulation results, the particle centres measured in the experiment are not as good as those in the simulation. Most of the particle centres change in both directions, and the displacements **d** measured between every two consecutive apertures are not even at all. It is really a challenge to deduce an accurate displacement **d**. In this situation, a wrong displacement ***d*** will lead to a wrong particle position and a wrong beam position.

In addition, due to the aberrations and distortions of the lens, the images captured from the peripheral rays are not as sharp as the images captured from the inner rays. When measuring the particle centres with the image moment method, the blurred images may have larger deviations than the bright sharp images. A small shift of the particle centre position may also result in a wrong displacement **d**.

In the field of view, some particles may stick together or overlap with each other. It also brings in the difficulties to find the accurate particle positions.

Noise effect is another crucial limitation. The real experiment is much more complex than the simulation. Just as mentioned in Section **6.2**, the background noise should be subtracted from the signal. During this process, it may bring in some errors.

Finally, because the unit of the displacement of particle centres is very small, the small deviations of every step will lead to a large error of the final results.

In summary, if the beam position cannot be calculated accurately, it is difficult to find the relationship between the particle real intensities with the theoretical data from Mishchenko code, and it therefore cannot realize the total-ratio-intensity method to improve the recovered distributions.

6.4 Summary

Chapter 6 presents some experimental results with the SMIT method. Firstly, the experiment setup is presented in Section **6.1**. Based on the analysis in chapter 5, A Four-hole mask is designed, and the wedge prisms are utilised to tilt the light into

different positions on the image plane. Section **6.2** shows some recovered distributions according to three different samples, with the nominal radius of 100nm, 150nm and 200nm respectively. Without a calibration to account for the different optical transmission of the different angle channels, the SMIT method cannot recover good distributions for all these three samples, since there are many false radii recovered due to the similar intensity ratios in the look-up table. However, after a correction, using the known particle size as calibration, although there are still a few false radii in the distribution, the reconstructed distributions are much better than before, and a majority of particles are in the range of the original data. In section 6.3, it combined the intensity data with the original SMIT method. Although it worked well in the simulation in chapter 5, Unfortunately, it failed to recover particle size distributions with the total-ratio-intensity in real experiment, because it is difficult to measure the accurate beam position. There are many factors resulted in the failures. which were discussed in detail after **Figure 6.13**. In the real experiment, some small measurement errors, the lens aberrations and distortions, and noises are the major limitations to find the accurate results.

7 Conclusions and Future Work

7.1 Conclusions

Particle characterisation has played a crucial role in various industrial and research fields in the last few decades, such as foods, chemical, pharmaceutical, environmental science etc. The extremely broad applications of particle characterisation have led to particle analysis techniques developing rapidly and robustly. Due to the different properties and natures of particles, it is impossible to find a single technique to apply for all particle types in different size ranges. Based on different techniques and theories, different instruments are designed to address specific problems and satisfy specific demand. The weaknesses of one approach may be the strengths of the others. In addition, the cost and sophisticated level in maintaining and operation are the other considerable criteria in determining a suitable technique for a specific demand. Chapter 1 has briefly reviewed the most common non-optical particle sizing techniques, such as sieves, sedimentations, electrical zone sensing, and acoustic analysis. The optical particle sizing techniques now play a critical role due to their high accuracy, rapid measurement time and ease of control. Static Light Scattering (SLS) and Dynamic Light Scattering (DLS) discussed in chapter 1 are the most robust and mature techniques to recover a particle size distribution. The SLS method is suitable for recovering large particles, whilst the DLS method is good for sub-micrometre ranges. A drawback of both SLS and DLS is 'intensity weighting'. If there is a distribution of particle sizes, the larger particles generally contribute a significantly greater proportion of the light than the smaller particles. Thus, the data

collected can be dominated by the larger particles and recovery of the smaller-size part of the size distribution can be of low accuracy. Recently, an alternative technique named Nano-particle Tracking Analysis (NTA) has been implemented. It tracks different particles simultaneously and analyses the trajectories of Brownian motion from individual particles in the liquid rather than the statistical measurement of the movements measured in DLS. A particle size distribution is formed by measuring the averaged movement of many individual particles. It is suitable for sub-micrometre ranges as well. An important advantage of the NTA method is that it produces a size distribution, which is not intensity-weighted.

Chapter 2 introduces an alternative particle sizing technique, Particle Movement Displacement Distribution (PMDD), which is also not intensity weighted. This method has some similarity to the NTA approach as it also investigates the Brownian motions of particles in solution to form a movement distribution. However, compared with the NTA method, it does not track individual particles over many frames, but it measures the centre of individual particles in every image. A vector histogram is formed based on the connection between the centres in the first frame and the centres in the next frame. According to this movement distribution, a maximum likelihood inversion method is applied to recover particle size distribution. A paper about this novel approach has been published in 2012 (57).

Further investigations on the PMDD method have been done in Chapter 3. It optimises various parameters based on simulation results, including time interval, exposure time, noises and sample concentration etc. 1s is the most suitable time interval, and the exposure time is around 20ms to 50ms. Generally a high signal to noise ratio (SNR) will produce better results. When the background level is around

200 in a 12-bit operation, and the background level is less than 20 in an 8-bit operation, the recovered mean radius has a 95% accuracy compared with the original value. That means the background noise in the real Hamamatsu camera used in the experimental work does not influence the results seriously. The best suitable sample concentrations are between $10^6 – 10^7$/ml. Finally, the optimum values of time interval, exposure time and particle concentration were used in conjunction with typical experimental values for the Poisson, background and quantisation noises, to assess the combined effect of all these effects. It shown that the PMDD method was capable to give a better performance compared with DLS in terms of area error (0.29 for PMDD compared with 0.32-0.34 for DLS).

In chapter 4, the PMDD method and a tracking method were compared. In the simulation, it compared different number of frames, and different minimum number of steps in a track. Both methods can recover particle size distribution very well when the number of frames is over 300 and the minimum number of steps in a track is over 5. However, the tracking method gave slightly larger area error and standard deviation than the PMDD method. In the experiment, both methods give good performances except for radius of 50nm. Both methods give wider distributions than the manufacturers quoted values. In each case, the tracking method has a wider distribution than the PMDD method; this result is consistent with the computer simulation results.

For bi-modal distributions, the PMDD method gave poor performance, and it can only reconstruct one peak in two size populations in a mixture. This is a drawback of the PMDD method, whereas the NTA method can recover bi-modal distributions (69).

Another novel particle sizing technique named Separated Multiple Image Technique (SMIT), which is similar to SLS, but is not intensity weighted, is introduced in Chapter 5. This image intensity method is based on the theory of the angular dependent scattering technique and individual visualisation together to reconstruct particle size. This novel approach is able to overcome the intensity domination issue by large particles as in SLS experiment. It is suitable for sub-microns ranges. The method employs a special imaging system with a four-aperture mask and wedge prisms to capture images in the selected directions. For the basic SMIT method, intensity ratios of individual particles at different scattering angles are measured, normalised, and then compared with a theoretical look-up table to deduce the best match particle sizes. The chapter also compares the SMIT method with the MIT method which is introduced by Nam Trung Huynh (81). It was found that former can record more particles and performs a better recovered distribution. In terms of numbers of particles which can yield a size estimate, the SMIT method can record up to 3 times more than the MIT method for the same sample concentration. In terms of the accuracy of the distributions obtained, simulation results showed that (see **Table 5.3**) the area error values were consistently lower for the SMIT method and the P value (see eq. 5.4) is consistently larger.

Moreover, SMIT can reconstruct bi-modal distributions, but it fails in giving the distribution ratios correctly for a wider (e.g. 100nm and 300nm particles) bi-modal distribution (P values for each peak were recovered as 30% and 67% compared with the simulated data with 50% for each peak). For a narrow bi-modal distribution (e.g. 300nm. and 350nm.), the recovered results from SMIT are similar to the original data (P values for each peak were recovered as 41% and 54% compared with the simulated data with 50% for each peak). In order to improve the SMIT's accuracy, Brownian

motion information is combined with the SMIT method, and the total-ratio-intensity method is introduced as well. In the simulation, when combining the Brownian motion information with the SMIT method, the results can be improved but the improvements obtained in simulations were very slight and not consistent eg. the P value did not improve at all and the area error was shown to improve from 0.45 to 0.39 for 200nm particles but for 100nm particles it actually increased from 0.36 to 0.45. In addition, the inclusion of Brownian motion information takes a longer experiment time and records fewer particles. The total-ratio-intensity method not only considers the normalised intensity ratios from the selected directions, but also compares the summed intensities from these selected directions with the predicted data. This method eliminates most of the false radius and further improves the results. For example, in a simulation the area error was reduced from 0.37 for SMIT alone to a value of 0.25 when SMIT was combined with the intensity data. These results suggested that an experimental investigation of this intensity approach might be would be useful.

Experimental work of the SMIT method has been presented in chapter 6. Three different particle samples, 100nm, 150nm and 200nm are chosen to verify the performance of the SMIT method. For the basic SMIT method (without calibration), it fails to recover good quality distributions for all of the samples. After calibration using data from a sample containing particles of known size, it provides a significant improvement on the recovered distributions. A majority of particles are in the range of the original data, but there are still a few false radii recovered. However, the lack of certainty about the actual particle size distributions means that it is not possible to quantify the accuracy of these results. The total-ratio-intensity method has been tried in this chapter. Unfortunately, it fails to provide a correct beam position, and then it

cannot achieve recovering particle size distributions in the real experiment. Some relevant analysis and discussions of the problems have been presented in this chapter.

7.2 Future Work

The Particle Movement Displacement Distribution (PMDD) technique depends on the Brownian motions of particles in solution. However, if the particles are not purely undergoing Brownian movement, such as the fluid flow influence, the technique may give a poor performance even if the adjustments are made. Therefore, the suitable particle container should be well designed to avoid any unwanted motion. Because the intensity is sensitive to the image background level, and the background noise should be subtracted from the measured intensity, therefore, a high quality camera with smaller background noise may improve the results, and the centroiding method for particle position detection needs to be improved as well to provide a good intensity subtraction. The PMDD method gives good performance to recover mono-modal particle size distribution, but it fails to reconstruct a bi-modal particle size distribution. In the future, if it is possible to combine the PMDD method with the individual tracking method from NTA together, it may possible to develop a hybrid technique that would also be able to recover a bi-modal particle size distribution with good accuracy.

The Separated Multiple Image Technique (SMIT) method compares the intensities from the frames with the predicted data. Although it provides good simulation results, the experimental results are not as good as those in the simulation. The intensities captured from real images are influenced by many factors, such as the optics

reflections, refractions, aberrations etc. Some better optics could be worth to try to offer an improvement of the recovered particle size distribution. A modified microscope objective may overcome the aberrations occurring at the cell (water)/glass (air) boundary (such an objective is available from Mitutoyo). Different design of the mask and placement of the wedge prism may be considered to minimise the reflection and refraction effects of the optics. In addition, changing the laser beam direction to obtain the normalised intensity ratios from different scattering angles may be helpful. In the real experiment in section 6.3, it fails to give the correct displacement ***d*** in eq. (5.11), and therefore it is difficult to find the exact beam/particle positions. A possible alternative optical arrangement that might minimise this problem is shown in Figure 7.1. It provides another detection system that is designed specifically to find the correct beam/particle positions. If this optical arrangement was proved to be feasible, then it would be possible to use the total-ratio intensity method (described in section 5.7) to find improved estimates for the particle sizes by eliminating more of the ambiguous results which reduce the final accuracy of the size distribution.

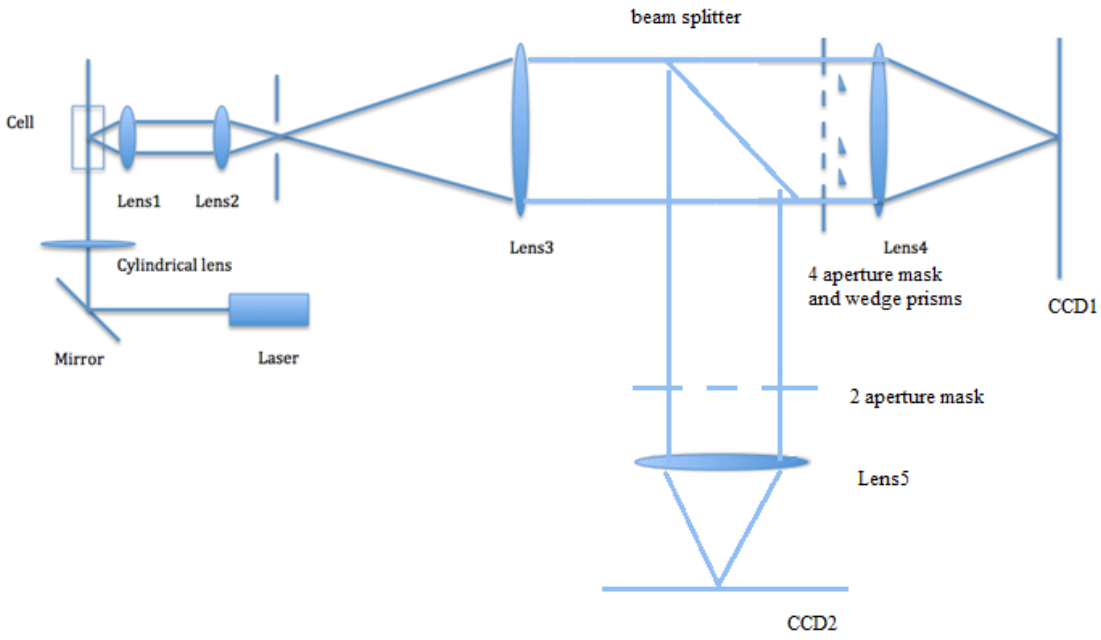

Figure 7.1: A schematic design for an alternative SMIT method.

Compared with **Figure 6.1(a)**, the new design adds a beam splitter, a new mask with two holes, and one more CCD camera. In this condition, some light can go through the four-hole apertures as the original SMIT design, whilst some light can go through the new two-hole apertures and form an image as **Figure 7.2**.

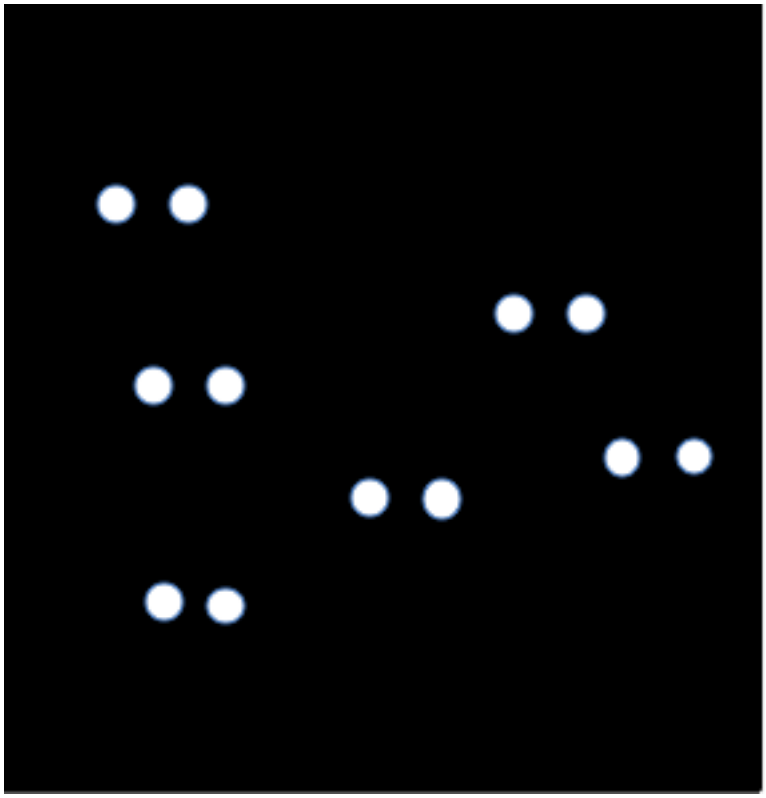

Figure 7.2: Image formation from two-hole aperture.

When designing the two-hole aperture, the space between the two holes should be large enough to form a clear image such as Figure 7.2. For a single particle, it should be a line group pattern. Then, the displacement between two peaks from these two different apertures for a single particle can be measured more correctly. Thus, it is possible to calculate the beam/particle positions with more accuracy and achieve success for the total-ratio intensity method. The key point to note is that the distance between the two peaks measured in this technique are only over a very small range of the CCD detector; in the experimental work described in section 6.3, the displacements needed to be measured between intensity peaks at different sides of the CCD array.

Appendix I: Dynamic Light Scattering

Light Intensity

The intensity of a specific wavelength is a function of the amount of energy through unit area perpendicular to the travel direction per unit time (53). The intensity of light is proportional to the square of the amplitude of the electric field, and is given by:

$$I = \frac{c\varepsilon_0 |E|^2}{2} \tag{A1-1}$$

$$I \propto |E|^2 \tag{A1-2}$$

where c, ε_0, and E is the light speed in vacuum, the electric permittivity of free space, and the amplitude of the electric field respectively.

The total scattered light amplitude can be expressed by the amount of scattered light by individual particles:

$$E = \sum_{n=1}^{N} a_n \exp(i\varphi_n) \tag{A1-3}$$

where a_n is the amplitude factor and φ is the phase factor for the n^{th} particle respectively.

$$\varphi_n = \frac{2\pi dn}{\lambda} \tag{A1-4}$$

where d is the difference in path lengths that the light has traversed when it reaches the detector.

Then, the averaged scattering intensity can be expressed by:

$$\langle I \rangle = \sum_{n=1}^{N} |a_n|^2 \tag{A1-5}$$

Autocorrelation Function

According to (28, 46), the first order electric field correlation function can be expressed as:

$$g^{(1)}(\tau) = \frac{\langle E(t)E^*(t+\tau) \rangle}{\langle I \rangle^2} \tag{A1-6}$$

For a poly-disperse sample, equation (**0.6**) can be represented by a function of particle size distribution $f(R)$:

$$g^{(1)}(\tau) = \int_0^\infty f(R) \exp(-\Gamma\tau) dR \tag{A1-7}$$

$$\Gamma = Dq^2 \tag{A1-8}$$

where ***D*** is the diffusion coefficient in formula (A**1-8**), and ***q*** is the scattering vector, which is determined by the wavelength of light ***λ***, the refractive index of the suspension ***n***, and the light scattering angle ***θ***, and is given by:

$$q = \frac{4\pi n}{\lambda} \sin\left(\frac{\theta}{2}\right) \tag{A1-9}$$

The intensity autocorrelation function $g^{(2)}(\tau)$ is the Fourier transform of the noise frequency spectrum, and represents the time domain equivalent of the frequency spectrum. The autocorrelation function $g^{(2)}(\tau)$ of the intensity fluctuation can be represented by the function of time ***I(t),*** and is given by:

$$g^{(2)}(\tau) = \frac{\langle I(t)I(t+\tau)\rangle}{\langle I\rangle^2} \qquad \text{(A1-10)}$$

According to Ford (1983) (3, 44), the frequency spectrum $P(\omega)$ of the intensity from randomly diffusing monodisperse spheres can be shown in a Lorentzian distribution:

$$P(\omega) = \frac{2Dq^2/\omega}{\omega^2 + (2Dq^2)^2} \qquad \text{(A1-11)}$$

where **D** is the diffusion coefficient, ***ω*** is the frequency and ***q*** is the scattering vector in equation (**A1-9**).

The Fourier Transform of a Lorentzian distribution is an exponential function; thus an autocorrelation function of the noise frequency spectrum will decay exponentially. The autocorrelation function for scattering from monodisperse spheres is expressed as:

$$g(\tau) = 1 + \exp(-Dq^2\tau) \qquad \text{(A1-12)}$$

According to the Siegert Relation (28, 45), the intensity correlation function that can be measured in the experiments is related to the electric field correlation function that is usually predicted from the theory as follows:

$$g^{(2)}(\tau) = 1 + \left|g^{(1)}\right|^2 \qquad \text{(A1-13)}$$

In a real experiment system, the autocorrelation function is measured as a function of:

$$g^{(2)}(\tau) = A\left(1 + \beta\left[g^{(1)}(\tau)\right]^2\right) \tag{A1-14}$$

Where $\boldsymbol{\beta}$ is a scaling factor dependent on the detection arrangement and $\boldsymbol{A}$ is the baseline offset, which is due to the uncorrelated sources and background scattering; ideally $\boldsymbol{A}$ is equal to 1.

Appendix II: Image formation

(a)

In order to form an image, the total scattered light expected to reach the detector from each particle is calculated. This calculation depends on the particle properties, its position within the illuminating beam, the intensity profile of the illuminating beam, and the collection angle of the imaging lenses.

Normally, lasers emit beams with a Gaussian profile which is operated on the fundamental transverse mode or "TEM_{00} mode" of electromagnetic radiation. The light with Gaussian beam means the transverse electric field of the light and intensity distributions are in Gaussian distribution. A simple Gaussian beam follows a normal distribution in formula (A2-1).

$$G(x,y)=\frac{1}{2\pi\delta_1\delta_2}\exp\left\{-(\frac{x^2}{\delta_1^2}+\frac{y^2}{\delta_2^2})\right\} \tag{A2-1}$$

Solid angle is a parameter influencing the image formation. It measures the probability of photons which impinge on the detector lens. It can be defined as (62):

$$\Omega=\frac{\pi R^2}{L^2} \tag{A2-2}$$

where ***R*** is the radius of the detector lens, ***L*** is the distance between the origin and the detector lens.

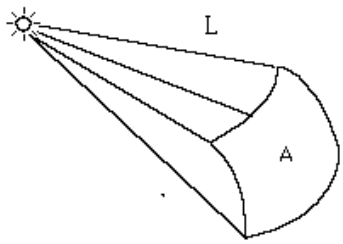

Figure 1: Solid angle sketch diagram. ***A*** is the area of the sphere while ***L*** is the radius of the sphere.

The intensity of every particle can be calculated from the laser power, the particle position in the illuminate beam, and the laser beam profile. Based on the quantum efficiency of the detector (0.25 when the wavelength is 532nm), the expected number of photons in each pixel can be calculated and then the detected number of photons is simulated by calling a random number from a Poisson distribution with the expected value as the mean.

(b)

The size of particle is a convolution of diffraction pattern with the radii of out of focus object.

Diffraction pattern

Diffraction of lens is a basic limitation in image optics even for an ideal lens without aberration. The image quality is affected by diffraction. Therefore, diffraction limited resolution of the lens should be considered in the experiment.

Diffraction occurs when the light is stopped by any obstacle. When the light passes through the lens, the lens is regarded as a circular stop. The intensity distribution of

light in the spot created in image plane is shown in Figure 2. The formula of the intensity distribution is derived from the following function (60).

$$I(P) = |E(P)|^2 = \left(\frac{2J(s)}{s} \right)^2 I_0 \text{; where } s = \frac{k\omega D_a}{2} = \frac{\pi\omega D_a}{\lambda} \qquad \text{(A2-3)}$$

where I_0 is the peak intensity, J_1 is Bessel function of the 1st order.

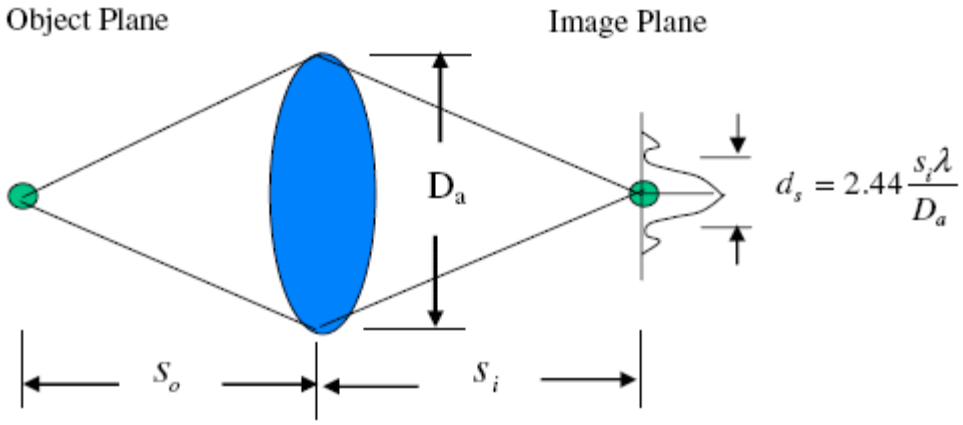

Figure 2: Airy function of width $d_s = 2.44\frac{s_i\lambda}{D_a}$

The intensity distribution oscillates with a strong central maximum followed by dark and bright rings with decreasing intensity. Basically, most of the energy is concentrated in the central maximum (Airy disk) which is limited by the first dark ring. The first zero in J (Bessel Function) occurs at $s = 1.22\pi$ which is the first dark ring position. The central maximum size can be deduced from the expression:

$$s = 1.22\pi = \frac{\pi\omega D_a}{\lambda} \qquad \text{(A2-4)}$$

Such that $\omega = {}^{d_S}\!/_{2s_i}$, yields the well known result for the diameter of the point spread functions.

$$\mathrm{d_s} = \frac{2.44 s_i \lambda}{D_a} \qquad \text{(A2-5)}$$

Therefore, d_s is the diameter of the Airy disk.

Circle of confusion (out of focus)

The thin lens is utilized to condense the light illuminated by the particles to CCD camera. During this process, since the particles are not exactly on the object plane and the optical spot caused by the light rays from the thin lens can not come to a perfect focus, therefore circle of confusion will generated through the thin lens. It will lead to a blur circle on the image plane which will have an impact on finding centre of particles.

According to the properties of thin lens, the diameter of the circle of confusion can be deduced. If the distance from object to thin lens and from the thin lens to image are S_1 and f_1 respectively, the relations related to focal length is formed by the thin lens formula:

$$\frac{1}{S_1}+\frac{1}{f_1}=\frac{1}{f} \tag{A2-6}$$

where f is the focal length.

The magnification of the lens is given by:

$$m=\frac{f_1}{S_1}=\frac{h_1}{h_0} \tag{A2-7}$$

If a spot which is out of focus is located at X'' (see Figure 3) in the image plane, a blur circle will occur. To calculate the diameter of the circle of confusion, the simple method is to calculate the diameter of the blur circle in a virtual image in the object plane, and then multiply by the magnification of lens.

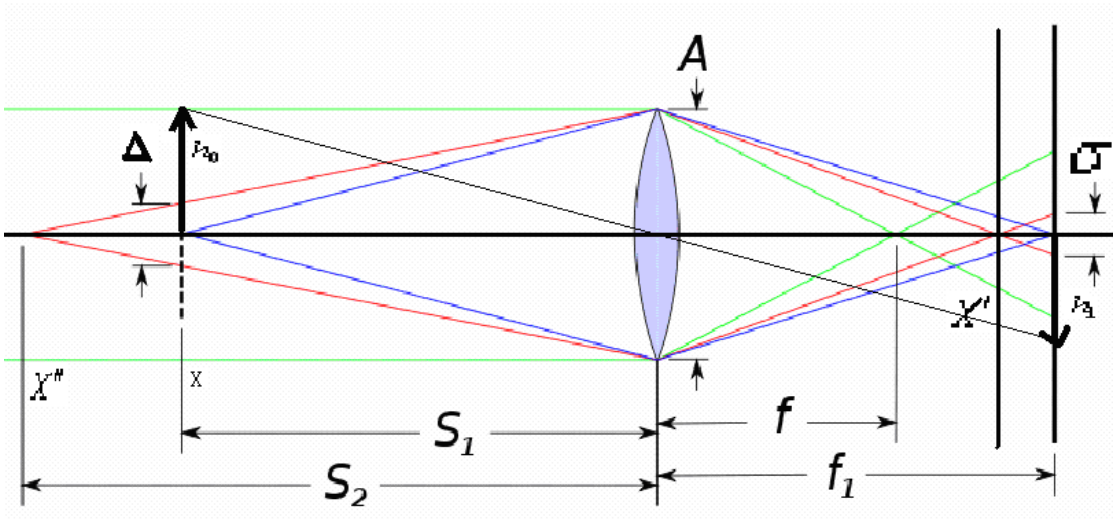

Figure 3: Geometrical illustration of the circle of confusion. One spot is out of focus at position $X^{"}$ and forms a blur circle with diameter σ .

According to the theory of similar triangle, the diameter from the virtual image in the object plane is proportional to the diameter of the lens:

$$\Delta = \left| \frac{x'' - x}{x''} \right| * A \qquad \text{(A2-8)}$$

The diameter of the circle of confusion in the focal plane is obtained by multiplying by magnification ***m***:

$$\sigma = m * \Delta \qquad \text{(A2-9)}$$

Finally, the size of particle is calculated from the convolution of diffraction pattern with the radii of out of focus object.

Appendix III: Poisson Noise, Readout Noise, Background Noise and Quantisation Noise in the Image Intensity Technique

Noise is a crucial parameter in the image intensity technique. This thesis mainly considers the Poisson noises, background noise and the quantisation noise of the CCD camera.

The image on a CCD is an array of pixels. Each pixel performs as a detector. The number of photons that reach a detector within a sample time follows a Poissonian distribution. The number of photon-electrons $\mathbf{n_p}$ that reach an image pixel $\mathbf{p_i}$ in a sample time $\mathbf{\Delta t}$ can be calculated by:

$$n_p = \overline{n}.\Delta t$$

where $\overline{n}$ is the mean count rate of photon-electrons.

Then, the brightness (count) $\mathbf{I_i}$ of pixel $\mathbf{p_i}$ is expressed as:

$$I_i = \frac{n_p}{g}$$

where **g** is the amplifier gain conversion coefficient (electrons per count) of a CCD camera.

A Poisson noise factor is defined by the reasonable maximum brightness of an image corresponding to an exposure time:

$$\alpha = \frac{n_{p-\max}}{g}$$

Where $\mathbf{n_{p\text{-}max}}$ is the number of photon-electrons at the reasonable maximum intensity pixel.

If the field intensity array of the image is defined as ***I***, the array of number of photons $\mathbf{N_e}$ in a given sample time corresponding to a Poisson noise factor $\boldsymbol{\alpha}$ can be expressed as:

$$N_e^{count} = N_e^{normalised}.\alpha = \frac{I}{\mathrm{I}_{\max}}.\alpha$$

Where $\mathbf{I_{max}}$ is the maximum field intensity of the image.

Practically, a readout noise from CCD camera is added into the output. Therefore, the array of number of photons $\mathbf{N_e}$ is given by:

$$N_e = g\frac{I}{I_{\max}}\alpha + r^2$$

where **r** is the Root Mean Square (RMS) value of the readout noise of a camera.

The photons reached the pixels follow the Poissonian distribution as follows:

$$N_e^{noise} = P(N_e)$$

where **P(x)** is a function to generate Poisson random numbers with mean **x**.

The brightness (count) array with noises can be obtained by the following equation:

$$N_e^{noise}(count) = \frac{N_e^{noise} - r^2}{g}$$

In addition, considering the background noise of the image, the simulated noisy image can be rewritten as:

$$I_{noise} = \frac{P(N_e)}{g} + b - \frac{r^2}{g}$$

where **b** is the background level with the unit of count.

Quantisation level of the CCD camera is another limitation of the image qualities. For example, the quantisation range is from 0 to 4095 counts for a 12 bit camera. Any value of $\mathbf{I_{noise}}$ bigger than 4095 (2^{12-1}) is clipped.

Thus, the final noise image $\mathbf{I_{final}}$ can be expressed as:

$$I_{final} = round(I_{soise})$$

8 Reference

1. Waurice Waite, (2009), Particle, Oxford Paperback Dictionary and Thesaurus, 3rd ed, Oxford University Press.
2. Controlling Coffee Quality Using Laser Diffraction, (2012), Application Note, Malvern Food and Drink Particle Measurement, access in (2012), online available:http://www.malvern.com/malvern/kbase.nsf/allbyno/KB001054/$file/MRK781-01.pdf.
3. Clive Washington, (1992), Particle Size Analysis in Pharmaceutics and Other Industries Theory and Practice, Ellis Horwood Limited.
4. Renliang. Xu, (2000), Particle Characterization: Light Scattering Methods, USA: Kluwer Academic Publishers.
5. Maria da Graca Rasteiro, Albano Jorge, (2007), The Influence of Particle Size Distribution on the Performance of Ceramic Particulate Suspensions, Particle & Particle Systems Characterization, Vol. 24, p. 101-107.
6. Terence Allen, (1997), Particle Size Measurement, Volume1, Powder Sampling and Particle Size Measurement, 5th ed, London: Chapman&Hall.
7. Martin J. Rhodes, (2008), Introduction to Particle Technology, 2nd ed, Australia: Wiley.
8. T. Santoro, G. Stotzky, L. T. Rem (1967), Electrical Sensing Zone Particle Analyzer for Measuring Germination of Fungal Spores in the Presence of Other Particles, Applied Microbiology, Vol. 15, No. 4, p. 935-639.
9. H.S.Chung, R.Hgg, (1985), The Effect of Brownian Motion on Particle Size Analysis by Sedimentation, Power Technology, Vol. 41, p. 211-216.

10. Alexander Bootz, Vitali Vogel, Dieter Schubert, Jorg Kreuter, (2004), Comparison of Scanning Electron Microscopy, Dynamic Light Scattering and Analytical Ultracentrifugation for the Sizing of Poly (Butyl Cyanoacrylate), European Journal of Pharmaceutics and Biopharmaceutics, Vol. 57, p. 369–375.
11. D. Fairhurst, A.S. Dukhin, Skin Delivery Systems, Chapter 11, Acoustic Attenuation Spectroscopy: A New Technique to Characterize the Stability and Structure of Semi- solid Topical Delivery Systems for Cosmetic and Pharmaceutical Applications, access in (2012), online available: http://www.particlesciences.com/docs/Skin_Delivery_Systems_Ch11.pdf.
12. Alexander K. Hipp, Giuseppe Storti, Massimo Morbidelli, (2002), Acoustic Characterization of Concentrated Suspensions and Emulsions. 1. Model Analysis, Langmuir, Vol. 18, p. 391-404.
13. Andrei S. Dukhin, Philip J. Goetz, (2001), New Developments in Acoustic and Electroacoustic Spectroscopy for Characterizing Concentrated Dispersions. Colloids and Surfaces, Physicochemical and Engineering Aspects, Vol. 192, p. 267-306.
14. Andrei S. Dukhin, Philip J. Goetz (1996), Acoustic and Electroacoustic Spectroscopy, American Chemical Society, Langmuir, Vol. 12, p. 4336–4344.
15. R. J. Potwora, L. R. Ingle, D. O. Rester, (1998), Powdered Activated Carbons a New Generation for Sugar Refining, International Sugar Journal, Vol. 100, p. 76-79.
16. Konák C, Jakes J, Stepánek P, Petrás F, Kárská M, Krepelka J, Perina J, (1991), Effect of Multiple Light Scattering on Transmitted and Scattered Light, Applied Optics, Vol. 30, p. 4865-4871.

17. Terence Allen, Keith Marshall, (1972), The Electrical Sensing Zone Method of Particle Size Measurement (the Coulter Principle), Bradford University.
18. Marcela Alexander, Douglas G. Dalgleish, (2006), Dynamic Light Scattering Techniques and Their Applications in Food Science, Food Biophysics, Vol. 1, p. 2-13.
19. J. D. Sherwood, (1987), Electrical Sensing Zone Method for Particle Size Analysis. Analytical Proceedings, Vol. 24, p. 277-281.
20. Andrei S. Dukhin, Philip J. Goetz, (2002), Ultrasound for Characterizing Colloids Particle Sizing, Zeta Potential Rheology, Elsevier Science.
21. Yunfei Sun, (2007), Data Inversion for Photon Correlation Spectroscopy (Ph.D thesis), University of Nottingham.
22. Yunfei Sun, John G. Walker, (2008), Maximum Likelihood Data Inversion for Photon Correlation Spectroscopy, Measurement Science and Technology, Vol. 19, 115302.
23. Robert Brown, (1827), A Brief Account of Microscopical Observations Made on the Particles Contained in the Pollen of Plants, and on the General Existence of Active Molecules in Organic and Inorganic Bodies, Philosophical Magazine, Vol. 4, p. 161-173.
24. Albert Einstein, (1905), The Motion of Elements Suspended in Static Liquids as Claimed in the Molecular Kinetic Theory of Heat, Annalen Der Physik, Vol. 17, No. 8, p. 549-560.
25. H. C. Van De Hulst, (1957), Light scattering by small particles, New York: John Wiley and Sons.
26. Paul A. Webb, (2000), A Primer on Particle Sizing by Static Laser Light Scattering, Technical Workshop Series: Introduction to the Latest ANSI/ISO

Standard for Laser Particle Size Analysis, Micromeritics Instrument Corp, access in (2012), online available: http://www.particletesting.com/docs/primer_particle_sizing_laser.pdf.

27. Marta Sartor, Dynamic Light Scattering: to Determine the Radius of Small Beads in Brownian Motion in a Solution, University of California San Diego, access in (2012), online available: http://physics.ucsd.edu/neurophysics/courses/physics_173_273/dynamic_light_scattering_03.pdf.
28. Charles Sidney Johnson, Don A. Gabriel, (1994), Laser Light Scattering, New York: Dover Publications.
29. Craig F. Bohren, (2010), Scattering by Particles, Pennsylvania, Handbook of Optics, Pennsylvania State University: The McGraw-Hill Companies.
30. David W. Ball, (1962), the Basics of Spectroscopy, Spie Press.
31. Michael I. Mishchenko, Joachim W. Hovenier, Larry D. Travis, (2000), Light Scattering by Nonspherical Particles, Theory, Measurements and Applications, Academic Press.
32. Martine Schneider, Timothy F. McKenna, (2002), Comparative Study of Methods for the Measurement of Particle Size and Size Distribution of Polymeric Emulsions, Particle & Particle Systems Characterization, Vol. 19, No. 1, p. 28-37.
33. E Vanden Bussche, Y De Deene, P Dubruel, K Vergote, E Schacht, C De Wagter, (2004), The Use of Static Light Scattering for the Structure Analysis of Radiosensitive Polymer Gels: a Literature Survey, Institute of Physics Publishing, Journal of Physics, 3rd International Conference on Radiotherapy Gel Dosimetry, p. 180-183.

34. Laser Diffraction Particle Sizing, access in (2011), online available: http://www.malvern.com/LabEng/technology/laser_diffraction/particle_sizing.htm.
35. Alan Rawle, Malvern instruments limited, Basic Principles of Particle Size Analysis, access in (2012), online available: http://www.atascientific.com.au/publications/wp-content/uploads/2012/07/Basic_principles_of_particle_size_analysis_MRK034-low_res.pdf.
36. Michael.I. Mishchenko, Larry D. Travis, (1998), Capabilities and Limitations of a Current Fortran Implementation of the T-matrix Method for Randomly Oriented, Rotationally Symmetric Scatters, Journal of Quantitative Spectroscopy and Radiative Transfer, Elsevier Science, Vol. 60, No. 3, p. 309-324.
37. Michael. I. Mishchenko, Larry D. Travis, Andrew A. Lacis, (2002), Scattering, Absorption, and Emission of Light by Small Particles, UK: Cambridge University Press.
38. Michael.I. Mishchenko, (1991), Light Scattering by Randomly Oriented Axially Symmetric Particles, Optical Society of America, Vol. 8 No. 6, p. 871-882.
39. Peter. W. Barber, Steven. C. Hill, (1990), Light Scattering by Particles, 1st ed, World Scientific Publishing.
40. J. W. Hovenier, C. V. M. Van Der Mee, (1983), Fundamental Relationships Relevant to the Transfer of Polarized Light in a Scattering Atmosphere, Astronomy and Astrophysics, Vol. 128, p. 1-16.

41. P. C. Waterman, (1965), Matrix Formulation of Electromagnetic Scattering, Proceedings of the IEEE, Vol. 53, p. 805-812.
42. Rorbert Pecora, (1976), Dynamic Light Scattering: Application of Photon Correlation Spectroscopy, New York: John Wiley.
43. Benjamin Chu, (1991), Laser Light Scattering, 2nd ed, New York: Academic Press.
44. Barton E. Dahneke, (1983), Measurement of Suspended Particles by Quasi-elastic Light Scattering, New York: John Wiley, p. 32-78.
45. Eric Jakeman, Kevin D. Ridley, Fluctuations in Scattered Light, access in (2012), online available: http://www.optica.unican.es/rno7/Contribuciones/ArticulosPDF/Jakeman.pdf.
46. Herman Z. Cummins, Edward Roy Pike, (1974), Photon Correlation and Light Beating Spectroscopy, New York: Plenum Press.
47. Stephen W. Provencher, (1982), CONTIN: a General Purpose Constrained Regularization Program for Inverting Noisy Linear Algebraic and Integral Equations. Computer Physics Communications, North-Holland Publishing Company, Vol. 27, p. 229-242.
48. Otto Glatter, Johann Sieberer, Heimo Schnablegger, (1991), A Comparative Study on Different Scattering Techniques and Data Evaluation Methods for Sizing of Colloidal Systems Using Light Scattering. Particle & Particle Systems Characterization, Vol. 8, No. 4, p. 274-281.
49. Dennis E. Koppel, (1972), Analysis of Macromolecular Polydispersity in Intensity Correlation Spectroscopy: The Method of Cumulants, Journal of Chemical Physics, Vol. 57, Is. 11, p. 4814-4820.

50. Bruce J. Berne, Robert Pecora, (2000), Dynamic Light Scattering with Application to Chemistry, Biology, and Physics, Canada: Dover Publications.
51. Mario. Bertero, Patrizia Boccacci, (1998), Introduction to Inverse Problems in Imaging, Bristol: Institute of Physics Publishing.
52. Edward Collett, (2005), Field Guide to Polarization, Spie Press Published.
53. Francis A. Jenkins, (2001), Fundamental of Optics, 4th ed, p. 230-231.
54. Kenneth S. Schmitz, (1990), An Introduction to Dynamic Light Scattering of Macromolecules, USA: Academic Press Inc.
55. Albert Einstein, Edited by R. Furth, Translated by A. D. Cowper, (1926), Investigations on the Theory of the Brownian Movement, Dover Publication Inc.
56. R. S. Longhurst, (1967), Geometrical and Physical Optics, 2nd ed, the University of California, Wiley Published.
57. John G Walker, Nam Trung Huynh and Rui Chen, (2012), Image Vector Histogram Approach to Nanoparticle Sizing, Applied Optics, Vol. 51, No. 5, p. 651-658.
58. C.Fosu, G W.Hein, B.Eissfeller, Determination of Centroid of CCD Star Images, Institute of Geodesy and Navigation Commission III, WG III/8.
59. Naftaly Menn, (2004), Practical Optics, Elsevier, Academic Press.
60. Carl D Meinhart, Steven T Wereley, (2003), The Theory of Diffraction-limited Resolution in Microparticle Image Velocimetry, Institute of Physics Publishing, Measurement Science and Technology, Vol. 14, p. 1047-1053.
61. Sidney F. Ray, (2002), Applied Photographic Optics: Lenses and Optical Systems for Photography, Film, Video, 3rd ed, Electronic and Digital Imaging.

62. A. Van Oosterom, J. Strackee, (1983), The Solid Angle of a Plane Triangle, IEEE Transactions on Biomedical Engineering, Vol. 30 No. 2, p. 125–126.
63. Mortimer Abramowitz, H. Ernst Keller, Kenneth R. Spring, Microscope Objectives: Optical Aberrations, The Florida State University, access in (2012), online available: http://micro.magnet.fsu.edu/primer/anatomy/aberrationhome.html.
64. Linos Photonics, access in (2011), online available: http://www.winlens.de/.
65. Alan C. Bovik, (2005), Handbook of Image and Video Processing, Elsevier Academic Press.
66. Bernard Widrow, István Kollár, (2008), Quantization Noise, Roundoff Error in Digital Computation, Signal Processing, Control, and Communications, Cambridge University Press.
67. Thermo scientific, access in (2012), online available: www.thermoscientific.com.
68. Bob Carr, Patrick Hole, Andrew Malloy, Philip Nelson, Matthew Wright, Jonathan Smith, (2009), Applications of Nanoparticle Tracking Analysis in Nanoparticle Research – a Mini-Review, European Journal of Parenteral & Pharmaceutical Sciences, Pharmaceutical and Healthcare Sciences Society, Vol. 14, p. 45-50.
69. Vasco Filipe, Andrea Hawe, Wim Jiskoot, (2010), Critical Evaluation of Nanoparticle Tracking Analysis (NTA) by NanoSight for the Measurement of Nanoparticles and Protein Aggregates, Pharmaceutical Research, Vol. 27, No. 5, p. 796-810.
70. Colin Sheppard, David Shotton, (1997), Confocal Laser Scanning Microscopy, New York: Springer-Verlag.

71. U. Durig, D. W. Pohl, F. Rohner, (1986), Near-field Optical-Scanning Microscopy, Journal of Applied Physics, Vol. 59, No. 10, p. 3318-3327.
72. Frank M. Etzler, Marie S. Sanderson, (1995), Particle Size Analysis: a Comparative Study of Various Methods, Particle & Particle Systems Characterization, Vol. 12, No. 5, p. 217-224.
73. Thomas Wriedt, (2003), Electromagnetic and Light Scattering-Theory and Application VII, Germany: University Bremen.
74. Jose G. DosRamos, Cesar A. Silebi, (1990), The Determination of Particle-Size Distribution of Submicrometers Particles by Capillary Hydrodynamic Fractionation (CHDF), Journal of Colloid and Interface Science, Vol. 135, Is. 1, p. 165-177.
75. Hamish Small, (1974), Hydrodynamic Chromatography – A Technique for Size Analysis of Colloidal Particles, Journal of Colloid and Interface Science, Vol. 48, No. 1, p. 147-161.
76. Terence Allen, (1997), Particle Size Measurement - Volume 2: Surface Area and Pore Size Determination, 5th ed, London: Chapman & Hall.
77. T. Schildknecht, (1994); Optical Astronomy of Fast Moving Objects Using CCD Detectors, Swiss Geodetic Commission.
78. A. Chubunichev, (1992), Algorithms of Digital Target Location and Their Investigations, ISPRS Journal, Vol. XXIX, Part B5, p.151-154.
79. Joseph W. Goodman, (2005), Introduction to Fourier Optics, 3rd ed, USA: Roberts & Company Publishers.
80. Suganda Jutanulia, Toshimitsu Asakura, (2002), Optical Fourier Transform Theory Based on Geometrical Optics, Optical. Engineering, Vol. 41, No. 1, p. 13-16.

81. Nam Trung Huynh, (2009), Novel Techniques for Particle Sizing, (Ph. D thesis), University of Nottingham.
82. Jeff Conrad, (2006), Depth of Field in Depth, large format page, access in (2012), online available: http://www.largeformatphotography.info/articles/DoFinDepth.pdf.
83. Jeff Conrad, (2006), An Introduction to Depth of Field, large format page, access in (2012), online available: http://www.largeformatphotography.info/articles/IntroToDoF.pdf.
84. F. G. Smith, J. H. Thomson (1971), A Degree Physics Optics, John Wiley & Sons Ltd.
85. Michael I. Mishchenko, Larry.D.Travis, (1994), T-Matrix Computations of Light Scattering by Large Spheroidal Particles, Optics Communications, Vol. 109, Is. 1-2, p. 16-21.
86. Michael I. Mishchenko, Gorden Videen, Victor A. Babenko, Nikolai G. Khlebtsov, Thomas Wriedt, (2004), T-matrix Theory of Electromagnetic Scattering by Particles and Its Applications: a Comprehensive Reference Database, Journal of Quantitative Spectroscopy & Radiative Transfer, Vol. 88, p. 357-406.
87. Michael I. Mishchenko, Larry D. Travis, Daniel W. Mackowski, (1996), T-Matrix Computations of Light Scattering by Nonspherical Particles: a Review, Journal of Quantitative Spectroscopy & Radiative Transfer, Vol. 55, No. 5, p. 535-575.
88. Melvin Lax, (1951), Multiple Scattering of Waves, Reviews of Modern Physics, Vol. 23, No. 4, p. 287-310.

89. C. KohAk, J. Jakes, P. Stepanek, F. Petras, M. Karska, J. Krepelka, J. Perina, (1991), Effect of Multiple Light Scattering on Transmitted and Scattered Light, Applied Optics, Vol. 30, No. 33, p. 4865-4871.
90. Sidney F. Ray, (1997), Applied Photographic Optics, 2nd ed, Focal Press.
91. Qiang Lin, Nigel M. Allinson, (2006), FPGA-based Optical Distortion Correction for Imaging Systems, Signal Processing, 8th International Conference.
92. Douglas A. Ross, (1991), Focused Laser Beam Effects in Optical Particle Sizing by Dynamic Light Scattering, Applied Optics, Vol. 30, No. 33.
93. L. A. Shepp, Y. Vardi, (1982), Maximum Likelihood Reconstruction for Emission Tomography, IEEE Transactions Medical Imaging, Vol. 1, Is 2, p. 113-122.
94. Ravi P. Agarwal, Maria Meehan, Donal O'Regan, (2001), Fixed Point Theory and Applications, UK: Cambridge University Press.
95. Iker Montes-Burgos, Dorota Walczyk, Patrick Hole, Jonathan Smith, Iseult Lynch, Kenneth Dawson, (2010), Characterisation of Nanoparticle Size and State Prior to Nanotoxicological Studies, journal of Nanoparticle Research, Vol. 12, Is. 1, p. 47-53.
96. H. Saveyn, B. De Baets, O. Thas, P.Hole, J.Smith, P.Van der Meeren, (2010), Accurate Particle Size Distribution Determination by Nanoparticle Tracking Analysis Based on 2-D Brownian Dynamics Simulation, Journal of Colloid and Interface Science, Vol. 352, No. 2, p. 593-600.
97. Andrew Malloy, Bob Carr, (2006), NanoParticle Tracking Analysis-The Halo TM System, Particle & Particle Systems Characterization, Vol. 23, Is. 2, p. 197-204.

98. Michael. I. Mishchenko, (1992), Light Scattering by Randomly Oriented Axially Symmetric Particles, Journal of the Optical Society of America, Vol. 9, Is. 3, p. 497-497.

99. Michael. I. Mishchenko, Larry D. Travis, Andreas Macke, (1996), Scattering of Light by Polydisperse, Randomly Oriented, Finite Circular Cylinders, Applied Optics, Vol. 35, Is. 24, p. 4927-4940.

100. Thierry Savin, Patrick S. Doyle, (2005), Static and Dynamic Errors in Particle Tracking Microrheology, Biophysical Journal, Vol. 88, p. 623–638.

101. NASA, Goddard Institute for Space Studies, access in (2012), online Available: http://www.giss.nasa.gov/staff/mmishchenko/brf/.

102. L.M. Lacava, B.M. Lacava, R.B. Azevedo, Z.G.M. Lacava, N. Buske, A.L. Tronconi, P.C. Morais, (2001), Nanoparticle Sizing: a Comparative Study Using Atomic Force Microscopy, Transmission Electron Microscopy, and Ferromagnetic Resonance, Journal of Magnetism and Magnetic Materials, Vol. 225, p. 79-83.